Aus der Radiologischen Klinik der Universität Heidelberg
Klinik für Radioonkologie und Strahlentherapie
Ärztlicher Direktor: Prof. Dr. med. Dr. rer. nat. Jürgen Debus

Treatment plan robustness in pancreatic patients treated with scanned ion-beam therapy: Inter- and intra-fractional aspects

Inauguraldissertation
zur Erlangung des Doctor scientiarum humanarum (Dr. sc. hum.)
an der
Medizinischen Fakultät Heidelberg
der
Ruprecht-Karls-Universität

vorgelegt von
Vania Batista
aus
Lissabon, Portugal
2016

Dekan: Prof. Dr. med. Wolfgang Herzog
Doktorvater: Prof. Dr. rer. nat. Oliver Jäkel

Contents

List of abbreviations

3D	Three-dimensional
4D	Four-dimensional, 3D plus time
4DCT	Time Resolved Computed Tomography
4DDRec	4D Dose Reconstruction
4DDSim	4D Dose Simulation
4DMRI	Time Resolved Magnetic Resonance Imaging
accWEPL	accumulated Water-Equivalent Path Length
ACS	Accelerator Control System
BDS	Beam Delivery Sequence
BEV	Beam's Eye View
CC	Cranio-Caudal
ConfInt	Confidence Interval
COM	Centre Of Mass
CN	Conformity Number
CT	Computed Tomography
CTV	Clinical Target Volume
DICOM	Digital Imaging and Communications in Medicine
DIR	Deformable Image Registration
DKFZ	German Cancer Research Center
DNA	DeoxyriboNucleic Acid
DOF	Degree Of Freedom
DRR	Digitally Reconstructed Radiography
DSC	Dice Similarity Coefficient
DTA	Distance To Agreement
DVH	Dose-Volume Histogram
FWHM	Full Width at Half Maximum
GD	Geometric Distortion
GM	Gradient Magnitude
GSI	GSI Helmholtz Center for Heavy Ion Research
GTV	Gross Tumour Volume
HD	Hausdorff Distance
H_{CTV}	Homogeneity Dose of the Clinical Target Volume
HIT	Heidelberg Ion-Beam Therapy Center
HLUT	Hounsfield Look-Up Table
HU	Hounsfield Unit
IC	Ionisation Chamber
ICE	Inverse Consistency Error
IES	Iso-Energy Slice
JD	Jacobian Determinant
IMPT	Intensity Modulated Particle Therapy

IMRT	Intensity Modulated Radiation Therapy
ITV	Internal Target Volume
LEM	Local Effect Model
LET	Linear Energy Transfer
Linac	Linear accelerator
LQ	Linear Quadratic
LMDOUT	List Mode Data OUTput of the beam delivery sequence
NIRS	National Institute of Radiological Science
NP	Number of Particles
MI	Modulation Index
MFO	Multifield Optimisation
MRI	Magnetic Resonance Imaging
MPOS	Motion Positions
MSE	Mean Squared Error
OAR	Organ-At-Risk
OER	Oxygen Enhancement Ratio
PACS	Central Picture Archiving Systems
PET	Positron Emission Tomography
PRV	Planning Organs at Risk Volume
PSI	Paul Scherrer Institut
PTV	Planning Target Volume
PV_{in}	Percentage of Voxels within an acceptance range
PV_{norm}	Normalized PV_{in}
QA	Quality Assurance
r	Pearson correlation coefficient
R^2	Coefficient of determination
RBE	Relative Biological Effectiveness
RP	Raster Point
RST	Raster Field
RT	Radiation Therapy
SFUD	Single Field Uniform Dose
SFO	Single Field Optimisation
SI	Superior-Inferior
SOBP	Spread Out Bragg Peak
TCS	Therapy Control System
TPS	Treatment Planning System
TRiP	Treatment Planning for Particles
VBM	Volumetric Boolean Mask
VFL	Vector Field Length
VOI	Volume Of Interest
WEPL	Water-Equivalent Path Length

Chapter 1

Introduction

1.1 Motivation

Pancreatic patients continue to have one of the worst prognosis, being the 7^{th} deadliest cancer worldwide (Ferley et al. 2013) and the 4^{th} in Germany, with a 5-year overall survival rate of 8% (*Cancer in Germany 2009–2010. 9th edition.* 2014). Usually patients with early-stage cancers undergo surgery, while chemo-radiotherapy is the standard option for advanced cancers. These patients suffer mainly from recurrences in the primary tumour periphery (Kessel et al. 2013), indicating the need of dose escalation to improve the local control while limiting side effects.
Ion-beam therapy with proton or heavy ion-beams has been pointed out as a possible alternative for these patients (Combs et al. 2013; Tsujii et al. 2013). Its physical characteristics offer the possibility for highly conformal treatments, while from a radiobiological viewpoint heavy ions increase the relative biological effectiveness specially in the tumour region (Durante and Loeffler 2010). Additionally, when the dose is delivered to the tumour through a beam scanning technique a potential gain in dose conformity is obtained, which is reflected in the widening of the therapeutic window (Moding, Kastan, and Kirsch 2013).
Nevertheless, a strong drawback from this precision radiotherapy modality is the high sensitivity of the ion range to density changes in the beam-path, which reduces the tumour coverage, increases the dose inhomogeneities and may cause overdose in normal tissues. These variations can result either from anatomy changes between treatment sessions (inter-fractional), patient positioning, patient's motion during the treatment delivery (intra-fractional) or beam application uncertainties (range, position and width).
Inter-fractional changes in pancreatic patients occur due to tumour volume changes, organ filling (intestine and stomach) and loss of adipose tissue (Dalal et al. 2012). Intra-fractional variations are caused by respiration and peristaltic induced movement (Goldstein et al. 2010; Kumagai et al. 2009). Besides range changes, these variations may result in an inhomogeneous dose distribution, as consequence of the interference between the dynamic beam delivery and the target motion in scanned beam delivery systems. This phenomenon is called interplay effect.
The assessment of the impact of the motion on the delivered treatment dose, and the evaluation of motion mitigation techniques to be implemented in the clinical environment, must be conducted prior to the application of ion-beams to pancreatic patients (Bert and Durante 2011). Consequently, from the pre-implementation phase to the actual irradiation of the patients, the application of scanned ion-beams to pancreatic

patients was investigated at the Heidelberg Ion-Beam Therapy Center (HIT) .

This dissertation was supported by the Deutschen Forschungsgemeinschaft (DFG) within the Klinische Forschergruppe Schwerionentherapie (KFO 214) and by the Heidelberg University Hospital.

1.2 Scope of this work

This dissertation focuses on the quantification of the dosimetric impact of the inter- and intra-fractional anatomic changes observed for pancreatic patients when treated with ion-beams delivered through a scanning system. Moreover, clinically feasible strategies were developed in order to increase the treatment robustness against the resulting range uncertainties and interplay effect.
The analysis is gradually accomplished through the definition of robust beam arrangement, evaluation of safety margins to the tumour, prediction of dosimetric changes based on pre-treatment imaging, and, finally, analysis of the influence of the breathing motion and its variability on the delivered dose.
The study is also split in a pre-implementation stage, i.e. prediction of the potential uncertainties and definition of protocols, and in the follow-up stage, in which the current patients were evaluated and changes to the current protocols suggested.

1.2.1 Structure of the dissertation

This dissertation is organised in 7 chapters. Chapter 2 gives an overview of the physical and biological characteristics of the ion-beams, technical issues in an ion-beam facility, the impact of organ motion on beam delivery, as well as the treatment planning process and the main challenges of pancreatic cancer. Chapter 3 gives an insight into the software and tools used in this work and describes their main functionalities and limitations.
Chapter 4 covers the inter-fractional motion and strategies to increase the planning robustness, while chapter 5 focuses on the assessment of the intra-fractional motion component and methods to deal with it. Chapter 6 gives an outlook of an MRI-based approach for motion monitoring, aiming to determine the importance of the motion detection via MRI, and to define the procedure to its inclusion in the clinical workflow for future patients.
Finally, a discussion of the results and conclusions is presented in chapter 7.

Chapter 2

Fundamentals and background

The combination of physical and biological advantages of ions beam irradiation over photon therapy contributed to the worldwide increase of this therapeutic modality in the last years. From the sixty-two worldwide facilities in operation just ten of them are prepared to deliver charged particles heavier than protons, as cited by the Particle Therapy Co-Operative Group (PTCOG).
This chapter reviews the main characteristics of charged particles beams, that made this technique arise as a potential therapeutic for many tumour locations, describes the workflow of an ion-beam treatment, the major drawbacks of this technique and concludes with the reasoning of its application in pancreatic patients.

2.1 General rationale for ion-beam therapy

Charged particles have been pointed as the ideal irradiation technique for a tumour in challenging locations, i.e., surrounded by risk organs, and also for radio-resistant tumours. These advantages emerge from the physical aspects of how their energy is deposited in tissues and how the radiobiology is affected due to the high density of energy depositions inside the cell.

2.1.1 Physical aspects

The growing application of charged particles in the radiotherapy field comes mainly due to its very characteristic depth-dose profile, which exhibits low entrance dose and a strong increase with a sharp fall-off dose at the end of its path - the Bragg peak (Schardt, Elsässer, and Schulz-Ertner 2010). This depth profile contrasts with the conventional photon beam, where the dose distribution in the patient suffers an exponential decline in depth, as shown in the figure (2.1 a).
The Bragg peak reflects the phenomenon that high energetic particles deposit relatively little energy when entering in the tissues but tend to deposit extremely large amounts of energy in a very narrow peak at the end of their range. This behaviour is due to the energy loss increasing with lower velocities, as shown below. The depth and magnitude of this Bragg peak is determined by the mass and charge, as well as the initial energy of the particle (IAEA 2008).
In clinical situations, with tumours of thickness of centimeters, the Bragg peak must be broadened by use of a superposition of beams with different energies, a so-called

spread-out Bragg peak, SOBP, (see fig. 2.1 b).

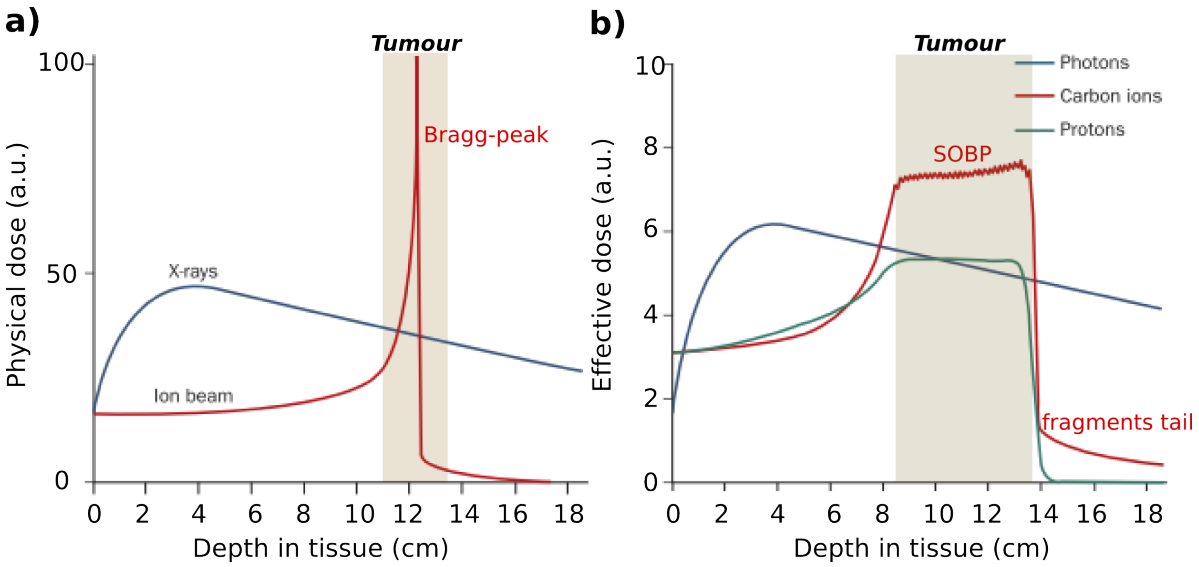

Figure 2.1: Depth dose profile comparison for photons, protons and carbon ions. a) Depth dose profile for X-rays and high-energy charged particles. b) For clinical targets sizes the spread-out Bragg peak (SOBP) distributes the dose within the tumour. The physical dose profile is corrected according to the RBE in the tumor region. The differential RBE of carbon ions leads to an increase of effectiveness specially in the SOBP as compared to protons. For the case of heavy charged particles, as result of nuclear interactions and fragmentation, a dose tail after the Bragg peak is formed. Image adapted from Durante and Loeffler (2010)).

Stopping power of charged particles

As in the case of photons the absorbed dose D, in Gray [Gy], is proportional to the mean energy deposited by the ionizing radiation in a mass element (IAEA 2007). For charged particles this mean energy is calculated as the product of the particle fluence and the energy loss of the particles per unit path length dE/dx, describing the slowing-down process of the particles in the tissue interaction, named as linear stopping power, i.e, $S = -dE/dx$.
For therapeutic energies ($\leq 220MeV$ for protons and $\leq 430MeV/u$ for carbon ions), the stopping power is mainly due to electronic interactions and the energy-loss is dominated by the inelastic interaction with the target electrons. It is given by the Bethe-Bloch formula (Linz 2011):

$$-\frac{dE}{dx} = \frac{4\pi e^4 Z_t Z_p^2}{m_e v^2}\left[ln\frac{2m_e v^2}{\langle I\rangle} - ln(1-\beta^2) - \beta^2 - \frac{C}{Z_t} - \frac{\delta}{2}\right] \tag{2.1}$$

This relativistic expression includes the shell correction factor, C/Z_t, the density effect correction, $\delta/2$, the nuclear charge of the projectile and target, Z_p and Z_t, respectively, the mass and charge of the electron, m_e and e, and the mean ionisation energy of the target atom, $\langle I\rangle$.

Range of particles

Given the energy-loss the total path length of the particle with initial kinetic energy *E* can be determined from its integration, which is referred as continuous slowing down approximation (CSDA) (ICRU 2005). Assuming that ions travel only straight ahead (negligible lateral scattering) the total path length is approximated to the mean range, *R(E)*, as in the equation (2.2).

$$R(E) = \int_{E}^{0} \left(\frac{dE'}{dx}\right)^{-1} dE' \tag{2.2}$$

However, the successive ionisations present small statistical fluctuations in the energy loss of the individual particles which leads to a broadening of the peak in the depth dose distribution, a phenomenon called range straggling (Newhauser and Zhang 2015).

Multiple Coulomb scattering

An ion passing close to a nucleus will be elastically deflected due to Coulomb scattering, losing a negligible amount of energy but experiencing changes in the trajectory, which although small are significant due to the large number of scattering events. This physical process is characterised by the scattering power (Newhauser and Zhang 2015).
The multiple Coulomb scattering will result in a considerable blur of the lateral penumbra sharpness for protons beams, but it is relatively small for heavy ions. This is simply due to the higher mass, which leads to generally smaller deflection. Hence, this small lateral deflection of heavy ions in the medium makes this therapeutic modality optimal for challenging locations, i.e, tumours surrounded by organs-at-risk (OARs).

Nuclear interactions and fragmentation

Charged particles undergo nuclear interactions with the target nuclei of the absorbed material. These interactions can be either elastic (leading to Coulomb scattering) or non-elastic. The latter are of strong significance for particle therapy as they result in the non-conservation of the total kinetic energy of the process: light fragments are created from the disintegration of the projectile and target nuclei, ions are extracted from the target and a build up of neutrons, protons and other secondaries occurs (Schardt, Elsässer, and Schulz-Ertner 2010).
For ions heavier than protons, with energies of several hundreds of MeV/u, nuclear interactions result mainly in the production of the projectile nuclear fragments. These lower-Z fragments retain most of the velocity and mass of the primary particle, but because of their lower charge their range is larger than that of primary projectile. As a consequence, a dose tail after the Bragg peak is formed, as depicted in the figure (2.1 b) for a carbon ions beam. Target fragments are also produced, but with very little energy, so that they do not lead to a significant change of the particle spectrum.

2.1.2 Biological characterisation

The potential of radiation to induce cell killing through DNA damage is quantified by the number and density of single or double strand break lesions in the DNA molecule (Joiner and Kogel 2009).
The number of surviving cells, when a tissue is irradiated with a certain dose is a common indicator of the therapeutic quality and is phenomenologically described by the linear-quadratic (LQ) model, which relates the fraction of surviving cells S after an absorbed dose D as described by the equation (2.3).

$$S(D) = e^{-(\alpha D + \beta D^2)} \tag{2.3}$$

The radio-sensitivity of cells is characterised by the parameters α and β parameters, which related to the way that the cell is inactivated, i.e. by a single lethal event or by accumulation of sub-lethal events, respectively (Joiner and Kogel 2009).

Relative biological effectiveness

Charged particles interact with targets differently than X-rays, hence their efficacy is defined by the Relative Biological Effectiveness (RBE), which represents the ratio of the X-ray dose divided by the dose of ion that results in the same biological effect. Therefore, in ion-beam therapy, the dose is referred as biological dose or RBE-weighted dose, i.e. the product of the absorbed dose and RBE, given in Gy (RBE) (IAEA 2007). The RBE depends on several parameters, including the cell type, the dose, the particle type and the beam energy. This yields a different RBE for each tumour location and treatment field that has to be modulated during the treatment planning in order to obtain an accurate calculation of the effective dose in tissues.
For protons, a constant RBE of 1.1 is used as an approximation to convert the physical dose to the biological effective dose (Bauer et al. 2016; Paganetti 2014), figure (2.2 a). However, studies showed that in the very distal part of the SOBP the RBE increases. This behaviour is known from in in-vitro studies, but it is not considered to be clinically relevant.
For carbon ions the RBE values are generally much higher and more variable, and its variation along the Bragg curve needs to be considered in treatment planning (see fig. 2.2 b). Also the tumour and ion species dependence has to be taken into account.
Different models are available to describe the RBE effect for each voxel of the tissues, like the approaches developed at the Lawrence Berkeley Laboratory (LBL), National Institute of Radiological Science (NIRS) and in the GSI Helmholtz Center for Heavy Ion Research (GSI).
The concept developed by GSI, also adopted by HIT, is called Local Effect Model (LEM) (Elsässer, Krämer, and Scholz 2008) and estimates the RBE for different ions and cell types as a combination of the clinical photon dose response and the microscopic track structure of the various ions in the spectrum of secondary particles.

Linear energy transfer and track structure

The linear energy transfer, LET, describes the deposited energy in the target medium by the slowing-down of the primary particles and is a particularly important concept

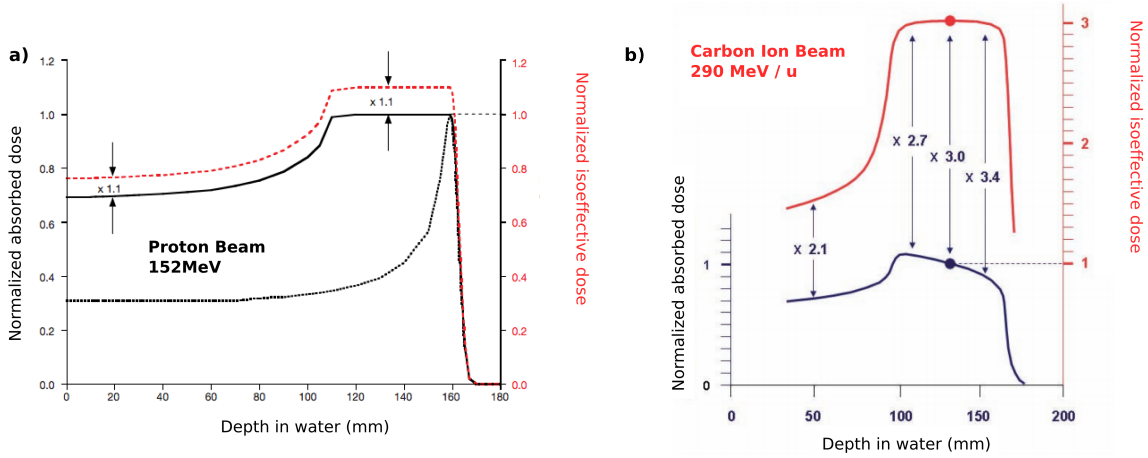

Figure 2.2: a)Variation in depth of the absorbed dose of a monoenergetic (dotted line) and a spread out (slid line) proton beam and the corresponding RBE weighted dose, assuming a factor of 1.1. at all depths.b) Depth dose profile of the absorved dose and isoeffective dose variations for a SOBP of a carbon ion-beam. The RBE increases with depth. Source IAEA (2008).

in particle therapy (Durante and Loeffler 2010; Schardt, Elsässer, and Schulz-Ertner 2010). This happens as RBE is directly related to LET and, therefore, increases with it for clinically relevant LET values. The LET of ion-beams is partically identical to the stopping power and thus depends quadratically on the projectile charge. Hence, fast moving light ions have low LET, and their biological effectiveness is close to that of X-rays; slow heavy ions have high LET, and are more effective than X-rays for killing cells (IAEA 2007).

For high-LET particles there is an enhancement of the biological effectiveness at the Bragg peak region, that is due to the dense ionisation on the primary particles tracks, which produces more DNA damage. Thus the inspection of the spatial distribution of deposited energy for different particles is an indicator of the biological effect induced by particles. Particles with a higher LET show a more dense track structure and hence larger biological effects caused by ionizing radiation. This is being considered as advantageous for the treatment of radio-resistant tumours.

Moreover, high-LET particles result in different biological response of the cells. One of these aspects is related with the oxygen enhancement ratio (OER), which measures the tumour sensitivity to the presence or absence of oxygen by the ratio of radiation dose required to produce a given effect with no oxygen present (hypoxia) to the dose required to produce the same effect in the normal oxygen concentration (normaxic). For these particles the OER is reduced, which is mainly beneficial in the treatment of certain radio-resistant tumours possessing a large percentage of hypoxic cells (Schlaff et al. 2014).

Another biological aspect affected by the LET is the cell cycle sensitivity to the radiation. Opposed to the photon irradiation in which radiation damages cells occurs mainly in the cell-division stage, using heavy ions the cycle sensitivity is very frail. This characteristic will be essentially important for slowly growing tumours, which are usually photon-resistant.

2.2 Implementation in a clinical facility

An ion-beam facility comprises different components and can exhibit different implementations of beam production, transport and delivery to the tumour. Consequently, the adopted Treatment Planning System (TPS) must be able to handle the facility features and optimise a clinically feasible plan.

2.2.1 Ion sources, accelerator and transport lines

Either proton or heavy ion-beams are produced in ion sources and then accelerated in order to reach the necessary depth in the patient. This corresponds approximately to an energy of 150 MeV and 250 MeV/u for protons and carbon ions, respectively, for 16 cm depth.
An injection system injects ions either directly from the source (e.g. for protons in a cyclotron) or from the low energy beam-line into the accelerator.
The accelerator can be either a cyclotron or a synchrotron. In a cyclotron the beam intensities can be controlled but not the extracted energy, which can only be achieved by means of passive degraders in the beam line. On the contrary, synchrotrons provide a pulse-to-pulse active energy variation but require an injection system and a more complex extraction system, as well as, energy dependent high energy beam-lines.

2.2.2 Beam delivery systems

The transport of the particle beam to the tumour and its distribution over the prescribed volume can be performed by a passive or an active delivery system, or a combination of both (Kraft 2000; Schulz-Ertner and Tsujii 2007).
The two extreme forms, the fully passive system (Chu, Ludewigt, and Renner 1993) and the fully active system (Haberer et al. 1993), are explained below.

2.2.2.1 Passive systems

In a passive system, as the one depicted in the figure (2.3 a), the beam is three- dimensionally modulated using physical and mechanical field shaping elements.
The initially mono-energetic sharp beam is broadened by a scattering device to a flat profile in the transverse direction. In depth, the Bragg peak is spread out by a range modulator for the total length of the tumour volume. This SOBP is then shifted in depth by absorber plates, named range-shifters.
For each patient and field, the lateral beam collimation is obtained by a physical collimator and distally by a range compensator that considers the tissue composition. This system has as limitation the fixed SOBP width, due to which the range adjustment at the distal contour of the target may result in dose deposition outside the proximal region of the target volume.
For treatments with carbon ions-beam it is also necessary to combine a rotating modulator wheel, or ridge filter, that produce a constant biological effect, which considers the RBE variation in depth. However, this hardware-generated RBE does not consider

the tissue-specific effects.

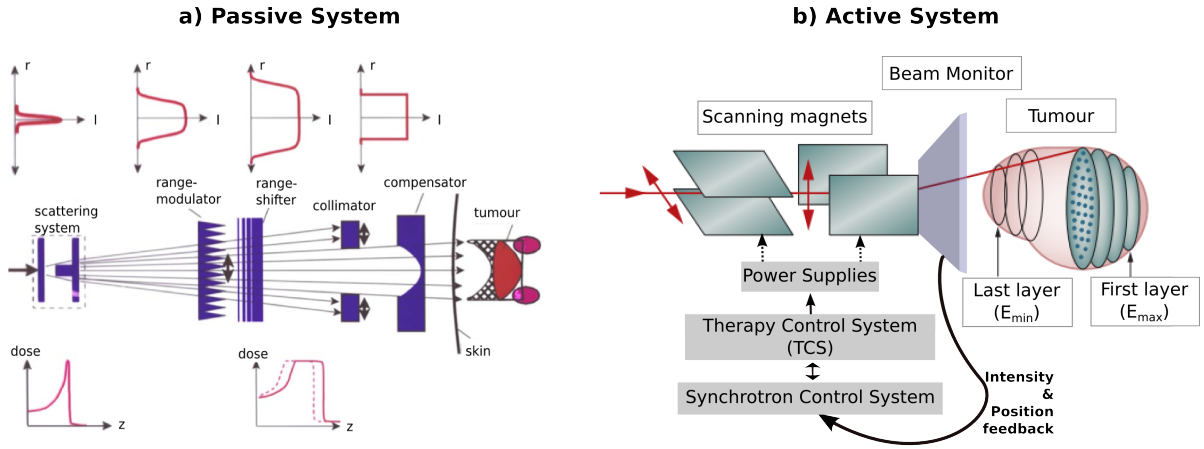

Figure 2.3: Diagram of two possible configurations for a beam shaping system:
a) Passive - the initial pencil beam is broadened by a scattering system. Thus, the beam is conformed to the target volume through beam shaping devices (i.e. collimator, compensator). Figure from Schardt, Elsässer, and Schulz-Ertner (2010)).
b) Active - scheme of the raster scanning system implemented at GSI and HIT, with representation of the dipole magnets for the beam deflection and the synchrotron control system for the variation of the beam energy, figure adapted from Durante and Loeffler (2010)). In contrary to the figure representation, at HIT and GSI the irradiation is performed from the proximal target slice (E_{min}) to the distal one (E_{max}) as consequence of the Therapy Control System (TCS) configuration.

Active systems

The implementation of an active scanning system is based on the sampling of the tumour in iso-energy slices (IES) and voxels. Each voxel is irradiated with a pencil beam where the energy of the beam is changed per slice by a range shifter or directly at the accelerator. There are some variations of the active beam scanning, for instance the ”spot scanning” system from the Paul Scherrer Institut (PSI) (Pedroni et al. 1995), and the ”raster scanning” technique developed by GSI (Haberer et al. 1993), and also installed at HIT. A diagram of the second one is depicted in figure (2.3 b).
In raster scanning systems each IES of the tumour is irradiated continuously point-by-point in a defined path through the deflection of the pencil beam in the horizontal and vertical direction using dipole magnets. While in spot scanning the beam is paused during the transition from one scan position to the next one. In depth, the energy of the pencil beam is adjusted resulting in irradiation of a different IES.
The advantage of active systems, compared with the passive beam delivery, is the high dose conformation to the target without the need of physical patient-specific compensators, collimators and modulator wheel. Moreover, active scanning systems allowed for the improvement of the treatment accuracy with a more complete modelling of the RBE for carbon-ion treatments (Elsässer, Krämer, and Scholz 2008; Krämer et al. 2000).

The Heidelberg Ion-Beam Therapy Center

The Heidelberg Ion-Beam Therapy Center, as part of the University Clinic of Heidelberg, is based on the pilot project initiated at GSI, where an experimental active unit was available before the building of the HIT facility (Haberer et al. 2004).
HIT has three clinical beam-lines, as shown in the scheme of figure (2.4), where one of them with a scanning ion gantry. The gantry allows the use of arbitrary beam directions in the patient anatomy, by combination of couch and gantry rotation. Additionally, an experimental beam-line is available for research purposes. All the rooms are equipped with the fully active intensity-controlled raster-scan system.
Three electron cyclotron resonance ion sources enable the use of protons, carbon, helium and oxygen beams, each at a single time (Winkelmann et al. 2014). Clinically, only the first two are used, while the others two are used for pre-clinical studies. Thanks to a Linear accelerator (Linac)-synchrotron, all the beam specifics can be controlled in energy, focus and intensity, resulting in a library of energies between 50 and 430 MeV/u, which corresponds to water-equivalent ranges from 2 to 30 cm, and spot sizes between 4 and 10 mm of full width at half maximum (FWHM) (Haberer et al. 2004).
The facility also comprises a combined positron emission tomography (PET) and computed tomography (CT) machine, that can be used to assess the accuracy of the ion range. After the treatment the distribution of the β^+-emitter in the tissues, which were formed in nuclear fragmentation reactions during the irradiation, can be used to determine the treatment accuracy by comparison with the Monte Carlo simulated activity distribution, based on the planned dose distribution (Bauer et al. 2013).
The patient positioning is verified in-room using fluoroscope and X-ray planar imaging. Exterior to the treatment room, for some indications, the positioning is also verified using the PET/CT machine.

2.2.3 Treatment planning systems

The treatment planning system must handle all the features and limitations facility-specific that affect the planning process. The facility characterisation is given by the Therapy Control System (TCS): whether the beam shaping system is passive or active; if it is carried out actively by spot scanning or raster scan; if the energy variation is a passive or active system and all other characteristics of each component that influences the planned dose (Jäkel 2012; Linz 2011). Beyond that, the used ion species also need to be considered in the beam and biological models.
Due to the facility-specific TPS requirements, the following description is adapted to the specifications of HIT, i.e, active energy variation with raster-scanned delivery, for protons and carbon ions, from the physics and biological point.
The current treatment planning used in the clinical routine at HIT is the Syngo® RT Planning (*Siemens Oncology Care Systems, Erlangen, Germany*), that was based on the research prototype TRiP98 (TReatment PlannIng for Particles), developed at GSI (Krämer and Scholz 2000; Krämer et al. 2000). Both systems were used in this dissertation and a detailed description of their functionalities and limitations is presented in the chapter (3.1). An explanation of the physical and biological models is described below.

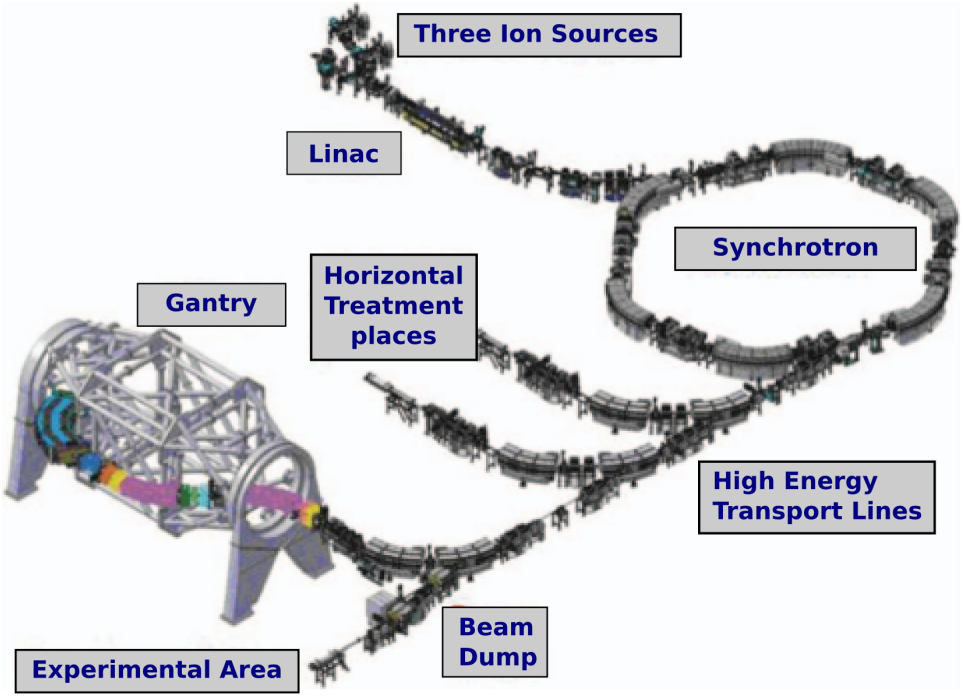

Figure 2.4: Overview of the HIT facility, with the representation of the ion sources, synchrotron, beam transporting lines, the three treatment rooms (two horizontal and one gantry) and an experimental area. Figure from Winkelmann et al. (2014).

Water-equivalent path length

The TPS must be able to perform dose calculation based on the patient-imaging data taken prior to the treatment. This is obtained from the CT information, where the Hounsfield units (HU), related to the electron density, need to be scaled to the corresponding equivalent depth in water. This conversion is performed by the water-equivalent path length (WEPL) concept and is given in a Hounsfield look-up table (HLUT), as represented in figure (2.5) for a carbon ion-beam.
The WEPL can be determined by measuring CT HUs of tissue equivalent phantom materials, and by their integral stopping powers of the charged particle under calibration. Afterwards, an stoichiometric calibration of CT HUs to particle stopping powers is performed (Rietzel, Schardt, and Haberer 2007; Schneider et al. 2002).
The WEPL parameter is used to characterise the beam penetration range into the patient anatomy and it is employed during the dose calculation stage.

Note that inaccuracies between the range of the planned and delivered beams can result in a potential mismatch of the target and dose to nearby critical structures. Moreover, the TPS besides the values from the CT correspondent to the patient's body, also the other treatment items, as immobilisation devices, such as treatment couch and all the components in the beam path, need to be considered during the treatment plan process (Newhauser and Zhang 2015).

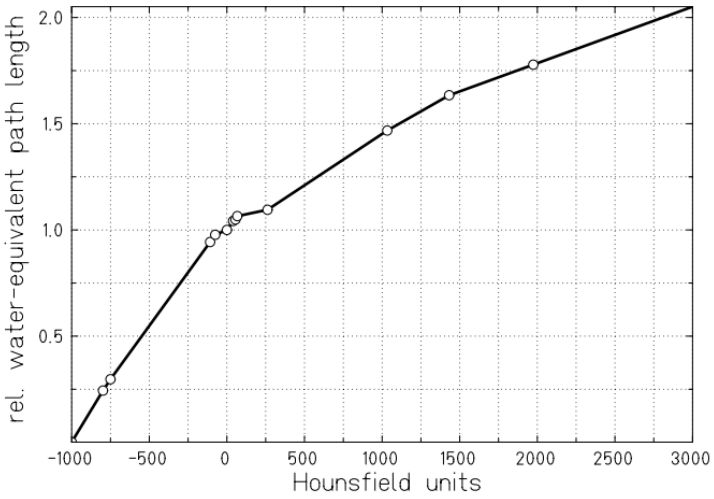

Figure 2.5: Representation of the Hounsfield look-up table for the carbon ion treatment planing. The measured data is represented by circles connected by the straight lines. Figure from Rietzel, Schardt, and Haberer (2007).

Model of the Bragg peak and SOBP curves

The beam model in TRiP98 describes each individual carbon pencil beam by a double Gaussian, considering not only the multiple scattering around the primary beam but also taking into account the nuclear scattering fragments resulting from the beam interacting with the nozzle materials. Relative to the proton beam model a single Gaussian is used. The total dose delivered by a beam D_{beam}, is the summation of the total number of pencil beams *npb* weighted by their specific particle number N_{bp} (cf. equation 2.4). The dose generated by an individual ion-beam of energy E_{beam}, centred at (x_0,y_0), at a *r* distance from the beam centre is given by the energy loss distribution d(E_{beam},z) dependent of penetration depth *z* and its lateral dose distribution *l(r,z)*, therefore assumed by a double Gaussian profile for carbon ions (Parodi, Mairani, and Sommerer 2013) and single for protons.

$$D_{beam}(E_{beam}, x) = \sum^{npb} d(E_{beam}, z).l(r, z).N_{bp} \tag{2.4}$$

For low-energetic heavy ion-beams (i.e. below about 150 MeV/u) the Bragg peak become very sharp driving the need of many energy slices to deliver a homogeneous dose distribution. Therefore, a passive beam shaping element, called ripple filter, is commonly used to broaden the Bragg peak in depth (Krämer et al. 2000). Additionally, the limitation of the monitoring to measure low particle fluences is also overcome, due to the increase of the minimum number of particles per point in comparison to the situation without ripple filter.

Transport models of the beams

For heavy ions, as carbon ions, the ion transport in the tissue must include not only the energy loss of the primary particle (beam attenuation), as for proton beams, but also the energy loss straggling and secondary fragments production.
These physical processes are calculated in TRiP98 using the YIELD transport model

(Krämer et al. 2000); wherein each slice of the target volume the ingoing and outgoing energy spectra, can be defined and related with the ingoing/outgoing spectra from the neighbour slices. The number of particles can change between slices due to the secondary particles generation. This information is given by the cross section of the parent species. The depth dose distribution is obtained from the energy integration across all the slices, which also includes the dose tail after the Bragg-peak. An alternative to this model is the description of fragmentation using a Monte Carlo algorithm, like FLUKA (Battistoni et al. 2016).
Concluding, the physical dose in tissue produced by each single beam is a function of its width, distance from the beam centre, the number of particles, and energy loss distribution (energy and depth dependent).

Biological dose

The biological model implemented at TRiP98 and Syngo® RT considers, for carbon ions, the RBE variation with the depth, dose and the fragment spectra of the entire beams. For heavy ions, this is not only implemented as a scaling factor but as an entire optimisation problem, where the biological interaction process is described by the LEM (Krämer and Scholz 2000).
The LEM combines the information of the cells response to the X-ray, the ion-track structure and the size of the cell nucleus, correlating the local ionisation densities to the biological effectiveness in each point of the treatment field. As a consequence the RBE distribution is not homogeneous as can be shown in figure (2.6) for a pancreatic patient in the TPS Syngo® RT.
For protons, a RBE of 1.1 is assigned for all beam energies and depths (ICRU 2007), as discussed in the section (2.1.2).

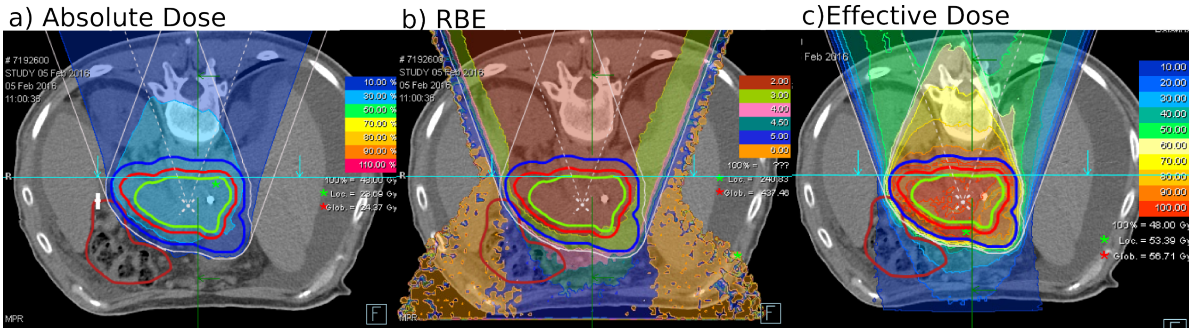

Figure 2.6: Transveral view of the distribution of the physical and biological dose with the respective RBE distribution for a pancreatic patient planned for carbon ions.

Plan optimisation

For facilities with active field shaping and energy variation, the TPS must be able to perform the treatment plan optimisation through the different combination of the beam intensities, positions and energies. In order to handle this complex library of parameters, the optimiser offers the inverse planning functionality. From the definition of the target prescription dose, constraints to the OARs and beam incidence directions, the optimiser determines the set of plan parameters that match the planner requests.

The plan optimisation to the desired dose distribution can be performed through Single-Field Uniform Dose (SFUD) or Intensity Modulated Particle Therapy (IMPT). When the plan is optimised using IMPT, it uses the full potential from the scanning delivery, hence all the treatment fields are optimised simultaneously resulting in beams that may be inhomogeneous in dose individually, while when summed up create a homogeneous dose. Consequently, more optimal dose distributions in terms of organ at risk sparing are achievable through the use of higher dose gradients. Lomax (2008c) stated that these plans are highly sensitive to set-up and range uncertainties. In contrast, with SFUD each field delivers a uniform dose distribution, through the different weighting of each spot but with lower dose gradients. However, strategies to improve IMPT robustness are possible and may result in better plans compared to the SFUD (Chen et al. 2012; Liu et al. 2012b).

Altogether, for a beam scanning facility, the output of the TPS is given in terms of the number of raster points (RPs) and their position in a defined order (scan path), for each iso-energetic slice of the target volume. Furthermore, a TPS in ion-beam RT should be likewise able to account for uncertainties, e.g. range, positioning and HU-WEPL conversion inaccuracies. This topic is addressed in the next section.

2.3 Uncertainties in ion-beam therapy

Several sources of uncertainties are present in the clinical application of ion-beams (Li 2012) which need to be quantified, the dosimetric impact evaluated, and incorporated in the treatment plan in order to increase the treatment robustness. Some of these uncertainties originate from:

- Range uncertainty;
- Patient set-up error;
- Patient anatomical and physiological changes;
- Intra-fraction organ motion;
- Relative biological effectiveness (RBE) approximations.

These sources of uncertainties can have random and/or systematic error components. While random errors may blur the dose distribution, systematic errors may cause a shift of the cumulative dose distribution relative to the target and target dose inhomogeneities (Van Herk 2004). A systematic uncertainty arises for example, if the CT underlying treatment planning is not correct, as a result the range uncertainty will be carried along all treatment fractions.
Note that for many of these uncertainties, if from a random source as a set-up error and intra-fractional motion, a fractionated delivery has the potential to mitigate their significance (Lomax 2008b; Wölfelschneider et al. 2015).

2.3.1 Range uncertainty

As stated in the previous section (2.2.3), the beam range is determined from the WEPL (Rietzel, Schardt, and Haberer 2007; Schneider et al. 2002). The conversion process from the CT numbers of the patient's anatomy along the beam path to tissue-to-water

relative stopping power ratio exhibits uncertainties, which translate into beam range uncertainties. Examples are the uncertainties from the determination process of the conversion curves, imaging artifacts (e.g. beam hardening effects) and weak dependence of CT numbers on tissue compositions (Li 2012).
Clinically, proximal and distal margins of up to 3.5% of uncertainty have been added to the calculated beam range to accommodate for such uncertainties, especially for scattered broad beam techniques (Yang et al. 2012). Nevertheless, this procedure can compromise the dose to critical organs distally located to the target. Hence, when possible, beam angles for which the OAR are distal to the target are avoided.
For scanning techniques, the method to account for range uncertainties is more complex (Albertini, Hug, and Lomax 2011) since it also needs to include the misplacement of individual beam spots and uncertainties in IMPT optimisation algorithms. One of the approaches under investigation is IMPT optimisation algorithm based on worst-case dose distributions that include range uncertainty as well as set-up errors (Liu et al. 2012b). Therefore, this method is recalled in the next point.

2.3.2 Patient set-up error

The potential patient misalignment is, in photon radiotherapy included in the treatment planning by the use of margins to the tumour (Van Herk 2004). In charged particles the use of target margins has been shown to have limited effect to overcome these uncertainties. Moreover, these variations, even in the range of milimetres, can strongly degrade the dose distribution specially for plans highly modulated, such as IMPT plans (Lomax 2008a,b).
The improvement of the plan robustness in ion-beams can be achieved by incorporating the uncertainty information into the optimisation process (Fredriksson 2012; Unkelbach et al. 2009). This computation considers the systematic and random errors and can either be performed probabilistic or non-probabilistic, whatever uncertainties are assumed to have a normal distribution and optimised the expected value of a weighted sum of quadratic dose deviations (Unkelbach et al. 2009), or minimising the worst case penalty (Fredriksson 2012; Lomax 2008b). In this worst-case dose distribution, every target voxel takes the lowest dose that can occur for any error scenario and every healthy tissue voxel takes the highest dose.Therefore, this approach tends to overestimate the effect of the possible uncertainties and result in dose distributions less conformal to the target volume.

2.3.3 Inter-fractional anatomical and physiological changes

Besides the set-up uncertainty, the patient also experiences anatomic variations along the treatment course. These inter-fractional changes are usually due to weight loss, tumour shrinkage and organ filling variations (e.g. stomach, bladder, intestine).
The finite range of ion-beams makes this technique highly sensitive to tissue density changes (Bert and Durante 2011). Hence, these anatomic changes may strongly affect the beam path length during the beam delivery, reducing the quality of the planned dose distribution as a consequence of the pencil beams over- or under-shooting.
The inclusion of this additional inter-fractional uncertainty factor in the beam range could be performed with some mitigation strategies, as adapted Planning Target Vol-

ume (PTV) margins that consider range changes without compromising the dose to the normal tissues (Park et al. 2012) and selection of robust beam angle configurations (Cabal Arango 2012). The robustness of these plans needs to be quantified using an adapted metric, like error-bars for dose distributions and dose-volume histograms, for which site-specific robustness planning protocols still need to be established (McGowan et al. 2015). A possible option is to evaluate the plan against a database to help in the selection of the optimal plan.
The increase of the plan robustness usually results in a decrease in plan conformality, therefore finding the balance between dose conformation to the target and plan robustness is one of the main tasks to establish a site-specific robustness thresholds (Albertini, Hug, and Lomax 2011; McGowan et al. 2015).

In summary, several strategies are in research to improve the treatment plan robustness. However, limited integration of robust planning in a commercial TPS is available. Actually, the only solution is provided by RaySearch Laboratories AB (2015) through the calculation of the *minimax* optimisation, in which the optimisation functions are considered under the worst case scenario (Fredriksson, Forsgren, and Hårdemark 2011). This tool does not take into account, however, any effects resulting from fractionation and this tend to overestimate the effects of the these uncertainties. Therefore, clinical plans usually don't include directly in the TPS the robustness assessment, as part of the evaluation process, and no metric is yet available to their evaluation.

2.3.4 Intra-fractional organ motion

From the intra-fractional side, the leading factors for daily changes in the dose distribution are the breathing, cardiac beat and peristaltic movements.
Besides the influence on the radiological path length, the intra-fractional motion is also responsible for the dose degradation. This effect occurs firstly due to the inter-field motion (Lomax 2008b) and can be stronger if the treatment is delivered using scanning techniques, where the temporal interference between the scanning beam movement and the organ motion produces inhomogeneous dose distributions, the so-called intra-field interplay effects (Bert and Durante 2011; Bert, Grözinger, and Rietzel 2008). The diagram of figure (2.7) represents the formation of this intra-field interplay phenomenon. The sensitivity of the dose distribution to the motion has been heavily investigated, since the results from Phillips et al. (1992) in which a small target motion (below 3 mm) conducted to dose changes of up to 20% relative to the expected.
Due to these effects, scanned beams have been mainly employed to static, or quasi-static tumours. Otherwise, this impact must be attenuated through motion reduction or adapted beam delivery and planning strategies (Bert et al. 2014; Engelsman, Bert, and Paganetti 2011). Therefore, an indispensable task is the accurate motion monitoring with an adequate latency time.
A review of the used methods in ion-beam therapy are given below.

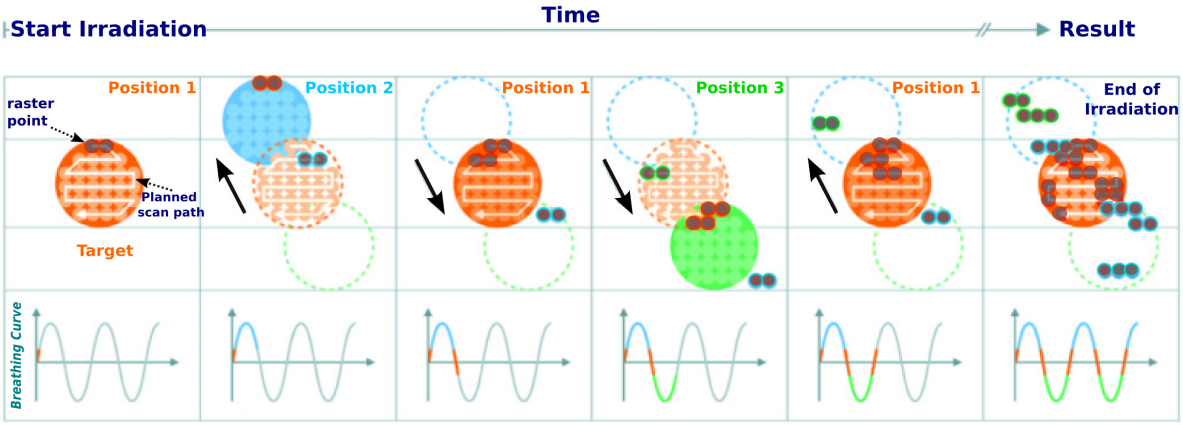

Figure 2.7: Diagram of a target that moves between maximum inhale (blue state) and maximum exhale (green state), according with the breathing displayed in the bottom curve. As a consequence, each raster point is delivered to a different target coordinate. Additionally, the beam moves along a pre-defined scan path within a slice, resulting at the end of the treatment in a dose degradation. Figure adapted from Bert, Grözinger, and Rietzel (2008)).

2.3.4.1 Motion monitoring

Several commercial systems are available for motion monitoring in radiation therapy. Its operation can be radiation-based, allowing the direct visualisation of the tumour motion, or based on a surrogate signal (e.g. breathing), which should be correlated with the tumour motion.
Concerning the systems for real time monitoring of the breathing, the most commonly available are the following:

- *Real-time position Management (RPM)* System, Varian Medical Systems. It is based on an infrared tracking camera and a reflective marker block.
- Spirometry-respiratory volume measurement, for example, the solution *Active Breathing Coordinator*, Elekta. It is a computer-controlled device that pauses the patient's breathing during the irradiation (assisted breath-hold).
- *AlignRT*, Vision RT. It maps the patient surface based on the triangulation signal from optical cameras.
- *Calypso system*, Varian Medical Systems. The system uses field generating coils implanted inside or close to the tumor whose positions are detected by an electromagnetic detector array.
- *AZ-733V Respiratory Gating System*, Anzai Medical Co.,Ltd. It uses a pressure sensor to detect the external respiratory motion.

The *AZ-733V Respiratory Gating System*, from here on called *Anzai*, was the system used in the dissertation, for the time resolved computed tomography (4DCT) acquisition and breathing monitoring of the patient during the treatment delivery. This system is constituted by a belt, which is fastened around the patient waist, a sensor port and a load cell (device of piezoelectric material). The sensor port is responsible for the amplification of the signal and it emits an analog signal to the *wave deck* hardware. Here, the signal is preprocessed, digitalised and sent as an input to the *Anzai* application software, running on an external computer. The software displays the motion and allows the setting of the control parameter of the *wave deck*. The tracer signal can be

manually corrected along the acquisition in magnification and position.
The working principle of the system is the translation of the pressure applied to the sensor, by the fastened belt across the chest, to inhale/exhale of the breathing cycle. The system assumes that the breathing cycle represents the tumour motion. The degree of correlation between these two data dictates the accuracy in the detection of baseline shifts, phase and amplitude changes of the tumour. Investigations on the correlation between the Anzai belt and other monitoring systems, as well the internal motion have been performed by several authors (Brevet 2011; Torres 2011). Brevet (2011) showed problems of reproducibility due to the system sensitivity to the location where the sensor is placed. However, was found for a thorax phantom a good correlation between the Anzai signal and the fluoroscopic data.

2.3.4.2 Motion mitigation strategies

Motion compensation methods can be organised into two main groups: (a) techniques in which the motion is eliminated/reduced, or (b) patient irradiation under free-breathing but accounting with the motion effects during the treatment planning or delivery.
Note that typically several of these strategies are combined.

a) Motion reduction techniques

The simplest method to reduce the impact of motion in the delivered dose is the direct elimination or mitigation of the patient's motion. Frequently applied breathing control techniques are for instance anaesthesia, breath-hold and abdominal compression.
Breath-hold in inspiration or expiration of the patient is the easiest to implement in the clinical routine. However, this method requires patient coaching, patient cooperation and small consecutive irradiation times. On the other hand, active breathing systems use a spirometer to automatically suspend the patients breathing in a defined respiratory cycle window.
The abdominal compression consists on a plate with a fixing structure to the couch, which mechanically applies pressure on the upper abdominal and limits the diaphragm excursion. This method has as limitation the discomfort to the patient, or even pain in some cases, only limits the breathing to a smaller amplitude, does not extinguish it, and is likely to foment irregular breathing curves and internal organ motion.

b) Methods under free-breathing

These kind of strategies can be applied to the treatment planning or on the delivery stage. If they are applied during the treatment the latency time needs to be evaluated and can strongly affect the quality of the irradiation.
The main advantage of these methods is the comfort to the patient and the treatment delivery under the normal patient's anatomy and physiology (no compression or spirometer). However, it requires adaptation of the treatment planning and/or delivery workflow.

b1) ITV-based treatment planning

The use of internal target volume (ITV) during the planning stage is a widely employed strategy in photon therapy. It is able to increase the robustness of the plan by considering the tumour location and size in each breathing phase, however, for dynamic techniques interplay may occur. By contrast, due to the range sensitivity introduced in particle therapy, this method is usually not enough to account for all the range changes

that might affect the plan quality and might strongly increase the dose in the normal tissues (Rietzel and Bert 2010).
An adapted approach to ion therapy is the use of WEPL-ITVs (Graeff, Durante, and Bert 2012), where the range changes resulted from the motion are quantified, based on the 4DCT data, and included in the plan optimisation process. This technique improves the target irradiation along the treatment but doesn't exclude interplay effects that will reduce the dose homogeneity.

b2) Beam rescanning

Rescanning techniques try to mitigate the dose degradation and interplay effect, between the beam scanning and the tumour motion, considering that the statistical average of local over- and under-dose has a homogeneous distribution. This method performs a multiple "repainting" of the optimised plan, which considers the full motion extension with a proportional reduction of the number of particles per scan position. There are two different approaches to deliver the treatment plan: iso-energy slice repainting or volumetric repainting (Graeff 2014; Schätti et al. 2013).
An issue associated with this technique is the lateral scanning and energy changing speed, which might compromise the effect of rescanning when the delivery and motion periods are in coherence (Bernatowicz, Lomax, and Knopf 2013). Moreover, rescanning may mitigate the interplay effects but not the target motion itself, therefore, range variations should be incorporated in the treatment planning (Rietzel and Bert 2010).

b3) Beam gating

Beam gating consists of tumour irradiation only during a specific window of breathing phases, resulting in a smaller ITV.
The application of this technique to ion-beam therapy, and specifically to active beam scanning, is feasible, although a residual interplay effect within the gating window can still result in dose degradation (Rietzel and Bert 2010). This effect can be reduced with some strategies, as beam gating with rescanning (Furukawa et al. 2007; Graeff et al. 2014) or decreasing the iso-range slice distance and increasing the pencil beams width, which is correlated to the amount of residual motion within the gating window (Bert et al. 2009).
Drawbacks of this technique are the strong sensibility to the beam gating modality, i.e. when phase-gating is used, baseline shifts and amplitude changes might be ignored, while in amplitude-gating mode baseline shifts might result in the selection of an inaccurate gating window. Additionally, it leads to an increases of the treatment time and the residual motion within the gating window can still influence the irradiation accuracy. Also, the fact that beam gating introduces correlation between the beam application and the patient motion might result in larger dose degradation, compared to the no-gating case, if the residual motion is not sufficiently small.

b4) Beam tracking

Contrary to the previously enumerated methods, beam tracking, besides restoring the dose homogeneity, keeps the irradiation volume smaller, as ideally the safety margins can be reduced.
Beam tracking consists in steering the beam in order to "follow" the tumour movement. Hence, this method requires that in real time the delivered plan is adapted based on the feedback from the current tumour position. This is expressed in scanned delivery by the adjustment of the lateral position and energy of each pencil beam (Bert et al.

2007; Saito et al. 2009; Water et al. 2009).
The latency time of the system plays here an important role, since it needs to be significantly lower than the scanning time between two consecutive scan positions, and the patient's motion due to breathing.
Another concern when performing tracking refers to the increase of the doses to the normal tissues, proximal to the tumour, as a result of the overlap of the beam entrance channels. Moreover, treatment planning and quality assurance protocols need to be adapted to include the uncertainties that might arise from this technique.

b5) 4D optimisation
Different optimisation methods have been developed to reduce the motion impact in scanning systems. The simplest way is to optimise the planned raster field (RST) to include the range changes from the 4DCT data (Graeff, Durante, and Bert 2012).
If besides this information, it is also included the correlation between the dose delivery timing and the motion surrogate, a 4D-RST could be optimised. This 4D-RST will define which beam spot is delivered in each 4DCT motion phase with the aim to obtain an uniform dose per motion phase (Graeff et al. 2014). In this case, it is necessary to ensure the synchronisation between the delivery and the patient motion during the treatment, which constitutes a weakness since changes in the the TCS need to be performed. A full discussion of the different methods can be found in Graeff (2014).
Also in this case, treatment planning and quality assurance protocols should include the verification of uncertainties associated with this technique.

2.4 Ion-therapy workflow for moving targets

Tumours under inter- and intra-fractional motion require an adaption of the treatment in order to mitigate its impact and increase the treatment robustness. An example of the workflow at HIT is shown in figure (2.8) and the description of each of the steps is furthermore explained.

2.4.0.1 4DCT acquisition

The inclusion of the motion information in the radiotherapy workflow is usually performed through the use of a 4DCT, in which the image of the moving object is retrospectively reconstructed according to the recorded breathing phase or amplitude of the monitored motion pattern (Farncombe and Iniewski 2013).
The 4DCT information is not only used to delineate the tumour and normal tissues in each of the motion phases, but also to quantify the movement of the tissues. Nevertheless, the patient's motion registered from the 4DCT is only a model formed by a set of images, based on a breathing signal that is assumed perfectly periodic and correlated to the internal organ motion, which does not ensure the reproducibility on the treatment day.
The image acquisition is usually performed over free breathing, therefore, the collection of images corresponds to different physical locations of the couch. During the reconstruction stage, the images are sorted over each breathing phase based on an external trace signal (e.g. Anzai sensor), which is synchronised in time with the CT acquisition.

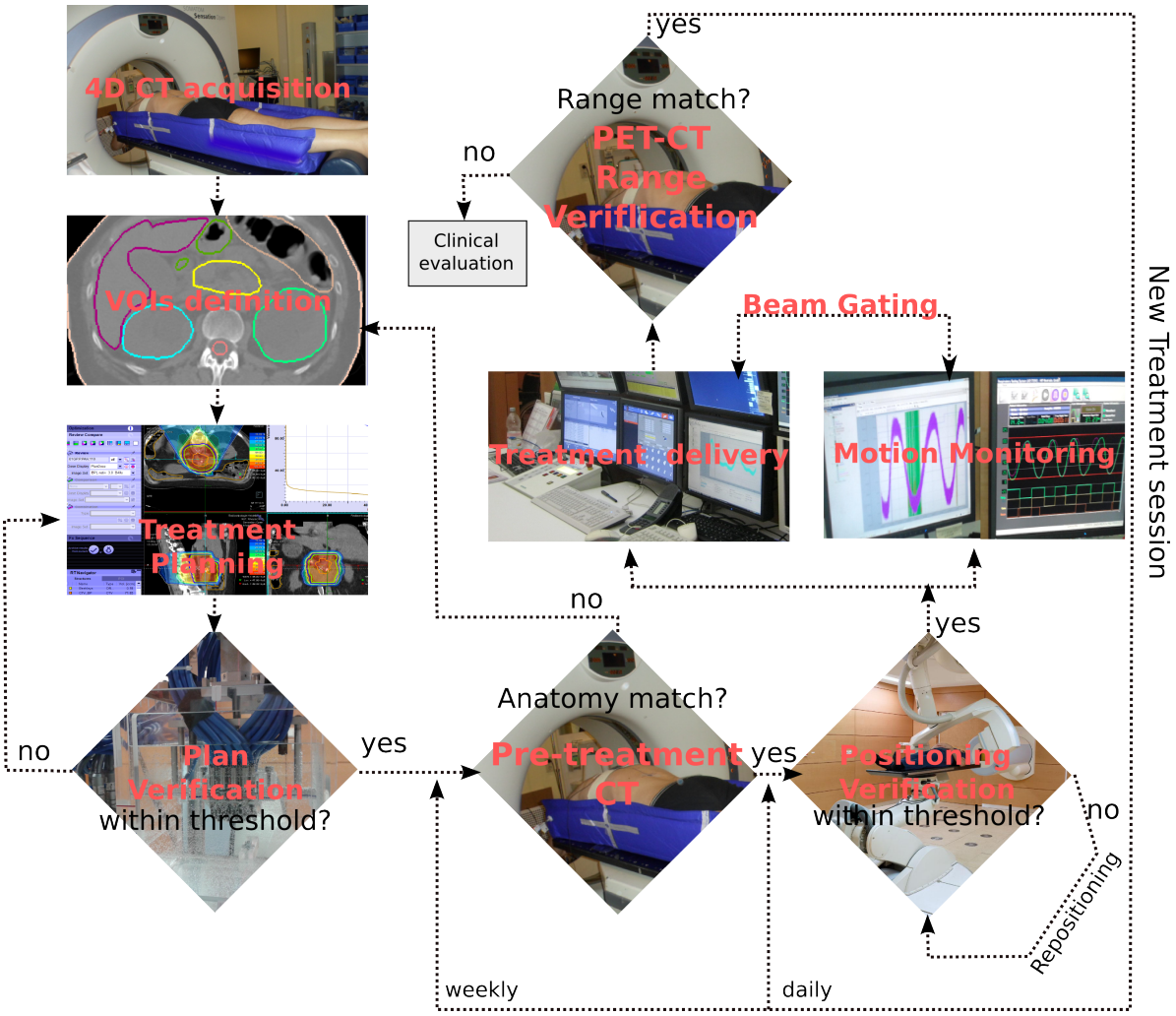

Figure 2.8: Diagram of the treatment stages at HIT for tumour locations subject to inter- and intra-fractional motion, where the distinguishing component is the acquisition of a 4DCT, the motion monitoring, and the pre-treatment CT. An example of patients that follow this protocol are the pancreatic patients.

The data sorting can be amplitude- or phase-based. When the Anzai pressure belt is used as monitoring system a relative phase-based sorting is performed.

2.4.0.2 Target and organs-at-risk definition

The target and OARs definition in ion-beam therapy uses the same concepts of the photon therapy, given in the ICRU report 50 and 62 (ICRU 1993, 1999), as displayed in figure (2.9).
The physician uses the information from a native CT, optionally also a registered CT with contrast, a Magnetic Resonance Imaging (MRI) or PET, to delineate the Gross Tumour Volume (GTV).
A margin is added to the GTV to account for microscopic disease, defining the designated Clinical Target Volume (CTV). Although the CTV is the volume intended to be irradiated, in order to consider random and systematic uncertainties, the volume taken for the treatment planning is the Planning Target Volume (PTV). The PTV should be large enough to allow the full coverage of the CTV during the entire treatment course, but as small as possible to spare the healthy tissues. Hence, the PTV is defined as the

CTV plus a set-up margin that can be asymmetric, depending on the included uncertainties.
In case of moving targets, these uncertainties need to consider all the motion-related issues by adding an intermediate step in the PTV definition, as suggested in the ICRU62 (ICRU 1999), through the inclusion of an internal margin (IM) to the CTV, which will define the Internal Target Volume (ITV). This ITV concept is usually generated based on the 4DCT motion information, either through the union of the CTVs in each breathing phase to represent the full set of possible positions of the tumour (Rietzel, Pan, and Chen 2005) or using the maximum intensity projection as criteria for the target volume contouring (Underberg et al. 2005).
However, for particle therapy, these geometric margin concepts are frequently not sufficient (Bert, Grözinger, and Rietzel 2008; Mori et al. 2008; Rietzel and Bert 2010), since the range variations and interplay effect are not included in their definitions. Hence, it should be replaced by a concept that comprises the information from the radiobiological path length and intra-fractional range changes.
Furthermore, the OARs should consider the internal motion being redefined as Planning Organs at Risk Volume (PRV).

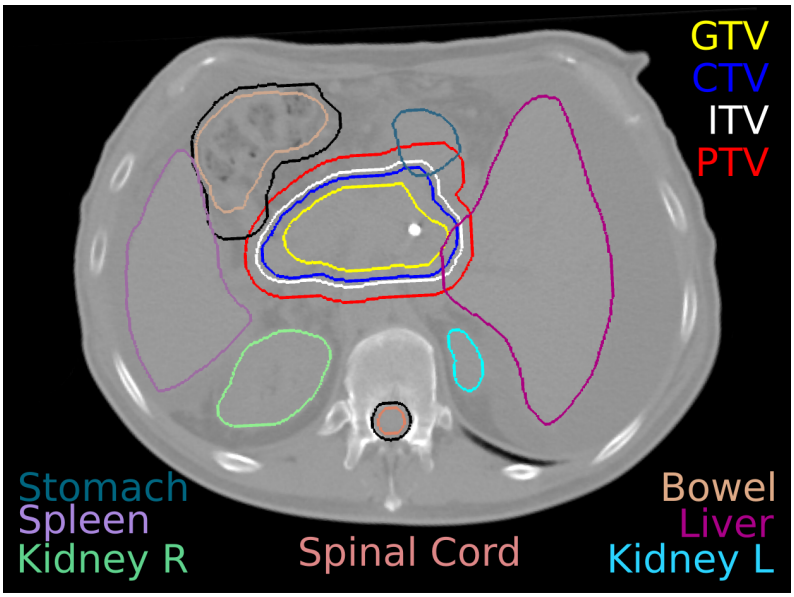

Figure 2.9: Transversal view of a CT of a patient showing the ICRU target concepts (GTV, CTV, ITV, PTV) and OARs. For the spinal cord and bowel is also shown the PRV (in black) used during the treatment planning to account for uncertainties.

The dosimetric recommendations for the PTV follow the photon-guidelines (ICRU 1999), i.e, the PTV total volume should receive between -5% and +7% of the prescribed dose. Hence, it is usual to quantify the PTV coverage by the volume receiving 95% of the prescribed dose (V_{95}), which should be superior to 95%, and the overdose volume as the PTV that receives more than 107% of the prescribed dose (V_{107}), which should be as small as possible. However, considering that the volume intended to irradiate is the CTV, and the PTV is just a strategy to reach this aim, V_{95} and V_{107} are usually referred to the CTV.
The target dose homogeneity (H_{CTV}) can be quantified by the difference between the dose covering 5% and 95% of the CTV volume, D_5 and D_{95}, respectively (eq. 2.6). This parameter quantifies the steepness of the Dose-Volume Histogram (DVH) and ideally

should be as small as possible.
Relative to the target dose conformity, the conformity number (CN) was used (eq. 2.6) (Van't Riet et al. 1997), where $V_{95\%CTV}$ is the volume of CTV (V_{CTV}) receiving at least 95% of the prescribed dose and $V_{95\%}$ is the overall volume that receives 95% of the prescribed dose. The CN will vary between 0 and 1, with 1 for a totally conformal dose to the target volume.

$$H_{CTV} = D_5 - D_{95} \tag{2.5}$$

$$CN = \frac{V_{95\%CTV}^2}{V_{CTV}.V_{95\%}} \tag{2.6}$$

Regarding constraints for the OARs, the most used guideline is the work of Emami et al. 1991, in which the constraints are given for a dose of 1.8 - 2.0 Gy per day, at 5 days to week schedule. Some effort has been done by several groups to update the normal tissues threshold dose, but still no consensus is available, mainly when speaking about the complications under ion-beam irradiation (Schlaff et al. 2014). Therefore, the common practice is still based on the experience with photon-irradiation and adapted to the clinical results from the previously irradiated patients.

2.4.0.3 Treatment planning for moving targets

A time-resolved (4D) TPS for moving targets in ion-beam therapy is of fundamental importance to account for the dose degradation as a result from the target motion and the beam dynamic (Bert et al. 2014). However, no commercial solution is currently available and a research-TPS is limited to some facilities.
The system available at HIT for research purposes is a 4D version of the TPS TRiP98 developed at GSI, designated as TRiP4D (Bert and Rietzel 2007; Eley et al. 2014; Richter et al. 2014a). TRiP4D has functions that allow time resolved dose calculation and dedicated 4D optimisation functions.
Relative to the 4D dose calculation, TRiP4D considers the specifications of the beam scanning system at HIT and is able to simulate the temporal interference between the beam and the target motion, given by an external surrogate signal. The information of the patient is taken from the 4DCT, while the beam delivery sequence (BDS) (i.e, number particles per spot, intensity level and beam pauses) is obtained from the accelerator control system (ACS).
The effect of the different breathing phases (states) in the tumour and patient geometry results in changes in the dose distribution when compared with the static case. This can be simulated through the use of transformation maps between states, namely the three-dimensional (3D) vector fields obtained from the deformable image registration (DIR) between each breathing phase and the reference one, usually end-exhale (0%Ex). So, as result of the use of these transformation maps the dose in each raster point (RP), distributed to the respective breathing phase CT, is summed up in the reference state, wherein the total dose is computed. All in all, the final dose is the sum of the contribution from each raster point in the respective breathing state.
The information about the singular time-resolved RP position is given by the temporal correlation between the BDS and the breathing pattern, figure (2.10).
A more detailed insight of the functionalities and limitation of this TPS, in the context of

this dissertation, is discussed in chapter 3.1.

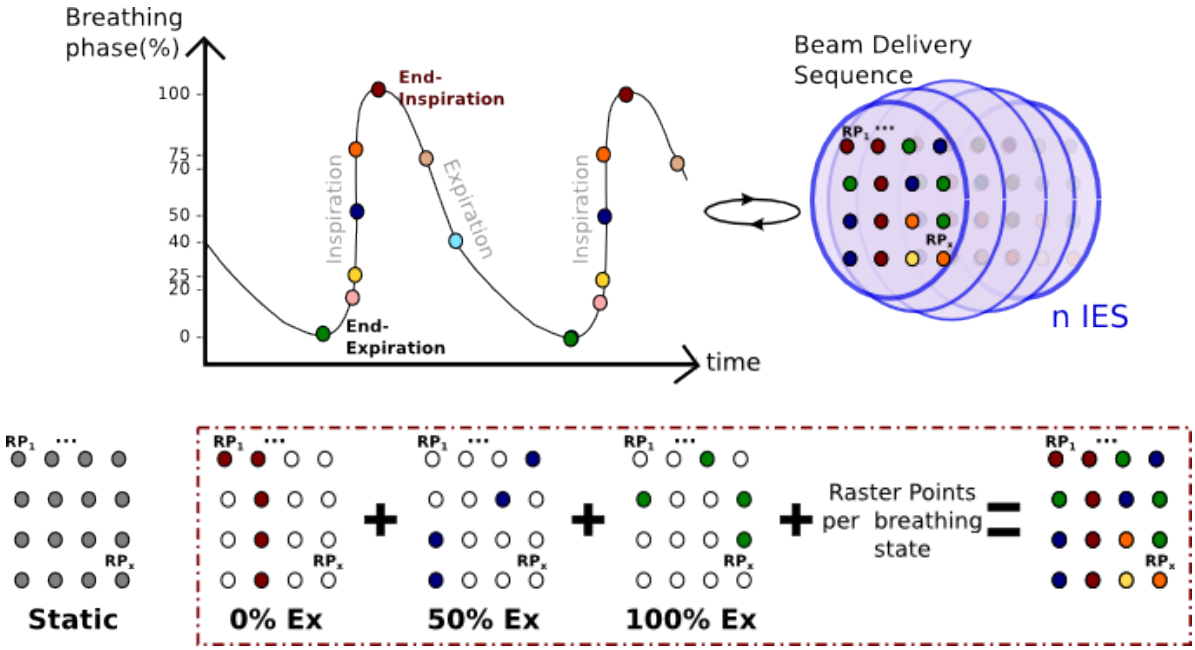

Figure 2.10: Diagram of the time-resolved dose forward calculation based on the correlation between the patient's breathing state and the respective irradiated raster points. The beam delivery sequence is sorted per breathing state (correspond to the different colours in the figure) and the dose is calculated in the respective 4DCT state. Hence, the total dose distribution is the summation of the dose delivered in the different CTs. The states 20%In, 25%In, 50%In,75%In,100%In correspond to the inspiration process (full-inspiration to end-inspiration), while 100%Ex, 70%Ex, 40%Ex, 0%Ex is the expiration process from full-expiration to end-expiration state. These sorting correspond to the used in this thesis.

Several investigations have been performed in order to assess how the scanning parameters can be adjusted during treatment planning in order to reduce the motion impact. Particularly the studies from (Bert and Durante 2011; Richter 2012; Richter et al. 2014b) in which the optimisation of the scanned parameters showed to be effective in the plan robustness, as the beam overlap through the change of the grid spacing, beam FWHM, beam energy layer spacing and ripple filter. However, not all the parameters are easily adjustable, since these depend on the ACS and TCS specifications. Moreover, aspects as the homogeneity of the number of particles in neighbouring raster points might have a superior potential to improve the intra-fractional robustness.
Another aspect of a 4D-TPS to be considered, besides the time-resolved dose calculation, is the potential to perform a 4D dose optimisation (Graeff et al. 2013). These methods are also implemented in TRiP4D, but were out of the scope of this thesis. Additionally, approaches like rescanning, beam gating and tracking also need to be included in a 4D-TPS, either in the optimisation process or with aim to perform 4D dose simulation.

2.4.0.4 Patient-specific quality assurance

To verify the reproducibility of the delivery system and motion monitoring method, a patient-specific quality assurance (QA) under motion condition is strongly suggested pre-treatment. Several approaches are under investigation (Batista 2015; Steidl et al. 2012), having in common the use of moving phantoms with dosimeters suitable for

ion-beam dosimetry (Bert and Durante 2011). Moreover, due to the non-uniform dose distribution, resulted from temporal interference between the scanned beam and phantom motion, a set-up with multiple ionisation chambers is recommended.
At HIT the dynamic set-up is based on the one for static dose verifications. For static cases the patient-specific QA is performed by transferring the treatment plan to a homogeneous phantom geometry and through comparison between the TPS calculated and measured dose. The phantom consists in a motorised water phantom with an array of 24 ionisation chambers (ICs). In its dynamic version, an in-house developed mini-water phantom is mounted on the commercial *QUASAR™ Respiratory Motion Platform*, which moves with a loaded respiratory motion profile of a patient (Batista 2015).

2.4.0.5 Patient immobilisation and positioning

The patient immobilisation must be able to reproduce the patient geometry from the moment of the planning CT acquisition, which will be used for the treatment planning purposes. Usually, in order to accomplish a reproducible positioning, stereotactic body frames, vacuum pillows or thermal plastic restraints are used.
As for the patient repositioning, a pre-treatment soft tissue imaging is suggested, particularly for abdominal patients. This helps to verify the daily extension of the geometric uncertainties resulting from the tissue deformations. Consequently, some of the recommended modalities are cone-beam CT or in-room CT.
As previously stated, the workflow at HIT (fig. 2.8) comprises daily orthogonal 2D X-ray acquisitions for bony match and an additional pre-treatment CT, for specific clinical indications (e.g. weekly for pancreatic patients).

2.4.0.6 Treatment delivery

For moving organs, as stated in the section (2.3.4.2), strategies to mitigate the motion effect during the treatment delivery need to be applied.
At HIT the Anzai system is used to monitor the respiratory motion during the treatment delivery as well as to control the gating treatment (when it is applied). The Anzai ouput is connected to a data acquisition system, EtherCat system, that correlates the breathing signal of the patient and the delivery temporal sequence of the accelerator. This information can later be used in the reconstruction of the delivered dose.

2.4.0.7 In-vivo range verification

After the treatment, the irradiated tissues emit $\beta+$ as a result from the produced secondary fragments during the beam delivery (e.g. ^{11}C, ^{10}C, ^{15}O). The distribution of these $\beta+$-emitters in the tissue can be visualised using PET-imaging.
Particularly important in the case of moving targets is the consideration of the activity washout during the analysis of the PET-images, which is possible through the acquisition of 4D PET imaging (Kurz 2014; Parodi et al. 2009).

2.5 Pancreatic cancer

The challenge of treating pancreatic cancer arises from the anatomic location, biology of the malignant cells and the internal motion of the organ itself and surrounding tissues.

2.5.0.1 Anatomy

Pancreas is an abdominal organ primarily responsible for the insulin and digestive enzymes production. Morphologically, the organ is divided into four sectors: head, neck, body and tail.
Its deep location in the abdomen, and in close proximity to many important structures such as the small intestine (the duodenum) and the stomach, are the major sources of difficulties in external radiotherapy. An example of the anatomy observed in a CT image is shown in figure 2.11.

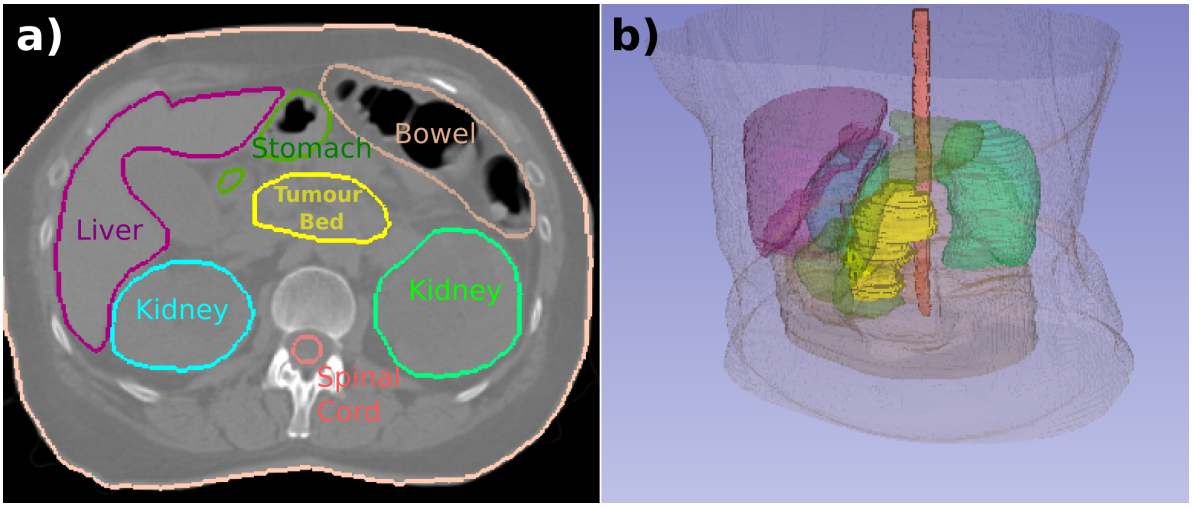

Figure 2.11: a) Transversal view of a computed tomography image of a pancreatic patient with the main surrounding organs delineated. b) 3D reconstruction of the patient anatomy.

2.5.0.2 Cancer types and therapeutic modalities

The classification of the cancer type is in accordance with its origin: endocrine or exocrine. Only five percent are tumours of the endocrine pancreas, the majority being exocrine tumours, which develop from cells that line in the system of ducts that deliver enzymes to the small intestine and are referred as pancreatic adenocarcionamas (Hansen and Roach 2007). Moreover, two-thirds of the cancers are present in the pancreas head.
For practical purposes, tumours are generally classified as resectable (Stage I, II), unresectable (Stage III), and metastatic (Stage IV). According to the tumour grade, size and symptoms the applied treatment is selected, e.g. surgery, adjuvant or concurrent chemo-radiotherapy, usually using gemcitabine or 5-FU (Li et al. 2004). Surgical resection is the main therapeutic, however, overall survival after surgery alone remains with a five-year survival rate of about 20% (Buchler, Kleeff, and Friess 2007).
Conventional photon therapy is usually performed using a three or four field design,

which uses high energy photon fields (e.g. 18MV) particularly for lateral or oblique fields for a prescribed dose of 45 Gy at 1.8 Gy /fx with a boost until 59.4 Gy, see figure (2.5.0.2). The main barrier to this therapeutic modality is the critical normal tissues tolerance, as liver, kidneys, small bowel, and spinal cord.
For locally advanced tumours, a recent analysis showed that most tumour recurrences occur within a 2 cm radius of the primary tumor (Kessel et al. 2013), indicating the need for dose escalation to improve the local control while keeping reduced side-effects. Thus, alternatives to conventional radiotherapy, which tolerate dose-escalation, have been sought. Such modalities are intraoperative radiotherapy (IORT), stereotactic body radiotherapy (SBRT), brachytherapy and ion-beam therapy.
The high precision of ion-beams, while delivering high doses to the tumour and sparing

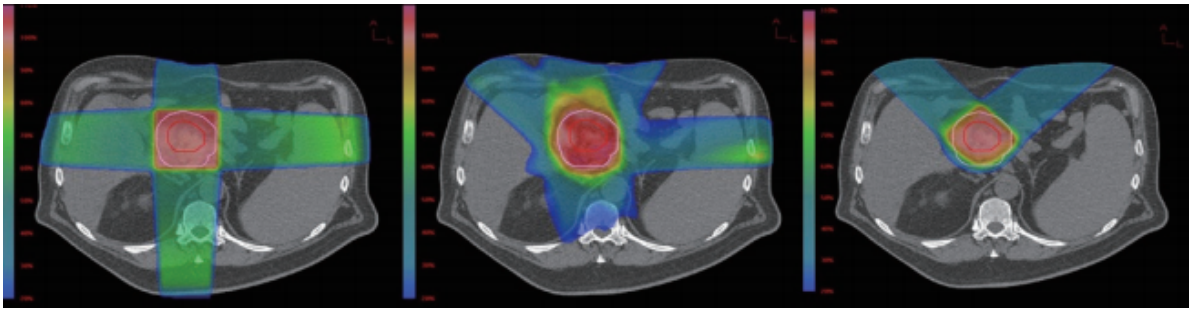

Figure 2.12: Axial view of a pancreatic patient and its dose distributions under different radiotherapy techniques. left) Tridimensional conformal photon radiotherapy; central) Intensity-Modulated Radiation Therapy (IMRT); right) Proton plan using a passive scattering beam system. Figure from Ling et al. (2015).

the OARs, incite its application in pancreatic patients.
Studies have been conducted to investigate the clinical application of protons (Ding et al. 2014; Nichols et al. 2014). Simultaneously, the use of carbon ions have been studied at NIRS and HIT (Combs et al. 2013; Shinoto et al. 2013; Tsujii et al. 2013).
While protons offer the possibility of a highly conformed treatments, carbon ion-beams exhibit additionally a RBE enhancement of 1.16 - 2.46 for pancreatic tumour cells and a low OER, which due to the large fraction of hypoxic cells in pancreatic tumours make them a promising treatment option (Yamada et al. 2010).
The obtained results from NIRS are extremely promising, where the dose escalation and concurrent gemcitabine-chemotherapy with carbon ion-beams radiotherapy have shown an increase in the tumour local control and in the overall survival (Shinoto et al. 2016; Tsujii et al. 2013). For patients receiving a higher dose (≥ 45.6 Gy (RBE)) the freedom from local progression rate was 83% at 2 years while the respective overall survival rate was 48%. Concerning side effects, low toxicity was detected, with only 15% of the patients exhibiting acute gastroduodenal ulcers of grade 1 or 2.
However, the finite range of ion-beams presents strong sensitivity to density variations, i.e. changes in the patient's anatomy, which might be a concern for these patients. This topic is covered in the following section.

2.5.0.3 Organ motion

The high sensitivity of the ion range to density changes in the beam path induces dose under- and over-shoots, leading to the tumour dose degradation. These variations can either result from inter-fractional anatomy changes, patient positioning or intra-fractional

motion.
In pancreatic patients, the inter-fractional changes are mainly due to tumor shrinkage, organ filling (bowel and stomach) and loss of adipose tissue. Horst et al. (2013) measured variations in the tumour location along the treatment course superior to 10 mm for a large percentage of patients, while Liu et al. (2012a) detected a significative inter-fractional organ deformations for abdominal organs (as pancreatic head, duodenum, and stomach) with an average maximum overlap ratio between the volumes based on planning and daily CTs of 80.2% for the pancreatic head.
Relative to intra-fractional changes, Mori, Shinoto, and Yamada (2014) and Mori et al. (2010) quantified the tumour motion for two sets of patients as (9.1 ± 0.4) mm and (6.7 ± 3.7) mm, respectively. These variations corresponded to changes in the maximal dose received by the kidney of 3%, with a conventional passive carbon ion-beam. Also Kumagai et al. (2009), pointed for the impact of the intra-fractional bowel gas movement, resulting in a mean dose degradation to the target of 3.5%. Despite this under- and over-dosage as a result from density changes, when the treatment is delivered with a scanning system, the interplay effect will additionally play an important role.

Chapter 3

Characterization of software and tools

This chapter explores the characteristics and technical issues of the software and tools available at HIT which were subsequently used in this dissertation.
The description of the main functionalities and limitations of these systems will help to understand and guide in the comprehension of the adopted protocols and obtained results in the following chapters (4) and (5).

3.1 Treatment planning systems

Two TPS were used in this study. Syngo® RT Planning is the clinical system currently in use at HIT, while TRiP98 is a research-TPS, developed as a prototype of Syngo® RT ,and therefore includes additional research features to the commercial system. One of the features is a 4D version able to perform time-resolved dose calculations, so-called TRiP4D.
Syngo® RT Planning and TRiP98 share the same base data. This base data corresponds to the description of the HIT scanner, accelerator energies, beam focus and intensities, RBE tables and HLUT data.

3.1.1 TRiP98

Definition and aim

TRiP98 is a command-line oriented TPS written in C programming language. It was developed during the GSI pilot project to fulfill the need of a planning system for heavy ions. It is particularly adapted for carbon (^{12}C), however, other particles are available as protons and oxygen (^{16}O).
Its main function is the calculation and optimisation of 3D dose distribution, both considering the physical and biological effects. Moreover, handling and processing of specific TPS data is possible.

Functionalities

A sketch of the general structure of TRiP98 is shown in figure (3.1).
Either for the purposes of dose calculation or optimisation the definition of the following

is primarily required:

- Projectile type (carbon, proton, oxygen,..)
- CT cube; describes the three-dimensional anatomy of the patient based on a CT data, given in terms of Hounsfield numbers, later on converted to particle ranges. This cube must be given in a binary format with extension *.ctx* and accompanied by a header file *.hed* that contains information about format, dimension, voxel size and byte order.
- Volumes Of Interest (VOIs); describes the contours of the target and the critical structures in the patient's CT. Each VOI contains the information of the tissue type and its shape defined per CT slice. The data is given in a file with the extension *.vdx* also accompanied by a header *.hed* file.

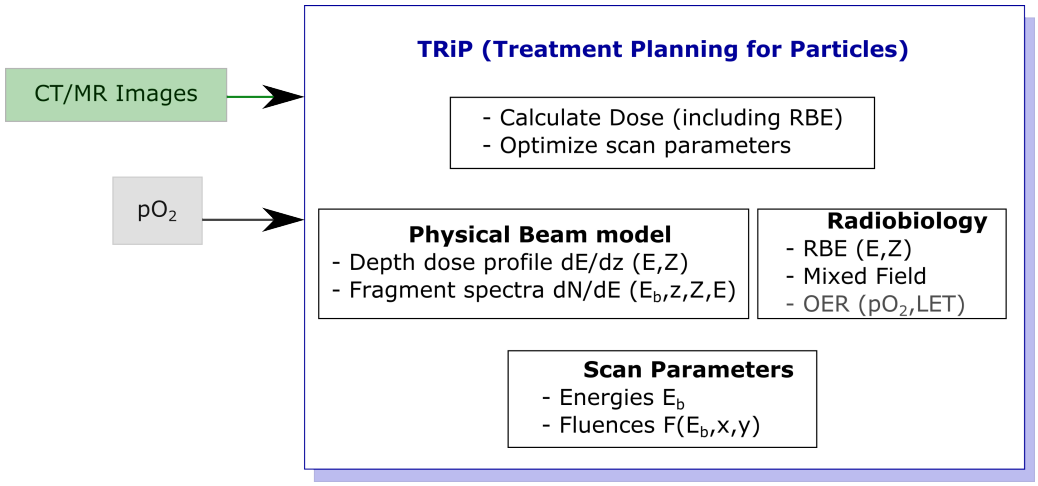

Figure 3.1: Diagram of the general structure of TRiP98. Drawn in grey is the recently included OER implementation. TRiP98's inputs are dependent on: particle charge (Z), actual energy (E) and initial beam energy (Eb), PET-3D map of oxygen concentration (pO2) and the dose averaged linear energy transfer (LET). Figure adapted from Krämer et al. (2014)).

Moreover, the facility-specific characteristics need to be incorporated. A list of examples is given below:

- Scanner capabilities, i.e. definition of the properties and limitations of the raster scanner system, as e.g.:
  - scanner path optimisation,
  - water equivalent offset between beam outlet and patient's volume,
  - minimum and maximum scanner step size in both dimensions,
  - lower and upper particle number limits to be allowed,
  - scanner coordinate limits,
- Table of accelerator energies - contains the energy steps and respective focus and intensity steps;
- Energy loss tables (dE/dx) - energy loss for various projectiles at various energies;
- Total reaction cross sections - includes the total cross sections for nuclear reactions of various projectiles at various energies;
- Fragment spectra - spectra are organised by the primary beam energy, wherein the spectral distributions at a particular depth is by the energy distribution described;
- Depth dose distributions - set of tables organised by primary beam energy;
- RBE data tables - used for the biologically equivalent dose calculation, it contains the cell specific RBE data as a function of particle species and energy;

- OER data tables;
- HLUT - describes the relation between HU and the WEPL.

Note that TRiP98 uses the coordinate system establish to the GSI scanner, as explained by Jäkel et al. (1997), therefore defined in terms of patient, room, couch or raster-scanner perspectives. This result in the need to convert IEC and DICOM coordinates to the TRiP system (e.g. isocentre, gantry and couch angles).

a) Dose optimisation

Dose optimisation is performed by means of inverse planning with respect to GSI's magnetic raster scan system in order to determine the plan parameters. Necessarily it requires the definition of the target volume and (physical or effective) prescription dose. First, the given target volume is divided into slices of equal irradiation energy, i.e IES. Thus, for each position in every slice, the number of particles required to obtain the prescribed dose distribution across the target volume is determined.
Other important features that need to be defined to control the optimisation process are:

- Isocentre coordinates, otherwise the centre of the target VOI is selected;
- Beam focus (FWHM), and lateral and depth spacing between subsequent peak positions;
- Contour extension - function to improve the dose conformation through the extension of the considered raster positions during optmisation, relative to the target volume;
- Dose extension - function to handle the maximum distance from which dose contributions are accepted from a specific voxel.
- Couch and gantry angles (in GSI coordinate system).

TRiP can perform either single field optimisation (SFO) or multi field optimisation (MFO). For that, the algorithms bortfeld, gradient, cjggrad, and fletcher-reeves are available. The algorithms give similar results, the only difference is the convergence time, with the fletcher-reeves being the faster one.
When biological optimisation is required, the RBE model for the target and residual tissues is accounted for, therefore the tissue type of each VOIs must be specified. The available biological algorithms are, the *classical* implementation of the LEM and the *low-dose* approximation of LEM at therapeutic dose levels (Scholz and Kraft 1996).
After a successful optimisation, the output is obtained as:

- Treatment plan - given by the raster scanner data *.rst*. This file contains the plan parameters needed to perform an irradiation with the defined scanner system, respectively projectile type, ripple filter (if applicable), gantry and couch angle and the complete description of the set of raster slices. Therefore, each IES is characterised by its energy, actual beam focus and step size, extension factors for contour and dose, the water-equivalent depth dose distribution for this energy, and the set of RPs per slice. Each RP contains the scanner (x, y) position and respective particle number, i.e. beam intensity.
- Dose cube - binary data cube (extension *.dos* with a respective *.hed* file) that contains the 3D dose distribution, either physical or biological;
- RBE and survival distribution (optional);
- DVH - the histogram of the dose distribution for the selected VOIs, exported in *.gd* format.

b) Dose calculation

The beam model included in TRiP98 accounts with the depth dose profiles but also with the nuclear fragment spectra, in the case of heavy ion-beams calculation. This uses the physical concepts defined in chapter (2) and was explained in section (2.2.3).
The algorithms available in TRiP98 are:

- Classic - dose calculation on the CT grid is performed by locating four neighbouring raster points for each voxel and interpolating the modified intensities.
- All points- account for all the neighbouring raster beam spots which may contribute to a given voxel. Hence, the Gaussian shape of each beam spot is explicitly calculated, i.e. pencil beam method.
- Multiple scatter - based on the *All points* method but considering the broadening of each beam spot as a function of depth.

Advantages & drawbacks

The main limitations of TRiP98 are:

- lack of a graphical user interface leading to a need for an auxiliary visualisation software (as Slicer RT, explained in section 3.3.1);
- input and output formats are not the standard DICOM format, however, external tools are available for the conversion of the main files;
- optimisation of the couch and gantry angles is not provided;
- optimisation is limited to the definition of the maximum dose constraint to each OARs, with a respective VOI-specific weighting factor. Hence, no dose-volume constraints are available.

However, the strengths of the TRiP98 as the scripting functionalities and the possibility to develop integrated new functions/modules are factors to propel its use. Some of these functions are discussed in the next sections as they were used in this dissertation.

3.1.2 TRiP4D

One of the versions that raised from TRiP98 was the TRiP4D, which is able to generate time-resolved treatment plans for moving tumours. Hence the estimation of the interplay effect and method to mitigate it (as rescanning, 4D optimisation,...) are available.

Aim

The idea of a 4D TPS is to allow the assessment of the tumour motion and the active delivery in the plan quality. TRiP4D was developed with the aim to be compatible with the clinical treatment planning workflow at HIT. Therefore, the 4DCT protocol and motion monitoring data available at HIT, i.e. motion acquired with the Anzai system (relative-phase based) were considered. Also, the BDS format at HIT was taken into acount and is readable by TRiP4D (Richter 2012).
TRiP4D includes all the established 3D treatment planning functionality, as well as the physical and biological beam model. Hence, 4D physical and biological dose distributions can be determined.

4D calculation process

The description of the 4D calculation process was presented in the section (2.4.0.3). Furthermore, figure (3.2) summarises the process by the workflow *B*.
The performance of a 4D calculation requires the following set of inputs:

- 4DCT data - given as a set of ordered discrete CTs. In order to calculate the total dose distribution, one of the phases needs to be defined as reference phase;
- patient transformation map (*.trf* file) - obtained through deformable registration between each breathing state and the reference phase. It is given to the TPS as the vector field of the deformable registration between states;
- treatment plan, i.e. the raster scanner data, *.rst* file;
- patient surrogate signal, acquired during treatment or other breathing curve representative of the internal/external surrogate signal, designed as *.mpos* file. Additionally, the following parameters need to be defined:
  - number of motion states and list of considered states,
  - state handling algorithm: amplitude-based (motion range), phase-based (0 - 360°), relative-amplitude-based (0 - 200%), time-based (0 - 100%) or hilbert-based (0 - 100%),
  - state direction - coordinated direction (x, y or z) in which the state division should be performed. For a system as Anzai, the corresponding direction is *x*, i.e. anterior-posterior in patient system;
- accelerator temporal information for each raster point, where the spill file is given in the *.lmdout* format.

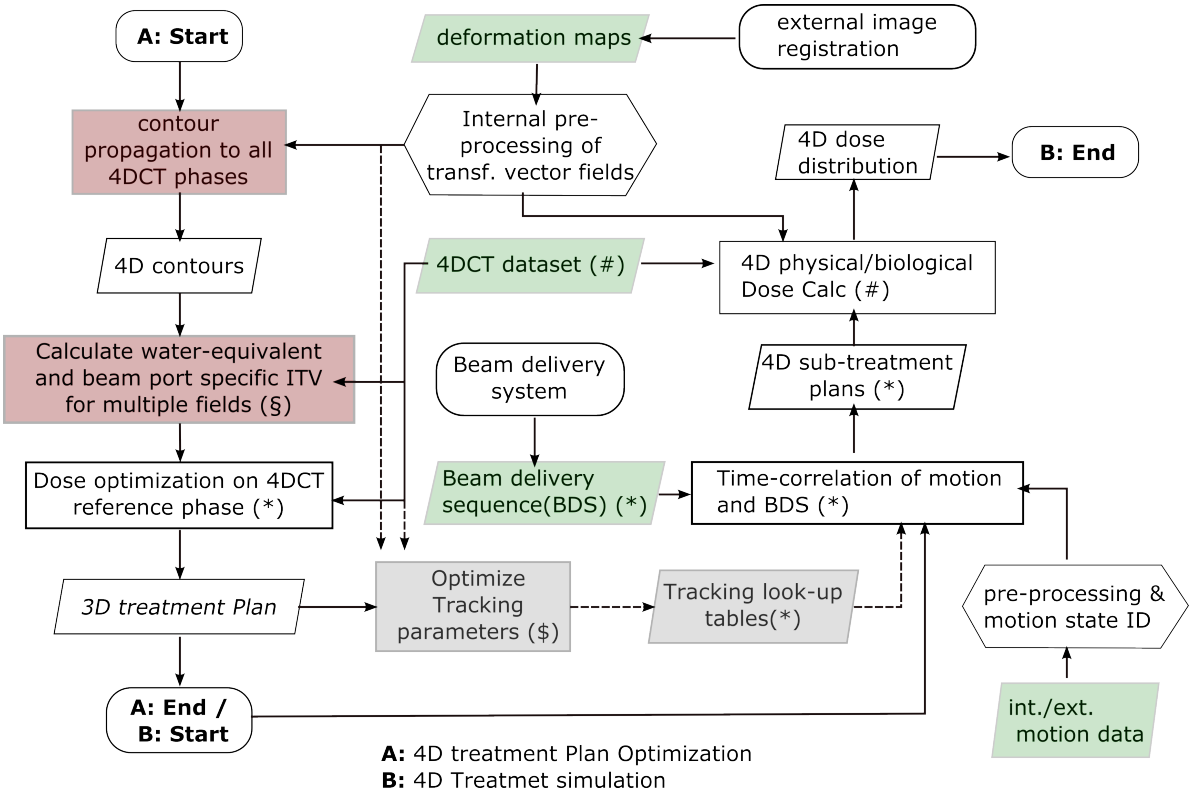

Figure 3.2: Workflow of the 4D optimisation (A) and dose calculation (B) processes implemented in the TPS TRiP4D according to Richter et al. (2013) and adapted from it. Input data is depicted in green boxes. Red boxes correspond to the modules discussed more in detail in this chapter. Optional modules are drawn in grey boxes. The modules (✳), (#), (§) and ($) are described by Bert et al. (2007), Gemmel et al. (2011), Graeff, Durante, and Bert (2012) and Lüchtenborg et al. (2011), respectively.

Additionally, in order to perform a reconstruction of a delivered dose the target motion and the beam position must be temporally correlated (see figure 3.2). Therefore, the beam delivery is divided into discrete phases in which sub-treatment plans are generated and dose calculated (Bert et al. 2007).

Additional functionalities

Besides the simple 4D dose calculation, TRiP4D also incorporates the following functions, some of them also shown in figure (3.2) by the workflow *A*:

- Beam tracking (Bert et al. 2007; Lüchtenborg et al. 2011) - the beam position is adjusted to the tumour motion in real-time based on pre-calculated correction vectors and compensating for potential dose changes in tumour areas;
- 4D segmentation (Richter et al. 2013) - integration of deformation maps to the transformation (i.e. propagation) of contours from a reference CT to another;
- 4D optimisation (Graeff et al. 2013) - different approaches are available, either based on the calculation of ITVs that includes range changes (Graeff, Durante, and Bert 2012), using rescanning or tracking parameters optimisation (Eley et al. 2014);
- Gating optimisation (Graeff et al. 2014): an example is the multigating technique, where specific beam spots are assigned to a defined motion phase during the treatment planning.

In preparation of the next chapter, the concept of 4D segmentation and 4D ITV optimisation are discussed in more detailed here.

a) 4D segmentation and propagation

The VOIs are usually defined by the physician just for the planning CT, which results in the lack of adapted contours to the 4DCT states. Therefore, an automated transformation of the manually delineated contours from the planning-CT to the reference 4DCT state and from this state to each of the 4DCT states, is a welcoming feature. Richter et al. (2013) implemented it through a 4D contour data model, a contour propagation algorithm, and a contour manipulation functionality.
Each VOI in TRiP98 is given as polygons on axial CT slices, which can be converted into the voxel space by defining which voxel belongs to a specific VOI. Concerning the 4D case, this was performed through the concept of Volumetric Boolean Mask (VBM). Here the 4D-VOIs are represented as boolean masks held in a CT-like dataset structure in which a single binary digit (bit) is set to ”1” if the voxel is inside of the VOI, and ”0” otherwise. The definition of the voxels inside or outside the contour is performed by the point-in-polygon ray-casting algorithm. In conclusion, for different motion states the respective VOIs will be represented by different bits. The diagram of the conversion process, i.e. polygon contour to VBM, is shown in figure (3.3).
Later the 4D-VOIs can either be an object of basic manipulations (e.g. geometrical unions or intersections) by simple bit mask operations or propagate based on deformable registration.
For the contours propagation, TRiP4D uses the VBM dataset structures to transform from the reference state, *r*, to all the others states, *s*, as shown in figure (3.3). Every voxel centre is displaced to its reference state position by the inverse deformation maps

obtained during the deformable registration between the reference state (fixed cube) and each of the others breathing stated (i.e. moving cube).
It must be taken into account that this propagation is intrinsically dependent of the quality of the registration performed and their deformation fields. Subsequently, the propagated contours need to be afterwards confirmed and the clinical implementation requires a physician inspection.

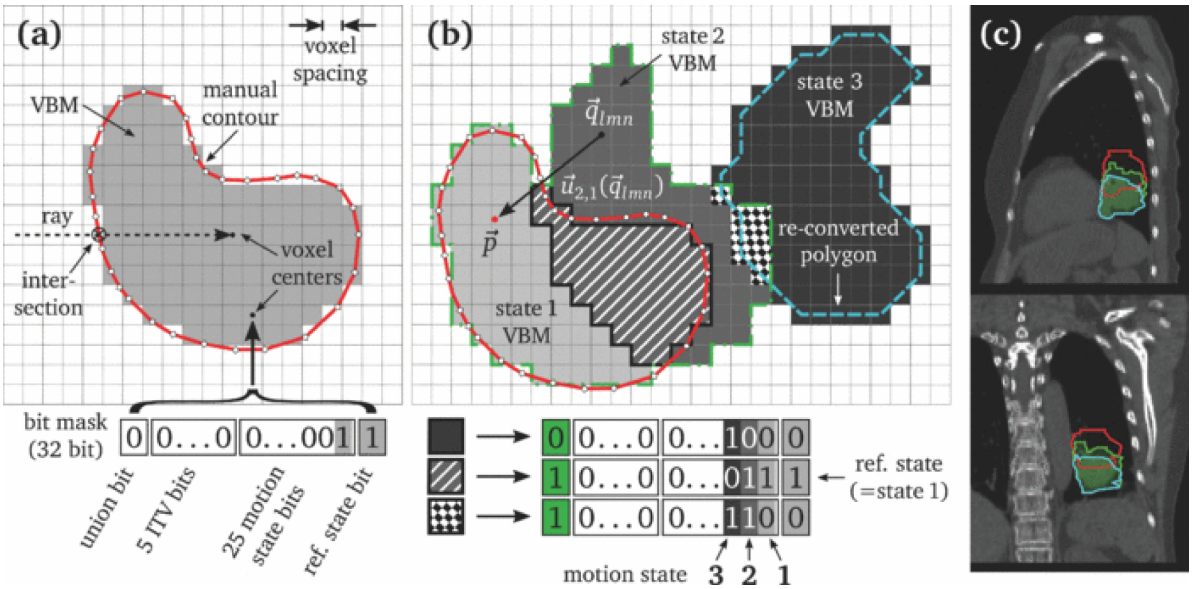

Figure 3.3: (a) Conversion from a polygonal contour (red solid line) into a volumetric boolean mask (VBM) (grey area). Inside voxels are determined based on the number of intersections of the polygon with a ray sent to the voxel centre - ray-casting algorithm. (b) Contour propagation by inverse transformation from a regular grid between the state 1 (light grey), 2 (dark grey) and 3 (darkest grey). (c) Patient example in sagittal and coronal CT slices of propagated GTV contours between the reference end-exhale state (red) and the end-inhale state (cyan). Source Richter et al. (2013).

b) 4D ITV optimisation

Target motion can be addressed in particle therapy through the use of ITVs (i.e. union of the CTVs in all motion states) with inclusion of the WEPL-changes along the BEV, named as ITV_{WEPL}. When this concept is applied field-specific as by Rietzel and Bert (2010) the margins applied to one beam lead to an unnecessarily increase in the target size for other fields, if a common target volume is desired. On the other hand in the approach used by Graeff, Durante, and Bert (2012) the margins are included into the field description itself, expressly through a different conversion HU into WEPL for each field. In brief, a modified HU-WEPL look-up table is used, in which the changes in WEPL are adopted. As consequence, the resulting dose distribution in beam's eye view (BEV) was determined by the WEPL and not by the geometric length. This WEPL conversion is performed for each raster point. Figure 3.4 shows the altered geometry-WEPL conversion.
Considering a 4DCT, the accumulated WEPL extent is defined from the minimum to the maximum WEPL value from all motion phases. In summary, the altered WEPL conversion modifies the targeted structure in the WEPL coordinate system, independently for each field. Hence, the target coverage is equivalent to the modified target volumes as originally defined by Rietzel and Bert (2010).

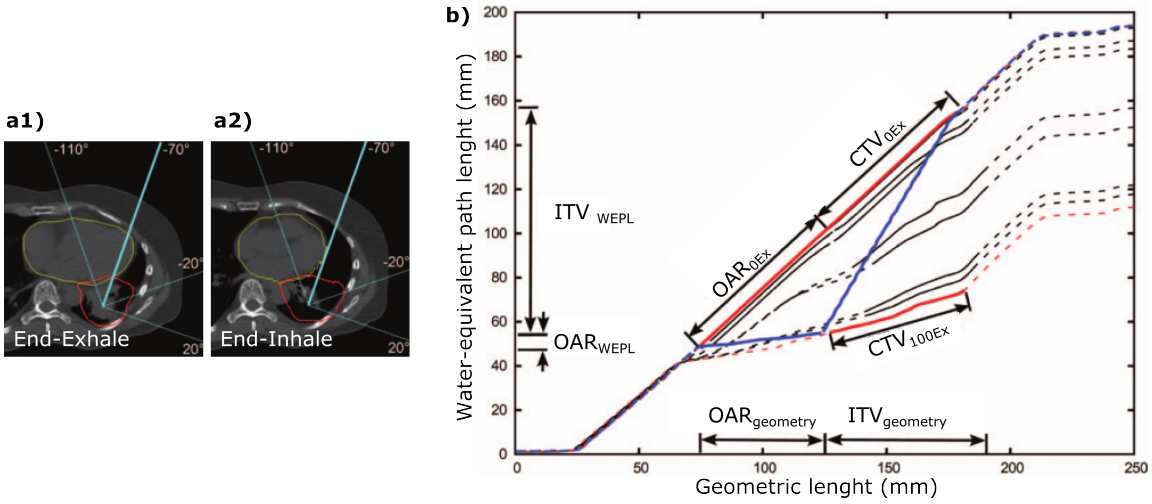

Figure 3.4: a1-a2) Axial CT slice at end-exhale (0%Ex) and end-inhale (100% Ex) showing the CTV (red) and the different beam directions. b) WEPL-conversion for the angle in bold of the figure a1-a2 for all the motion phases, with 0%Ex and 100% Ex in red. The beam is 0%Ex crosses mainly homogeneous soft tissue while in 100% passes 100 mm of lung tissue (i.e. lower WEPL). The blue line shows the final altered WEPL conversion for this beam position. Source Graeff, Durante, and Bert (2012)).

The 4D optimisation is then performed considering the WEPL-ITV for the reference state and including the CTV for a subset of additional phases. In conclusion, the result is a single irradiation raster scan file applicable to all motion phases in which the target is continuously irradiated while sparing the OARs. The number of beam positions and their geometric location thus remain unchanged. Instead, additional equations are included describing the dose deposition of each beam position to each target/OAR voxel during specific motion phases.

Advantages & drawbacks

The fact that TRiP4D is not a clinical product is maybe one of the main limitations, however it is also the essential reason for its continuous research and constant development of new functions.
Some of the functionalities are limited to the GSI scanner system, as multi-gating or rescanning, since it requires changes in the TCS, not easily accomplished in a clinical facility.
Furthermore, an extensive application of the TRiP4D functions to a larger number of patients could result in a better understanding of their potential and limitation.

3.1.3 Syngo® RT Planning

Syngo® RT planning is the commercial solution provided by Siemens Healthcare for treatment planning with scanned protons and carbon ion-beams. It is based on TRiP98 models, however, further developments were later performed by Siemens.
The dose is calculated for both protons and carbon ions by pencil beam algorithms as explained in the chapter (2.2.3). The effective dose for carbon ion-beam therapy is applied by the local effect model, while for protons a fixed value 1.1 is used.

Functionalities

The TPS is integrated with the PACS (Picture Archiving and Communication System) network, which allows the data exchange with the treatment console and the direct plan transference after its approval.
The system is DICOM RT based, i.e. the data is read and written in the *RTCT*, *RTStruct*, *RTPlan* and *RTDose* formats. The system is divided into the following modules:

- Patient modelling;
  - contouring of OARs and targets - Allows operation between contours, 3D visualisation and interpolations,
  - image registration features - Useful for the contouring using auxiliary imaging modalities (as MRI, PET or even CT with contrast agent). Moreover, allow the rigid registration (12 degrees of freedom, DOF) with follow-up CTs for further forward dose calculation;
- Treatment planning;
  - plan definition - Selection of the beam configuration (number and angles), isocentre location and definition of the prescription dose,
  - dose optimisation - Iterative optimisation through the definition of the dose constraints, optimisation strategy (IMPT or SFUD) and technique (absolute of effective dose). The Target and OARs constraints can be given in terms of minimum and maximum dose, upper and lower Dose-Volume limits,
  - dose calculation,
  - review and compare - Evaluation of the dose distribution per beam and total, absolute or effective, and combination between dose distributions (difference, summation). Possible to visualise the beam spot distribution in BEV with underlying Digitally Reconstructed Radiographs (DRR).
  - definition of the fractionation scheme,
  - plan reporting;
- Plan verification - The plan is transferred to a verification phantom (water phantom with 24 equidistant ICs) and then the dose is recalculated within the phantom. Later the plan is irradiated at the treatment machine and compared with the TPS doses for each IC.

Advantages & drawbacks

The clear advantage of this system is the user-friendly features and the direct communication with the treatment delivery system. However, some relevant capabilities are missing such as:

- beam time structure, i.e. it neglects the subsequent nature of the beam scanning process and any target motion;
- deformable registration features;
- the inclusion of uncertainties in the dose calculation (set-up, range, internal motion, etc.);
- scripting functionalities.

3.2 Image registration

As explained in the previous section, an indispensable step to perform a 4D dose calculation is the use of deformable registration, for the contours propagation between CTs and also for transformation of the raster points position between states.
Besides deformable image registration, rigid registration is also required when considering CTs from different acquisition sessions, and a bony matching needs to be performed to ensure the correct patient positioning.
Plastimatch was the software elected for these tasks. It is an open source software for image computation (`http://plastimatch.org/`), able to perform volumetric registration of CT, MRI, and PET.

Plastimatch - functionalities

Plastimatch supports several 3D image file formats, as DICOM, Nifti, NRRD and MetaImage (mha). Moreover, is able to convert between most of these formats and perform processing of the image data.
Deformable image registration (DIR) can be performed using B-spline (Shackleford, Kandasamy, and Sharp 2010) or Demons methods (Sharp et al. 2007a). Also algorithms of the *Insight Segmentation and Registration Toolkit* are implemented.
The DIR process can be controlled through different cost functions, including normalised mutual information, normalised correlation, mean reciprocal square differences, mean squared error (MSE) and gradient magnitude (GM) difference. Hence, multi-modality image registration is theoretically possible.
Tools for converting and manipulating vector fields and other geometric transforms are available, as well as the creation of synthetic vector fields.
Plastimatch also features others handy utilities which are not directly related to image registration. In highlight, the gamma criterion, manipulation of images (directions, voxel size, interpolations, cropping) and comparison of binary volumes (Dice similarity coefficient - DSC, Hausdorff distance - HD and contour mean distance) are implemented.

Plastimatch - advantages & drawbacks

Several retrospective studies in the field of motion assessment described the application of this software as Kumagai et al. (2009), Mori, Shinoto, and Yamada (2014), and Mori et al. (2010), which gives a research background regarding its accuracy and capabilities.
Moreover, the fact that it is an open-source software, means that the development of new functions is continuous and users/developers mailing-list is highly helpful.
No graphical interface is provided with the software, however, it was implemented also as plugin in 3D Slicer platform. This system will be discussed in the next section.
Plastimatch also lacks in landmark-based rigid registration, surface matching registration and 2D-2D registration functions.
Regarding the DIR quality, since the 4D calculation is strongly dependent on it, a 3D slicer plug-in can be used (see section 3.3.1).

3.3 Evaluation tools

As previously stated, TRiP and Plastimatch are command-based software, without graphical user-interface but with functions that allow batch execution. Therefore, the adopted visualisation interface (3D Slicer) and manipulation libraries (ROOT based) are described below.

3.3.1 3D Slicer

3D Slicer (Fedorov et al. 2012) is a software platform for analysis and visualisation of medical images, and for research in image guided therapy.
It supports multi-modality imaging including MRI, CT, Ultrasound, nuclear medicine, and microscopy.

Functionalities

The software is extensible, with plug-in capabilities for adding algorithms and external applications. Therefore, different research groups developed additional modules, some of them suit the needs of this dissertation. Those plugged modules are *SlicerRT*, *SlicerTRiP* and *Registration Quality*.

a) SlicerRT

SlicerRT (Pinter et al. 2012) is a result of the joint collaboration between C. Pinter, A. Lasso (PerkLab, Queen's University) and K. Wang (Princess Margaret Hospital, University Health Network Toronto).
The main modules from this extension are: DICOM-RT import, segmentations, dose-volume histogram, dose accumulation and comparison, contours comparison, and integration with Plastimatch functions.

b) SlicerTRiP

This module was originally developed by Kitware Inc. and Isomics Inc. and later adapted by K. Anderle from GSI in order to upload TRiP cubes to the 3DSlicer interface. Dose and CT cubes can be directly readable in TRiP98 formats. Binary masks of structure and VBM, with multiple bin states, are also recognised.
The visualisation of the dose distribution is accomplished using a colour-wash range defined by the prescription dose, overlying the CT image and structure set.
Additionally TRiP DVH files (in *.gd* format) can be loaded and the DVH is displayed.

c) Registration quality

This extension was a collaboration between GSI, HIT and University Clinic of Erlangen, having as main contributors J. Woelfelschneider, T. Brandt, D. Richter and K. Anderle. Its aim is to provide an intuitive and systematic method to evaluate the quality of the image registration. The available qualitative and quantitative tools include:

- Import of data in Plastimatch format - reference, warped image (transformed), and vector and inverse-vector fields uploaded in .mha format. Possible to define a VOI to constraint the evaluation;
- Image checks - comparison between the reference image and the warped image can be performed by false colour or check-board pattern overlay, and by the calculation of the absolute difference cube;
- Vector field checks - using the concepts of Jacobian Determinants (JD) and Inverse Consistency Error (ICE).

Figure (3.5) shows an example of this evaluation.
The calculation of the determinant of the Jacobian matrix gives the information of how the volume changed between the two registered images (i.e. expansion or contraction), where values equal to one represent no volumetric variation (Sarkar et al. 2012). The ICE corresponds to the euclidean norm of the inverse vector field and is used to check the consistency of the mapping between the two images (Bender and Tomé 2009).

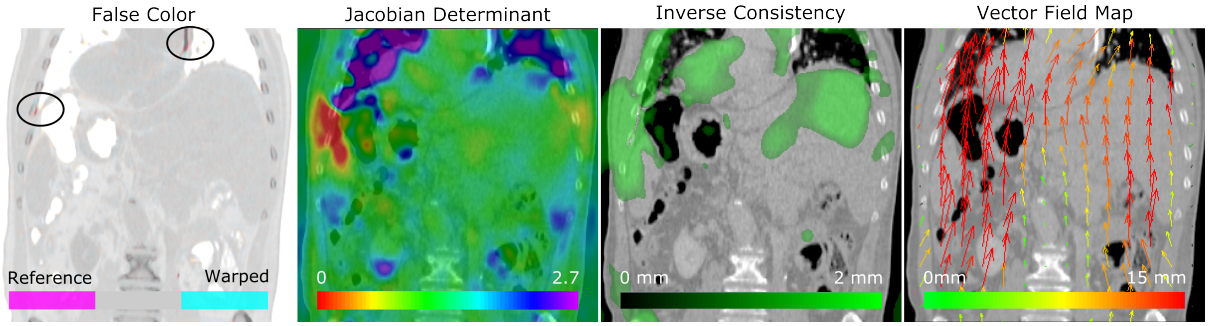

Figure 3.5: Coronal view of the DIR quality assessment between a 0%Ex and a 100%Ex state CT. The *False Color* image corresponds to the overlay between the (reference) 0%Ex CT and the transformed 100%Ex CT (i.e warped image), in which two regions with observable differences are highlighted by the black circle. The values of the JD and ICE can also be overlaid in the patient CT, and be used to identify regions in which the vector field can have inconsistencies. Finally, the displayed vector field map is also shown, in which the direction and length quantifies of the transformation between images is represented by each arrow.

3.3.2 ROOT libraries

A serie of ROOT libraries, named MvtLibraries, were developed by Richter (2012) and adapted to suit the needs of this thesis.
These libraries include TRiP functions and are able to handle the majority of the objects required by TRiP, such as dose and CT cubes, structure sets, breathing signals and treatment plans.
In particular, some of the classes and functions are:

- MvtCube: handles CT, dose and vector-field cubes. Offers processing functions, as conversion of data type, scaling, override of values, subtraction or summation of cubes,...
- MvtCubeStats: compute statistical evaluation of the data cubes (e.g. median value, V95, homogeneity, conformity, etc.)
- MvtMotion: manipulates motion files (*.mpos*), as e.g. its extension or scaling.

3.4 Accelerator modelling

The simulation of the accelerator response during a plan irradiation is a pre-requisite for the ”prediction” of the 4D dose distribution under a specific patient's breathing. Based on the treatment plan the idea is to simulate the beam delivery sequence (BDS), i.e. the TRiP .lmdout input file. With this aim, the tool makeLmdout was developed by GSI (Steidl 2011), and later adapted to the HIT's synchrotron by M. Härtig (University Clinic of Heidelberg).
The makeLmdout version used along this thesis, here named makeLmdout-MH, corresponds to the HIT's accelerator model, where the accelerator is considered in pulsed mode, repeating accelerator cycles (aprox. 10s) and equipped with an active intensity feedback control (DIC). In this model, the synchrotron is injected with the maximum number of particles in every request. Then, during the extraction process, a feedback mechanism extracts only the particles at the requested intensity.

3.4.1 makeLmdout-MH

The simulation is based on a base data obtained from irradiated plans and considering the acceleration times, energy dependence and random intensity fluctuations.
This tool requires as input the following information:

- treatment Plan (.rst file converted to .xml format);
- motion File (.mpos file);
- spill Info, where the accelerator spill duration and pause length is specified;
- gating window information (optional);

In summary, this tool will generate as output the file containing the random simulation of the accelerator timing and intensity patterns, which corresponds in TRiP to the *.lmdout* format.

3.4.2 Conversion CVS to TRiP formats

During the irradiation of the patient its breathing signal and the accelerator delivery sequence can be recorded through the EtherCat system, as already stated in section (2.4). This simultaneous acquisition will result in a coincident time stamp between the .mpos and the .lmdout signal. The EtherCat's output is given in a Comma-separated values (CVS) format that needs to be converted into TRiP4D formats.
In-house developed scripts, by N. Chaudhri (Heidelberg Ion-Beam Therapy center), called *CVS2MPOS* and *CVS2LMDOUT*, convert the .cvs file to the .mpos and .lmdout formats, respectively.
The *CVS2MPOS* script requires as input the .cvs file, the definition of the sampling rate, the processing filter to use (e.g. the implemented band-pass butterworth filter of 2^{nd} order, from 0 to 0.25Hz), and the lower and upper breathing phase thresholds.
Finally, the *CVS2LMDOUT* script processes and converts the .cvs file into the .lmdout based on the raster file information, i.e. treatment plan.

3.5 Water-equivalent path length calculations

In ion-beam therapy the density variations in the particle path are included in the dose calculation through the concept of WEPL. The assessment of the WEPL variations may be used as a fast method to detect inter-fractional changes. Therefore, a software able to calculate it in a clinical scenario was pursued.
HIT is part of the SPARTA (Software Platform for Adaptive multimodal radio- and particle-Therapy with Autarcic extensibility) consortium, which aims to develop software that can improve therapy planning and optimise patient-specific treatment. Project that is supported by the German Federal Ministry for Education and Research (BMBF).
Within this project at HIT the modular framework MeVisLab (`http://www.mevislab.de/`) was adopted for image processing research and development of a PET-based beam range verification tool (Bauer et al. 2013; Unholtz et al. 2011).
The selection of MeVisLab for the aim of this thesis was due to: (i) its modular structure that allows to integrate easily new algorithms and functionalities; (ii) the aim of using WEPL as metric to guide plan adaptation falls into the SPARTA project; and (iii) MeVisLab already provide modules many of the necessary tools for this end.
The fully automated workflow implemented in MeVisLab in the context of PET-range verification includes:

- connection to local data base and central picture archiving systems (PACS);
- mono-modal rigid image registration;
- multi-modal visualisation of dose distributions, CT images and PET images (simulated and measured);
- range comparison analysis for arbitrary modality images. (Chen et al. 2015).

Inspired in this workflow the module for CT-CT WEPL comparison, named MVL$_{CT-Veri}$, was developed by W.Chen (Heidelberg Ion-Beam Therapy Center).

MVL$_{CT-Veri}$

This module fuses the following features:

- simultaneous import of two CTs and reference Structure Set from the PACS network;
- affine rigid registration;
- rotation of the CT in BEV's direction, based on isocentre coordinates, gantry and couch angle;
- definition of a VOI pertaining to one of the structure set VOIs;
- calculation of WEPL values: absolute values, summation along beam path, differences and standard deviations;
- visualisation of the results in 2D colour-maps and histograms.

The calculation of the 3D WEPL cube is performed based on the HLUT relative to the CT scanner written into the CT's DICOM tag, i.e. includs the HLUT data of HIT. This is performed individually for each of the uploaded CTs.
In order to speed up the conversion CT-WEPL, the calculation is only performed for a defined VOI. This VOI is set from a selected structure plus a dilatation or contraction margin in BEV.
The establishment of a workflow and the realisation of its application is explained in detail in the next chapter.

Altogether, the presented set of software and tools will be used in the next chapters, in which the details of its application will be translated into the research needs of this thesis.

Chapter 4

Inter-fractional motion

4.1 Aim of this chapter

In this chapter the dosimetric impact of anatomical variations of the target, and surrounding normal tissues, on the plan quality along the treatment course will be evaluated. Moreover, different approaches to mitigate their impact will be investigated.
Firstly, the significance of the beam configuration for the plan robustness to inter-fractional changes is presented. In a second study the influence of planning margins is assessed. Furthermore, this chapter also proposes a prediction method to assess the impact of daily variations on the plan quality based on pre-treatment CT imaging.
It has to be emphasised that the evaluated and proposed methods are dependent on the available TPS and are aimed to be clinically applicable to the HIT workflow.

4.2 Materials and methods

4.2.1 Dataset description

A set of ten pancreatic patients, already treated with photon radiotherapy, was used in an in-silico analysis of the inter-fractional plan quality for the treatment with scanned carbon ions. This set of patients will be referred as *dataset A* along this work.
All the patients were imaged with CT in 5 weeks for positioning verification purposes. All the acquisitions were in free-breathing and with the same CT acquisition protocol. The CT images were registered to the first week CT, CT_1, through rigid registration. CT_1 was used as planning CT. Registration was performed by bony anatomy matching and was validated using anatomical landmarks and visual inspection.
All weekly-CTs included physician-approved contours of the GTV from each imaging session. The CTV was defined as the GTV plus an isotropic margin of 5 mm.
The CTV variation in volume and centre of mass (COM) over the treatment for each patient was evaluated. The ΔCOM corresponds to the length of the vector displacement between the CT_1 and the follow-up imaging sessions, CT_i, from the centre of mass of the contoured CTV. The CTV volume was measured in cubic centimeters and the relative variation to the planning VOI was determined by $\Delta V = (V_{CTV1} - V_{CTVi})/V_{CTV1}$.

4.2.2 Treatment plan optimisation and dose forward calculations

Treatment plans were optimised and calculated using TRiP98, using the beam base data and RBE dataset from HIT.
Plans were tailored to deliver carbon ion IMPT to the ITV, aiming to get full coverage of the CTV, with a biological dose of 15 x 3 Gy (RBE). The spinal cord, kidneys, stomach and bowel were considered as OARs and plans were optimised to respect the tolerance dose suggested by the literature (Bentzen et al. 2010; Emami et al. 1991). The same α/β equal to 2 was used for the various organs.
The plans were generated for a scanning raster spacing of 3 x 3 mm in lateral direction and a iso-energy slice spacing of 3 mm water-equivalent for a pencil beam focus of 10 mm FWHM. These parameters were adopted from the work from Richter (2012), for moving targets.
In order to improve the dose conformation to the target, raster points around the ITV were considered in a margin of a factor of 0.9 applied to the focus FWHM for each IES. The dose optimisation was performed considering the dose contributions for every voxel within a maximum distance of 3 sigma of the focus size and using the algorithm fletcher-reeves.
The physical dose calculation relied on the method *all points*, while the biological effects were then considered through the use of the *low dose* algorithm (see chapter 3.1 for details).
Relative to the follow-up imaging, the dose forward calculation was then performed for the four rigidly registered CTs by direct application of the raster-scan sequence obtained from the previous optimisation. The same TPS and algorithms were employed.

4.2.3 Beam geometry selection

Since the selected beam entrance channel affects the plan quality, as result of density variation along the beam path, plan robustness can potentially be improved through the selection of a beam geometry which is less susceptible to density fluctuations. Hence, for each patient, six plans for different beam geometries for the first week CT were generated. A sketch of these beam directions is shown in figure (4.1).
The selection of these beam geometries considered the preceding work from Dreher et al. (2015), in which OAR constraints and target coverage were assessed in the generation of clinically feasible plans.

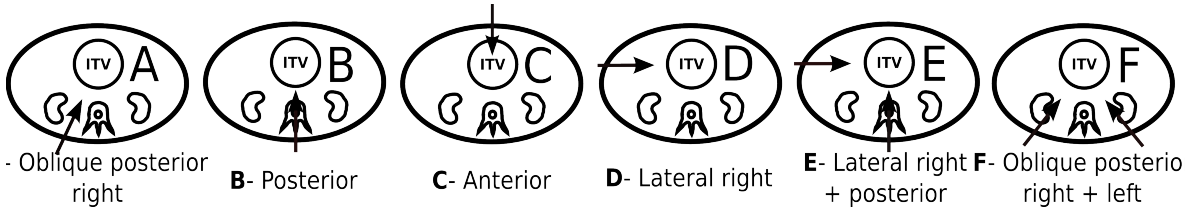

Figure 4.1: Diagram of the six beam configurations (A to F) evaluated for inter-fractional plan robustness.

4.2.4 ITV definition: From geometric to range-margins

In order to incorporate inter-fractional changes through the use of margins, three approaches to define an ITV for dose optimisation were investigated. These are outlined

in the figure (4.2) and described below:

- Geometrical, ITV_G. Geometric expansion of the CTV by application of a 3 and 5 mm symmetric margin, ITV_{G3} and ITV_{G5}, respectively. Results were compared with the use of no additional margin (ITV_{G0}).
- Uniform range-margin, ITV_{HU}. Based on the geometric concept (ITV_G), a uniform range-margin was introduced into the optimisation by replacing the HU values in an isotropic CTV-ITV margin of 3 or 5 mm with the patient-specific median density of the pancreas. These VOIs were respectively defined as ITV_{HU3} and IITV_{HU3}. In addition, the areas inside the ITV_{HU}, in which the density was less than twice the standard deviation of the median CTV HU value, were also overwritten.
- Beam specific, ITV_{Asy}. Based on a water-equivalent-path length ITV, ITV_{WEPL}, it was used to assess the needed margins to overcome the range uncertainties, caused by anatomy variations along the treatment couse. This ITV_{WEPL} considers the changes of the WEPL over the set of weekly-CTs. To this end, an adaptation of the method defined by Graeff, Durante, and Bert (2012) was employed, using the TPS TRiP4D, but considering the set of inter-fractional CTs (cf. chapter 3.1). The ITV_{WEPL} was generated/optimised from the set of follow-up CTs and respective CT-specific CTV contours. In this process, the range changes were computed for all the CTs in the defined beam directions giving origin to a modified HU-WEPL look-up table (cf. chapter 3.1). During the plan optimisation, the algorithm ensures an adequate CTV coverage along the imaging set. As product of this optimisation, not only the dose distribution but an ITV_{WEPL} contour per beam direction was obtained. From this ideal ITV_{WEPL} per patient were then defined beam-specific ITV (ITV_{Asy}) built from the patient's population variations. Details of this generalisation are given below.

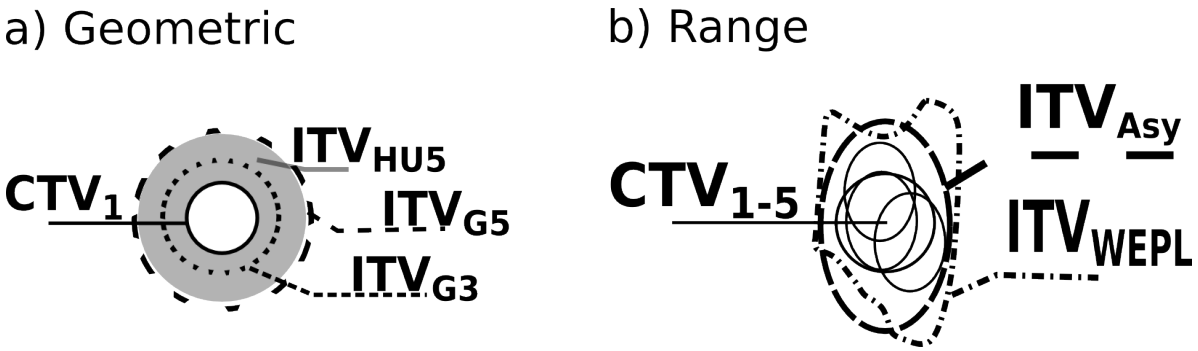

Figure 4.2: Scheme of the ITV concepts used during the plan optimisation. a) Geometric margins of 3 and 5 mm applied to the CTV, named as ITV$_{G3}$ and ITV$_{G5}$, respectively. Also depicts the uniform range margin of 5 mm (ITV$_{HU5}$), which considers an override of the CT densities during the optimisation stage in a margin of 5 mm around the CTV. b) From the different CTV contours (CT$_1$ - CT$_5$) the ITV_{WEPL} was calculated in order to ensure the full coverage of the CTV along the treatment course accounting with the density variations in the beam path. The ITV_{WEPL} for each beam direction is then generalised to a ITV_{Asy}, not patient-specific.

The definition of a suitable PTV was out of the scope of this thesis, as margins for set-up, range and beam application uncertainties are subject of a separate investigation. Likewise intra-fractional motion uncertainties were also not considered in this chapter and will be handled in chapter (5.1).

4.2.4.1 Data analysis

For all the geometries and ITV concepts, the target coverage was evaluated through the assessment of the dose received by the weekly CTV (CTV_1 to CTV_5). The considered parameters were the CTV volume that receives more than 95% of the prescribed dose ($V95_{CTV}$), the volume of the CTV that receives more than 107% of the prescribed dose ($V107_{CTV}$), the mean and maximum dose to the CTV. Additionally, the CTV dose homogeneity and conformity were also evaluated through the parameters H_{CTV} and CN, respectively, as given by the equations (2.6) and (2.5). This evaluation was performed using ROOT MvtLibraries (see section 3.3.2.
The field-specific ITV_{WEPL} was evaluated by comparison with the CTV_1 and ITV_{G5}, in terms of volumetric changes (ΔV) and ratio of the overlapping volumes, here done by the Dice Similarity Coefficient (DSC) (Birkfellner et al. 2012). The DSC is a tridimensional overlapping similarity measure, mathematically expressed by the equation (4.1), where the number of voxels of the A (reference) and B (evaluated) volumes are considered.
To extract the information of the margins direction and size, the variation of the centre of mass (ΔCOM) and the Hausdorff distance (HD) between ITV_{WEPL} and CTV were evaluated (Birkfellner et al. 2012). The HD identifies the largest of all distances from the contour under evaluation to the closest voxel on the reference contour (Birkfellner et al. 2012). To reduce the patient specificity when applying this concept to other patients, the 95^{th} percentile of the HD as evaluation metric was selected, HD_{95}.
Both volumetric parameters were evaluated using the 3DSlicer software, cf. chapter (3.3.1). A diagram of these two metrics is shown in the figure (4.3).
The COM variation was measured in CT coordinates (x,y,z) and then converted to the HIT beam scan coordinate system using the couch and gantry angles (Jäkel et al. 1997). Hence, the evaluated COM values were transformed to lateral, depth and cranio-caudal directions, relatives to the beam entrance direction.

$$DSC(A,B) = \frac{2|A \cap B|}{|A| + |B|} \tag{4.1}$$

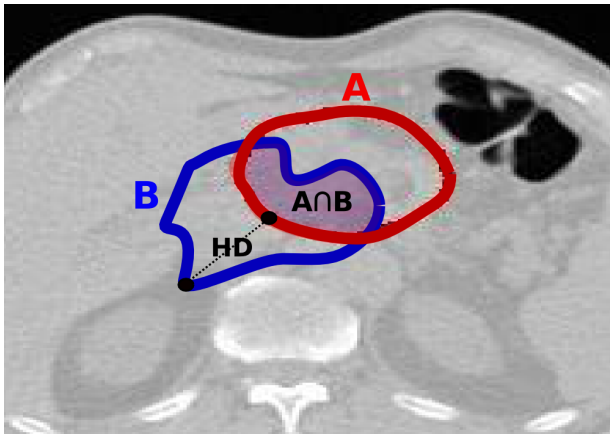

Figure 4.3: Graphic representation of the Hausdorff distance (HD) and Dice Similarity Coefficient (DSC) for comparison of the contour B against the reference contour (A). The HD corresponds to the largest distance between a point from the volume B and the closest voxel on the reference contour. DSC is obtained by the ratio of the overlapping volume between contours ($A \cap B$) and the summation of the individual volumes.

4.2.5 Assessment of anatomic variations through WEPL-maps

4.2.5.1 Aim

A major constraint to perform plan adaption is the complexity and time consumption required. In ion-beam therapy, the concept of water-equivalent path length (WEPL) describes the density of the transversed material in the particle path. During dose calculation, it is the WEPL that accounts for the particle range in the beam trajectory, through the transformation between the CT system (i.e HU) into the water-equivalent system.
Since the WEPL is only dependent on the HU-value, its calculation is a quite fast process that could be implemented as verification procedure based on a pre-treatment CT (Mori et al. 2009). However, this method just includes the variations as consequence from different densities, without performing a dose calculation, i.e, ignoring the different beam intensities and energies in each raster point. Therefore, a correlation between these two quantities, dose and WEPL, needs to be established in a way to define an acceptance threshold for which the patient can be safely treated or the treatment plan re-calculated for the new CT. Neverthless, this method doesn't dispense a clinical evaluation and an investigation of the reasoning for such WEPL variations.
To sum up, the aim of this section is to suggest a method to estimate the impact of anatomical changes on the dose distribution based on WEPL variations and correlate them with dosimetric indicators to assess the need of re-planning. The purposed workflow need to be clinically feasible, i.e. end-to-end within an acceptable time (below 10 min) and an intuitive decision-making process.

4.2.5.2 Material and methods

For the same set of patients, dataset A, the dose distributions optimised for the CTV_{G0} and the forward dose distributions for each of the weekly CTs were accounted. In order to assess the correlation between the dose distribution variation and the WEPL changes, the WEPL-maps per individual beam direction were calculated, corresponding to the beam configurations A-D of the figure (4.1).
The WEPL cubes were calculated and evaluated in the MeVisLab platform, available and partially developed at HIT. For the intended functions of this chapter a newly developed module $MVL_{CT-Veri}$ was employed (cf. chapter 3.5). $MVL_{CT-Veri}$ was specifically created for the computation of the WEPL in follow-up CT images on a regular basis with an intuitive user interface (see figure 4.4).
In a pre-processing stage, performed in an additional MeVisLab module, all the CTs, which include a stereotaxic frame and the imaging couch, were cleaned up from these devices to the external contour size.
Regarding the WEPL assessment, the adopted workflow is outlined in the figure 4.5 and described below.
In a DICOM manager module, the reference CT, respective structure set, and the CT under evaluation, were loaded into the $MVL_{CT-Veri}$ main module. Since the dataset A was already rigidly registered in the previous study the registration step was skipped.
Subsequently, both CTs were rotated into the BEV according to the plan informations (isocentre, couch and gantry angles). In figure (4.4 a) the menu for the plan definition is shown and figure (4.6) shows the rotation of a patient in BEV for an oblique posterior

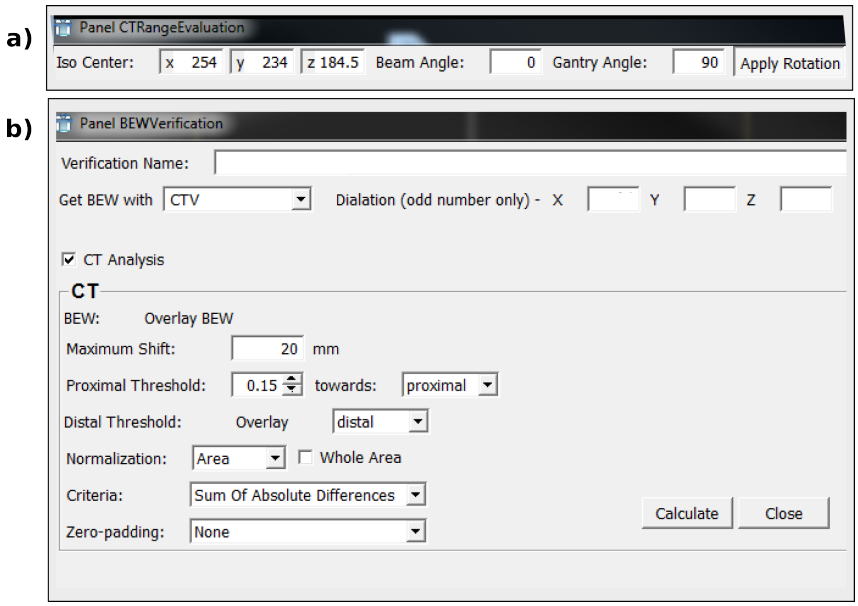

Figure 4.4: MeVisLab Interface in the MVL$_{CT-Veri}$ module. **a)** Menu for the definition of the isocentre, gantry and couch angles with the function to apply a CT rotation in BEV. **b)** Main menu for the definition of the parameters used during the WEPL calculation.
Note: this image was modified to fit into the page width discarding functionalities related to other modules.

beam.

Secondly in the menu b), depicted in figure (4.4 b), the WEPL calculation parameters were set up. Starting by the definition of the VOI$_{WEPL}$ in which the WEPL will be computed; such is performed through the selection of a reference structure plus an additional margin. Hence, in BEV the VOI$_{WEPL}$ is defined by this dilatated structure while in beam direction is limited by the patient's skin to the proximal or distal side of the structure. A sketch of this volume, VOI$_{WEPL}$, is presented in figure (4.7).
In order to be clinically relevant and correspondent to the dose calculation results, the VOI$_{WEPL}$ was selected as the CTV plus a dilatation margin of 4.8 x 4.8 x 4.5 mm. In the proximal-distal direction the patient surface was defined as starting point, i.e., considering 15% of the CT value in BEV, and the distal edge of the CTV plus the additional expansion of (aprox.5 mm) as ending point (see fig. 4.7).

The WEPL is then calculated, for each voxel inside the VOI$_{WEPL}$, from the HLUT of the respective CT. Thus, the accumulated-WEPL (accWEPL) along the beam path of the VOI$_{WEPL}$ was computed. The differences of the accWEPL between each CT and planning CT (ΔaccWEPL) were evaluated through the 2D difference colour-maps and histogram. These differences (ΔaccWEPL) correspond to the sum of absolute differences.
Additionally, to help in the interpretation of the results, MVL$_{CT-Veri}$ possesses a synchronised cursor to move between maps, and simultaneously, within the unidimensional overlaid profiles of the CT Hounsfield Units along the defined axis.

Regarding the definition of a correlation between dose distribution and WEPL maps, $V95_{CTV}$ and H_{CTV} were considered as metric of the dose distribution quality, while the WEPL was evaluated by: (i) mean of the variations (ii) standard deviations; (iii) variance of the ΔaccWEPL; and (iv) percentage of voxels of the ΔaccWEPL with less that 3mm$_{water}$ variation (PV_{in}). The PV_{in} parameter is the easiest method to quantify the ΔaccWEPL based on its histogram, where the area of the histogram between a defined

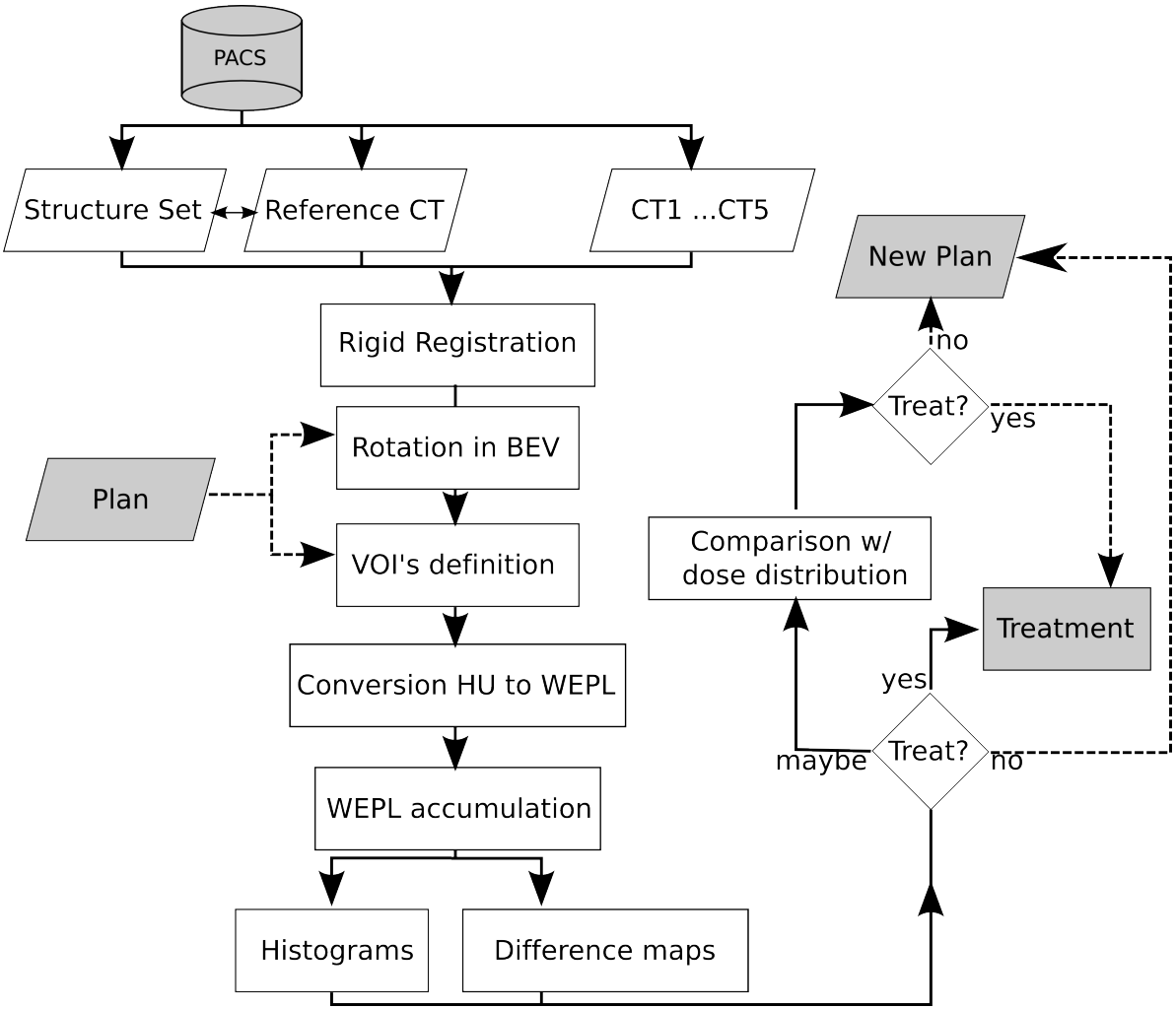

Figure 4.5: Diagram of the proposed workflow for the quantification of the anatomic variations and clinical decision on the subject of re-planning. The grey boxes correspond to functions outside the MVL$_{CT-Veri}$ module. The dashed lines correspond to a non-direct data connection.

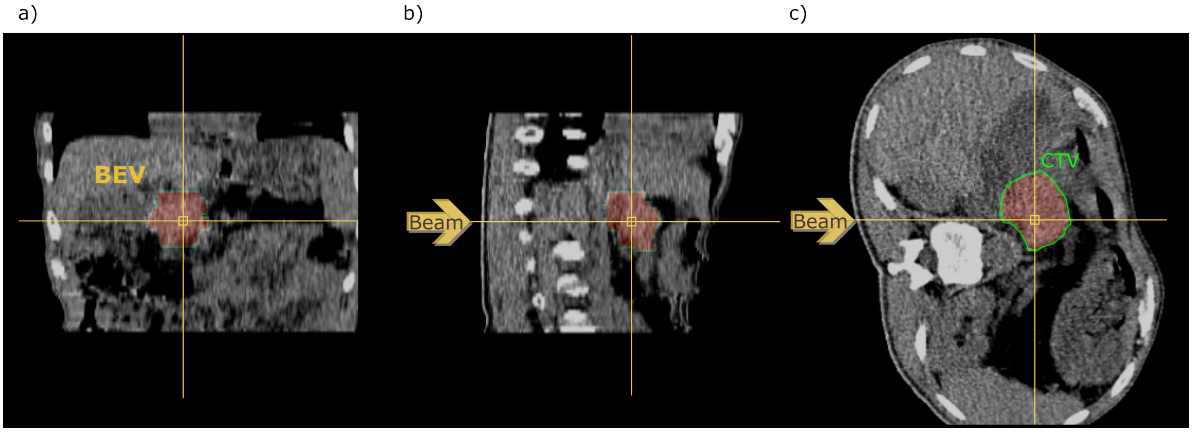

Figure 4.6: Example of the BEV rotation of a CT for a oblique posterior beam. The module MVL$_{CT-Veri}$ displays the CT in the three new axis after rotation, where a) correspond to the BEV, and b) and c) to the other two directions (x, y) with the beam always coming from the left side.

acceptance threshold, e.g. from -3 to 3 mm$_{water}$ difference, can be used as criterion for the accWEPL evaluation.
Additionally, the gamma-index γ (Low et al. 1998) was adapted for the comparison of

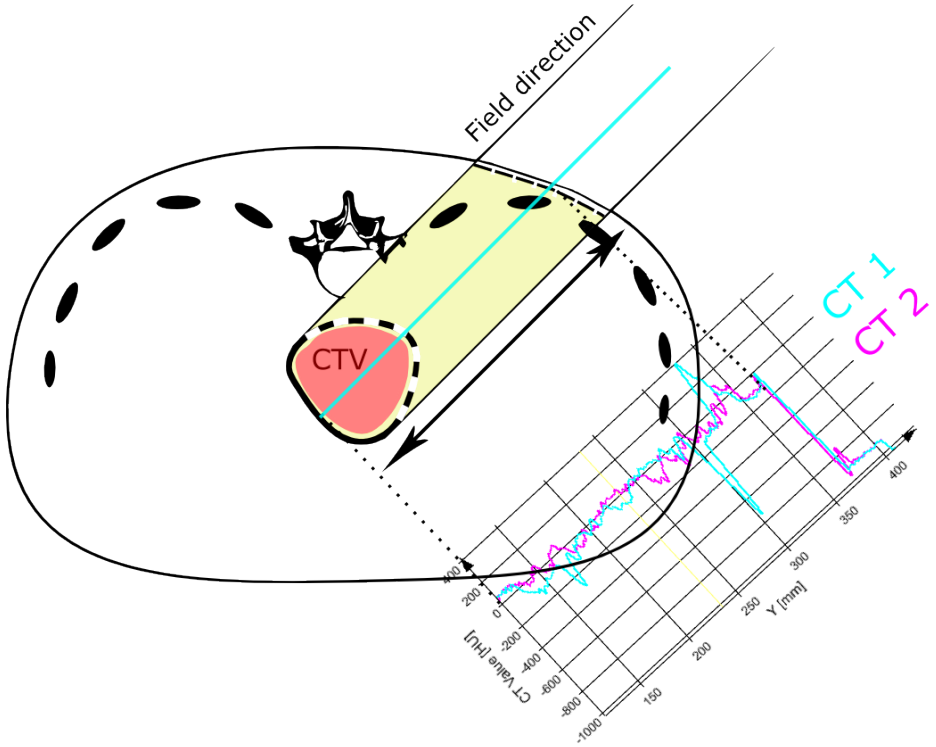

Figure 4.7: Sketch of the definition of the VOI for the WEPL evaluation (yellow region) defined based on a contour (here the CTV, in red) plus a dilatation margin. In the proximal direction starts from the 15% of the maximal CT value for every CT voxel. Distally it is limited by the CTV plus a defined margin.

the dose distributions from the planning CT and weekly-CT, where for all the points the dose difference between the two distributions,D_{pCT} and D_{wCT}, respectively, and determined the distance between the points r_{pCT} and r_{wCT}. This criterion gives the spatial information of the dose differences in the normal tissues, not possible through the $V95_{CTV}$. The gamma-index, as given by the equation (4.2), was calculated using the Plastimatch software and evaluated in terms of percentage of voxels with γ < 1 (i.e. gamma passing-rate, gamma$_{p.rate}$), gamma index distribution and fail-map (i.e, red colouring for the voxels with $\gamma > 1$). The acceptance criteria of 3% dose difference (Δd) and 3mm distance to agreement (DTA) was chosen. The

$$\gamma = \sqrt{\frac{[D_{pCT}(\vec{r}_{pCT}) - D_{wCT}(\vec{r}_{wCT})]^2}{\Delta d^2} + \frac{|\vec{r}_{pCT}, \vec{r}_{wCT}|^2}{DTA^2}} \tag{4.2}$$

The measure of the correlation accuracy was assessed using the Pearson correlation coefficient (r) and the p-value. The Pearson correlation indicates the strength of the linear association between two parameters, while the p-value determines the statistical significance in a hypothesis test.
A linear regression was calculated for the data and evaluated in terms of the coefficient of determination (R^2), the distribution of the residuals and the confidence internal (ConfInt) [2.5%; 97.5%]. The complete statistical analysis was performed using R scripts (Pruim 2011).

Note that, in first instance, the evaluation was performed just for the single beams configurations with the aim to exclude issues arising from the multi-fields plan optimi-

sation, once the WEPL is always a calculation per-field. The use of multiple beams will be addressed in section (4.4).

4.3 Results

The impact of anatomy and range changes on the target coverage and dose homogeneity among beam geometries, margins concepts, patients and fractions was initially explored. Volume and COM variations (figure 4.1) of the CTV along the treatment were used to transcribe the dose degradation effect into clinical reasons.
Finally, the applicability of the ΔaccWEPL criterion as translator of the anatomy changes into dose distribution modifications is presented.

4.3.1 Variability of the volume and positioning of the target

The individual CTV volume and positioning, for each CT and patient, was measured and compared with the reference volume, CTV_1. The total results are presented in the table (4.1). It was noticed the maximum volume and COM variation for patient A1, while patient A5 shows a nearly constant CTV volume along the treatment course, and patient A10 exhibiting a steady COM. In average this set of patients showed a decrease of the CTV volume along the treatment (-2.6%±5.5%) and a ΔCOM for all the CTs within the range [0.0; 7.7] mm.

Table 4.1: Dataset A - description of the CTV mean and standard deviation variation in volume (ΔV) and position (ΔCOM), relative to the initial volume.

Patient	ΔVolume (%)	ΔCOM (mm)
A1	-10.5±6.5	3.7 ±2.1
A2	-8.2±8.2	2.3±0.2
A3	-1.0±2.5	2.2±1.8
A4	-4.9±2.7	2.5±0.9
A5	0.2±0.8	1.2±0.8
A6	2.3±0.5	2.2±0.4
A7	1.8±4.1	1.4±0.1
A8	2.0±2.1	0.5±0.2
A9	-6.2±0.8	1.8±0.1
A10	-1.1±0.7	0.3±0.2
Mean	-2.6±5.5	1.8 ±1.3

4.3.2 Beam geometry

The beam geometry showed a substantial impact on target coverage and homogeneity over the treatment course. The summary of the results for the V_{95CTV} is laid out in the table (4.2). The evaluation of the CN, D_{maxCTV} and median doses can be found in the appendix (A.1.1).

Table 4.2: Comparison of the dose distributions in terms of V_{95CTV}, expressed by the mean and standard deviation over all patients and weekly-CTs per beam incidences and ITV-concepts. The margins ITV_{G0}, ITV_{G3} and ITV_{G5} correspond to the simple geoemtric expansion of the CTV by a 0, 3 or 5 mm margin, respectively. In ITV_{HU3} and ITV_HU5 an uniform density VOI was used during the optimisation process, while the forward dose calculation used the original CT's densities. The ITV_{Asy} correspond to the testing of the assymetric concept based on the ITV_{WEPL}, therefore the forward dose calculation for all the CTs and patients was only performed for the less robust beam configurations, i.e. C and D.

	V_{95CTV} Gy (RBE)					
Margin \ B.geom	A	B	C	D	E	F
ITV_{G0}	95.6±2.8	96.4 ±2.7	88.7±7.0	90.8±5.6	98.0±2.0	98.9±1.5
ITV_{G3}	98.1±1.7	98.6±1.6	92.6±6.4	94.0±4.2	98.9±1.7	99.5±1.2
ITV_{G5}	99.2±1.2	99.4±1.2	95.8±5.2	96.7±3.1	99.4±1.3	99.6±1.2
ITV_{HU3}	98.1±1.6	98.6±1.6	92.6±6.3	94.2±4.1	99.1±1.4	99.5±1.2
ITV_{HU5}	99.2±1.2	99.4±1.2	95.8±5.1	96.8±3.0	99.4±1.2	99.6±1.2
ITV_{Asy}	n.a	n.a	97.5±3.9	98.1±2.1	n.a	n.a

The configuration C and D (cf. figure 4.1) showed the worst mean average coverage as well as standard deviations along the treatment. Resulting in a constant V_{95CTV} decrease, regardless of the used margin, as visible in the respective columns in table 4.2 and in the figure 4.8 a). In terms of H_{CTV} (see fig. 4.8 b) these beam geometries tend to be less homogeneous dose distributions along the treatment course. Moreover, it is also visible a mean increase in the CN of (0.08±0.07) comparative to the other geometries (0.02±0.04), considering all the patients, CTs and margins concepts. Figure (4.9) shows some examples of dose distributions with different beam geometries. Additional dose distributions are presented in the appendix (A.4) and (A.5).
The results from C and D are related with the observed range uncertainties in the anterior abdomen region due to the inter-fractional variability of the patient anatomy (bowel, stomach and weight loss). Figure (4.9) discloses these inter-fractional changes contributors through the axial view of the dose distribution in one of the follow-up CTs for four patients. In particular, patient A3 exhibits a strong under-dose when planned for an anterior beam as result of density changes in the bowel/stomach. Another example pointing for the lack of robustness of an anterior beam, is the patient A8 that exhibits accentuated weight loss, this is visible in figure (4.9) from the comparison of the distribution between the first and last week CT.
Relative to Patient A1, is observed that even when used an oblique posterior beam, due to the target deformation, resulted in a V_{95CTV} reduction of approximately 4% for one of the CTs, although the tumor COM shift was below 3mm.
As example of a plan with a lateral right beam, patient A10 (fig. 4.9 c) shows range changes as resulted from the bowel and liver position leading to health tissues overshooting.
It is noticed that although the geometry D is not robust against inter-fractional changes, the use of this beam direction combined with a robust one, as the case of the geometry E, will improve the dose distribution along the treatment course. This fact is a consequence of the reduction of the weight of the non-robust beam compared with the single beam irradiation.
In summary, V_{95CTV} for non-robust geometries decreased by up to 30% and 28%, for a 3 mm and 5 mm margin, respectively (fig.4.8). Considering all the patients, CTs and margins for the set of the geometry C and D, this correspond to a mean variation of the V_{95CTV} of (-4.5±4.8)%, the H_{CTV} of (4.3±6.5)% and the mean dose of (-0.03±0.04)

Gy (RBE) /fx. In contrast, for the others beam's configurations (A, B, E, F), the V_{95CTV}, H_{CTV} and mean dose were nearly conserved, i.e. mean variations along patients, CTs and margins of (-0.7±1.2)%, (0.5±1.3) and (-0.01±0.03) Gy (RBE)/fx, respectively. Relative to the V_{107CTV} and maximum dose, no significant differences were found. All these results are available in more details in the appendix (A.1.1).

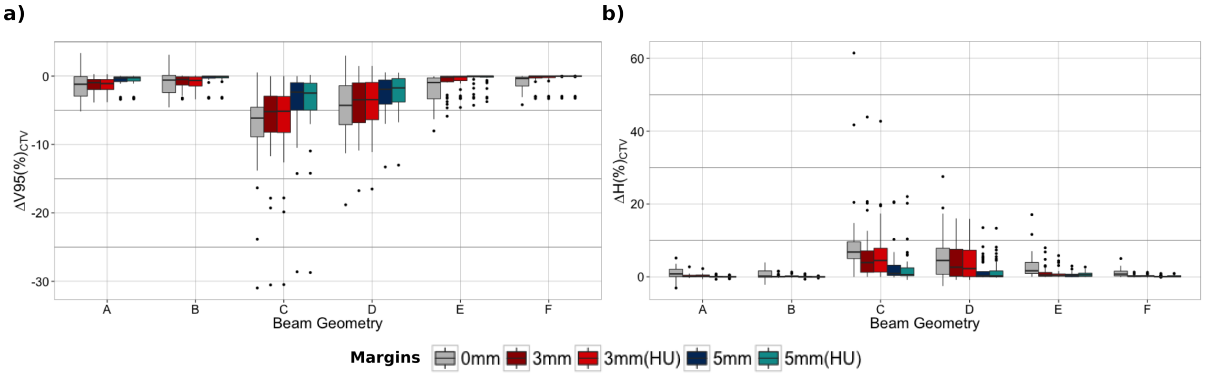

Figure 4.8: Results from the CTV dose evaluation from the weekly dose distribution obtained from different optimisations (in beam direction and ITV) comparatively to the planned dose distribution. **a)** Variation of the V_{95CTV} **b)**Variation of the H_{CTV}. Each box represents 25 - 75% of the data, with the median value represented as the solid line and the outlier as the dots.

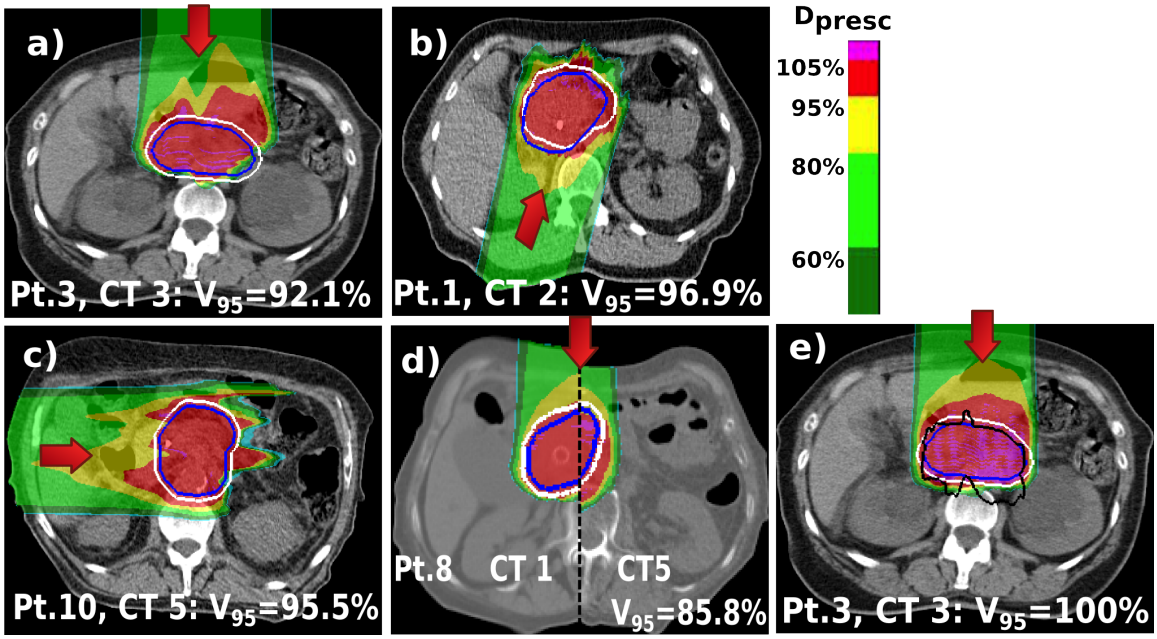

Figure 4.9: Forward dose distribution of the optimised plan for the ITVG5 (white contour) in one of the weekly CTs for four different patients exhibiting different inter-fractional changes. Depict is the value of the V_{95CTV}, in the respective CT, for the CTV (in blue). **a)** Patient A3 for an anterior beam as results of changes in the bowel/stomach. **b)** Patient A1 with an oblique posterior beam showing tumour deformation. **c)** Patient A10 planned with a lateral right beam with bowel and liver position alterations. **d)** Patient A8 for an anterior beam exhibiting an accentuated weight loss between the CT_1 and CT_5. **e)** Dose distribution for the same CT and patient as in the figure a) but showing the retrospectively determined ITV_{WEPL} (black contour) in comparison to the ITV_{G5} and the dose distribution for the new optimisation.

4.3.3 ITV concepts

The selection of a robust beam geometry (as A, B, E and F) together with the use of geometric margins showed to be able to mitigate some of the effects coming from the inter-fractional range changes, as seen in the table (4.2) and figure (4.8). The figure (4.10) details the use of a 5 mm margin, per patient and beam configuration, where the use of the ITV_{G5} was enough to keep the mean V_{95CTV} above 99% for the named robust geometries.
From the outliers of figure (4.8 a and b) is concluded that even for the more robust geometries there are cases of patients, and isolated fractions with dose degradation, however only a maximal variation of 3.4% in the V_{95CTV} was reached (when using the ITV_{G0}). The analysis of these particular cases, was found to correspond to patients with changes in the tumour volume and COM (e.g. figure (4.9 b). To overcome these situations the use of the two oblique posterior beams (configuration F) showed to be more stable along the treatment course.
Other analysed option to increase the plan robustness was the use of symmetric range-uniform margins, ITV_{HU}. The results of the forward dose distributions for all the patients, also presented in the table (4.2) and figure (4.8), led to the conclusion that the used of 3 and 5 mm HU-uniform was not sufficient to mitigate the extreme range changes in the anterior and lateral beam direction, without significant improvement over the geometric concept. Hence, these conclusions drove to the investigation of asymmetric margins.

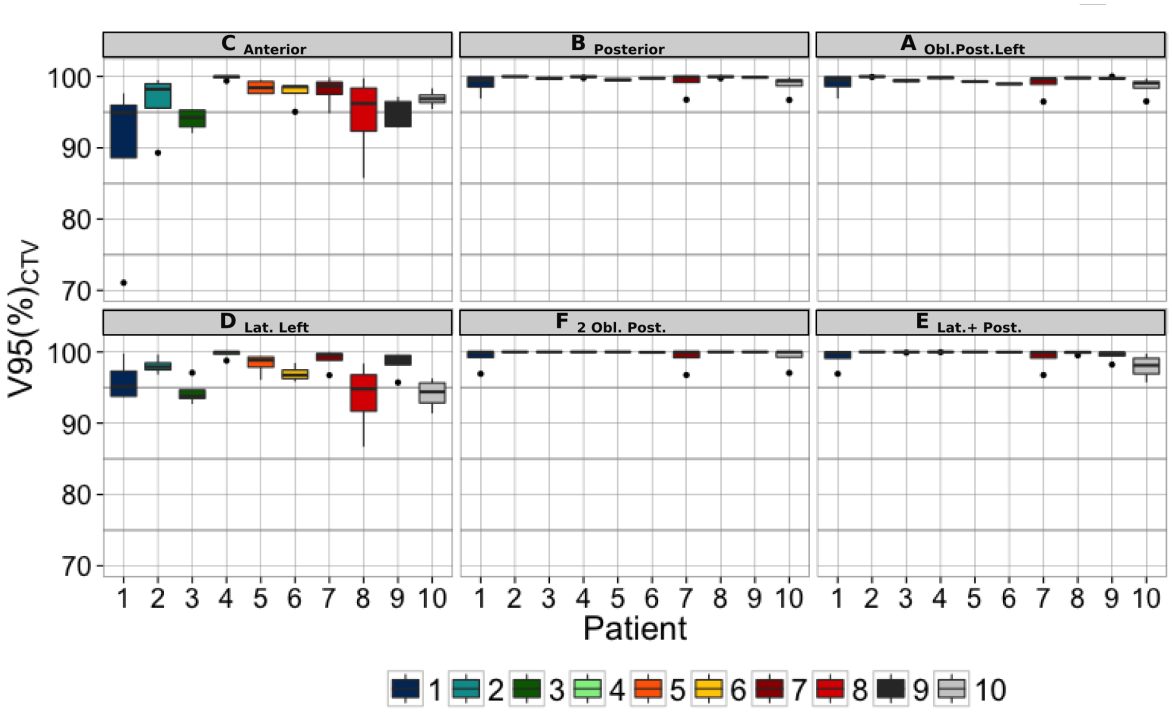

Figure 4.10: Distribution of the V_{95CTV} per patient and beam geometry of the dose distributions obtained from the forward calculation of the treatment plan optimised to the ITV_{G5}.

4.3.3.1 Asymmetric margin analysis

The obtained ITV_{WEPL} per beam direction, which includes the range variations along the weekly-CTs, allowed to get the information of how asymmetrically the ITV needs to be defined to maintain the CTV coverage. A representative example of the ITV_{WEPL} shape for an anterior beam is shown in figure (4.9 c).
The ITV_{WEPL} size and shape necessary to keep the CTV coverage does not need to be volumetrically larger than a 5 mm expansion, with the analysis of the ITV_{WEPL} volume showing a volume (-26.0$\pm$6.3)% smaller than the ITV_{G5}, as result of tight margins in the lateral direction to the beam and a margin increase for the non-robust beam geometries in the depth beam direction. The complete results of the ITV_{WEPL} for each patient and beam's incidence is outlined in the appendix (A.1.
The margin size and expansion direction were assessed from the COM variation and HD_{95} value. The mean V_{95CTV} over the course of the treatment when no margins are applied, was used as metric of the inter-fractional changes per beam direction. Its correlation with the DSC and the HD_{95} led to the selection of the HD_{95} as indicator of range changes, due to a positive linear relation (r=0.78) versus the smaller correlation coefficient of the DSC (r=0.63), as seen in the figure (4.11. This might be a result of the lack of directional information obtained from the DSC. The p-value was found for both correlations to be below 0.001.
The analysis of the volume and ΔCOM of the obtained ITV_{WEPL} is presented in terms

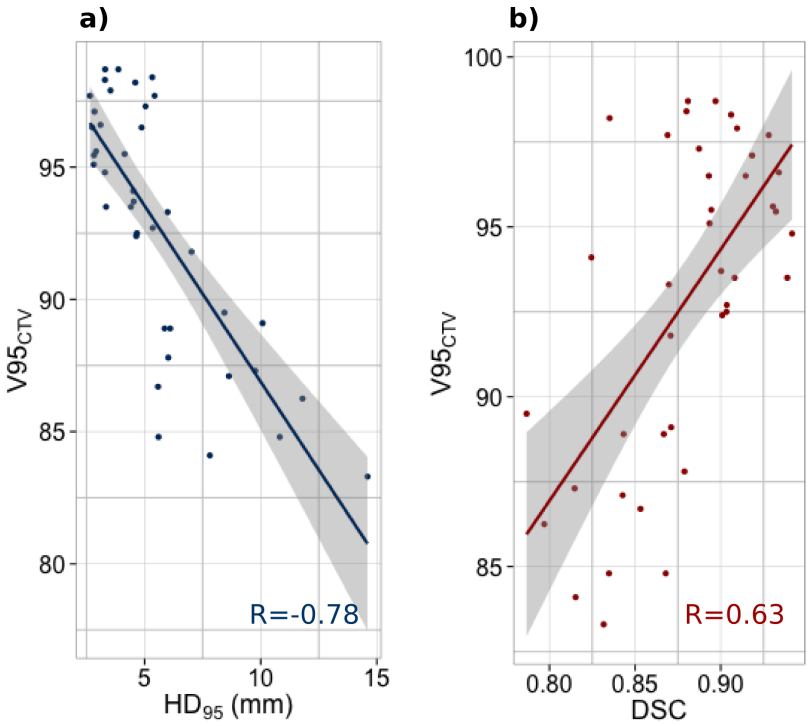

Figure 4.11: Correlation between the HD_{95} and DSC with the V_{95CTV} in the figure a) and b), respectively, for all the evaluated beam configurations. In grey the 95% confidence interval is drawn.

of median and quartiles values in table (4.3). A better interpretation of the results is possible through the figure (4.12), where the ΔCOM is depicted along the three axis relative to BEV (depth, lateral and cranio-caudal). Additionally, figure (4.13 b) shows the HD_{95} per beam direction and gives the Pearson correlation coefficient for the HD_{95} -V_{95CTV} relationship, with the beam direction. From this image is shown that the Pear-

son correlation coefficient has different values with beam direction, as result of the small variation of V_{95CTV} is this sample.

In brief, the ΔCOM give us the information of how the ITV_{WEPL} expands/contracts

Table 4.3: Evaluation of the calculated ITV_{WEPL} by: volume comparison with the ITV_{G5} (mean, minimum and maximum are shown); directional expansion relative to the CTV (HD_{95}); COM variation relative to the CTV. The reported values as $Q_{25\%}$ and $Q_{75\%}$ correspond respectively to the first and third quartiles of the data.

	ΔV ITV$_{G5}$-ITV$_{WEPL}$		**CTV exp. (mm)**	**ΔCOM depth (mm)**	**ΔCOM lateral (mm)**	**ΔCOM cc (mm)**
Param. / Beam	**Mean(%)**	**[Min;Max](%)**	**$Q_{75\%}$ of HD_{95}**	**[$Q_{25\%}$;$Q_{75\%}$]**	**[$Q_{25\%}$;$Q_{75\%}$]**	**[$Q_{25\%}$;$Q_{75\%}$]**
A,F1	-28.0	[-35.3,-22.6]	4.5	[-1.2; -0.3]	[-0.2;0.3]	[-0.3;0.5]
B,E2	-27.9	[-36.5,-22.1]	4.5	[-0.8 -0.5]	[0.0;0.2]	[-0.3;0.5]
C	-16.9	[-30.5,-8.4]	10	[-5.3;2.8]	[-0.2;0.5]	[-0.2;0.4]
D,E1	-26.9	[-37.2,-15.5]	6.8	[-3.1;0.4]	[0.1;0.7]	[-0.2;0.9]
F2	-28.7	[-35.9,-21.4]	5.0	[-0.7;0.7]	[-0.1;0.5]	[-0.3;0.4]

relative to the CTV, while the HD_{95} says how much. To explain this statement in detail let's get the example of the geometry C. From fig. (4.13 a) results that the margin to apply to the CTV to cover all the cases was superior to 10 mm in one of the directions, i.e just 75% of the evaluated ITV_{WEPL} volumes were up to 10 mm. From figure (4.12) it is clear that for the geometry C no strong COM variation was detected in the lateral and cranio-caudal BEV direction, so this large margin will have to be added in depth direction (ΔCOM > 5 mm), larger in the proximal edge of the beam for the majority of patients. Therefore, this 10 mm margin (valid in 75% of the patients) will be asymmetrically distributed in depth, where from the $Q_{25\%}$ and $Q_{75\%}$ of the ΔCOM (cf. table 4.3) corresponds to a proximal expansion of 10 mm ($\approx 10/2 + 5.3$) and a distal increase of 7 mm ($\approx 10/2 + 2.8$).

Using the same thought, it results that for the geometry D the required ITV_{Asy} margin, to cover 75% of the dose distributions, corresponds to 6 mm and 3 mm in the proximal and distal direction, respectively.

Based on these results, new plan optimisations were performed for these asymmetric ITV (ITV_{Asy}) that cover 75% of the sample. Regarding the lateral and cranio-caudal direction an expansion of 2.5 mm in each direction was applied. The delivery of these new plans to each weekly-CT, showed an improvement of the V_{95CTV} superior to 2% relative to the use of a geometric 5 mm expansion, depicted in the last row of the table (4.2). This proved the validity of this concept, improving the target coverage even with less robust beam geometries. However, the increase of the geometric margin will result unwanted doses to the normal tissues.

For robust geometries the analysis showed that the use of a symmetric margin is suitable, where 5 mm was enough for 75% of the evaluated fractions. The results pointed toward a minimal margin of 3.5 mm needed to overcome the uncertainties coming from the inter-fractional changes.

4.3.4 WEPL-maps for detection of inter-fractional changes

For all the patients the accWEPL were calculated for the four different beam entrance channels, i.e., anterior, lateral left, posterior and oblique posterior left to the patient anatomy, designed as *Ant*, *Lat*, *Pos*, *Obl* along the results discussion. The ΔaccWEPL

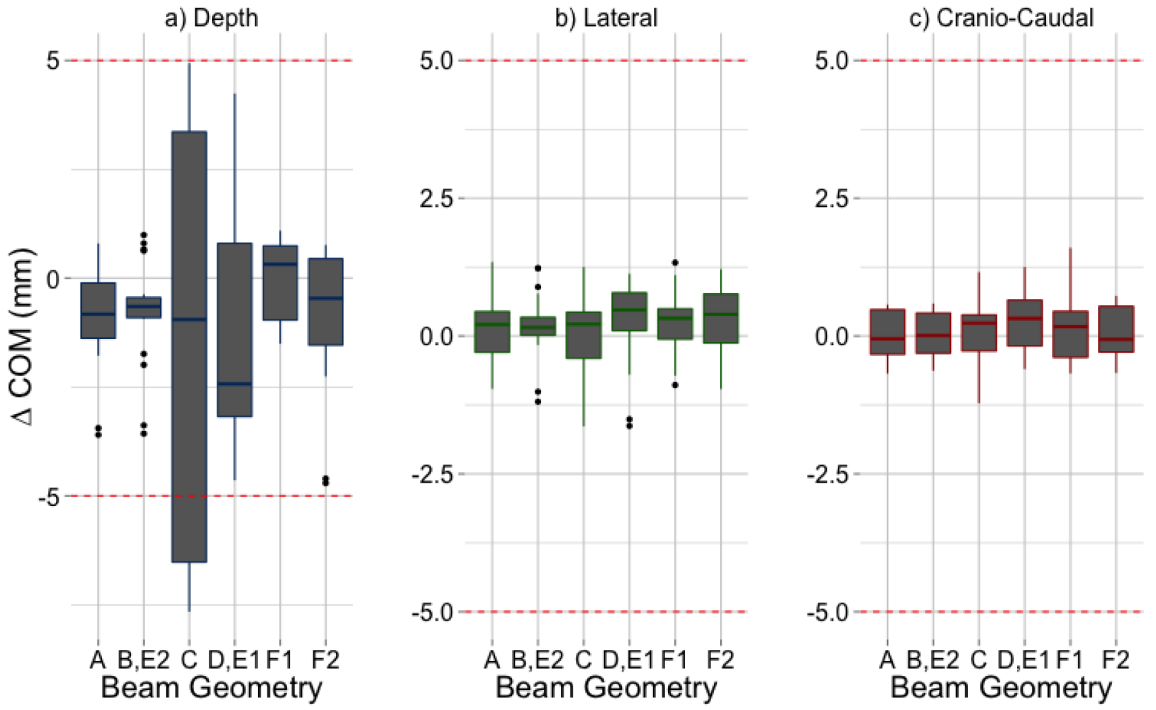

Figure 4.12: Variation of the COM of the ITV_{WEPL} relative to the CTV in the longitudinal (a), lateral (b) and superior-inferior (c) direction with respect to the beam entrance channel.

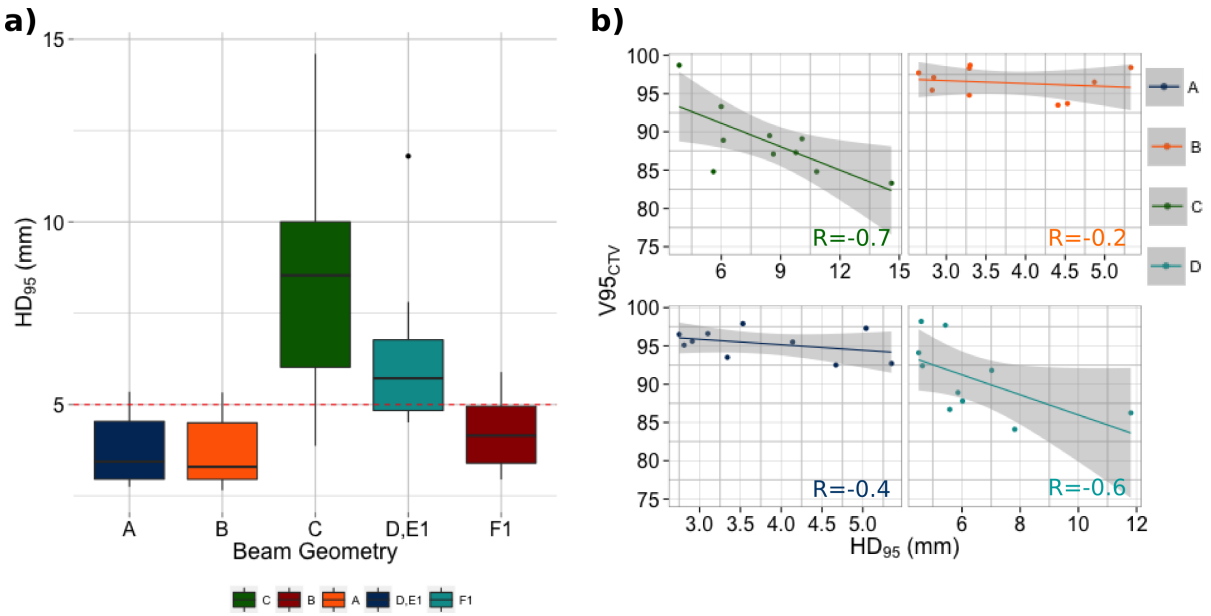

Figure 4.13: Changes of the HD95 as function of the beam geometry, with each box showing 25-75% of the data. b) Correlation, per beam direction, between the CTV V95 mean dose for the weekly CTs (plan optimised to the ITV_{G0}) and the HD95. In grey the 95% confidence interval is drawn.

was obtained from the comparison between each weekly-CT to the planning-CT. Afterwards, the ΔaccWEPL was evaluated using different parameters and correlated with dosimetric parameters, as $V95_{CTV}$, H_{CTV} and $gamma_{p.rate}$.

4.3.4.1 ΔaccWEPL evaluation

The complete evaluation of the ΔaccWEPL for all patients and CTs is presented in the appendix, table (A.2), while a summary of these results per beam angle is shown in figure (4.14).

From the first overview of the ΔaccWEPL distribution, it is again concluded about the

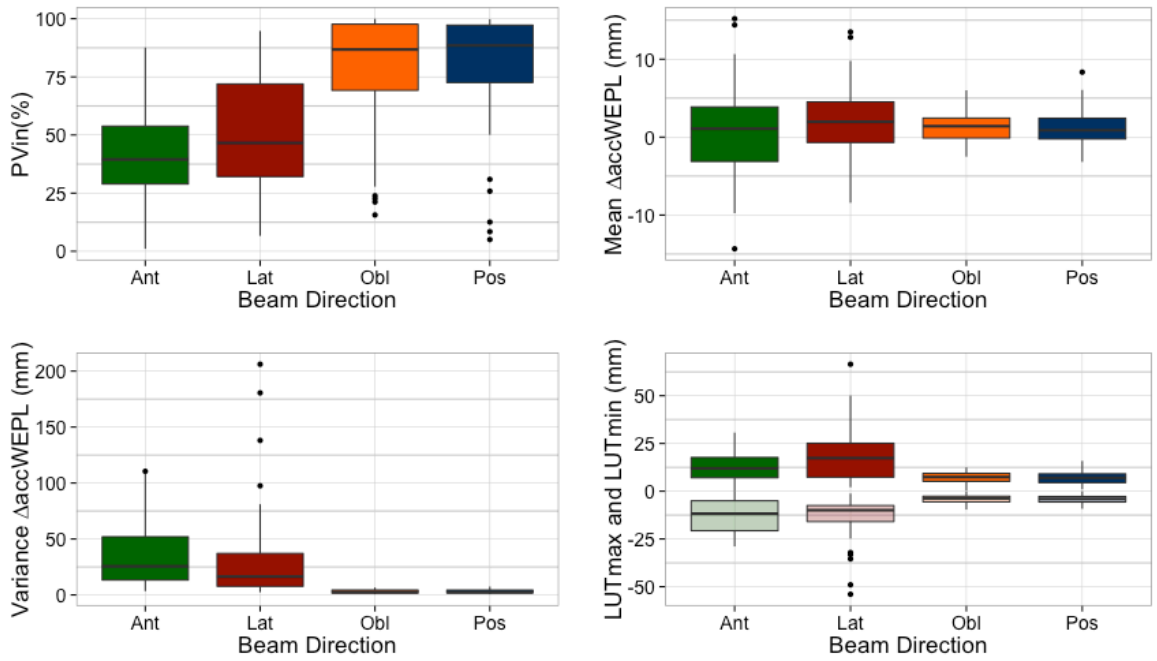

Figure 4.14: Resume of the evaluation performed to the ΔaccWEPL maps along the specific beam direction in BEV for all the patients by comparison of each week-CT with the planning CT. The plots show the variations of the accWEPL maps per beam incidence in terms of percentage of voxels within a [-3;3] mm_{water} variations (PV_{in}), mean ΔaccWEPL, variance of the ΔaccWEPL and the LUT_{min} and LUT_{max}.

robustness of some beam directions against inter-fractional changes. This is explained by the average of the patients and CTs showing smaller ΔaccWEPL for the posterior and oblique posterior beam incidence, i.e. smaller box width of the ΔaccWEPL mean and variance and around zero (figure 4.14.

An illustrative example of the analysis performed, per patient and pair of CTs, is depicted in figure (4.15). Shown is the case of patient A1 where an anterior beam is applied to the CT_1 (CT_{Plan}), CT_3 and CT_4. By comparison with the CT_{Plan} an increase of the air amount comparative to the planning CT is noticed. This results in a strong reduction of the number of voxels below the defined PV_{in}, i.e. inside the interval of [-3;3] mm_{water} variations. This evaluation is possible either though the visual analysis of the bi-dimensional ΔaccWEPL map, where regions with high ΔaccWEPL are shown in lighter colours (fig. 4.15 b) or by the histogram of the accWEPL diferences, in which the PV_{in} is delimitated by two horizontal green lines (fig. (4.15 c). For the case of this patient it is also concluded that the inter-fractional anatomy chances are stronger in the CT4 than in the CT3 comparatively with the CT_{Plan}. This postulate is confirmed when looking for the dose distributions forward calculated for these CTs, where the obtained $\Delta V95_{CTV-G0}$ is of 5.5% and 31.0%, respectively.

To demonstrate this relationship between dose and accWEPL, in figure (4.16) the ΔaccWEPL (through the parameter PV_{in}) and the parameters from the dose distribu-

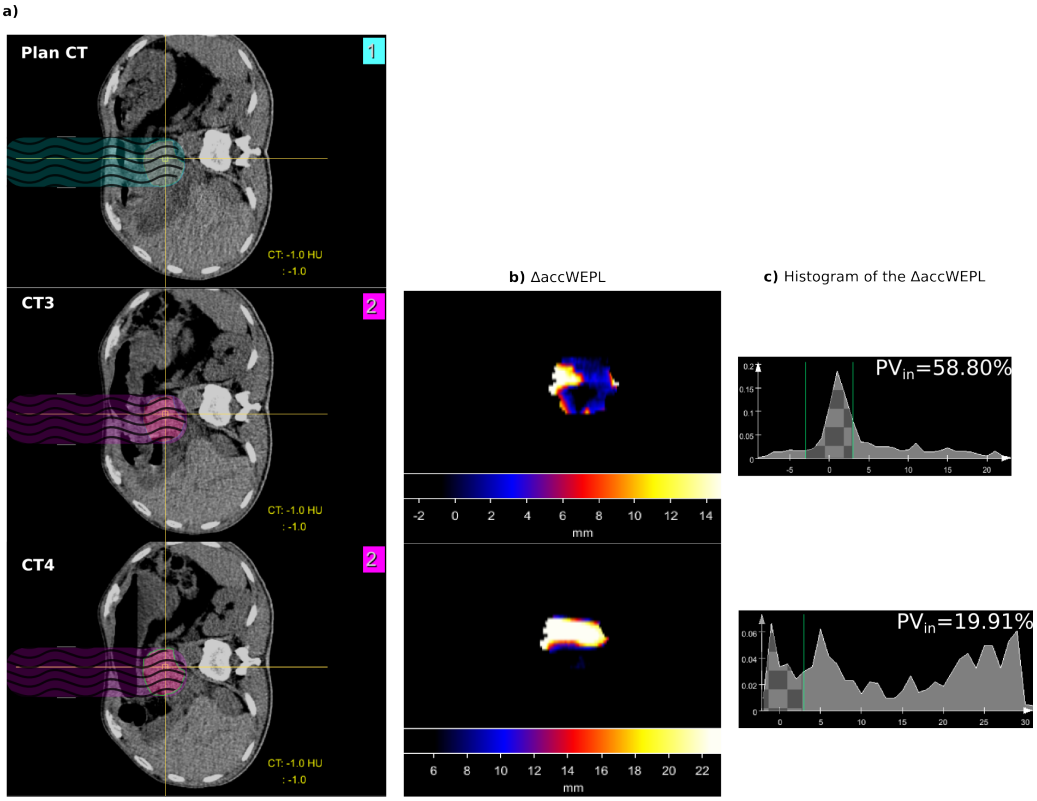

Figure 4.15: Example of the performed evaluation in the MeVisLab module for the patient A1, for which the accWEPL in the CT3 and CT4, were compared to the CT$_{Plan}$ in anterior BEV (a). The results are then presented through ΔaccWEPL 2D maps (b) and respective histograms (c). For the histogram of ΔaccWEPL differences a PV$_{in}$ for a selected acceptance range was defined. In this study the range of [-3;3] mm$_{water}$ was selected, and is shown in check-board in this figure.

tion (V95$_{CTV-G0}$ and gamma$_{p.rate}$) for patients A1 and A8 using an anterior beam, are drawn simultaneously. From here is observed that variations in the V95$_{CTV}$ were detected by the concept of PV$_{in}$. The PV$_{in}$ value is, however, not representative of the same V95$_{CTV}$ or Gamma$_{p.rate}$ value. Another example is outlined in figure (4.17) for patient A3 and A4, where the PV$_{in}$ along the treatment weeks showed strong variation with the use of a posterior beam, when no significant variation in the V95$_{CTV}$ was measured.

The situation of patient A3 is justified due to the non-sensitivity of the V95$_{CTV}$ to changes in the dose distribution outside the target volume, fact that was detected when using the gamma index for comparison of the dose distributions, being visible that the changes due to the accWEPL variations occur for the OARs, as in this case the bowel, see figure (4.18). On the other hand, for patient A4 the same wasn't observed, where the gamma$_{p.rate}$ presents constant along the week-CTs. Another important conclusion about patient A4 is the constantly low PV$_{in}$, not showing an anatomy change over one week, but a systematic variation. The inspection of the CT-value of the planning CT in one of the week-CTs (e.g. CT$_3$) gives the hint about a systematic positioning error, at least when the positioning is bone-based as performed in this analysis, see figure (4.19) for the illustration of this case. From the x-profile, a difference in the beam entrance is visible. It is this variation that results in the low PV$_{in}$, however it does not correspond to a strong decrease in the V$_{95CTV}$ (98.4±1.0 % for the set of four week-CTs). One possibility, to justify this can be the fact that the accWEPL doesn't consider the beam characteristics. Then the same ΔaccWEPL in two different CT can lead to a different

impact in the dose distribution depending of the used beam intensity and energy. The complete evaluation for each patient, beam incidence and CT is available in the appendix from (A.6) to (A.9). Additionally figure (A.3) shows more examples of the accWEPL maps and its histogram of differences.

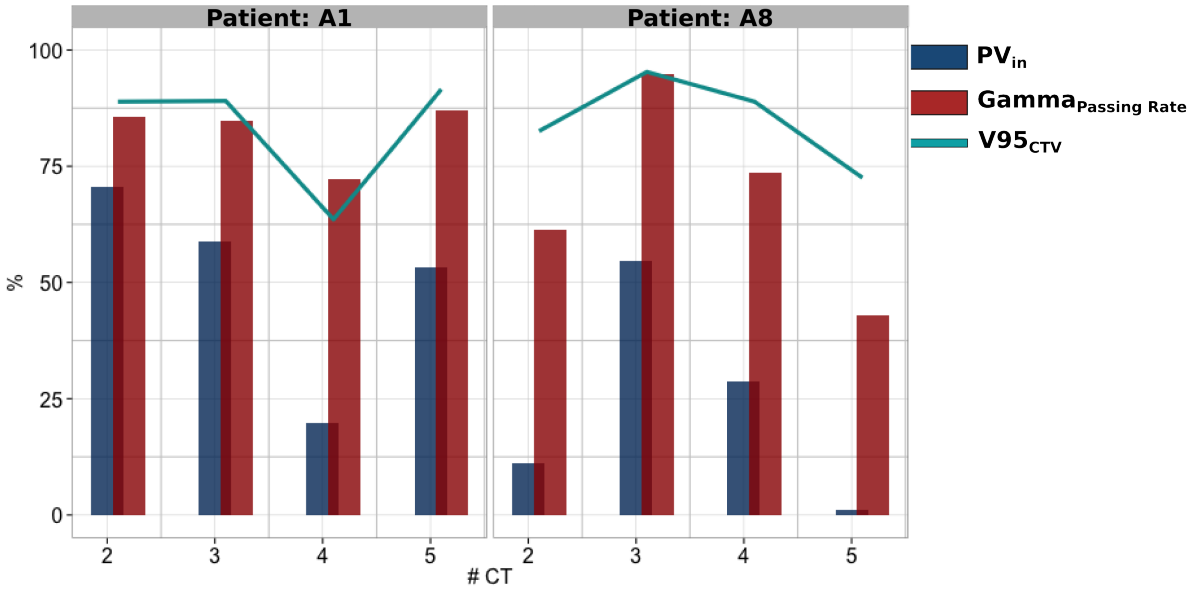

Figure 4.16: Comparison for patient A1 and A8 using an anterior beam of the variation along the week-CTs of the ΔaccWEPL (through the concept of PV_{in}), $V95_{CTV}$ and $Gamma_{p.rate}$.

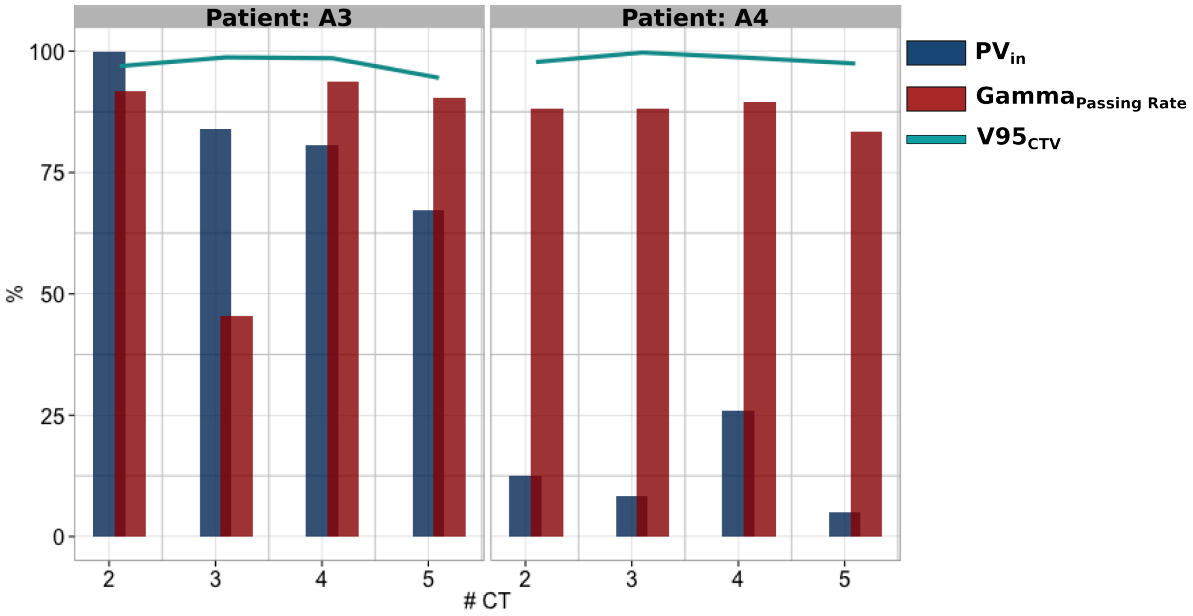

Figure 4.17: Comparison the patient A3 and A4 using a posterior beam of the variation along the week-CTs of the PV_{in}, $V95_{CTV}$ and $Gamma_{p.rate}$.

4.3.4.2 Definition of the correlation accWEPL to dose

Aiming to establish a correlation between the variations on the accWEPL and the dose distribution, linear regressions were tested between different parameters and the sta-

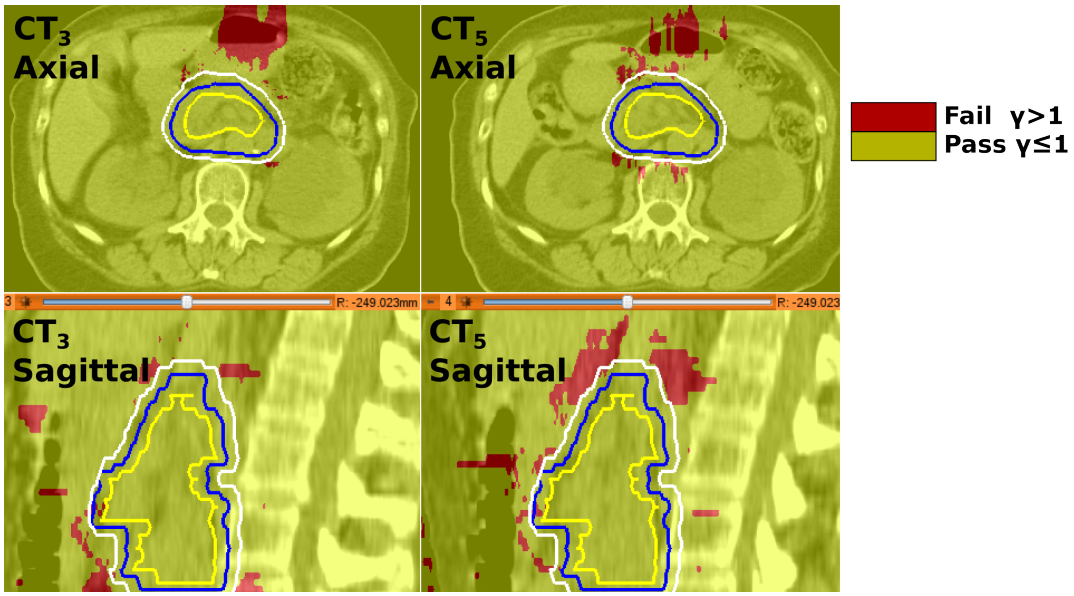

Figure 4.18: Comparison of the Fail-Map for the Gamma Index for patient A3 using a posterior beam for the CT3 and CT5.

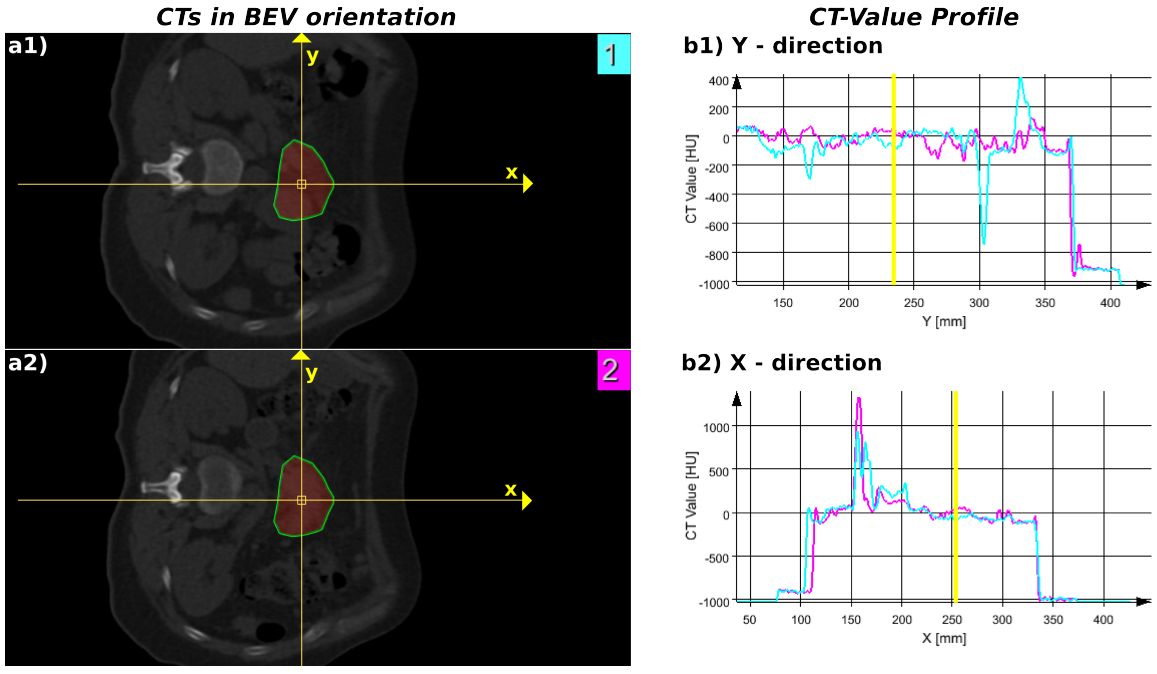

Figure 4.19: Comparison of the CT_{plan} (a1) and CT_4 (a2) for the patient A4, using the unidimensional CT value variation along the axis x (i.e., the posterior beam incidence) and y.

tistical relevance from them was assessed.

In order to check whether each parameter is normally distributed, statistical requirement for the definition of confidence levels, the Shapiro-Wilk test (Pruim 2011) was performed. The distribution of these parameters is depicted in figure (4.20), and the Shapiro-Wilk test showed that PV_{in} and V_{95CTV} have both normal behaviour.

Considering this, the correlation between the PV_{in}, V_{95CTV} and $gamma_{p.rate}$ was evaluated, as shown in the figure (4.21). The PV_{in} parameter set forth to have the better balance between the V_{95CTV} and $gamma_{p.rate}$ correlation, i.e. target information and dose distribution in the normal tissues. The linear regression for these two parameters is presented in the table (4.4) with the respective R^2, which showed up to be small as

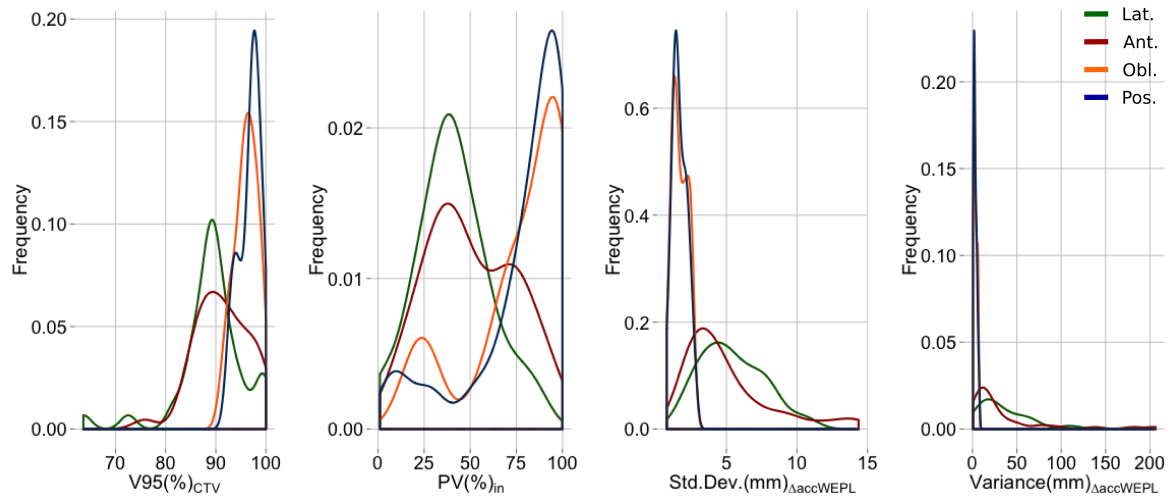

Figure 4.20: Density distribution per beam direction of the V_{95CTV}, PV_{in}, standard deviation of the ΔaccWEPL and its variance.

a consequence from the spread of the data around the linear fit. To assess the differences from each point to the regression line, the residual values were determined. The median residual is close from zero with a significantly low quartiles which supports the use of this linear fit.
Moreover, the correlation between the PV_{in} and the V_{95CTV} was also verified per beam angles, showing to be always positive, however stronger for the anterior and lateral beam as result of the reduced variance of the sample for the other beam's direction (small statistic relevance).

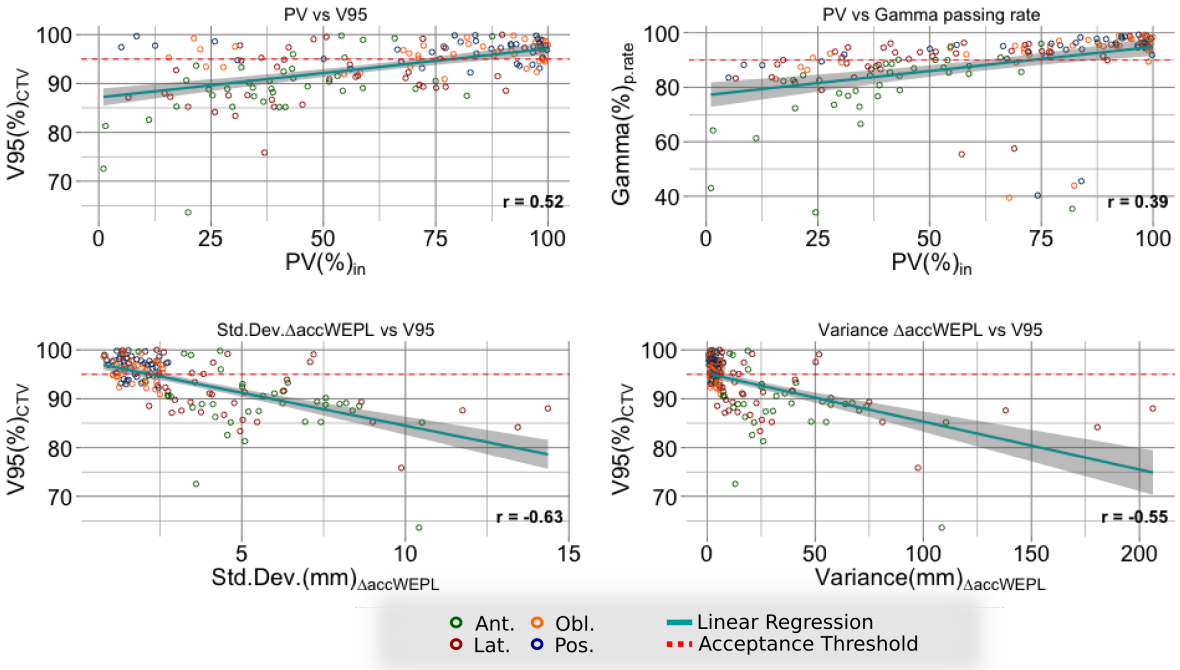

Figure 4.21: Graphic of the dispersion of the dosimetric quantities (i.e. $V95_{CTV}$ and Gamma passing rate) versus the WEPL evaluation parameters (PV_{in}, standard deviation and variance of the ΔaccWEPL). The Pearson correlation (r) is shown for each relationship. The red dashed line corresponds to the defined acceptance threshold of the dose distribution. In grey the 95% confidence interval is drawn.

Table 4.4: Statistical evaluation of the correlation between the PV_{in}, $V95_{CTV}$ and gamma passing rate.

	PV_{in} vs	
Parameter	**$V95_{CTV}$**	**$gamma_{p.rate}$**
Linear fit (y=A+B.X)	A=87.15; B= 0.10	A=77.10; B=0.18
Conf.Interval [2.5%; 97.5%]	A 85.4; 88.9	72.53;81.68
	B 0.07;0.13	0.11; 0.24
R^2	0.2729	0.1523
Residual [Q1;Median;Q3]	-2.63;0.29;2.89	0.64;3.17;5.23
p-value	<0.001	<0.001
r-pearson	0.52	0.39

With the model settled, the prediction condition can now be drawn. Thus, considering the linear regression between the $V95_{CTV}$ and the PV_{in}, if a preservation of the $V95_{CTV}$ above 95% the PV_{in} is a intend, it will need to be superior to 66.1% with a confidence interval of 49.1 - 83.1% for a confidence level of 50% (see the *Linear fit* of table 4.4) . In the same way, if the aim is to have a gamma passing rate above 90% come out that PV_{in}, in a confidance level of 50%, will have to be superior to 63.1%, with a confidence interval of 44.8 - 81.5%.
In conclusion, for the defined $V95_{CTV}$ and $gamma_{p.rate}$ acceptance levels, based on the usually adopted clinical criteria, a PV_{in} below approximately 65% might mean a clinically significant change in the dose distribution, which should be verified through the dose forward calculation. Moreover, values below 45% (i.e. lower limit of the confidence interval) indicate inevitably a degradation of the original dose distribution, at least in terms of the normal tissues, and an adapted plan is strongly suggested.

4.4 Clinical evaluation

The presented concepts and conclusions were evaluted by a master student supervised by the author (Asim 2016), for the set of patients under treatment at HIT and the clinically delivered plans.
The summary of the application to the these patients is outlined here.

4.4.1 Material and methods

From the twenty pancreatic patients treated at HIT from 2014 to April 2016 using protons or carbon ions, a subset of fifteen patients were included in this dissertation, see table (4.5). However, in the context of this inter-fractional evaluation, just eleven of them include weekly CT imaging and are discussed in this chapter. This dataset will be redeemed is the next chapter for intra-fractional inspection.
All the patients were prone positioned and had a free-breathing CT for planning purposes. The treatment planning was done using the TPS Syngo® RT Planning, IMPT or SFO technique (cf. table 4.5), with an IES spacing of 3 mm and a minimum pencil beam FWHM of 10 mm for carbon ions and 8 mm for protons. Plans were optimised to cover the CTV with an homogeneous effective dose while keeping the dose to the OARs to the clinical dose constraints. In order to reduce sources of inter-fractional variations, the adopted beam geometry matches the conclusions from the previous study

Table 4.5: Dataset H: Description of the set of patients (Pt.) treated at HIT containing the description of the dose prescription (total and by fraction), particle used (protons or carbon ions) and number of control CTs. The adopted beam configuration (*B.config*) follows the naming of the figure 4.1.The patients highlighted in grey were excluded from this analysis.

Pt.	T. dose Gy (RBE)	F. dose Gy (RBE)	Particle	B.config.	Optim.	week-CTs
H1	45+9	1.8	p	F	IMPT	5
H2	45+9	1.8	p	F	SBO	3
H3	45+9	1.8	p	F+B	IMPT	3
H4	45+9	1.8	p	F	IMPT	3
H5	45+9	1.8	p	F	IMPT	-
H6	45+9	1.8	p	F	IMPT	3
H7	54	2	p	F	IMPT	3
H8	45+9	1.8	p	F	IMPT	3
H9	45+9	1.8	p	F	IMPT	4
H10	48	4	^{12}C	F	IMPT	1
H11	45+9	1.8	p	F	IMPT	5
H12	45+9	1.8	p	E	IMPT	6
H13	48	4	^{12}C	F	IMPT	-
H14	48	4	^{12}C	F	IMPT	-
H15	45+9	1.8	p	F	IMPT	-

(i.e. posterior beam directions) and is set in table (4.5).
Regarding the weekly-imaging, the number of sessions that each patient underwent along the whole treatment course is detailed in table (4.5). These CTs were performed using the PET/CT scanner at HIT (Siemens Biograph mCT, Siemens Molecular Imaging) under the same CT protocol, patient positioning, free-breathing and without contrast.
Weekly-CTs were rigidly registered with their respective planning-CT using the 3D slicer software. The matching criteria included bones i.e. vertebral column and ball-bearing fiducial, which were placed on patient skin for alignment at the time of scanning. The registration considered 6 DOF.

Forward calculations of the treatment plan

Forward calculation of the dose distributions for the rigidly registered CTs and the planning CT were performed using TRiP98.
The plan quality assessment was based on ICRU (1999) criteria:

- Target Volume - V95$_{CTV}$, V95$_{PTV}$, PTV maximum dose (Dmax$_{PTV}$), PTV minimum dose (Dmin$_{PTV}$) and PTV mean dose (Dmean$_{PTV}$);
- OARs - spinal cord (Dmax$_{Cord}$), both kidneys (V40$_{kidney}$) and bowel (V20$_{bowel}$, V80$_{bowel}$), i.e. maximum, and volume receiving 40%, 20% or 80% of the precribed dose, respectively;
- Comparison between dose distributions - gamma index (Δd 3%/ DTA 3mm)

accWEPL assessment

The analysis was performed on the MeVisLab framework, using the module MVL$_{CT-Veri}$, in a similar workflow to the one described in section (4.2.5).
In the registration stage all the CTs were rigidly co-registered, in the same manner as it

was done for dose forward calculation, i.e. using the same image registration parameters acquired from 3D Slicer into the $\text{MVL}_{CT-Veri}$ module.
Since the WEPL calculation is performed for one treatment field at a single time and these patients possess multiple beams, one beam was evaluated at a time. The VOI_{WEPL} used for the calculations was defined by the initial CTV as a reference volume, additionally a margin of 1 mm in x, y directions (anterior-posterior and left-right) and 3mm in (superior-inferior) z direction was added. The accWEPL was originated from the WEPL sum along the beam path, starting from the patient surface to: (i) the distal edge of the VOI_{WEPL}; and (ii) to the proximal edge of the VOI_{WEPL}. The sketch of these two methods is shown in figure (4.22).
The evaluation was done using the accWEPL difference map and histogram of tissue

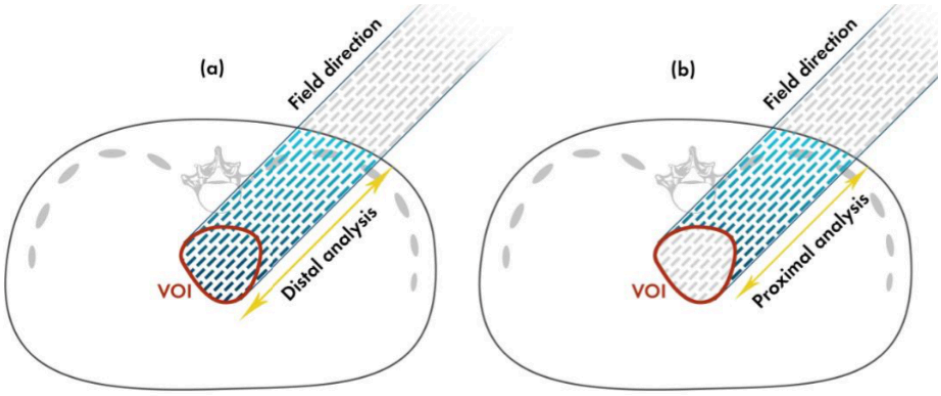

Figure 4.22: Diagram of the accWEPL calculation through the distal and proximal edge of the VOI_{WEPL}. Image coutesy of Z.Asim

variation among planning-CT and weekly-CT by the PV_{in} parameter.
To evaluate the total plan a weighted average of the PV_{in} for each beam was considered by taking into account the respective field weight, here considered as approximation the number of particles, designated as PV_{norm}. This strategy doesn't consider the dose delivered by the beam but approximate beam weight by the number of particles. This is especially meaningful for some patients, as the patient H3, in which case one of the beams delivers significantly less dose (30%). In general, this weighting is nearly constant (50$\pm$10 % per beam).
To evaluate the correlation among WEPL and dosimetric parameter, PV_{norm} was correlated with the ΔV95_{CTV}, ΔV95_{PTV}, $\text{gamma}_{p.rate}$ and V20_{bowel}, where Δ corresponds to the difference with the planned dose distribution. The correlations were measured using the Pearson correlation coefficient (r) and the linear regressions were calculated. Considering the results of the previous study (in section 4.3.4.2) and the clinical reasonable variations of the forward calculated dose distributions, action and tolerance level were narrowed. For the variation in V95%, either for CTV or PTV, 2% and 3% variation was set as tolerance and action level respectively. Similarly, for $\text{gamma}_{p.rate}$ 97.5% and 96.5% were considered as tolerance and action level respectively.

4.4.2 Results

A short summary of the main results and conclusions are here presented as validation of the previously suggested, in terms of beam geometries, margins and assessment of

inter-fractional changes through WEPL-maps.

Forward Calculations of the treatment plan

The results for the $\Delta V95_{CTV}$ are shown in figure (4.23).It is concluded that the majority of the treatment fractions were kept below 5% variation (mean of 2.0$\pm$2.9 %), with patient H12 as an exception with three out of six fractions above this threshold.
It comes out from the forward calculations in the follow-up CTs, a relatively small variation of the PTV coverage (2.2$\pm$1.8)% with 23% of the fractions with a $\Delta V95_{PTV}$ superior to 3%. Regarding the variation of the $Dmax_{PTV}$, it fluctuates among 0.02 Gy (RBE) /fx and 0.5 Gy (RBE)/fx. Nevertheless, the $Dmean_{PTV}$ was fairly consistent along the treatment course.
To quantify the impact in the overall dose distribution, the gamma index was computed

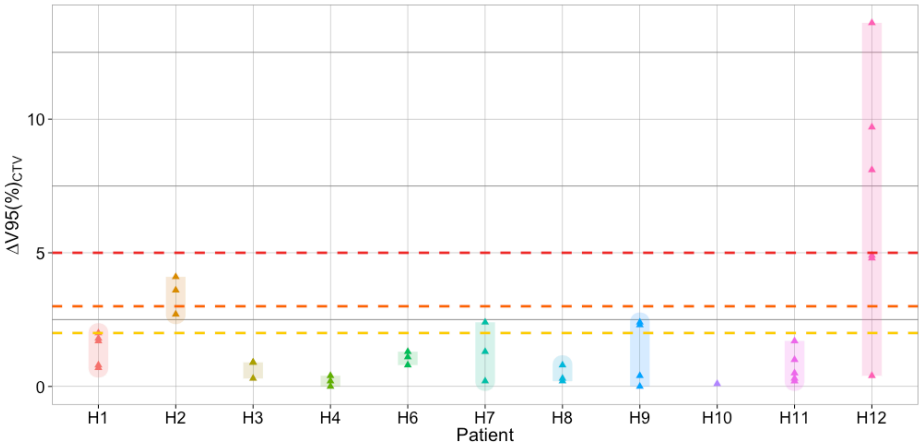

Figure 4.23: Variation of the $V95_{PTV}$ along the weekly-CTs for all the patients comparatively to the CT_{plan} dose. The dashed lines indicate the 2%,3% and 5% of $\Delta V95_{CTV}$, respectively.

for each dose distribution calculated in the weekly-CT versus the one in the CT_{plan}. This analysis reveals that the gamma passing rate was in general high (97.4 $\pm$1.7)% varying between 91.3% and 99.7%.
Relatively to the OARs doses, the strongest impact was found to be for the bowel, with variations of the $V80\%D_{bowel}$ that can reach 8.0% and with the $V20\%D_{bowel}$ ranging within [-11.1;9.6]%. As far as kidneys and spinal cord are concerned no significant differences were found.
It was concluded that the dose distributions with lower $gamma_{p.rate}$ correspond to the higher dose delivered to the normal tissues compared with the planned distribution (Asim 2016).

accWEPL assessment

The obtained PV_{norm}, considering first the distal analysis, for this set of patients varied between 23.0% and 98.7% with an average of (67.5 $\pm$16.9)%. Comparisons with the proximal analysis showed no significant differences between the two methods, with two thirds of the fractions below to 3%. This finding supports the fact that in the majority of the evaluated cases the density variations occur in the beam path before reaching the

target volume, while the target density changes are almost negligible.
Figure (4.24) shows an example of the evaluation performed for patient H11, in which CT_1 is compared to the CT_{plan}. The presented example corresponds to the geometry F and depicts a case where low density of the bowel results in a high accWEPL difference. The $gamma_{p.rate}$ showed to be reasonable for this case (97.7%), the $V95_{PTV}$ and the OARs doses had a variation below 2%. Just a closer look at the dose distribution showed the reason for this low PV_{norm} which is related with the high doses in the soft tissues, see figure (4.25).

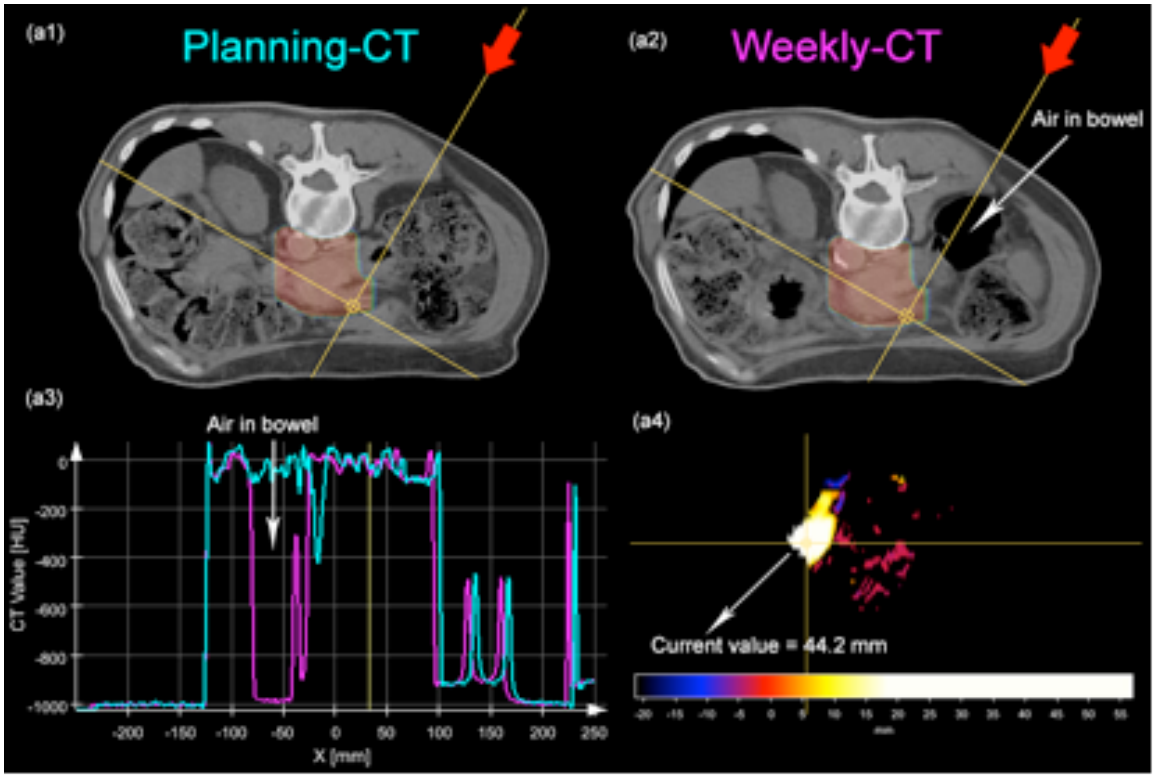

Figure 4.24: Evaluation of the accWEPL for the patient H11 for the CT_1 (a2) comparatively with the CT_{plan} (a1) for the oblique posterior right field. (a3) shows the difference in the CT value for a profile drawn along the beam path. This difference will be translated in accWEPL changes as the pointed to in image a4). The yellow axis in image a4) can be moved along the ΔaccWEPL in order to measure its current value. Moreover, this axis is synchronously moved in the CT of the patient (a1 and a2) and the unidimensional profile (a3) to help in the interpretation of the results. As example of this evaluation method the axis was in this figure placed after a region of large density variations, i.e. air in the bowel compared to the planning CT.

In order to evaluate the correlation between dose and accWEPL in figure (4.26) the relationship between the plan quality parameters (i.e. $\Delta V95_{CTV}$, $\Delta V95_{PTV}$ and $gamma_{p.rate}$) with the PV_{norm} is shown. It raises that $\Delta V95_{CTV}$ and PV_{norm} were weakly correlated (r = -0.05), however when looking for the p-value the high value (0.78) leads to the conclusion about the low statistic relevance of this sample in this correlation. The same can also be concluded when considering the small $V95_{CTV}$ variations for most of the fractions. The correlation improves when the proximal VOI_{WEPL} is considered (r = -0.21).
In pursuit of taking a more significant volume to quantify the dose distribution, the relation between the PV_{norm} and both $\Delta V95_{PTV}$ and $gamma_{p.rate}$ was evaluated. Although the PTV is not the clinically relevant volume to be irradiated, in this approach it is ex-

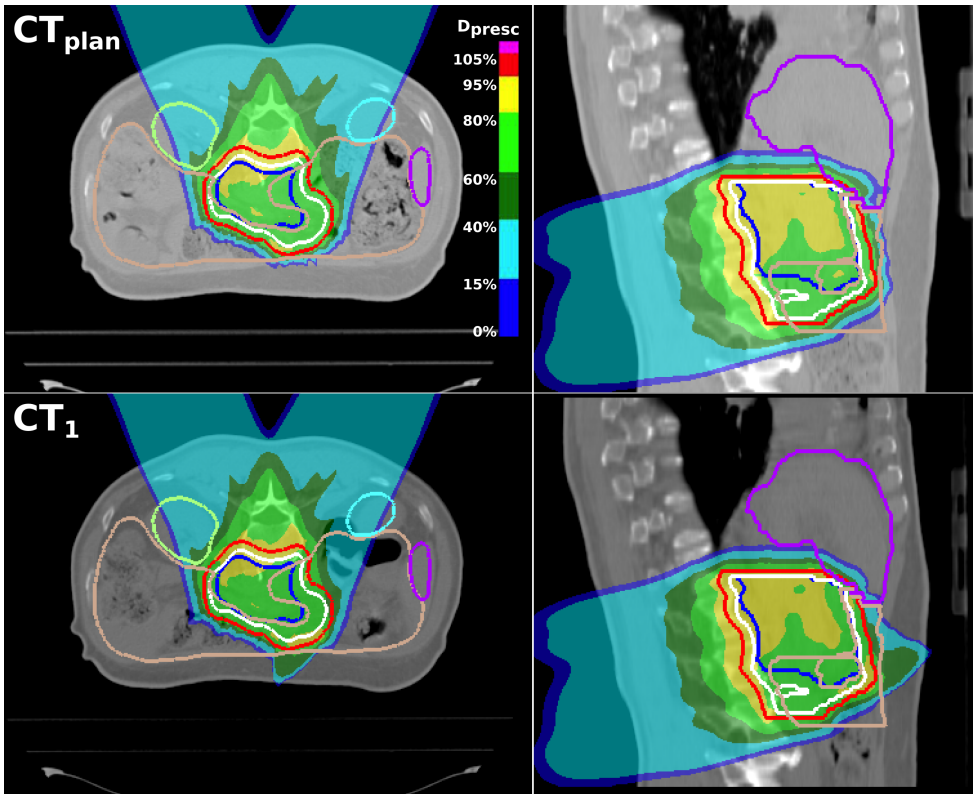

Figure 4.25: Transversal and sagittal view of the dose distribution of patient H11 from the forward calculation in the CT_{plan} and CT_1. The CTV, ITV and PTV are drawn in blue, white and red, respectively.

pected that it allows to account with variations in the dose distribution immediately surrounding the CTV. Additionally, it will allow to spread the data sample, since the detected mean $\Delta V95_{CTV}$ was only of 2%. Both the $V95_{PTV}$ and $gamma_{p.rate}$ showed a strong correlation with the PV_{norm} in the distal analysis, with a person correlation of -0.6 and 0.7, respectively, and p-value below 0.001.

The fact that the gamma criterion considers the entire variations in the dose distribution clearly is closest to the information given by the PV_{norm}. This was detected for several patients, where the inter-fractional anatomy changes strongly affected the bowel doses without compromising the CTV dose. The same conclusion is also obtained when looking for the number of false positives (high PV norm but low gamma) and false negatives (low PV norm but high gamma), which has reduced in comparison to $V95_{PTV}$ correlation, because the gamma index gives a complete information of dose distribution (target, OARs and normal tissues).
Therefore, based on the linear regression between $V95_{PTV}$ and the $gamma_{p.rate}$ with the PV_{norm} the calculated action and tolerance levels are defined in the table (4.6). The tolerance level corresponds to the linear fit value, while the action level to inferior interval of the confidence level (for a 50%). Additionally, the results obtained in the previous analysis (section 4.3.4.2) are also shown.
In short, the obtained results for this set of patients under real clinical situation, i.e. beam configuration and plan optimisation strategy, culminate in similar action and tolerance levels than in the previous evaluation, in which only single beams were considered. This validates the method and settled reference levels for further patients. However, a decision is always dependent of the understanding of which were reasons that affected the WEPL and of the clinical report of each patient.

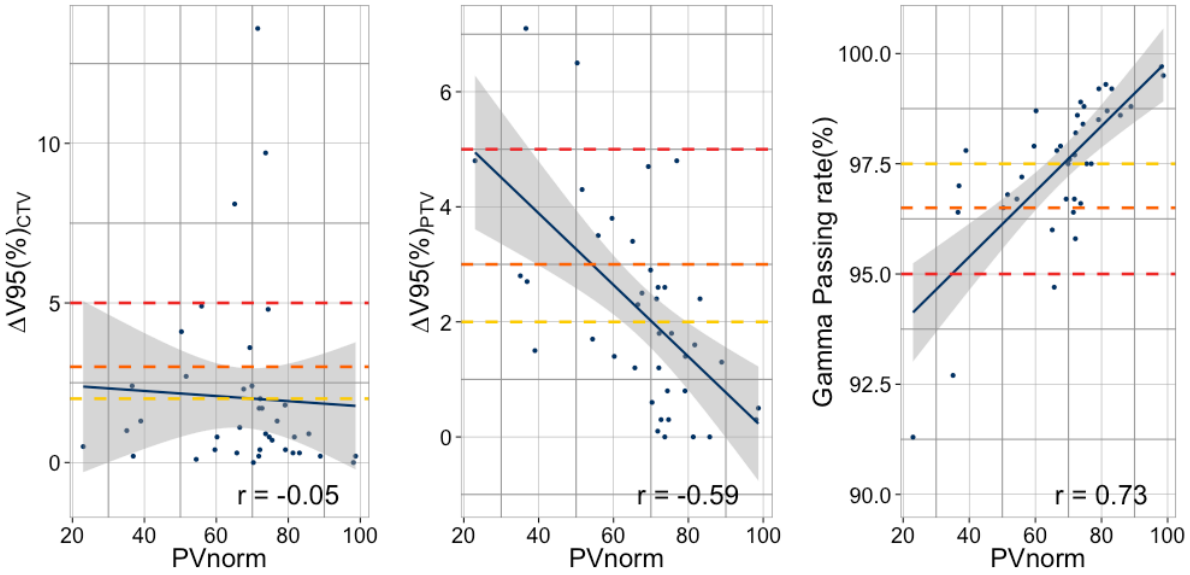

Figure 4.26: Correlation of $\Delta V95_{CTV}$, $\Delta V95_{PTV}$ and gamma passing rate with the PV_{norm}. The person correlation coefficients (r) are written in the correspondent graph. The blue line corresponds to the linear regression and the respective 95% confidence band in grey. The dashed lines correspond to the acceptance levels defined, with yellow, orange and red, corresponding to the acceptance thresholds of 2%,3% and 5% for doses and 97.5%,96.5% and 95% for the gamma passing rate.

Table 4.6: Action and tolerance levels obtained from the linear regression $V95_PTV$ and the $gamma_{p.rate}$ with the PV_{norm}. The results are presented for different threshold criteria. The last row corresponds to the value obtained in the previous analysis for a different dataset, considering single fields and using the CTV as VOI.

Volume	Beam	Threshold		PV_{in}	
		Δ dose	$gamma_{p.rate}$	Tolerance L. (%)	Action L. (%)
PTV	Multiple	2.0	97.5	68.3	59.5
PTV	Multiple	3.0	96.5	61.9	53.1
PTV	Multiple	5.0	95.0	51.0	41.8
CTV	Single	5.0	95.0	64.8	45.1

4.5 Summary and discussion

In conclusion, the combination of two oblique posterior beams with a geometric margin can be robust to the majority of the inter-fractional changes affecting pancreatic patients, and yields to acceptable dose coverage for most patients and fractions. However, daily anatomy variations may be large and routine soft-tissue imaging and adaptation strategies will likely improve the treatment. Moreover, the evaluation of the WEPL from the pre-treatment CT will help to detect extreme anatomy variations and prevent the treatment with a plan that might substantially decrease the dose in the target and/or over-dosage the healthy tissues. This method can still be improved, and the correlation between the variation of the accWEPL and dose distribution strengthened, by (i) the use of gated-CT images, to avoid influence of motion artifacts and differences in the pancreas positioning due to the averaging breathing; (ii) consideration of the positioning shifts applied to the patient at the specific treatment day; and (iii) removing the

surgical clips from the WEPL evaluation, to avoid too strong changes in the accWEPL that might mask anatomical changes.
Relative to the population-based asymmetric ITV margins may be a feasible clinical strategy to account for density changes and to reduce the irradiated volume. However, a patient-specific concept, either based on a series of pre-treatment images (e.g. MRI) or adapted along the treatment course (e.g. control CTs and MRIs), will be worthwhile to the improve the plan quality.

Chapter 5

Intra-fractional motion

5.1 Aim of this chapter

The intra-fractional motion as result of the patient's breathing is also a concern for pancreatic patients. Moreover, the dose delivery using a scanning system results in interplay effects and consequently in dose degradation.
The goal of this chapter is to quantify the impact of the patient's motion on the dose distribution and to assess the need of mitigation techniques.
Before the implementation of the pancreatic irradiation at HIT the plan robustness to the intra-fractional motion for different beam geometries was evaluated, such study is presented in section (5.2.1), with the respective results in section (5.3.1). Subsequently, for patients under treatment at HIT the dose distribution under motion was simulated pre-treatment (section 5.2.2), and furthermore the delivered dose was reconstructed for some of the treated fractions (section 5.2.3). The results of this evaluation are shown in section (5.3.2).
In this chapter the results from the time resolved dose calculations will be designed as *4D Dose Simulation* (4DDSim), when the accelerator beam delivery sequence (BDS) is unknown and consequently simulated, and as *4D Dose Reconstruction* (4DDRec) when the BDS and the breathing signal correspond to the measured data during the patient treatment.

5.2 Material and methods

5.2.1 4D dose simulations - dataset B

When a pre-treatment 4DCT is available a prediction of a set of possible dose distributions, as resulting from different interplay patterns, can be simulated. This simulation relies on a sample of the patient's breathing, the treatment plan information (beam spots, positions, energies) and on a set of simulated accelerator irradiation patterns.
The first step of this study, prior to the beginning of treatments for pancreatic patients at HIT, was to use an available dataset of patients, previously treated at the University Clinic of Heidelberg, to assess the impact of HIT's delivery method in the plan quality.

5.2.1.1 Patients and imaging description

Seven patients with a planning CT and a 4DCT, acquired in the same imaging session, constitute the set of patients included in this section (referred as *dataset B*). The planning CTs of the patients included the outline of kidneys, liver, bowel, stomach and spinal cord.
The planning CTs and 4DCTs were acquired under free-breathing in the Somaton Sensation Open (*Siemens, Erlangen, Germany*), which performs a relative phase-based reconstruction considering the surrogate signal of the motion-monitoring system AZ-733V Respiratory Gating System, *Anzai Medical Co, Tokyo, Japan*, (cf. 2.3.4.1, and called as *Anzai*).
The 4DCT was sorted in eight predefined states: 0%Ex, 40%Ex, 70%Ex, 100%Ex, 75%In, 50%In, 25%In and 20%In, where *In* correspond to the inspiration and *Ex* to the expiration state. The state 0%Ex is the end-exhale and 100%Ex is the end-inhale state (as seen in fig.2.10).
Due to the contrast agent in the planning CT, CT_{BPL}, this CT was ignored. Hence, the end-exhalation CT, named as CT_{0Ex}, was used for planning purposes.
All the CTs were pre-processed in order to remove couch and indexing devices.

5.2.1.2 Treatment plan optimisation

The dose distribution was biologically optimised using the TPS TRiP98 for a geometric ITV, which was in first approximation originated from a generic 5 mm expansion of the CTV_{0Ex}, based on the mean motion of the CTV for this patient-population.
The plans were optimised for a prescription dose of 3 Gy (RBE) in 15 fractions with carbon ion-beams.
The CTV_{0Ex} was obtained through contour propagation of the physician's delineated contours on the CT_{BPL} using the vector field from the deformable registration between the CT_{BPL} and the CT_{0Ex}. This process follows the one outlined in section (3.1.2).
Algorithms and planning parameters follow the definition in the previous chapter (4.2.2).
The selected beam geometries, for which the plan robustness was evaluated, were based on the previous results of the inter-fractional study, where two so-called robust geometries (single posterior beam and two oblique posterior beams) and one non-robust geometry (single anterior beam) were used for comparison, that in figure (4.1) correspond to the geometry B, F and C, respectively.

5.2.1.3 Image registration

The deformable image registration (DIR) was performed using Plastimatch (see chapter (3.2) for details), using two stages of a B-Spline algorithm (Shackleford, Kandasamy, and Sharp 2010).
The registration was performed between the CT_{BPL} and the reference 4DCT state, CT_{0Ex}, with the aim of contour transformation. Moreover, each of the 4DCT states was registered against the CT_{0Ex} with the objective to be used as motion information during the calculation of the time resolved dose distribution.
The quality of the deformable image registration was assessed using the *Registration Quality Module* of the software SlicerRT (see chapter 3.3.1) through visual inspection

and numerical quantification, such as the determinant of the Jacobian matrix (JD) of the vector field, inverse consistency error (ICE) and mean absolute difference. Due to the aim of this section to be the evaluation of different beam geometries, the DIR analysis was performed for the complete CT volume, since different beam directions were considered.

5.2.1.4 Breathing signal and irradiation patterns

Since this set of patients was treated with photon therapy without 4D image guidance, no breathing signal during the treatment was recorded. Therefore, to simulate the breathing signal for these patients a regular trajectory with a regular period of 3 seconds (Lujan motion, Lujan et al. 1999) and an irregular breathing curve corresponding to other patients were used. The example of these two signals is shown in the figure (5.1). The dose distributions resulting from these two signals were compared to estimate the effect of different surrogate signals.

The beam delivery structure was simulated using the tool *makeLmdout-MH* (see section 3.4), whose inputs were the previously optimised treatment plan, the breathing signal (both cases) and the accelerator spill information. The spill was characterised by the maximum beam hold time of 20.0 s, the maximal extraction time of 5.0 s, pause length and pause length at the end-of-plane of 4.2 s. These parameters were based on the accelerator characterisation performed by M.Härtig (University Clinic of Heidelberg). As output of the *makeLmdout-MH* the BDS in TRiP format is directly generated. In order to describe the spectrum of possible irradiation scenarios, which result in different interplay patterns, a temporal shift to the starting phase of the surrogate signal

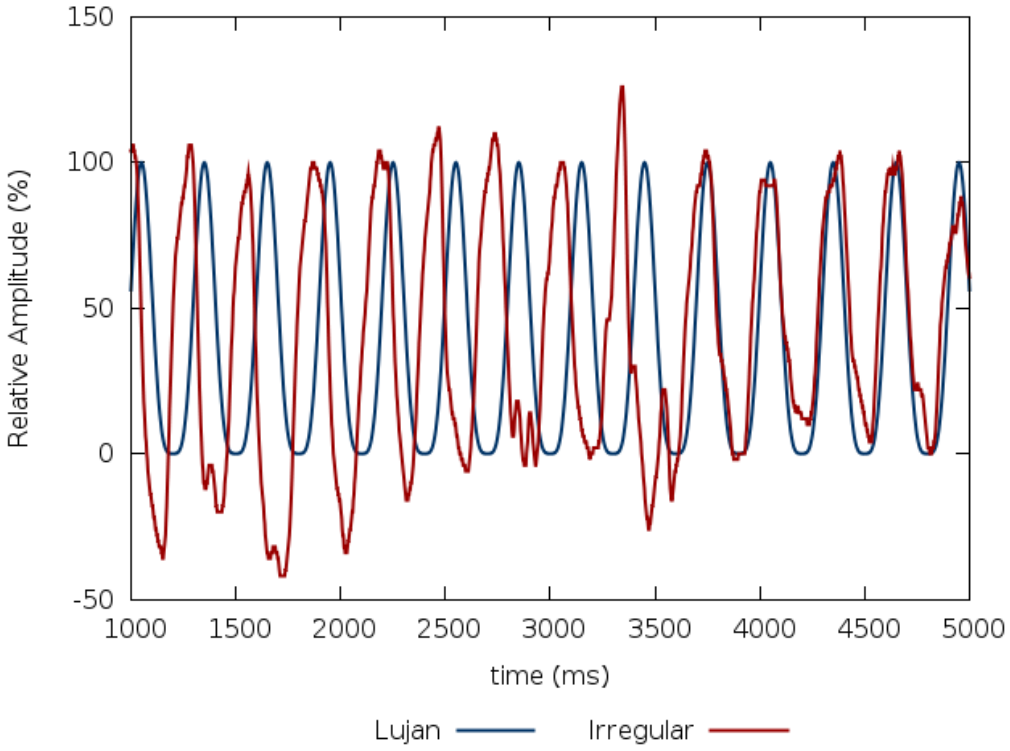

Figure 5.1: Sample of the breathing signals employed for the simulations of the patient B3: regular signal (Lujan shape) and irregular.

was applied, i.e. a temporal delay of the starting of the breathing signal. This will correspond to the irradiation of a different raster point at a defined breathing phase. Studies from Hild, Durante, and Bert (2013) and Richter (2012) showed that the manipulation of the starting breathing phase is sufficient to cover the variability of the interplay patterns. In brief, in order to cover the influence of the asynchronous between the beam delivery and the breathing signal, temporal shifts in the breathing starting phase were induced. These shifts were spaced 350 ms in a total of ten different irradiation starting points for each of the two breathing signal types (Lujan and irregular).

5.2.1.5 Time resolved forward calculation of the dose distribution

The TPS TRiP4D was used for the forward calculation of the dose distributions considering the breathing influence. Each calculation was based on the treatment plan information (raster points, energies and beam focus), breathing signal and in the simulated accelerator temporal pattern.
The breathing data was set for eight motion states in one direction (x in this case due to the 4DCT acquired with the Anzai breathing belt), considering a relative amplitude-based sampling and normalised to 0-200%, i.e. inspiration corresponds to 0-100% and expiration up to 200% of the signal amplitude. More details about the used mode can be found in the section (3.1.2).
The spill information was described by the simulated *lmdout* signal, which is temporally correlated with the breathing signal.
Additionally, the vector fields obtained of the DIR between each of the 4DCT states and the reference state (selected as CT_{0Ex}) were also given as input.
For comparison with these calculations, where the interplay effect is considered, the calculations were also performed in the individual 4DCT-states in which range variations and displacements affect the plan quality, discarding the dynamic irradiation. These simulations were called *quasi-4D*.
Calculation and biological algorithms correspond to the ones used in the plan optimisation.

5.2.1.6 Evaluation methods

The internal motion of each patient was quantified using the vector field information, particularly through the measurement of the median vector field length (VFL) inside the CTV_{0Ex}, which was obtained from the DIR between the CT_{0Ex} and each of 4DCT states. The maximum of these values will be used as quantification of the intra-fractional tumour motion, usually corresponding to the CT_{100Ex}.
The dose distributions, namely the static, the quasi-4D and the 4DDSim, were evaluated taking as metric the V_{95CTV} and H_{CTV} (cf. section 2.4.0.2).
Note that the 4DDSim correspond to a set of dose distributions, as representative of different interplay patterns, giving rise to the need of displaying the results as mean and standard deviations and the DVHs as band-DVHs.

5.2.2 4D dose simulation of the treated patients at HIT - dataset H

In this and in the following section (5.2.3), the same set of patients was adopted. This set of patients, *dataset H*, corresponds to the patients treated at the Heidelberg Ion-Beam Therapy Center since the beginning of the clinical application of ion-beams to pancreatic patients.

5.2.2.1 Patients and imaging dataset description

From the total number of pancreatic patients treated at HIT since 2014, shortly presented in chapter (4.4), a subset of fourteen underwent monitoring of their breathing signal and beam delivery sequence during the irradiation. The description of the dataset H is presented in table (5.1), expressed by the treatment planning parameters (prescription dose, particle type, beam configuration and optimisation technique), the existence of pre-treatment breathing signal acquisition and the number of fractions with online monitoring of the breathing and irradiation sequence.
The planning CTs and 4DCTs were acquired under the same condition of the dataset B, i.e., in the *Somaton Sensation Open* scanner using the motion-monitoring system Anzai for the phase-based sorting for the eight predefined phases (0%Ex, 40%Ex, 70%Ex, 100%Ex, 75%In, 50%In, 25%In and 20%In).
Concerning the patient positioning, they were immobilised using a vacuum mattress and in prone position, as shown in figure (5.2). This positioning is a consequence from the need of irradiation using posterior beams, in order to reduce the inter-fractional anatomy variations in the delivered dose, and the limitation of the Syngo® RT TPS to incorporate the density of couch and indexing support in the planning process. As consequence of this prone immobilisation no abdominal compression was used and the patients were irradiated under free-breathing.

Table 5.1: Dataset H: Description of the set of patients treated at HIT, containing the information of the total dose prescription (*T.dose*), and per fraction (*F. dose*), particle used (protons or carbon ions), plan optimisation technique, existence of pre-treatment breathing signal (y- yes, n- no), number of treatment fractions with recorded monitoring (*Fx.monit*). The adopted beam configuration (*B.Config*) follows the naming of the figure 5.3. Since no breathing information was recorded in the treatment, the patient H10, marked in grey, was excluded from the intra-fraction study.

Patient	T. dose Gy (RBE)	F. dose Gy (RBE)	Particle	B.Config.	Optim.	Pre-TT Breath.	Fx.monit
H1	45+9	1.8	p	F	IMPT	y	2
H2	45+9	1.8	p	F	SBO	y	1
H3	45+9	1.8	p	G	IMPT	y	1
H4	45+9	1.8	p	F	IMPT	y	3
H5	45+9	1.8	p	F	IMPT	y	4
H6	45+9	1.8	p	F	IMPT	n	3
H7	54	2	p	F	IMPT	n	1
H8	45+9	1.8	p	F	IMPT	y	1
H9	45+9	1.8	p	F	IMPT	y	1
H10	48	4	^{12}C	F	IMPT	n	-
H11	45+9	1.8	p	F	IMPT	y	3
H12	45+9	1.8	p	E	IMPT	y	6
H13	48	4	^{12}C	F	IMPT	y	2
H14	48	4	^{12}C	F	IMPT	y	1
H15	45+9	1.8	p	F	IMPT	y	1

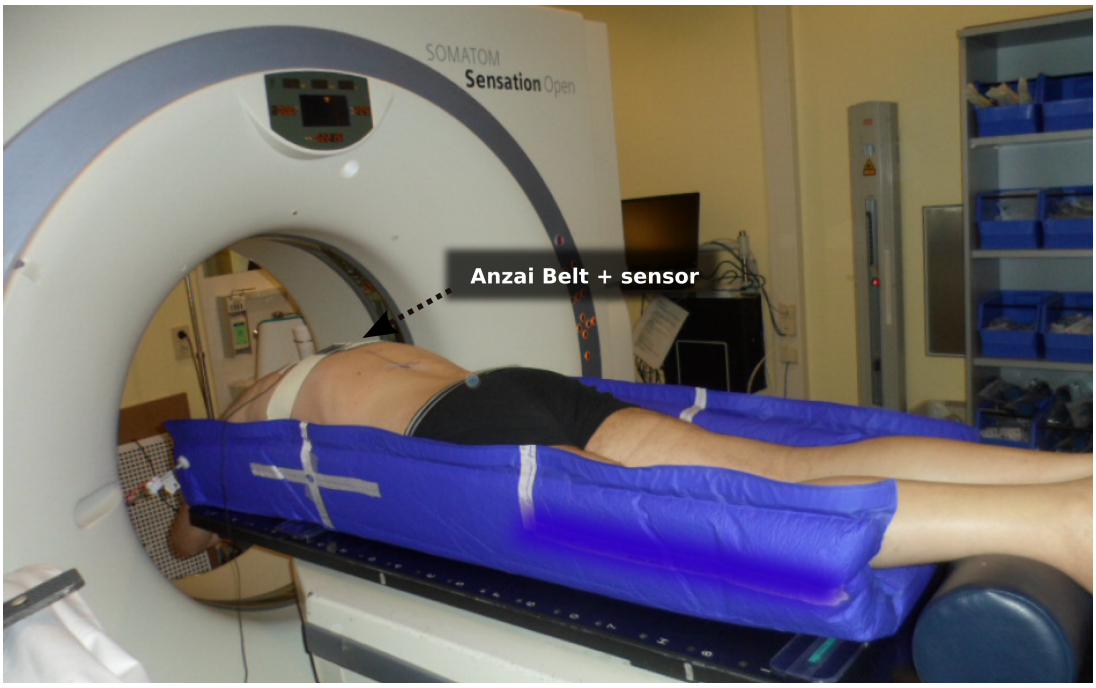

Figure 5.2: Patient positioned in prone in a vacuum mattress during the 4DCT acquisition, which uses the Anzai sensor as trigger signal.

5.2.2.2 Treatment plan

The treatment planning was performed using the TPS Syngo® RT Planning, previously described in section (3.1.3), which uses the LEM model for the effective dose calculation of the carbon ions and a fixed RBE of 1.1 factor for protons.
In general, the plans were optimised using IMPT for an initial dose of 45 Gy (RBE) - 54 Gy (RBE) with an additional boost of 9 Gy (RBE) for some cases, as referred in table (5.1).
For the proton-beam's plans a scanning raster spacing of 3x3 mm in lateral direction and an iso-energy slice spacing of 3 mm water-equivalent, for a pencil beam focus of 8 mm FWHM, was used. While for carbon ion-beams a pencil beam of 10 mm FWHM was choosen. The selection of these parameters is a result of the previous study from Richter et al. (2014b), in which the interplay effects are minimised for an enlarged FWHM of the pencil beam.
The selected beam configuration for each patient was consequence of: (i) superior inter-fractional robustness of ion-beams posterior to the patient (according to the results from the previous chapter); and (ii) spares the OARs (spinal cord and kidneys) of unwanted doses. From these facts, followed that thirteen out of the total number of patients were planned with two posterior oblique fields. The remaining two cases were planned with a different geometry as consequence of OARs constraints, however also considered robust from the inter-fractional point. The used beams arrangements are illustrated in figure (5.3).

For all the cases, the plans were optimised to the PTV in order to deliver the prescribed dose (D_{presc}) to the CTV while keeping the OARs doses below the dosimetric constraints. These are in general given by: kidney $V_{40\%D_{presc}}$ < 80%, spinal cord D_{max} < 45 Gy (RBE) and bowel D_{max} < 90% D_{presc}. Due to the short distance between the tumour bed and the intestine, the prescribed dose wasn't achieved for all the patients over the complete CTV.

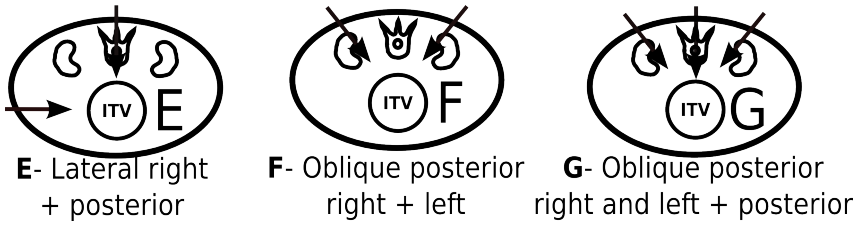

Figure 5.3: Beam configurations adopted for the dataset H, in which the patients were prone positioned.

The PTV was assigned as an ITV expansion, by 7 mm in beam direction and 5 mm laterally, while the ITV was inferred from the 4DCT motion information.

5.2.2.3 Image registration

The 4DCTs were rigidly registered using the bony anatomy to the CT_{BPL} for patients in which differences above 2 mm between the two acquisitions were found.
Regarding the quality of the 4DCT deformable image co-registration, it followed the procedure described in the previous section (5.2.1).

5.2.2.4 Breathing signal and irradiation sequence

A pre-treatment acquisition of the breathing signal was performed for twelve of the patients during the CT_{BPL} acquisition session, as indicated in the table (5.1) by the column *Pre-TT Breathing*. For the other two patients the Lujan motion with a regular period of 3 sec was considered.
The asynchronism patterns between beam delivery and breathing were considered by the same procedure as for the dataset B (5.2.1.4), i.e. using a pre-treatment breathing signal plus a set of five sequentially shifted breathing signals by 500ms.

5.2.2.5 Time resolved forward calculation of the dose distribution

The calculation of 4DDSim was performed using TRiP4D according with the process explained in section (5.2.1.5). For both particles types, the dose forward calculation followed the same parameters as in the Syngo® RT TPS, differing just for the proton plans, where just the physical dose was computed in TRiP. One of the parameters tuned in order to approximate the results between Syngo® RT and TRiP, was the dose extension factor, which is the maximum distance to which the neighbouring voxels are considered to contribute with dose to a specific voxel. For carbon ion-beams the found value correspond to 1.4 and for protons to 2.2 times the focus value for each IES. However, to keep the effect of other disregarded factors minimum, e.g. the models to consider multi-scattering, fragmentation and other unknown factors of a commercial TPS, the dose distribution was also calculated in the static case, i.e. for the CT_{BPL}, and this dose distribution was considered as reference for the comparison.

5.2.2.6 Evaluation methods

The evaluation of the dose distributions followed the same process as described in section (5.2.1), with the assessment of the internal motion for each patient through the mean VFL and the dose distributions evaluated in terms of V_{95CTV} and H_{CTV}, in comparison to the static case.
For simplification, only the initial plan was considered in the evaluation and the dose distribution for the boost plan was ignored.

5.2.3 4D dose reconstruction of the treated patients at HIT

The set of patients and the available imaging correspond to the one described in the section (5.2.2).
In order to accomplish the planned beam directions, all the patients were treated in the gantry room each treatment fraction. The patient positioning was verified in-room by a 2D-3D bony anatomy image registration between the orthogonal X-ray taken at the isocentre and the DRRs calculated from the planning CT. This match allows to determine the translational and rotational shifts to apply to the treatment couch for the accurate patient positioning at the isocentre.
Once a week a pre-treatment CT was performed for soft tissues control, which were evaluated in chapter (4.4) in the context of the inter-fractional motion analysis.

5.2.3.1 Breathing signal and irradiation sequence

After the treatment of the patient the calculation of 4DDRec was performed based on the measured data (breathing and irradiation sequence) during the irradiation of the individual treatment fractions. The number of available fractions with monitoring data is listed on the table (5.1).
The Anzai system was used for the motion monitoring during the irradiation. In general the signal acquisition was performed at a rate of 25 msec/sample (40Hz).
During the patient irradiation, the Anzai output was connected to a data acquisition system, EtherCat system, that correlated the breathing signal and the beam delivery temporal sequence of the accelerator in time. The sampling time was defined as 0.15msec and 0.25msec for protons and carbon ions, respectively. The output of the EtherCat system in *.csv* format was then converted in the TRiP4D formats using scripts developed at HIT (*CVS2LMDOUT* and *CVS2MPOS*) as explained in section (3.4.2).

5.2.3.2 Time resolved forward calculation of the dose distribution

Taking into account the monitoring data recorded of the patient, i.e. breathing signal and the time correlated BDS, the calculation of 4DDRec was performed with the same procedure of the 4DDSim, see section (5.2.2). The difference resides only in the BDS (*.lmdout*) and motion (*.mpos*) data, which correspond to a real patient treatment fraction, instead of a simulated situation.

5.2.3.3 Evaluation methods

The obtained 4DDReco distributions were compared with the static distribution and with the respective set of pre-treatment 4DDSim, in terms of target dose differences (V_{95CTV} and H_{CTV}) and DVHs.
To evaluate the impact of the dose modulation on the plan robustness to intra-fractional changes and interplay events, the normalised standard deviation of the number of particles per slice was evaluated ($\overline{\sigma_{IES}}$). This parameter is given by the equation (5.1). There, $mean_{ies}$ is the mean number of particles in a specific IES and σ_{IES} is the respective standard deviation in a total of *n* iso-energy slices.

$$\overline{\sigma_{IES}} = \frac{\sum_{IES=1}^{IES=n} \frac{\sigma_{ies}}{mean_{ies}}}{n} \tag{5.1}$$

Furthermore, in order to account for variations between adjacent raster points, the concept of the Modulation Index (MI) was applied. The MI was adapted to ion-beams from the concept developed by Webb (2003) for IMRT with the aim to measure the complexity of the beam structure. It is calculated from the treatment plan information (given by the raster field from each field) using the equation (5.2) and (5.3). First, the magnitude of the difference between the intensity from neighbouring raster points (rp) is calculated though $\Delta = |I_{rp} - I_{rp-1}|$. Secondly, the number of raster points (*np*) that in each IES are above a threshold of the standard deviation of the IES (defined as $\delta = 1.2$) is counted. This parameter is called *N* and is the base of the function *F*, see equation 5.3.
The function *F* quantifies the modulation of a plan by the measure of changes in adjacent raster points that exceed a certain fraction of the standard deviation in the specific IES. Hence, the area of this spectrum of deviations, i.e. area below the *F* function, gives the degree of modulation, MI.
The value of δ was selected in a manual iterative process in a way to be sensible to strong variations in the standard deviation of the *np*. Therefore, the value of δ was varied, and the resulting function *F* compared with the dose distribution per beam in order to get for clinically homogeneous plans, a function *F* with a small value and gradually larger for regions with larger dose gradients.

$$MI = \int_{IES=1}^{IES=n} F(np)_{\delta} \tag{5.2}$$

with,

$$F(np)_{\delta} = N_{\Delta>\delta}/(np-1)_{IES} \tag{5.3}$$

Since both parameters are applied per field a weighted mean per plan for the different fields was used. The weighting was approximated by the number of particles per beam.

5.3 Results

5.3.1 Dataset B : 4D simulations

5.3.1.1 Image registration quality

The DIR was evaluated through the comparison of the two most opposing states, i.e. 0%Ex and 100%Ex, by visual inspection and by calculation of the parameters JD, ICE and absolute differences. These results are shown in table 5.2.
The results showed a good JD (close to 1) and ICE (close to 0), which point out for the accuracy of the obtained vector field to be used in the 4DDSim. A low ICE is also particularly important for the accuracy of the transformation of the contours.
Relative to the absolute difference between the original image and the transformed one, in average differences of 14 HU were found. However, the visual inspection of the images, by overlay, showed a good agreement in the pancreas region, with the major differences in the liver-lung interface.

Table 5.2: Evaluation of the Deformable image registration evaluation for the fixed 0%Ex state and the moving 100%Ex. The values correspond to the mean value over all the patients. The quantitative parameters were the determinant of the Jacobian matrix (JD), inverse consistency error (ICE), absolute difference between the reference image (0%Ex) and the transformed image, measured for the complete CT VOI.

Parameter	*Mean ± Std.Dev*	*Range (min,max)*
JD_{mean}	1.0±0.1	1.0 ,1.0
$JD_{[min;max]}$	[-0.2±0.3; 5.1±2.5]	[-0.7, 0.2 ; 2.7, 8.9]
ICE (mm)	0.6 ±1.1	(0.4,1.0)±(0.6, 2.0)
Abs.Diff (HU)	14.1±33.4	(12.2,18.8) ± (27.5, 40.0)

5.3.1.2 Motion analysis

For this set of patients the mean length of the motion vector in the CTV region was (4.7±2.7) mm, with the major contribution in the cranio-caudal direction (4.1±2.7mm). The respective values per patient are presented in the table (5.3).
The average ITV had the volume of 399±140 cm^3 for the respective CTV of 261±97 cm^3 .

5.3.1.3 Influence of breathing pattern

The comparison of the 4DDSim distributions obtained from the use of two different breathing patterns, regular and irregular, showed differences in the V_{95CTV} not larger than 3%. The summary of the results is shown in figure (5.4) and in table (5.4).
From the figure 5.4 is shown that for both breathing patterns the mean values (horizontal solid line in the boxplot) are similar for each of the beam geometries. The variation of the boxplot width is associated with the different simulated interplay patterns. This leads to the conclusion that the variation of the breathing starting phase results in a stronger variability in the dose distribution than an irregular breathing. This result may,

Table 5.3: Dataset B: Description of set of patients used in the intra-fractional motion evaluation pre-implementation at HIT. It includes the information of the CTV size in the planning CT. It is also shown the median vector field length (VFL) that corresponds to the mean length of the vector field between the reference breathing phase (0%Ex) and the most extreme phase, usually 100%Ex, inside the CTV.

Patient	CTV Volume (cm^3)	median VFL (mm)
B1	346.2	3.2
B2	233.3	6.5
B3	116.8	3.1
B4	284.2	3.8
B5	274.5	5.5
B6	174.0	1.2
B7	398.1	9.6
Mean $\pm$ St.dev.	261.0 $\pm$ 96.5	4.7 $\pm$2.7

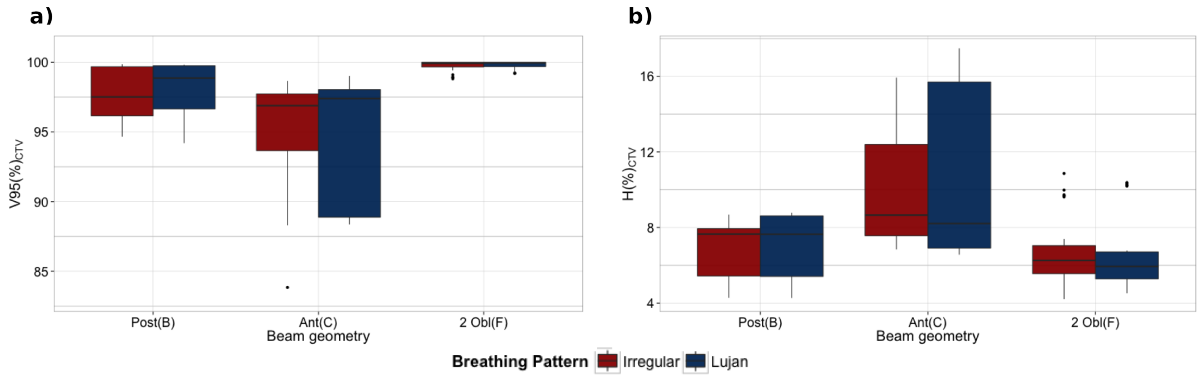

Figure 5.4: Distribution of the V_{95CTV} (a) and H_{CTV} (b) for the dataset B by beam geometries and motion type. Each boxplot is defined by the median value (solid black line), the 25% and 75% percentiles and outliers (full black circles). The blue boxplot represents the results using a regular breathing, while the red plots the irregular breathing curve.

however, arise because the 4DDSim were performed phase-based in a relative scale (i.e. 0-200%) and hence, amplitude variations do not affect the results. The reason for the selection of this mode for 4DDSim is related with the Anzai working principle and 4DCT acquisition method.

5.3.1.4 Dose degradation and homogeneity in the target

From the single phase forward calculations (named as quasi-4D), the quantification of the V_{95CTV} differences relative to the static case showed reduced influence of the range changes as a consequence of the intra-fractional anatomy variations. The worst case was for the anterior beam direction, a non-robust geometry from the inter-fractional point of view, with a mean decrease of the V_{95CTV} below 1%, with a maximum of 2.2%. Table 5.4 summarises the results.

However, when the interplay effect is taken into account, using the 4DDSim and considering both breathing patterns, the use of a single anterior beam leads to a mean reduction of the V_{95CTV} of (94.9$\pm$4.2) % and an increase in the H_{CTV} from (2.6$\pm$0.6) % to (10.2$\pm$3.6) %. On the other hand, when using a single posterior beam, the V_{95CTV} decreases only to (97.7$\pm$1.7) % and the H_{CTV} changes to (7.0$\pm$1.5)%.

The interference between the patient breathing and the temporal delivery structure, i.e.

Table 5.4: Comparison of the 4D dose distribution for three different beam configurations (B= posterior beam; C= anterior beam; F= two oblique posterior beams) through the mean and standard deviation of the V_{95CTV} and H_{CTV} for all the patients, breathing and interplay patterns in case of quasi-4D and 4DDSim. For comparison the results for the static case are also shown.

Beam Configuration:		**B**		**C**		**F**	
FW	**Breathing**	V_{95CTV} (%)	H_{CTV} (%)	V_{95CTV} (%)	H_{CTV} (%)	V_{95CTV} (%)	H_{CTV} (%)
static	no	100.0±0.1	2.8 ± 1.2	99.7 ± 0.4	2.8 ± 0.5	100.0 ± 0.1	2.7±2.7
quasi-4D	no	99.7 ± 0.4	3.0 ± 1.0	99.5 ± 0.6	2.7 ± 0.6	99.9 ± 0.3	2.9 ± 2.6
4DDSim	Lujan	97.9±1.9	7.0±1.6	94.8 ±4.2	10.5±4.0	99.8 ± 0.3	6.4±1.7
	Irregular	97.6 ±1.7	7.0±1.5	95.3 ± 3.5	10.0±2.9	99.8±0.3	6.5±1.6

the interplay effect, is attenuated for all the patients when two oblique posterior beams are used. For these cases there is no significant influence in the V_{95CTV} values. However, the interplay effect still results in an increase in the H_{CTV}, approximately to the double of the static case.
Figure 5.5 shows a representative patient case, patient B3, of one of the simulated dose distributions, for different beam configurations.
For patients with larger target internal motion (> 5 mm), the use of a single posterior

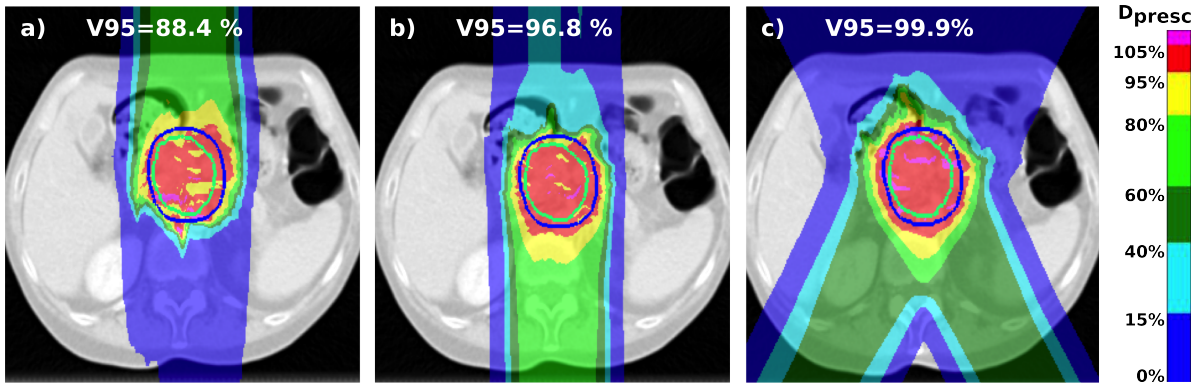

Figure 5.5: Example of a dose distribution of the Patient B3, with a regular breathing pattern for the set of tested geometries. Treatment plans were optimised for the ITV of 5 mm (blue line) and evaluated for the CTV_{0Ex} (green line), the respective V_{95CTV} are shown.

beam might not guarantee a V_{95CTV} above 95% for all the simulated scenarios (8% of the dose distributions).

In conclusion, the use of two oblique posterior beams was the only tested geometry that showed no significant influence of the variation of the breathing trajectory or breathing starting phase. This supports the need of multiple beams in order to average out the interplay effect and improve the quality of the delivered dose. Moreover, for all the evaluated cases the target coverage was found below 3% difference relative to the static delivery.

5.3.2 Dataset H : 4D simulations and reconstructions

This section covers the evaluation of the dataset H from the intra-fractional motion point of view. It includes for the patients treated at HIT, the pre-treatment 4D simulation and the reconstruction of the delivered dose in some of the treatment fractions.

5.3.2.1 Motion and DIR evaluation

The results of the DIR quality assessment are shown in table (5.5), for the CT VOI and the beam path VOI. This beam path VOI is shown in figure (5.6) together with the visual inspection of the DIR.
It was concluded from this analysis that the vector field is invertible (small ICE) and the patient suffers no changes in volume (JD equal to 1). Relative to the absolue differences, it correspond to small differences along the CT image are in average not significant.
For this set of patients the mean volume of the CTV of the main plan was 256±125

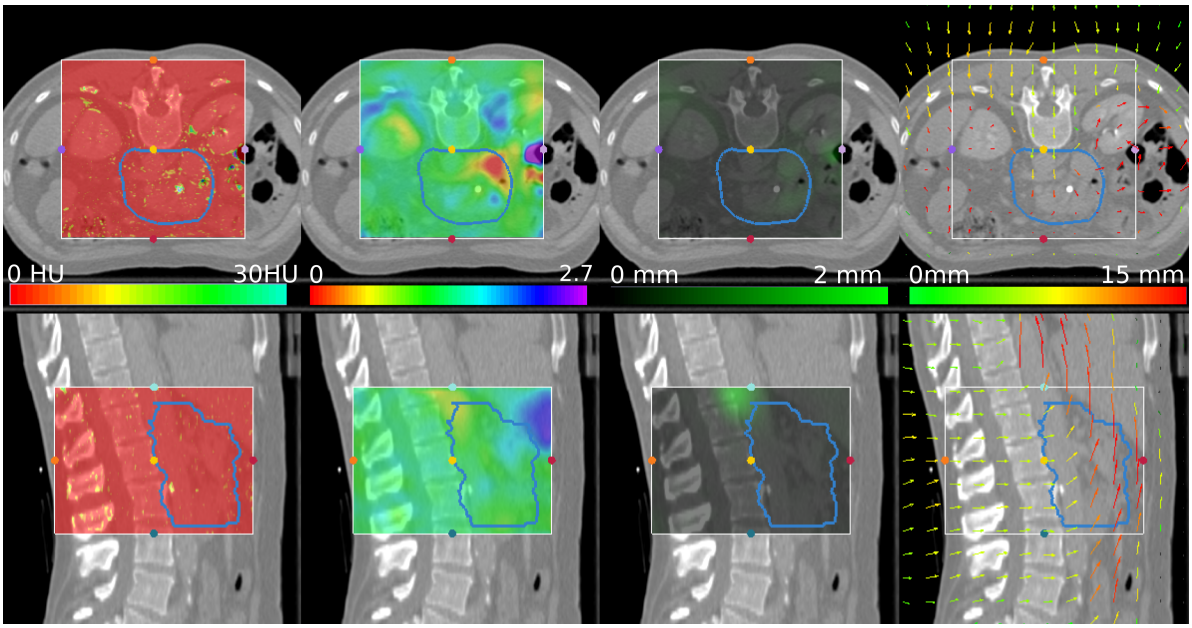

Figure 5.6: Evaluation of the deformable image registration between the end- and full-exhale state for the patient H1. The software used was the Slicer 3D through the evaluation of the absolute difference, determinant of the Jacobian matrix, Inverse Consistency Error and vector field (shown from left to right).

Table 5.5: Evaluation of the deformable image registration between the end- and full-exhale state for the patient H1, shown by the mean and standard deviation inside the full CT or in the beam path VOI of the absolute difference, determinant of the Jacobian matrix and Inverse Consistency Error.

Parameter	**VOI**	Mean± Std.dev.
JD	Body	1.0±0.1
	Beam Path	1.0±0.1
ICE (mm)	Body	0.6±0.9
	Beam Path	0.7±0.8
Abs.Diff (HU)	Body	15.3±27.8
	Beam Path	33.0±34.4

cm^3 for an ITV 442±253 cm^3.
The mean vector field length inside the ITV is shown in the table (5.6). The median of the vector field for this set of patients was 5.5± 3.8 mm, ranging from 2.2 to 12.7 mm, comparable with the one from the dataset B. The main component of the motion was detected in cranio-caudal (z) direction, followed by the anterior-posterior (y) direction.

Table 5.6: Median length of the vector field, obtained by DIR between the reference state (0%Ex) and each of the breathing states, inside the ITV for the largest difference relative to the 0%-Ex state. The directions x, y and z correspond to the left-right, anterior-posterior and cranio-caudal directions, relative to the patient, respectively.

	Maximum of the median VFL (mm)	
Patient	$\vec{x}$; $\vec{y}$; $\vec{z}$	$\vec{r}$
H1	0.2; 2.2; 8.2	**8.7**
H2	0.2; 0.9; 6.8	**6.9**
H3	0.6; 1.2; 4.1	**4.6**
H4	0.9; 1.1; 2.7	**3.1**
H5	0.2; 0.5; 3.2	**3.3**
H6	0.0; 0.8; 4.2	**4.5**
H7	0.8; 0.3; 4.6	**4.6**
H8	0.2; 1.0; 2.6	**4.1**
H9	0.8; 1.8; 4.2	**4.7**
H11	1.0; 1.5; 4.6	**5.0**
H12	0.3; 0.0; 12.6	**12.7**
H13	0.9; 0.1; 4.6	**5.0**
H14	0.1; 0.0; 3.0	**3.1**
H15	0.1; 1.1; 1.9	**2.2**
Mean $\pm$ Std.dev.	0.5$\pm$0.3; 0.9$\pm$0.6; 4.8$\pm$2.7	**5.2$\pm$2.7**

5.3.2.2 4D simulations Vs static situation

Due to differences in dose calculation between TRiP and Syngo® RT the evaluation of the 4D dose distributions was performed by comparison to the static dose distribution also calculated with TRiP.
Figure (5.7) gathers the 4DDSim V_{95CTV} difference relative to the static case, for all the patients and simulated starting phases. Note, that the results for the 4DDSim correspond to the propagated CTV (CTV_{0Ex}) from the CT_{BPL} to the reference state CT_{0Ex}.

The first impression from these results may be that the delivered plans were not as much robust against intra-fractional motion as expected from the previous simulations with dataset B, section (5.2.1). The variation of the V_{95CTV} reached values up to -28.0% with a mean of (-7.6$\pm$7.6)%. Regarding the H_{95CTV}, it was also strongly affected by the interplay, and displacements, going from (15.9$\pm$7.5)% in the static case to (27.8$\pm$8.5)% under motion (see appendix A.2 for the full results).
To guide in the interpretation of the results figure (5.8) shows the DVH for the CTV of the reference dose distribution (i.e. static) and of the set of 4D simulations, for two extreme cases. Patient H12 corresponds to the patient with largest internal motion (> 10 mm), which is the reason for the broad DVH and a mean reduction of the V_{95CTV} of (-15.8$\pm$8.1)%. In contrast, patient H15 with a mean tumour motion below 3 mm shows a reduction in the V_{95CTV} of just (-6.7$\pm$1.6)%.

This analysis assumed that the dose degradation was strongly affected by the internal motion amplitude. Therefore, the variation of the V_{95CTV} was represented against the internal motion amplitude in figure (5.9).

This comparison suggests that some patients, like H1, H2, H12 and H13, fall in red group (> 5mm motion and >5% of CTV dose reduction), however, other patients, as H7, are not conforming to this hypothesis. In resume, from figure (5.9) its is observed, that five patients for which the motion amplitude was below 5 mm the target suffered

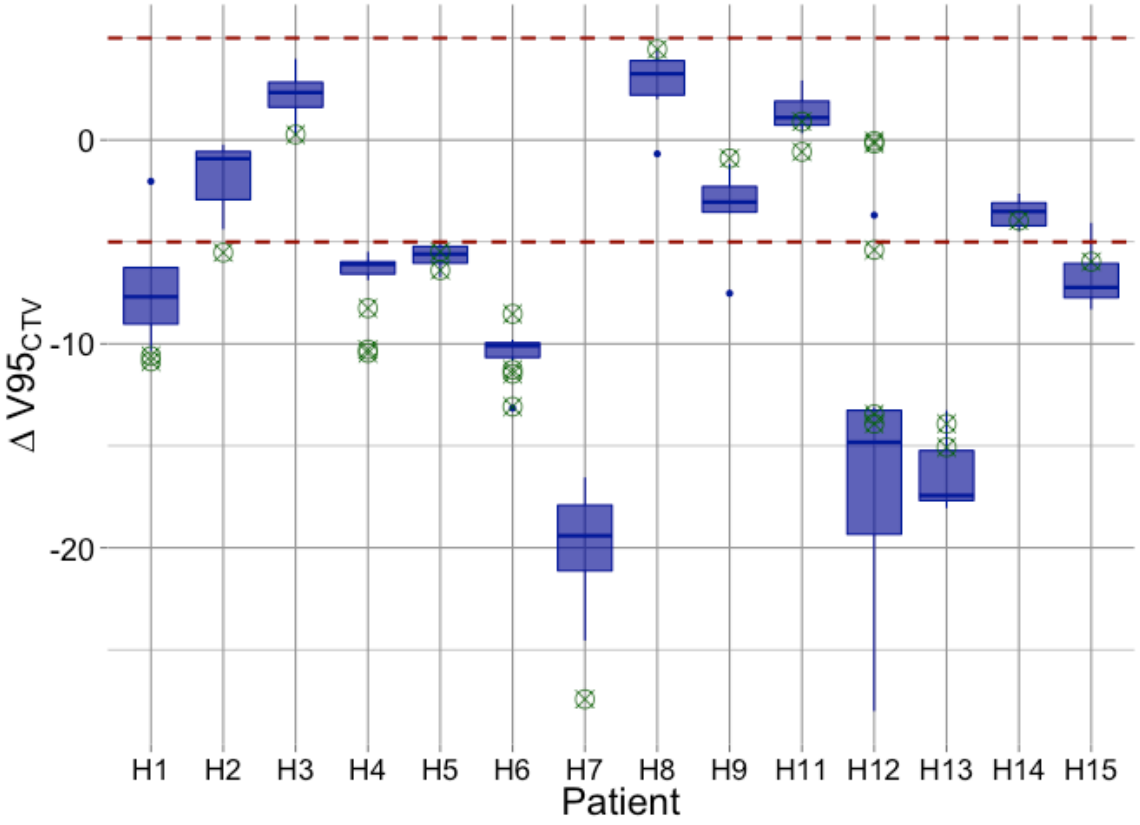

Figure 5.7: Differences of the V_{95CTV} for all the patients relative to the static dose distribution value. Each boxplot corresponds to the five simulated interplay patterns from the 4DDSim, while the green crosses are the results from the 4DDReco. The red dashed lines define the 5% of variation in comparison with the static dose distribution, and is here used to help in the detection of the patients with major deviations.

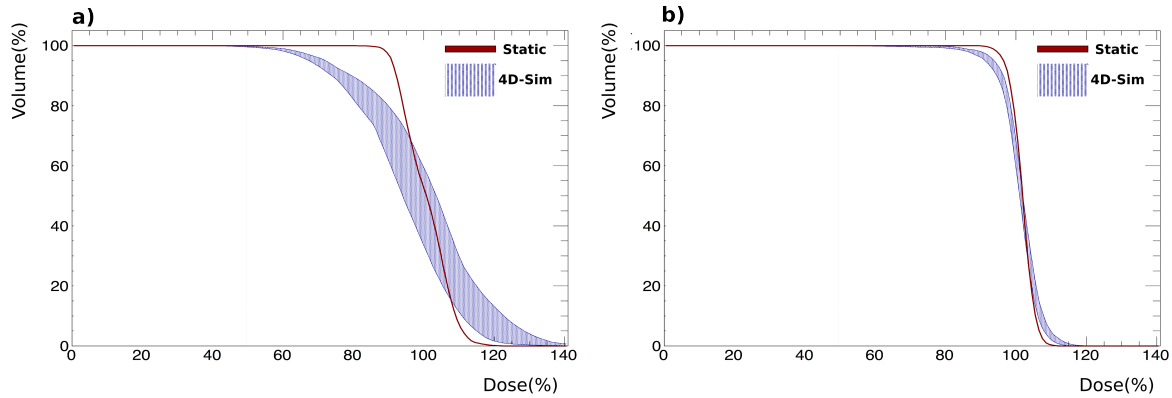

Figure 5.8: DVH of the patient H12 (a) and H15 (b) for the CTV_{0Ex} in the static case (red line) and for the set of 4DDSim as the blue band.

a significant dose degradation (yellow region of fig.5.9). Another conclusion, was that any patient with a median motion superior to 5 mm was detected with a reduced target degradation (grey region in graph 5.9), although no linear correlation was found between the two parameters. This justifies the need to monitor the motion amplitude for pancreatic patients, along the treatment, and apply some strategy to reduce its impact (e.g. gating, robust optimisation, rescanning, etc).
Considering this remaining issue, in the next sections the 4DDReco and the treatment

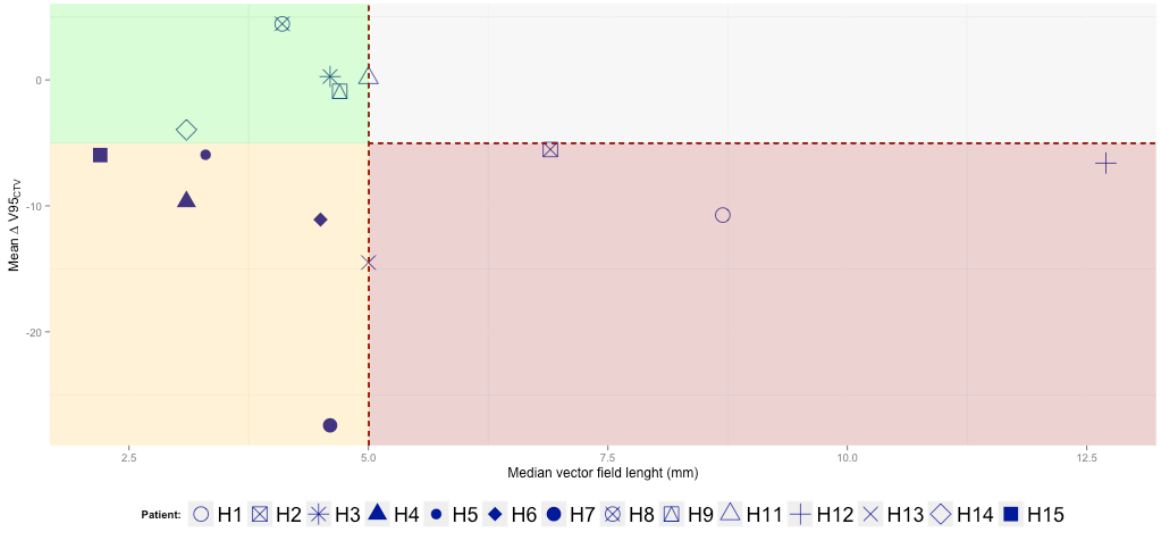

Figure 5.9: Mean difference of the V_{95CTV} between the static and the 4DDSim versus the median vector field length inside the ITV. Red region corresponds to large motion and consequently high dose degradation, while green are patients with a robust dose distribution against intra-fractional motion. The yellow region corresponds to patients where the motion amplitude is small (<5 mm) but a reduction in the V_{95CTV} is demonstrate. A region without cases was found, grey area, which correspond to a no patients with large motion and small V_{95CTV} variations.

plan were evaluated.

5.3.2.3 Reconstructed Vs simulated dose distributions

The evaluation of the 4DDReco is shown also in the figure (5.7), by the green crosses, overlaid with the static and 4DDSim results. From this graph, it is observed that the 4DDSim resulted in a good approximation of the robustness of the plan for some patients, while for other can be used as an indicator of the probability to get a dose reduction on the CTV, either by the mean or width of the boxplot.
Figure (5.10) shows the dose distribution for the patient H3 in the static, 4DDSim and 4DDReco situation, in which is observed similar conclusion obtained from the 4DDSim and 4DDReco. Nevertheless, other patients (as H7 and H12) exhibit a 4DDReco significantly outside the predicted set of 4DDSim.
In general, patients with minor internal motion tend to have more similar 4DDSim solutions, i.e. a small interplay effect and therefore a small box width in figure (5.7). However, the number of calculated simulations showed limited capability to describe all the possible interplay patterns, as the ones detected during the 4DDReco. Despite, the failure of the 4DDSim in the quantification of how much the dose is degraded, it is able to detect if a plan is or is not robust, at least the order of the differences can be understood as a probability indicator.
From the visual inspection of the dose distributions, as the example shown in figure (5.10), it was observed that the static plans were highly modulated for many patients. This was related with dose constraints to the OARs (mainly bowel), which result in sharp dose gradient between the GTV and the bowel contour. Hence, other studied conjecture was the influence of the plan modulation on the robustness to the breathing motion. Therefore, the next section addresses this question.

The dose distributions and DVHs for others patients are available in the appendix (A.2).

For the patients showing higher tumour motion amplitude, i.e. H1, H12 and H13, the beam delivery using beam gating was additionally simulated using a standard gating window of 50%Ex-50%In. These simulations showed a reduction of the interplay effect, as shown in table (5.7), with reduction of the standard deviation of the $V95_{CTV}$ and H_{CTV} for the set of simulations, however the residual motion still compromises the dose distribution. Another factor to consider in this approach, is that beam gating will introduce a correlation between the beam application and the breathing motion, thus any residual motion will affect the dose distribution always in a similar way. Therefore, dose fractionation will not attenuate the interplay effect, since the effect will be fairly the same.

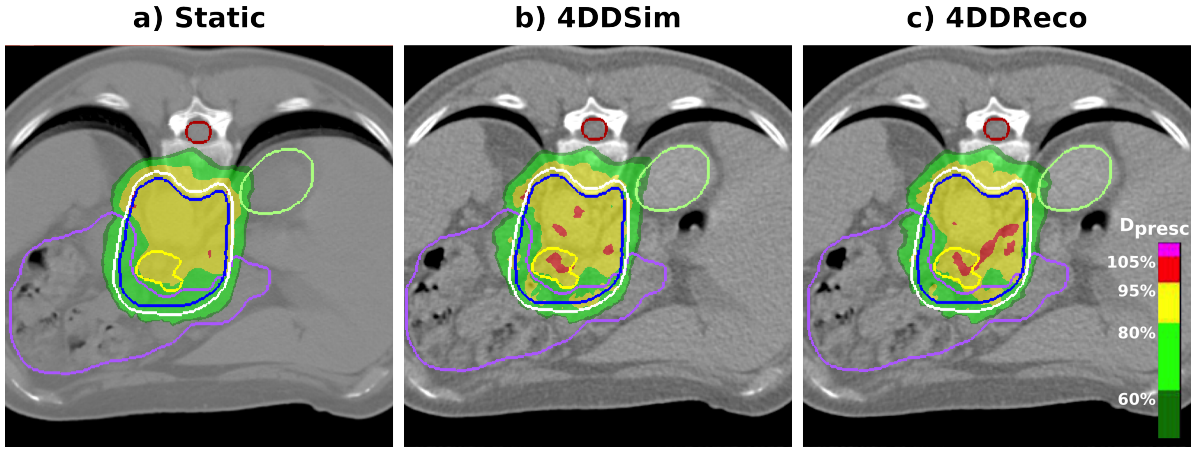

Figure 5.10: Dose distribution in the transversal CT view for the patient H3 in the static (a), one of the simulated cases (b) and in the reconstructed fraction (c). In yellow, blue and white, the GTV, CTV and ITV are displayed, respectively. The dose distribution was tailored in order to keep the bowel (in purple) below the dosimetric constraints. In a) is shown the planning CT, while in b) and c) is the CT_{0Ex}.

Table 5.7: Comparison of the plan quality parameters of the CTV (homogeneity H_{CTV} , $V95_{CTV}$ and $V107_{CTV}$) relative to the static case, for the beam delivery under free-breathing and beam gating, for the simulated 4D dose distributions (4DDSim). The mean and standard deviation values correspond to the set of 5 simulations performed in each case.

Patient	4DDSim	ΔH_{CTV}(%)	$\Delta V95_{CTV}$(%)	$\Delta V107_{CTV}$(%)
H1	Free-Breathing	11.4±2.8	-5.7± 3.6	21.3±4.1
	$Gating_{50\%Ex-50\%In}$	10.9±1.1	-2.6±0.7	21.5±2.5
H12	Free-Breathing	28.9±5.8	-11.7± 7.3	11.1±8.8
	$Gating_{50\%Ex-50\%In}$	27.0±5.6	-12.0±4.8	9.5±3.5
H13	Free-Breathing	2.9±1.0	-14.7± 2.1	0.6± 0.7
	$Gating_{50\%Ex-50\%In}$	2.5±1.3	-13.2± 1.6	0.9±0.4

5.3.2.4 Impact of dose modulation

The modulation index for all the patients of the dataset H was determined. In order to understand the differences between the plans, the MI for the dataset B using the two oblique beams were also calculated. Figure (5.11) compiles the result for all the plans.

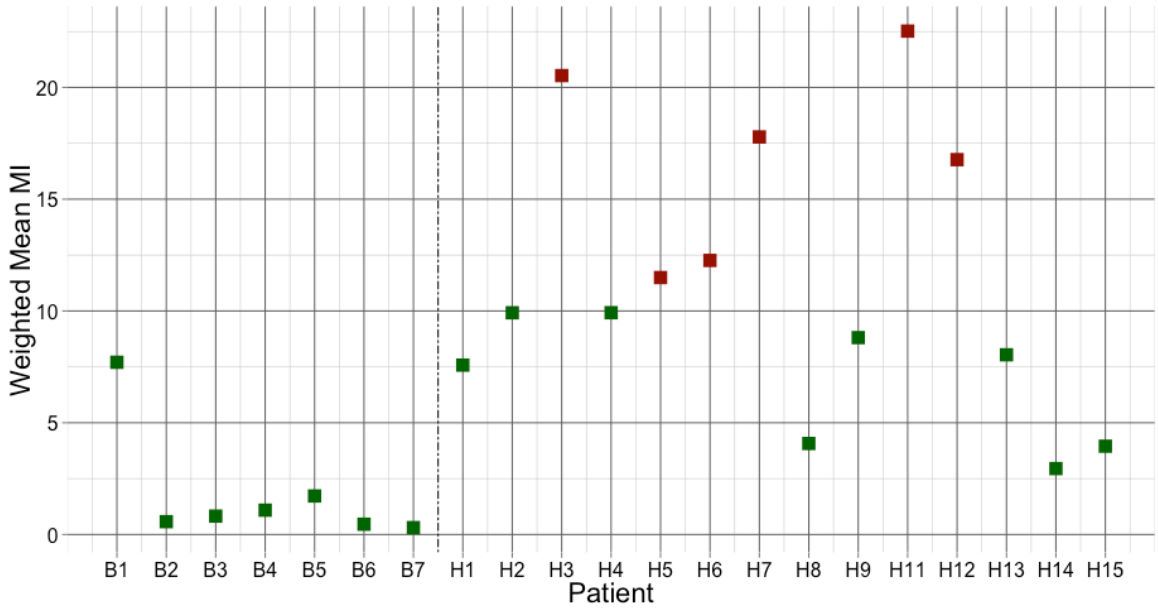

Figure 5.11: Beam-weighted Modulation Index per patient. The patients B1 to B7 correspond to the patients from the section (5.2.1), whose plans where optimised using the TPS TRiP98. The set of patients H1 to H15 had the treatment plan optimised using the TPS Syngo® RT and correspond to the clinically applicable plans. To help in the visualisation, the red squares correspond to the plans whose MI were superior to 10, and green squares to the ones below or equal to 10. This threshold was selected in order to be superior to the maximum value of the dataset B.

As example of this MI variation patient H9 and H11 were selected because although both patients exhibit the same amount of tumour motion (median VFL inside the ITV), their 4D dose distribution varies significantly. In figure (5.12) the function of the modulation *F*, in which the MI corresponds to the area below the curve, is represented for these cases. In general, as in the example of the patient H11, it was observed, that the plans optimised in Syngo® RT tend to have a stronger modulation at the tumour borders. This effect is related with the proximity of OARs, otherwise the shape of the function is similar to the one for the patient H9. Hence, the MI is commonly larger for Syngo® RT, as compared to TRiP, as a result of the number of OARs used during the optimisation process, significantly smaller in TRiP. In general, Syngo® RT prioritises the OARs constraints against the tumour irradiation, which result in the increase of the MI when more constraints are defined. Moreover, and maybe the main source of differences, is the optimisation method used by the two TPS. Syngo® RT uses a Broyden–Fletcher–Goldfarb–Shanno (BFGS) algorithm to solve the optimization problem, which solution does not have a regularization the number of particles between neighbour raster points. Otherwise, TRiP uses a conjugate gradient method to obtain a smoother distribution of particles in the target volume.
Figure (5.12) shows also the mean and standard deviation of the number of particles per IES for the patients H9 and H11. From these two concepts no clear conclusion is directly possible. To help in its interpretation, the overall results are summarised in table (5.8), while the MI graphs for all the patients are shown in the appendix (A.6).

From these results it can be concluded that the value of $\overline{\sigma_{IES}}$ is not as so representative of the plan heterogeneities as the MI. From the theoretical point, $\overline{\sigma_{IES}}$ should be higher for plans with major intensities differences between raster points. However, because this concept ignores the location of the raster points, it may not be representative

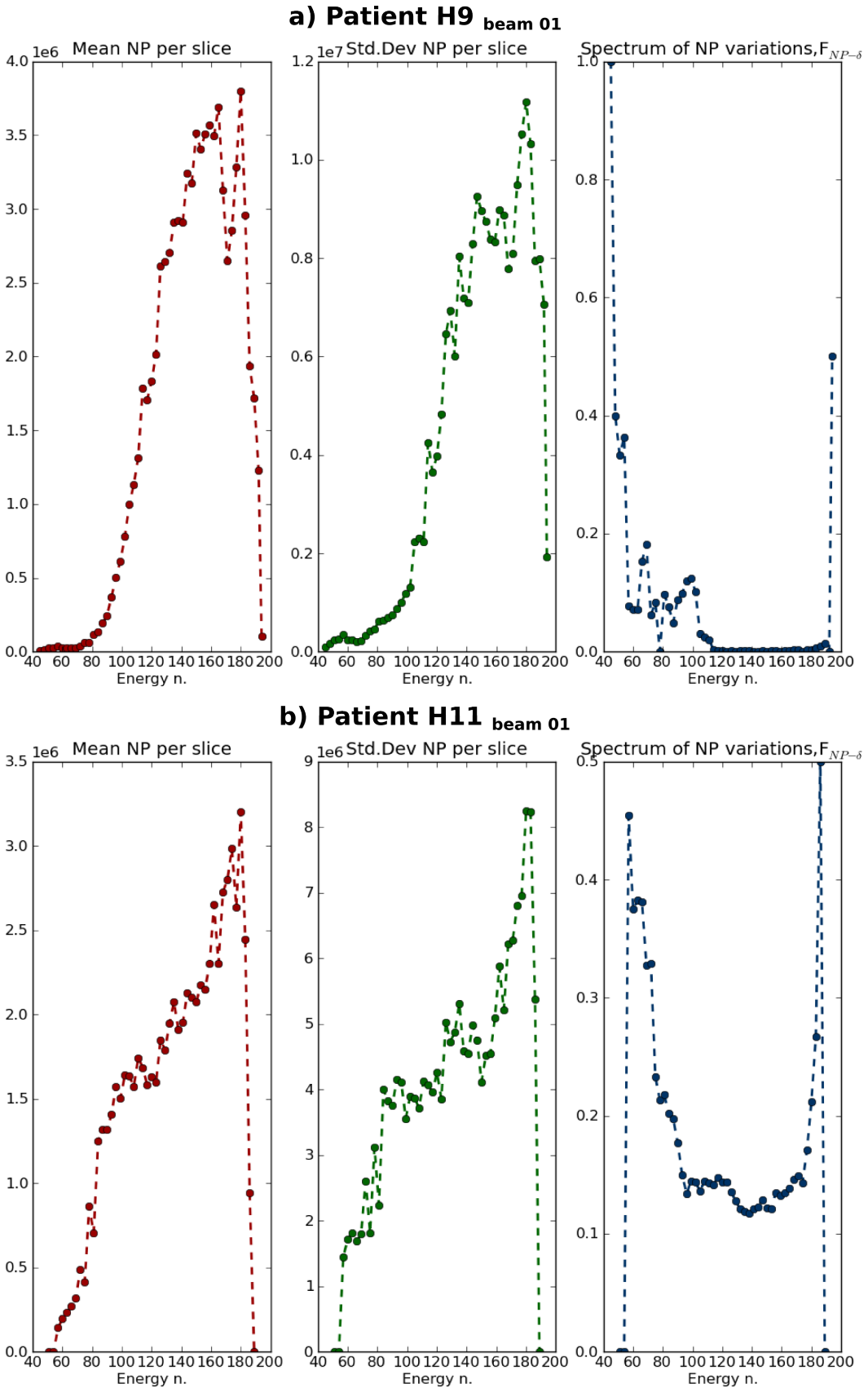

Figure 5.12: Distribution along the IES of the modulation function, mean and standard deviation of the number of particles (NP) for the beam 1 of patient H9 (a) and H11 (b).

Table 5.8: Mean and standard deviation of the variation of the $V95_{CTV}$ and H_{CTV} for the 4DDSim and 4DDReco and for the respective plans the calculated $\overline{\sigma_{IES}}$ and $MI_{weighted}$.

Patient	$\Delta V95_{4DDSIM+4DDReco}$ (%)	$\Delta H_{4DDSIM+4DDReco}$ (%)	$\overline{\sigma_{IES}}$	$MI_{weighted}$
H1	-8.1±3.0	11.7± 3.7	2.7	7.6
H2	-2.3±2.2	12.7±2.6	3.6	9.9
H3	1.9±1.4	7.8±3.3	6.4	20.5
H4	-7.4±1.9	12.7±0.6	5.2	9.9
H5	-5.8±0.6	12.1±2.9	4.2	11.5
H6	-10.8±1.5	13.2±2.0	4.2	12.3
H7	-20.9±3.9	20.7±2.4	5.3	17.8
H8	2.9±1.8	16.3±1.8	3.9	4.1
H9	-3.1±2.2	8.1±3.1	4.3	8.8
H11	1.2±1.0	0.6 ±1.0	3.1	22.5
H12	-11.6±8.6	30.0±5.9	5.1	16.7
H13	-15.9±1.9	3.2±0.7	3.5	8.0
H14	-3.6±0.7	1.3±0.6	3.3	3.0
H15	-6.0±1.5	4.2±1.3	4.8	4.0

of the plan modulation.
An alternative method to verify this relationship between dose degradation under motion and plan modulation is through the visual inspection of the dose distribution per radiation field. Another two cases are shown in figure (5.13), in which patient H12 with high MI is compared with patient H13 with MI below 10. Although patients H12 and H13 were both planned with IMPT, the dose distribution is quite homogenous per field in the case of H13, as depicted by the distal profile for each of the beams (5.13-a1,2). In contrast, the plan of the patient H12 (5.13-b1,2) shows a higher dose for the beam 01, with the beam 02 just adding dose to the regions not completely covered by beam 01. The profile in beam direction for this beam 02 (5.13-b2) shows the high gradients inside the target, which complements the dose to the lateral profile of the beam 01 (5.13-b1). As consequence, the tumour motion will result easily in raster points mispositioned.

Although, for many patients the combination of the motion amplitude and the MI can justify the dose degradation, there are some cases still to be explained. Considereing patient H15 as an example (see fig.5.9 and 5.11), in which the reduction of the $V95_{CTV}$ of more than 5% wasn't expected, i.e. small motion and small MI should produce a small $\Delta V95_{CTV}$. This can be a consequence of the sensitivity of the V95 parameter that just measures a point on the DVH and not the overall change in the DVH shape. If instead of looking for the $V95_{CTV}$, the $D_{medianCTV}$ is analysed, then patient H15 is not significantly affected by the interplay effect since its $D_{medianCTV}$ under motion is (181.5±0.8) cGy (RBE). For other patients in which MI is high, as the case of H11 the $D_{medianCTV}$ was reduced to (177.5±0.8) cGy (RBE).

5.4 Summary and discussion

The results allow to conclude that the use of two oblique posterior beams can mitigate the influence of intra-fractional motion and the interplay effect. Nevertheless, patients with internal motion amplitude superior to 5 mm require precaution, and strategies to

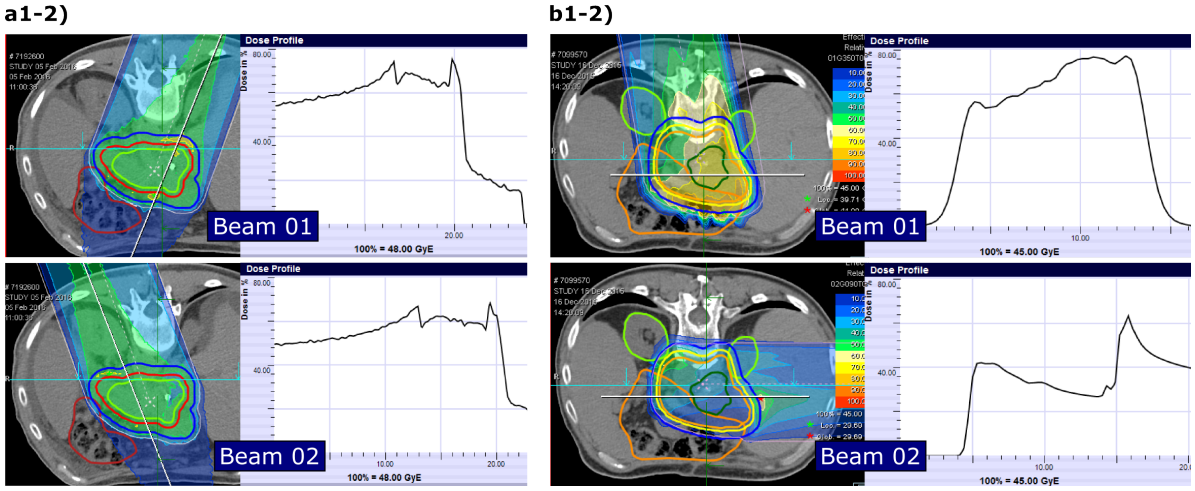

Figure 5.13: Transversal slice of the dose distribution and dose profiles for each beam of patient H12 and H13. a1-2) Example of patient H13 where a homogeneous dose distribution is delivered for both beams as also visible by the dose profile in beam direction along the white solid line shown in the dose distribution. b1-2) The case of patient H12 that has a total homogeneous dose distribution but which resulted of the overlap of two heterogeneous dose distribution for each individual beam. The example of the same dose profile for each of the beams shows that the beam 02 complements the dose distribution of the beam 01.The mismatch of this overlay, as result of the breathing motion, lead to target under-dosage.

reduce impact in the irradiation should be considered.

Another aspect to be considered is the plan optimisation, where plans with stronger modulation, as resulting from high dose gradients and inhomogeneous number of particles in neighbour raster positions, result in a plan with less robustness against range and positioning uncertainties. Therefore, the inclusion of robustness into the optimisation process is demanding and will allow to use the full potential of beam scanning techniques without compromise the plan quality.

The introduced modulation index showed promising results to support the treatment plan evaluation. Further implementation of it application to the clinical routine still need to be performed, as well as, optimisation of thresholds and more accurate methods to account for multiple beams.

Regarding the potential of 4D dose simulation in the prediction of the movement influence in the delivered plan, its main weakness is the surrogate signal used. In this study was assumed a perfect correlation between breathing and organ motion, however, it was shown by different authors (Brevet 2011; Torres 2011) a weak correlation in some patients. Alternative methods to monitor the patient internal motion should be explored, or strategies to assess the daily correlation with the existing external surrogate signal should be investigated.

Chapter 6

Outlook: Magnetic resonance imaging for motion detection

6.1 Motivation

Pancreatic cancer patients are very susceptible to anatomical changes along the treatment delivery, mainly as a result from the respiratory motion, which affects the dosimetric plan quality. 4D dose reconstructions based on a 4DCT dataset allow to estimate the impact of the organ motion and the originated interplay from a scanned beam delivery in ion-beam radiotherapy. However, 4DCT is limited in the identification of baseline-shifts and irregular patterns, as a consequence of its acquisition and reconstruction process, as described in section (2.4.0.1).
One solution that has been rising in radiation therapy (RT) is the application of MR-sequences with the capability to sort the images according to a trigger signal, namely 4DMRI. Additionally, pancreatic cancer treatment is strongly affected by the poor soft-tissue contrast in CT-imaging; hence MRI would add excellent soft tissue contrast to the target definition.
The application of MRI-data for ion-beam has the potential to be used in the motion detection, including the feature of inter-variability of the intra-fractional motion, and therefore, in the motion sampling of the specific patient and in the definition of an individualised robust plan against motion. Moreover, it might be used for real-time monitoring of the internal patient motion - if an integrated solution is available - and for online adaptation strategies , such as beam gating or tracking.
The aim of this section is to assess the existing issues to the application of MRI imaging for motion assessment and to quantify the impact of intra-fractional motion detected by 4DMRI.
In summary, this chapter intends to answer the following questions:

- Is it clinically feasible?
- What needs to be adapted in the clinical workflow?
- Will the workload increase?
- Which additional information can be obtained?
- Which is the clinical role of this new imaging modality in radiotherapy?

6.1.1 Principles of magnetic resonance imaging

Unlike CT and PET, MRI does not use ionising radiation to obtain a body image. MRI takes advantage of the high percentage of hydrogen atoms in the human body and uses the magnetic properties of the protons.
While the patient is placed into a magnetic field its protons of the hydrogen atoms are aligned to the magnetic field. When a radio frequency (RF) pulse is emitted from the scanner the protons follow a precession to out of the alignment. Succeeding to the end of the pulse, the protons will re-align with the magnetic field and the MRI signal dissipates. The description of how the signal changes in time is named as relaxation.
The different MRI signals are resulting of the different densities and relaxation properties of the tissues. Two types of relaxation happen: spin-spin and spin-lattice, which are respectively described by the relaxation times T1 and T2. In the process of T1 relaxation the protons longitudinal magnetisation recovers after the RF pulse. The T2 signal originates when the protons dephase, which results in decay of the transverse magnetisation.
In brief, the spatial encoding of the MRI signal is accomplished through the use of superimposed magnetic fields, gradients, which perturb the main magnetic field, and cause hydrogen protons in different locations to precess at slightly different rates.

6.1.2 MRI in radiotherapy treatment planning

MRI has been arising as a modality with a high potential for use in radiation therapy, due to its high spatial resolution, ability to image with superior soft tissues contrast, compared to CT, and the absence of additional radiation dose to the tissues.
However, the direct implementation of MRI in the RT workflow is subject to several difficulties. When MRI is used to help in the tumour delineation, rigid registration between multi-modal image data is required and additional uncertainties need to be taken into account. Further, if the treatment planning is only MRI-based no electron density is available and therefore no dose calculation can be directly performed.

6.1.2.1 Artifacts and geometric distortions

In addition to the previously mentioned points, MRI images are highly susceptible to artifacts and geometric distortions. Image artifacts are caused by a variety of factors that may be patient related such as physiologic motion, metallic implants or foreign bodies, or due to the acquisition process, as finite sampling, FOV size, k-space encoding, RF overflow and among others. These artifacts will then result in an MRI not representative of the true patient anatomy.
Geometric distortions are caused by magnetic field inhomogeneities in the main field and non-linearity of the gradients (Torfeh et al. 2016).
Some artifacts don't affect the diagnostic quality of the MRI, however that doesn't mean that they won't influence the RT planning process, since all the anatomy in the beam path needs to be considered during the dose calculation process. Depending of the application, i.e. target delineation or dose calculation, RT images are required to have resolution in the order of 1-3 mm, constance of the pixel value and high contrast.

6.1.2.2 MR in motion management

Besides the already pointed advantages of the use of MRI in RT, another encouraging feature is the possibility to perform motion monitoring in larger acquisition intervals, with more periodicity and without additional radiation to the patient.
Motion is usually included in RT through the use of 4DCT, however the many associated limitations are well known. First, daily imaging is restricted as consequence of the increase of the dose to the patient that results in an under-sampling of the possible intra-fractional motion variations. Then, the measured anatomical motion is confined to a 10 min acquisition in addition to the fact that the represented breathing cycle by the 4DCT corresponds to an average along the acquisition time.
For these reasons, 4D-MRI has been sought as an alternative or additional method for the direct characterisation of the internal motion of the patient (Boye, Lomax, and Knopf 2013; Moteabbed, Schuemann, and Paganetti 2014).
The application of this technique is limited to some scanners, which may be the reason for the lacking of a standard 4D-MRI technique for RT. One of the approaches is to use fast MR sequences to continuously acquire images from all respiratory phases and then retrospectively sort these images by respiratory phase. Consequently, the data sorting requires some kind of surrogate signal, either external (e.g. MRI pressure belt) or internal (e.g. using a navigator slice at a fixed position (Siebenthal et al. 2005).
This first attempt to perform 4DMRI for pancreatic patients, followed the approach developed by Rank et al. (2016) and is described in the following section.

4DMR acquisition sequence

The method proposed by Rank et al. (2016) is based on a 3D-encoded gradient echo sequence with a radial stack-of-stars sampling, named *Radial Vibe* in the Siemens scanners. In this approach the k-space center of the radial acquisition is used as navigator in the estimation of the motion amplitude. During the reconstruction process the radially acquired spokes (i.e. radial projections of the k-space) are transformed onto a rectilinear grid. These sequences are strongly affected by streak artefacts that arise from the under-sampling in each motion phase. Therefore, the reconstruction method applied here performs a motion-compensation (MoCo), pre-processing of the data based on the motion estimation, between each of the motion phases. This information is obtained from the VFs calculated between phases. Additionally, a motion estimation using a high-dimensional total variation algorithm (HDTV) is performed in order to minimise the image artifacts.
In summary, the method MoCo-HDTV shows potential for the generation of a 4D time resolved MRI with low streak artifacts and high image sharpness and will be subsequently applied in this testing phase.

6.2 Material and methods

6.2.0.1 Patients and imaging

The patients H13, H14 and H15, discussed in the previous chapter (5.1), which had a planning CT, 4DCT and respective structure set were additionally imaged with MRI. The MRI acquisition was performed in the National Center for Tumor Diseases (NCT), Heidelberg, which is adjacent to HIT, using the scanner Magneton Aera 1.5T, *Siemens, Erlangen, Germany*. The patients were positioned, as in the planning CT and treatment, in prone immobilisation with the hands raised above their head in a vacuum mattress. No contrast agent was used and the patients where imaged under free-breathing.
In order to fix the vacuum mattress to the MRI couch a wood flat base with adjustable plastic pins was developed at DKFZ (see figure 6.1). The RT isocentre, marked in the mattress, was used to align the patient into the MRI scanner and to place the body coil in the VOI.
The MRI's sessions were scheduled along the treatment course. The total number of

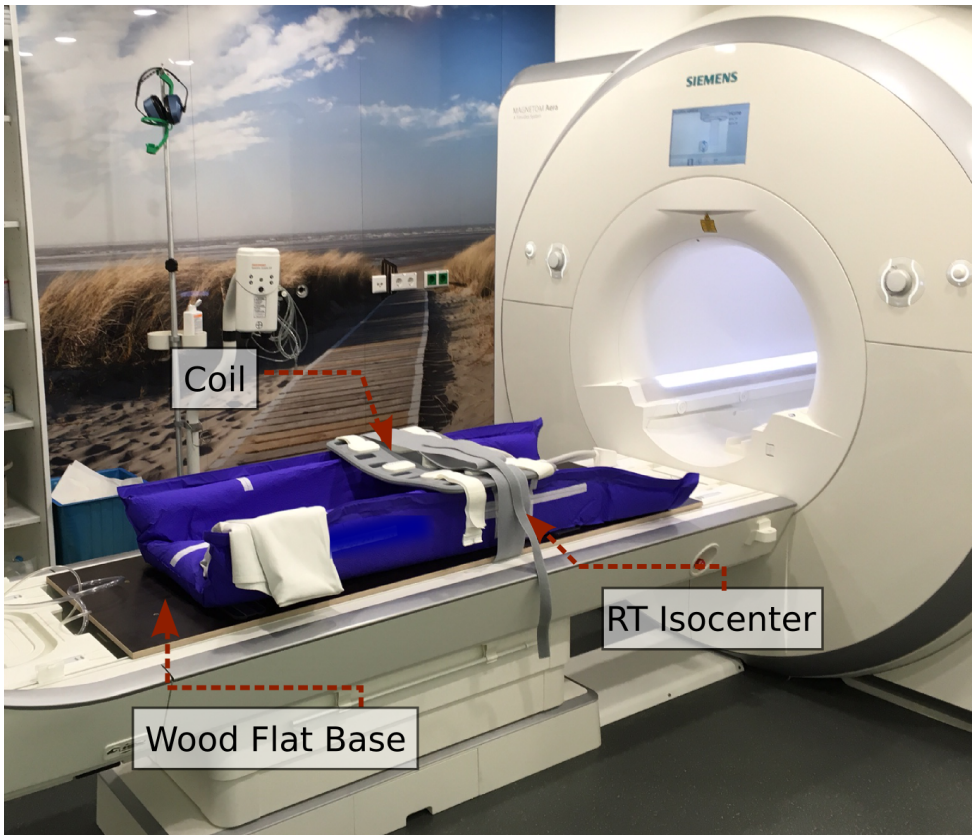

Figure 6.1: Setup of the MRI acquisition for the pancreatic patients treated at HIT and imaged in the National Center for Tumour Diseases (NCT). The apparatus consists of the patient specific vacuum mattress indexed to a wood flat base that is attached to the MRI's couch. The body coil is then placed in the patient's RT isocentre.

acquisitions per patient is shown in the table (6.1). Each session included a T2-gated or breath-hold acquisition, a diffusion-weighted echo-planar, 2D cine in coronal and sagittal planes to the tumour location and a *T1-Radial Vibe* sequence. This last method, previously described in the section (6.1.2.2), was the only considered in the following analysis.
The *T1-Radial Vibe* sequence was performed with a repetition time of 3.3 s, an echo

time of 1.6 s, 2504 radial spokes, a FOV of 400x400 mm^2, pixel spacing of 1.56 mm, slice thickness of 4 mm and fat suppression active. The acquisition time was approximately 8 min for all the sessions.

Table 6.1: Description of the subset of patients used for the assessment of the 4DMRI functionality. It includes the maximum median vector field length (median VFL) measured for these patients using the 4DCT, the number of MRI sessions and which MRI reconstruction strategy was performed. The *full reconstruction* uses the entire raw data, while the partial reconstruction is split in time the raw data and reconstruct three sequential 4DMRI.

				Reco.Strategy	
Patient	**CT**	**max. VFL_{CT} (mm)**	**MRI session**	**Full**	**Partial**
H13	✓	5.5	2x	✓	✓
H14	✓	1.2	1x	✓	✓
H15	✓	9.6	2x	✓	✓

6.2.0.2 Image reconstruction and processing

The available *T1-Radial Vibe* sequence in the Magneton Aera scanner doesn't include the sorting and reconstruction of the phase-based sequence, therefore for the recorded raw data a post-reconstruction was performed.
The 4DMRI was reconstructed based on the method MoCo-HDTV (see section 6.1.2.2), developed by (Rank et al. 2016). The application of this algorithm in the context of this work was performed by the working group E0401 and E0404 of the Department of Medical Physics in Radiation Oncology (DKFZ).
This reconstruction algorithm has available different modes, which allow the definition of the number of bins, overlapping width between bins, how the raw data is divided in amplitude, definition of image filters, definition of the starting breathing phase and others.
Considering the approach here investigated, the first phase was defined as end-exhale (i.e. bin 0) and for the sharpest width of signal distribution as possible, for a overlapping phase width between bins of 10% of the entire respiratory cycle and the sorting considering the global maximum.
The self-gating signal is used for the 4DMRI reconstruction in two schemes:

- Full - the complete raw data (2504 spokes) is included in this reconstruction. The sorting is performed through the self-gating signal of the entire acquisition in 20 overlapping motion phase bins. This scheme represents the averaged breathing cycle in the acquisition time.
- Partial - the raw data is split in three approximately equal sets (800, 800 and 900 spokes), sequentially distributed along the acquisition time course. The data of each of these sets is then phase-sorted and used for the reconstruction of 10 bins per breathing cycle. Therefore, for this method a total of 3 x 10 bins were reconstructed.

The self-gating signal used for the data sorting in these two methods is exemplified for patient H13 in the figure (6.2).

After the image reconstruction, the MRI data was processed in order to match with the planning CT properties, such as the image data type, orientation and pixel spacing.

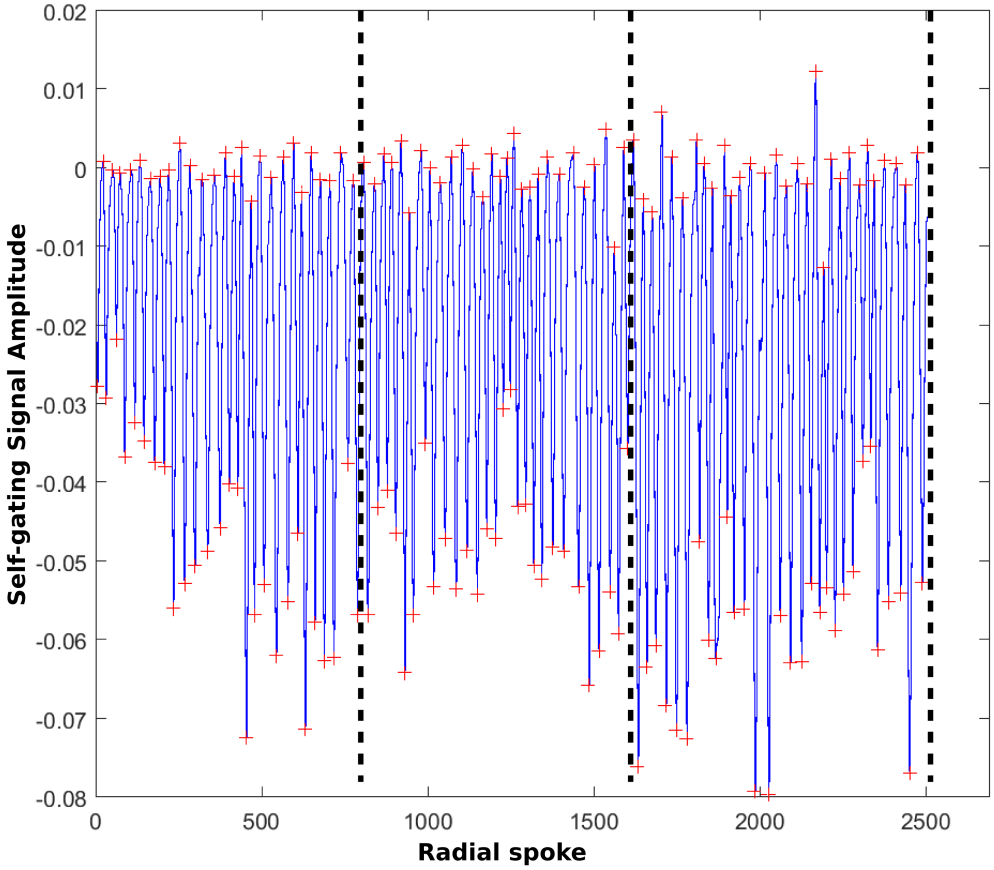

Figure 6.2: Self-gating signal magnitude for each radial spoke of the first session of patient H13. The dashed vertical lines correspond to the splitting of the signal into three dataset for partial reconstruction.

This step has to be done for the DIR process implemented in Plastimatch. The data processing steps are described in the flowchart of figure (6.3).
Additionally, a first approach to correct the geometric distortion correction was performed for the patients H13 and H14. This process is based on the DIR between the original Siemens corrected image (not sorted in bins) and an average of all the reconstructed bins. From this DIR is then obtained a corrected vector field that is applied to each individual bin. This correction was performed using the software Plastimatch with a set of B-Spline functions and as cost function the gradient magnitude (see section 3.2 for details). The images with correction of the geometric distortion (GD) will be called ”GD-corrected” and the other ”sorted raw”.

6.2.0.3 Deformable image registration

The previously described pre-processing of the MRI and CT data (cf. figure 6.3) was performed for all the patients and imaging sessions.
The method tested in this work to generate a 4DCT based on the 4DMRI was based in DIR between images. The goal is to evaluate the feasibility of this approach and associated issues.
The DIR was executed between each of the MRI-bins and the reference bin, i.e., bin 0, and between each of the MRI-bins and the planning CT. Both DIRs were performed us-

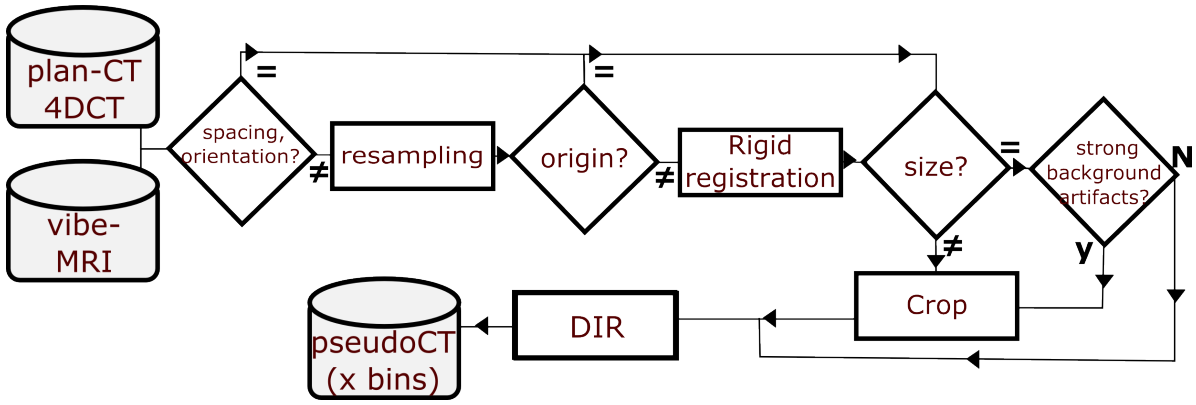

Figure 6.3: Flowchart of the processing steps performed to the MRI data. The planning-CT, 4DCT and 4D-MRI were convert to match in their pixel spacing and orientation. In order to simplify the deformable registration process, the images were firstly registered using rigid registration based on bone anatomy and cropped to removed background artefacts of the MRI.

ing the software Plastimatch (presented in the chapter 3.2). Different procedures were adopted for each case and, therefore, are individually described below.
The DIR quality was evaluated using the SlicerRT module (cf. section 3.3.1) through the parameters: determinant of the Jacobian matrix (JD), inverse consistency error (ICE) and absolute difference between the reference and transformed image. These parameters were calculated for the full image, for a VOI including the beam path and for a VOI restricted to the ITV volume. These VOIs are exemplified in the figure (6.4).

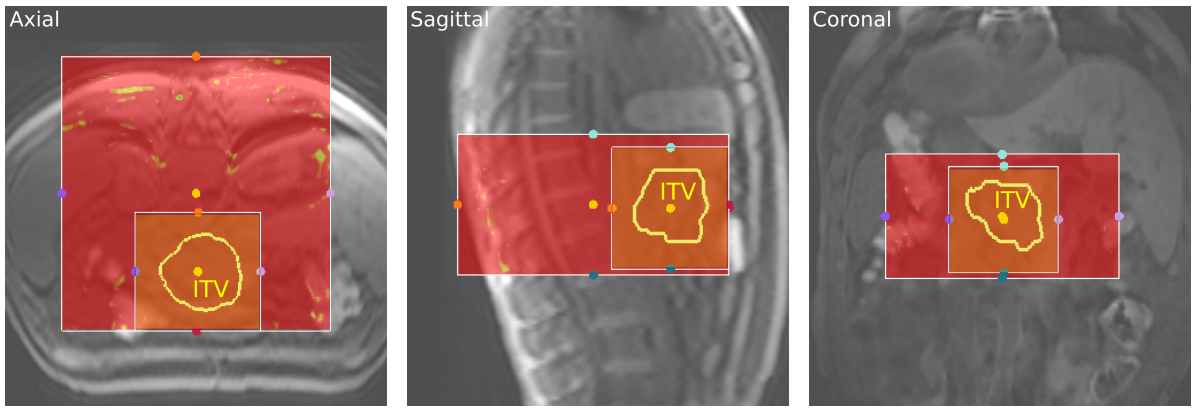

Figure 6.4: VOIs used for the evaluation of the DIR quality. The yellow box corresponds to the VOI restricted to the ITV volume, the red box includes the ITV and the beam path, i.e. posterior oblique right and left field. The evaluation for the full image was also performed, named as ”Body”.

a) Image registration: MRI$_{bin-ref}$-MRI$_{bin-i}$

The aim of this registration is to provide the vector fields that describe the anatomy motion along the different bins relative to the reference one. These transformations will be one of the essential pieces of the 4DDSim. Further, this data will be also used to characterise the tumour motion as will be explained in the section (6.2.0.4.)
By virtue of being images from the same modality of imaging, the DIR was performed using a sequence of two registration stages, both for a B-Spline function with a regularisation (or smoothness) factor of 0.005 and using as cost function metric the mean squared error (MSE).

The bin 0 was defined as reference bin and set as fixed image, the others bins were defined as moving images. Due to the configuration defined during the image reconstructions, the bin 0 corresponds to the end-exhalation breathing phase.

b) Image registration: MRI$_{bin-i}$ - CT

Because the DIR is a much more complex procedure, which is as consequence of the multi-modality images, an iterative process was performed to determine a better strategy to register CT to MRI. As first approach, the multi-modality registration was performed with the aim to obtain a CT$_{MRI}$, i.e, the planning-CT deformed to match with the MRI's anatomy in each of the bins, and to propagate the contours from the planning-CT to the MRI dataset. Alternative methods, as DIR CT to MRI$_{bin-0}$ and subsequent registration between MRI-bins will be scope of a further investigation.
Several problems were faced during the DIR, such as the influence of the MRI's artifacts in the registration process and the different origins of the CT and MRI-cubes. The latter, due to the requirement of the initial stage of the DIR of a minimum overlap between the two images. This alignment was performed through the rigid registration of the bony anatomy and the resulting images were used as input to the DIR.
With respect to the image artifacts, background noise and B1 field inhomogeneity, the MRIs were cropped to the 4DCT size in order to exclude them from the DIR. Additionally, this process will permit the propagation of the structures set between the images, which requires the same image size.
Different deformable registration attempts, using different parameters, algorithms and metrics were performed. The better DIR result was obtained using mutual information as similarity metric, a sequence of two stages of a B-Spline function, a histogram equalisation in 400 levels and a very small regularisation factor 0.5E^{-5}.
The DIR was performed for each of the bins as fixed-image and the planning CT as moving image. Thus, the obtained warped (i.e. transformed) image corresponds to the CT$_{MRI}$ for each of the bins.
Some of the bins from the obtained 4DCT$_{MRI}$ were co-registered to crosscheck if the motion information from the 4DMRI was kept. The reference bin was considered the bin 0, CT$_{MRI-0}$. This registration was performed using the procedure described in the previous section.
Additionally, the inverse registration, planning-CT as fixed-image and MRI$_{bin0}$ as moving-image, was calculated to allow the propagation of the contours from the planning-CT to the reference MRI bin (see section 3.1.2 for details about the transformation process).

6.2.0.4 Motion characterisation

The extracted vector fields from the registration MRI$_{bin-ref}$-MRI$_{bin-i}$ were used to quantify the median motion inside the ITV for each of the sessions (full and partial reconstructed). The used ITV corresponds to the propagated VOI from the planning-CT to the MRI$_{bin-ref}$.
The obtained results were compared with the 4DCT vector field length.

6.2.0.5 Generation of 4DCT$_{MRI}$

As previously described, the fact that no information regarding the electron density in the MRI is available, this is solved through the use of multimodal DIR between each of the MRI bins and the planning CT. However, this 4DCT$_{MRI}$ was obtained from the phase sorting of the k-space centre that doesn't correspond directly to the breathing motion. As compared to the 4DCT acquisition protocol, in which an external surrogate (e.g. pressure belt) is used, in this 4DMRI acquisition any breathing signal is measured. The phase information is required when giving the 4DCT$_{MRI}$ as input to TRiP4D, in order to organise the CTs$_{MRI}$ bins within the breathing cycle (0%Ex to 0%In).
The strategy adopted to overcome this issue was to use the cranio-caudal motion of the liver as surrogate signal. Hence, the vector fields obtained from the DIR MRI$_{bin-ref}$-MRI$_{bin-i}$ were evaluated inside the liver for the z-component. The bin 0 was defined as 0%Ex and the corresponding bin to the maximum median length of the vector was defined as 100%Ex. All the others bins, were linearly normalised to this range considering their median vector length in z.

6.2.0.6 Plan optimisation

In order to discard inaccuracies arising from the CT$_{MRI}$ creation and propagation of structures, new treatment plans using the TPS TRiP98 were optimised for the CT$_{MRI-0}$, i.e. 0%Ex state and respective transformed contours. The optimisation was performed using the same particle, prescription dose and beam geometry of the original Syngo plans. The settled goal was to cover the PTV with the prescription dose while keeping the OARs constraints.
In order to obtain comparable results, using the same OARs constraints a new plan was also optimised in TRiP98 for the 4DCT$_{0\%Ex}$.
These new optimisations were only performed for the sorted raw images, while for the GD-corrected images the original Syngo optimised plan was used.

6.2.0.7 Time resolved dose calculation

4D dose calculations were performed using the TPS TRiP4D for the respective patient's surrogate-breathing signal acquired with Anzai during the immobilisation day, in an analogue process to the 4DDSim described in the section (5.2.2).
The irradiation temporal patterns were generated using the same procedure of the chapter (5.2.2) but for this plan CT$_{MRI-0}$-optimised and also considering five different interplays as result from a successive temporal shift of the starting phase of 500ms. The reference image was defined as the CT$_{MRI-0}$ and considered a relative amplitude sorting of the bins (see chapter 3.1.2 for details).
For all the patients, using the CT$_{MRI}$ raw images, the 4DDSims based of the 4DCT and 4DCT$_{MRI}$ were performed using the TRiP-optimised plan and compared with the static case. Additionally for patient H13 and H15, 4DDSims using the original Syngo® RT treatment plan and the CT$_{MRI}$ GD-corrected were performed.

6.3 Results

6.3.1 Deformable image registration: $MRI_{bin-ref}$ - MRI_{bin-i}

The summary of the evaluation of the DIR $MRI_{bin-ref}$-MRI_{bin-i} is shown in the table (6.2).
The obtained transformed image and vector fields showed satisfactory results, i.e. JD close of 1, small ICE and absolute differences. Therefore the corresponding vector fields were used for the 4DDSim calculations.

Table 6.2: Deformable image registration evaluation for the fixed bin 0 and the moving bin 10. The quantitative parameters were the determinant of the Jacobian matrix (JD), inverse consistency error (ICE), absolute difference between the reference image (bin 0) and the transformed image. The presented values correspond to the mean and standard deviation.

MRI_0-MRI_{10}		**H13**		**H14**	**H15**	
Parameter	VOI	Session 1	Session 2	Session 1	Session 1	Session 2
JD	Body	1.0±0.1	1.0±0.1	1.0±0.0	1.0±0.1	1.0±0.1
	Beam Path	1.0±0.1	1.0±0.1	1.0±0.0	1.0±1.0	1.0±0.1
	ITV	1.0±0.1	1.0±0.0	1.0±0.0	1.0±0.0	1.0±0.0
ICE (mm)	Body	0.3±0.6	0.4±0.7	0.2±0.3	0.4±0.6	0.7±1.1
	Beam Path	0.2±0.2	0.2±0.2	0.1±0.1	0.1±0.1	1.0±0.2
	ITV	0.1±0.1	0.1±0.1	0.1±0.1	0.1±0.1	0.1±0.1
Abs.Diff (voxel value)	Body	6.0±14.6	6.5±15.6	1.8±5.2	2.9±7.5	4.5±10.1
	Beam Path	18.6±18.1	17.5±17.4	4.0±5.1	10.2±9.7	12.1±11.7
	ITV	11.7±12.0	12.6±11.8	2.4±2.4	7.6±6.9	9.6±10.1

6.3.1.1 Motion evaluation

For the set of vector fields, the median vector length inside the propagated-ITV to the reference bin, ITV_{bin0}, was evaluated. Figures 6.5, (6.6) and (6.7) show the results of the three patients in each of the imaging sessions and reconstruction method (full and partial) comparatively to the 4DCT analysis. In all the cases the phase sorting was based on the z-component of the median vector field length inside the liver.
Relatively to each of the vector components, the cranio-caudal direction showed to correspond to the main motion direction, with the anterior-posterior direction showing amplitude below 1 mm and the lateral direction neglected. The details for each imaging session are available in the appendix, figures (A.14) to (A.16) .

The case of patient H13 is an interesting example that justifies the need to include the irregular behaviour of the breathing amplitude when performing 4DDSim. In this case, the average breathing along the 8 min of the 4DMRI for both sessions fairly matches with the information of the 4DCT, however, the partial MRI data shows a variation of its breathing amplitude along the acquisition. This result is also confirmed when looking for its radial spokes magnitude of one of the sessions, shown in the figure (6.2). Nevertheless, the fact that the partial data shows smaller amplitude compared with the full reconstruction is not yet clear. This might be related with the reconstruction method or with lost of motion information when less spokes per bin are used. This issue will be investigated in a future study, through the adjustment of the reconstruction parameters and improvement of the DIR quality.

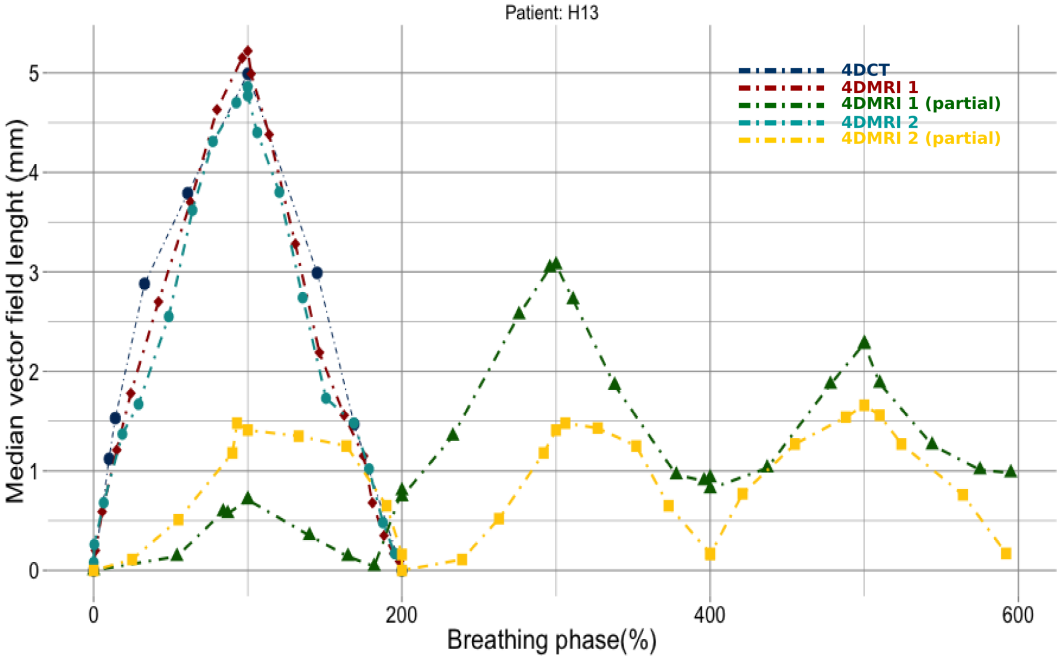

Figure 6.5: Median vector field length inside the ITV per breathing phase for patient H13 for the 4DCT, 4DMRI sessions 1 and 2 using the full or partial raw data for the image reconstruction.

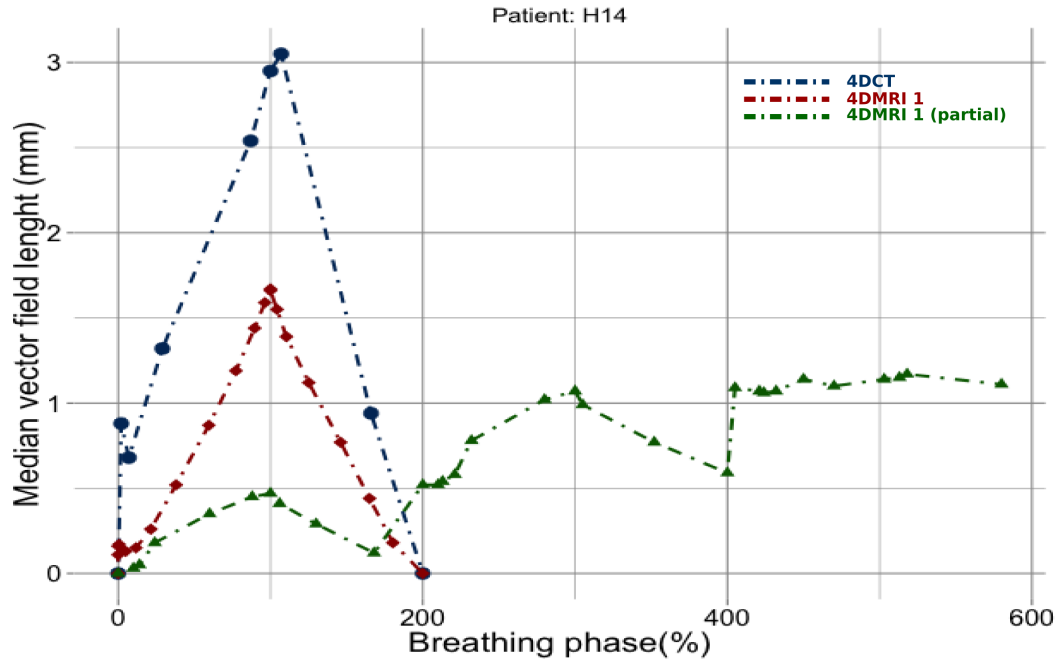

Figure 6.6: Median vector field length inside the ITV per breathing phase for the patient H14 for the 4DCT, 4DMRI session 1 using the full or partial raw data for the image reconstruction.

Another meaningful example is the patient H15, figure (6.7), in which the detected motion amplitude of the 4DMRI in the session 1 was twice larger than the 4DCT. Also the patient H14 showed an irregular behaviour, with a mean difference of 1.5 mm between 4DCT and 4DMRI sessions. For this patient, it was also detected that for the third part of the acquisition time (fig.6.6), although the liver showed a z-component of motion, the pancreas itself showed reduced motion. This aspect justifies the need of an internal

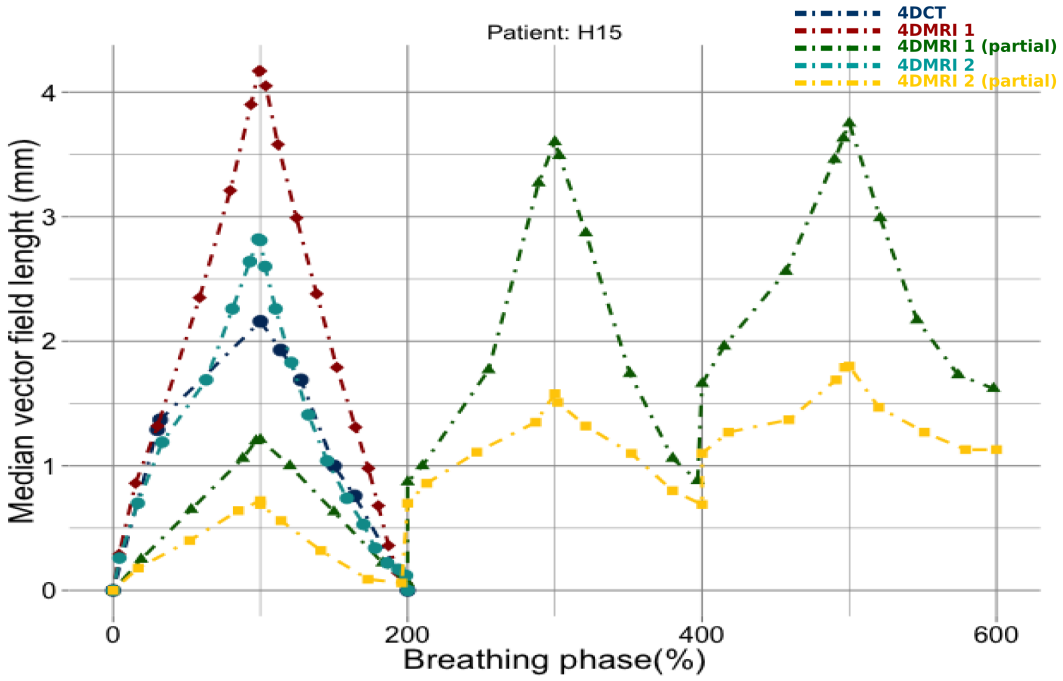

Figure 6.7: Median vector field length inside the ITV per breathing phase for patient H15 for the 4DCT, 4DMRI sessions 1 and 2 using the full or partial raw data for the image reconstruction.

motion detection for pancreatic patients.
In conclusion from the analysis of these three patients, it is suggested that the breathing induced tumour motion is susceptible to daily variability. However, this investigation should be enlarged to include more patients and more imaging sessions per patient.

6.3.2 Deformable image registration: MRI$_{bin-i}$- CT

As result of the deformable image registration the transformed CT, the so-called CT$_{MRI}$, was evaluated by visual inspection, as shown in the example of the figure (6.8). The consistency of the vector field was also quantified by the JD and ICE and is shown in the table (6.3).

Table 6.3: Evaluation of the multi-modality DIR quality in terms of the determinant of the Jacobian matrix (JD) and the Inverse consistency error (ICE) for the bin 10 in the full reconstruction.

CT$_{MRI-10}$-MRI$_{10}$		**H13**		**H14**	**H15**	
Parameter	VOI	Session 1	Session 2	Session 1	Session 1	Session 2
JD	Body	1.1±0.2	1.0±0.1	1.0±0.2	1.1±0.2	1.1±0.2
	Beam Path	0.9±0.1	0.8±0.1	0.5±0.1	0.8±0.1	0.8±0.1
	ITV	1.0±0.2	0.8±0.2	0.6±0.2	0.9±0.2	0.8±0.1
ICE (mm)	Body	11.8±7.2	21.6±10.7	32.2±22.8	14.3±9.6	11.7±7.9
	Beam Path	10.3±3.6	12.3±3.8	27.9±9.8	15.7±5.7	14.3±3.8
	ITV	10.4±4.1	14.0±4.1	38.7±14.1	12.5±7.0	12.4±5.3

From these results, the judgement about the quality of the registration is straightforward, since JD and ICE showed higher values. The ICE value that for this case is in average 18.3 mm, for the body VOI, compared to the CT-CT DIR of 0.4mm, which deserves special attention. This high value implies that the correspondence mapping

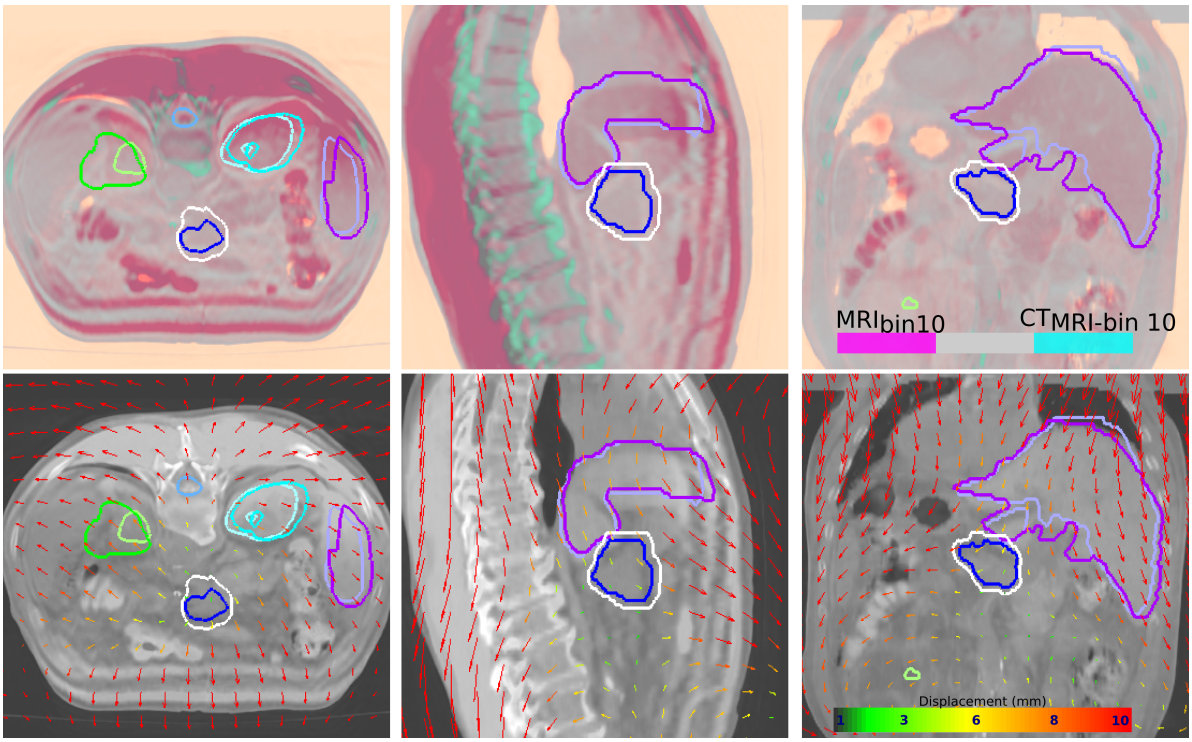

Figure 6.8: Visual inspection of the DIR MRI-CT for the example of the patient H13, 1^{st} session for the bin 10. Upper images show the *false colour* comparison between the original MRI-bin10 and the transformed planning-CT, i.e. CT_{MRI-10}. From this overlay some mismatch between the two images (i.e. blue or pink colour) is detected, which is however small in the central body region. Structures of the original planning-CT and CT_{MRI-10} are also superimposed. Kidneys and liver are represented by the light colours for the original VOI and by the dark colours for the propagated to the bin 10. ITV_{bin10} is represented in white and CTV_{bin10} in dark blue.

between the pair of images is not consistently pointwise, hence the inverse vector field won't result in the same initial image. This effect can be a consequence from the registration algorithm used which wasn't able to match the patient's surface between the two images and a small regularisation parameter was used.
Another method to evaluate the registration quality is through the overlay of the transformed structures into the transformed image. This because the structures are transformed through the inverse field while the CTs_{MRI} are generated by the forward vector field. From this analysis the same conclusions were obtained, i.e. a good agreement in the pancreas volume and larger differences were noticed in the periphery of the patient's body.

6.3.2.1 Propagation of contours

Another method to access the quality of the registration is through the evaluation of the location of the propagated contours.
For all the MRI-sessions the contours of the planning-CT were transformed by the respective vector field to the MRI_{bin-0}. One example is shown in the figure (6.8) in which the original contours of the OARs (light colours) are superimposed to the transformed OARs.
For some sessions the agreement with the OARs contours with the OARs visible in the CT_{MRI} was acceptable, as the shown example, while for others the reduced con-

sistency of the inverse field in the periphery of the patient's body result in a lack of a disagreement between the contour and the anatomy.

6.3.2.2 Generation of 4DCT$_{MRI}$

By visual inspection of figure (6.8) the agreement between the MRI and the CT$_{MRI}$ is acceptable in the VOI region. However, when comparing the CT$_{MRI}$ with the original planning CT, as shown in the figure (6.9), a deformation in the patient surface is observed.
This effect is a result of the geometric difference observed in the MRI, particularly larger for the most distant voxels from the centre of the image, and anatomical differences between the MR and CT sessions. The obtained CT$_{MRI}$ transported these effects, however, this effect shouldn't affect the results since the plan was optimised to the CT$_{MRI}$ image and respective structure set. Namely, since all the images are deformed in the same manner, the geometrical relationship is kept and the optimised dose to the CT$_{MRI}$ can be used for 4DDSim.
The extracted motion vector between each CT$_{MRI-i}$, for the bin i, and the CT$_{MRI-0}$ compared to the vector MRI$_{bin0}$-MRI$_{bin-i}$ showed to conserve the major component of the motion. From the evaluation of a subset of 4 bins (3,7,12,17) the average differences between the median vector fields length were of (-1.7$\pm$1.1) mm, with the magnitude of the vector field MRI$_{bin0}$-MRI$_{bin-i}$ always smaller and showing larger deviations for the registrations with higher ICE value.

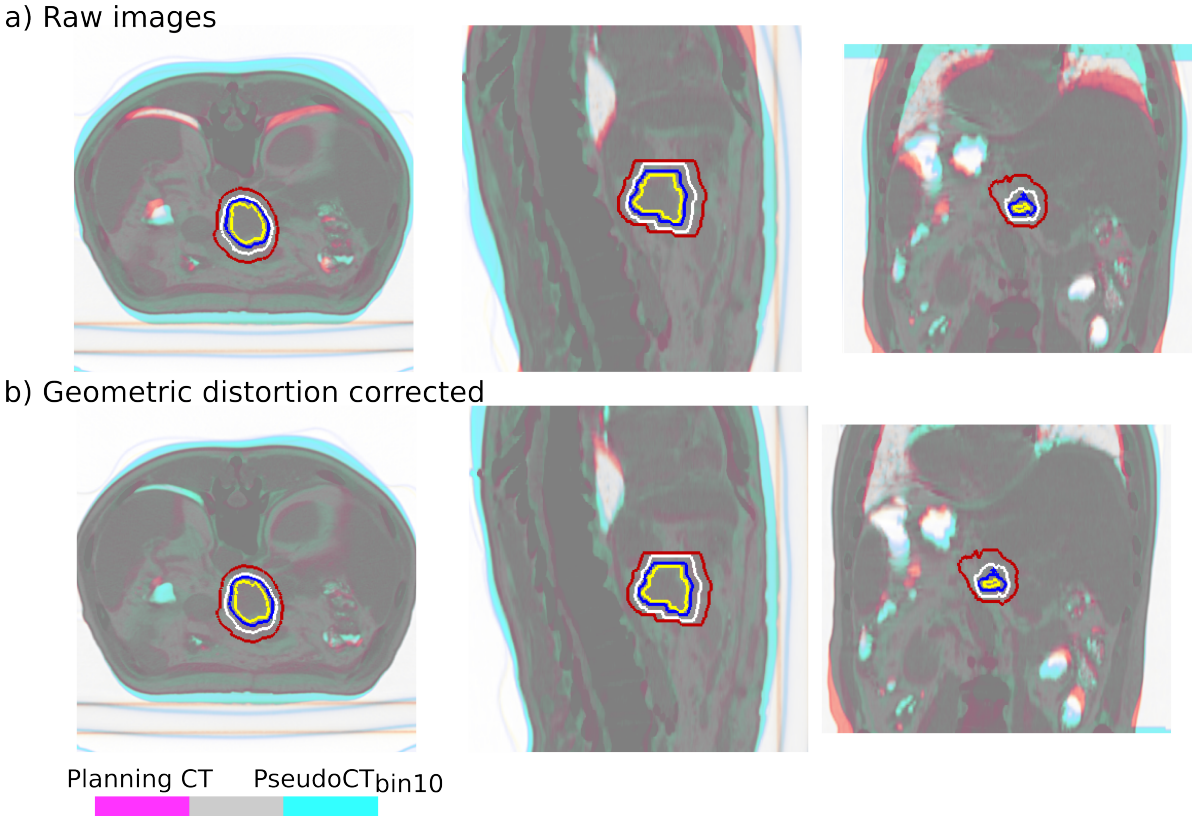

Figure 6.9: Overlay of the planning CT with the CT$_{MRI-10}$ for patient H13 in which the differences in the patient's external surface are visible, for the case of the raw images. Using the geometric distortion correction the differences are minor.

6.3.3 Dose calculation

The results of the 4DDSim for each imaging session is shown in the figure 6.11. All the plans that gave origin to these results were optimised using the same constraints and using TRiP and showed an MI of 1.7$\pm$1.3, with the highest value for the patient H14 (MI of 3.2) and with minor differences among the different plans of the same patient.

Unexpectedly the patient H14, which shows a small motion amplitude, demonstrated

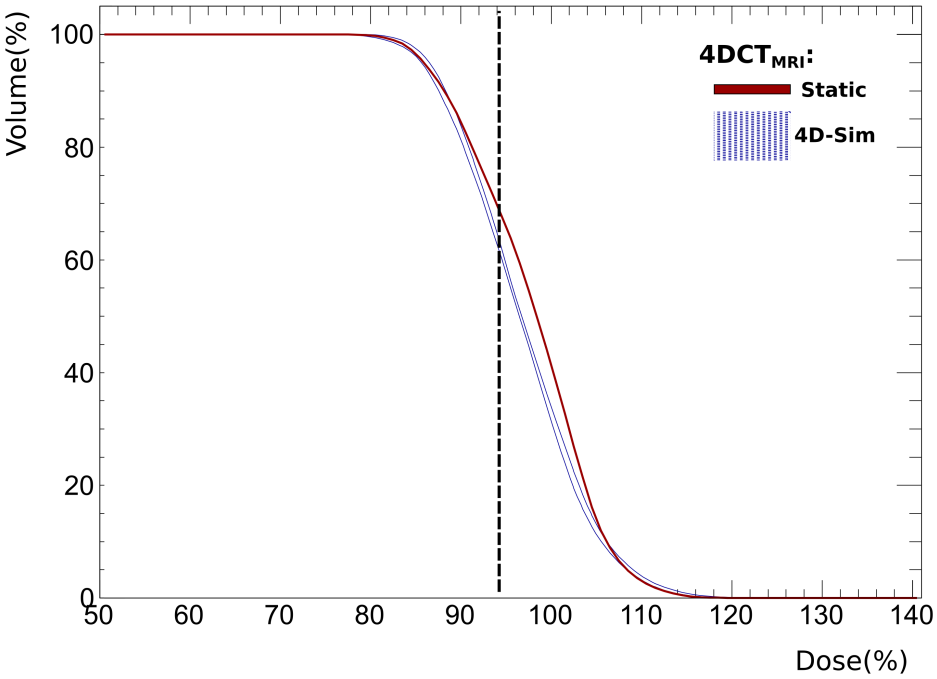

Figure 6.10: CTV Dose Volume Histogram of the patient H14 in the static case (red line) and in the set of 4D dose simulations (blue band).

ΔV95% superior to 5%, however when evaluating the H$_{CTV}$, as in the figure 6.11-b, or the median dose (3.9$\pm$0.05 Gy (RBE)/fx) no significant differences were found. An interpretation of these results is suggested when the DVH$_{CTV}$ for the static and 4DDSim dose distributions are compared (figure 6.10). In order to spare the OARs, the CTV is not completely covered by the prescription dose and the DVH$_{CTV}$ got a broad shoulder in the V95 region, resulting in a strong difference, that is not significant in terms of plan quality.

Relative to the patient H13, which shows the same breathing amplitude for the 3 sessions (CT, MRI-1,MRI-2), no strong differences were detected. Patient H15 showed consistent 4DDSim results using the 4DCT data with this new optimisation and the optimised by Syngo-RT. Relative to the 4DDSim using the 4DCT$_{MRI}$ minor deviations in the V95$_{CTV}$ were found as consequence of the small target motion (below 5 mm).

Regarding the dose calculation using the original Syngo® RT plan, the results are summarised in figures (6.12) and (6.13). For both patients, H13 and H15, differences in the target coverage between imaging sessions are shown, pointing again for the need of more imaging data to accurately assess the impact of intra-fractional motion in pancreatic patients.

Figure (6.14) shows the dose distribution for the patient H13 using the GD-corrected CT$_{MRI}$ in the static and 4DDSim situation. Differences between the static dose distribution in the CT and CT$_{MRI}$ result from changes in the patient 's anatomy between

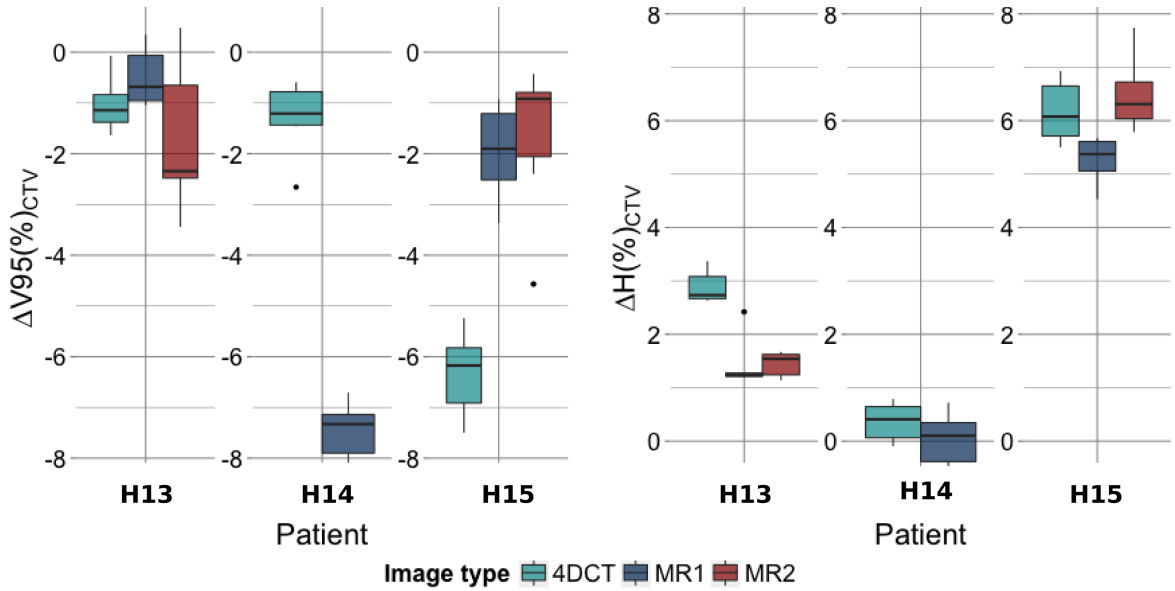

Figure 6.11: Changes of $V95_{CTV}$ and homogeneity of the CTV relative to the static case for the patients imaged with 4D-MRI and 4DCT as result of a set of five 4D dose simulations with different breathing starting phases.

sessions and therefore related with inter-fractional changes.
The differences between these 4DDSim and the previous cases (CT_{MRI} optimised) are the result from the different delivered plans and from the anatomy changes in the beam entrance as result of the geometric correction. However, the same order of differences were detected for the some cases (e.g. patient H13 session 1 and patient H15 session 2). Further investigations still need to be conducted, with the aim to understand the main reason for the differences, how the 4DDSim changes with the MRI reconstruction parameters, and which is the impact of the surrogate signal in the calculation.

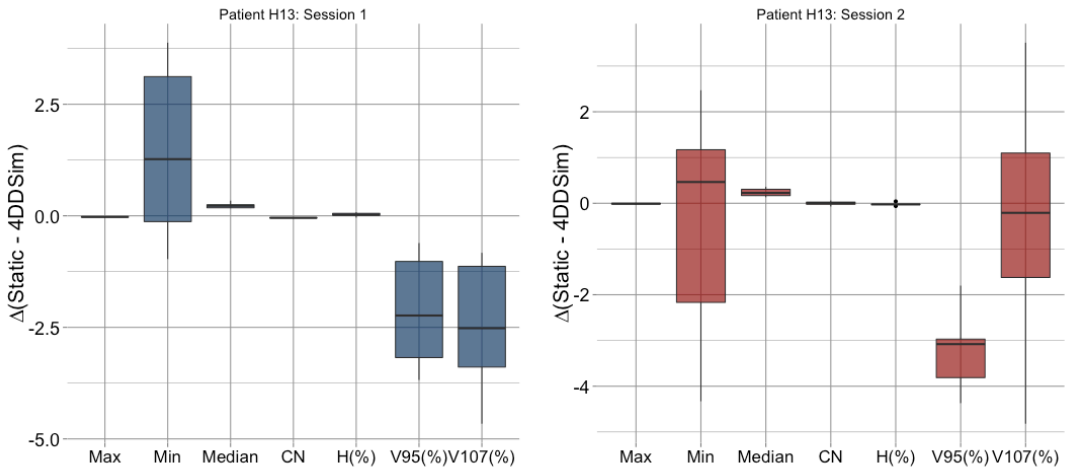

Figure 6.12: Variation of the plan evaluation parameters between the static and the 4DDSim situation for patient H13 using the GD-corrected MRI data of the sessions 1 (blue boxes) and 2 (red boxes). CTV maximum, minimum and median dose are in Gy (RBE) and the homogeneity, V95 and V107 in percentage of differences.

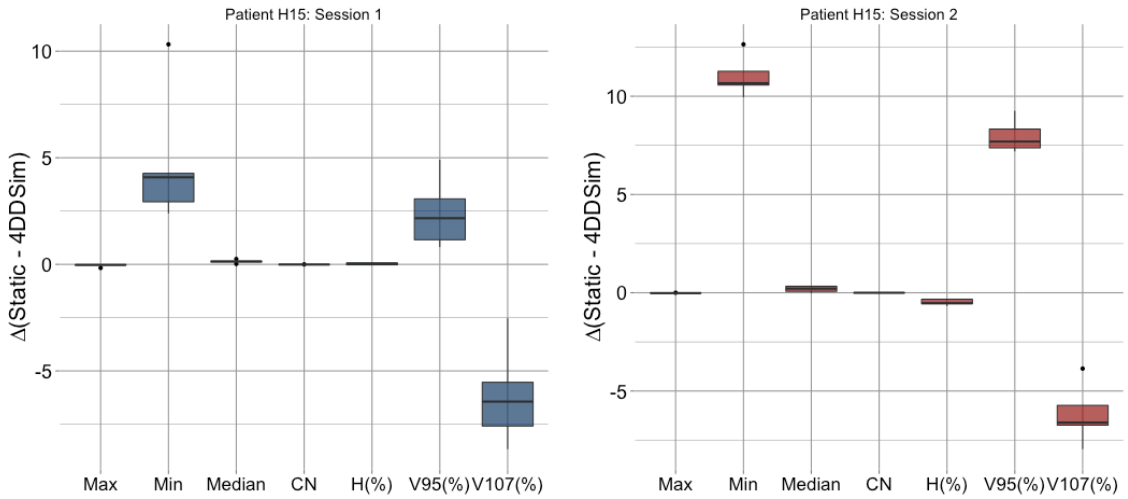

Figure 6.13: Variation of the plan evaluation parameters between the static and the 4DDSim situation for patient H15 using the GD-corrected MRI data of the sessions 1 (blue boxes) and 2 (red boxes). CTV maximum, minimum and median dose are in Gy (RBE) and the homogeneity, V95 and V107 in percentage of differences.

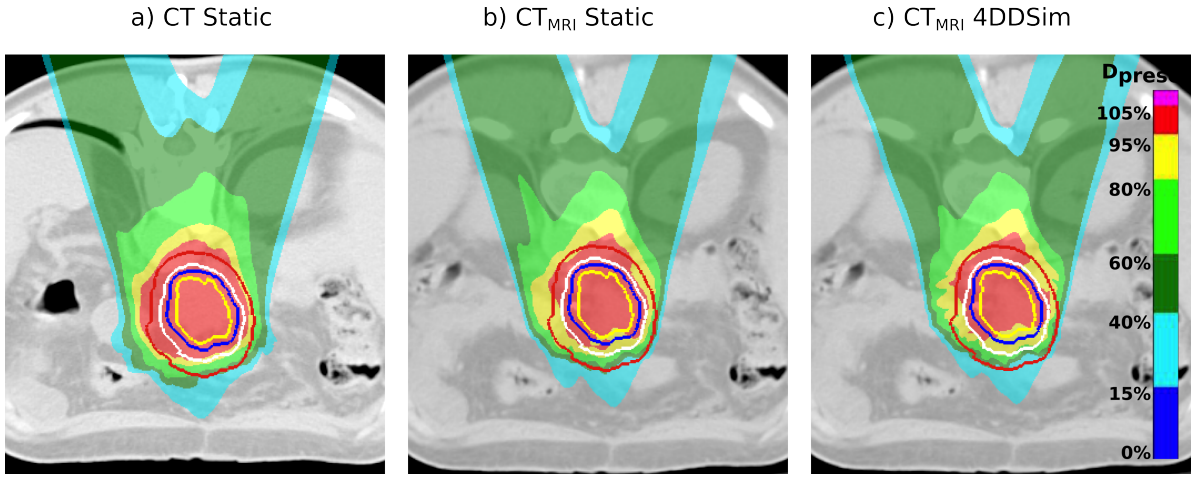

Figure 6.14: Transversal view of the dose distribution for patient H13 in the CT and CT$_{MRI-0}$ static case and in one of the 4DDSim scenarios. GTV, CTV,ITV and PTV are represented in yellow, dark blue, white and red, respectively.

6.4 Summary and discussion

Many approximations were performed in this first approach to the use of MRI for the purpose of 4D dose calculations. However, it becomes clearer which are the main issues to be aware of and which alternative approaches might be worthwhile investigating. Starting from the reconstruction of the 4D-MRI, the used method MoCo-HDTV showed significant improvement of the image quality in terms of reduction of artifacts. An important advantage of this reconstruction method is the definition of a large bin number, without significant reduction of the image quality and the option to split the raw data in intervals. This last point is of major importance to monitor baseline shifts and intra-fractional variations. It also offers more options of sorting modes that would improve quality of motion data and might open a new era to explore detailed motion sampling. However, this algorithm is still slow and the results are not available directly after the

imaging session, at the current stage.
Concerning the generation of the 4DCT$_{MRI}$, another method to evaluate is to reduce the number of multi-modality registrations, by just transforming the planning-CT to the MRI-bin 0 and then creating a set of 4DCT$_{MRI}$ transforming this CT$_{MRI-0}$ to each of the bins using the MRI-MRI registration vector fields. This method might reduce the uncertainties from consecutive multi-modality registrations, as the detected geometric differences of the MRI compared to the CT.
The use of an external surrogate signal, as a pressure sensor, is an alternative to test and evaluate differences in the dose distribution when using different breathing signals. Also the influence of the artifacts in the MRI needs to be well defined, mainly the geometric distortion and susceptibility effects, that might cause position errors of several millimeters. The reduction of these effects, will later allow the direct forward calculation of the dose in the 4DCT$_{MRI}$, that is the main scope of this technique. Therefore, the variability of the intra-fractional motion, that can be obtained from the partial data reconstructions, can be included in the 4DDSim calculations. This will result in a 4DDSim based on multiple breathing cycles instead of an average cycle (current procedure).
In conclusion, the clinical implementation of 4D-MRI as a tool to determine uncertainties in the dose delivered to the tumour is a feasible approach. To include it in the clinical workflow, minor changes need to be done, since the same patient's positioning is possible, the scanner location is close to the therapy rooms and the acquisition of a time resolved MRI is achievable in a session of 30 min (including positioning). The image processing and reconstruction need to be automatised and the major challenge still resides in a deformable image registration for inter-modality matches, with less artifacts and higher accuracy.
This technique will furthermore allow to include the follow-up MRI of the patient and an adaption of the target contour along the treatment, without additional image dose to the patient. The data can be also used to improve the treatment robustness through the sampling of the probable range uncertainties and further inclusion in the treatment planning process.
Additionally, this can be used as a method to categorise the patient in terms of breathing pattern robustness. The evaluation of the consistency of the correlation between breathing signal and the pancreas internal motion, the variability of the breathing amplitude and frequency will help in the definition of the patients requiring more monitoring and mitigation strategies during the irradiation.

Chapter 7

Discussion and conclusion

The Heidelberg Ion-Beam Therapy Center (HIT) started in 2011 to treat moving targets, in particular hepatocellular carcinomas. Nevertheless, the clinical implementation to treat pancreatic patients isn't a straightforward procedure, since the different tumour location and the distinct anatomical variations along the treatment course will compromise the planned treatment differently. Therefore, a pre-implementation phase was conducted between 2013 and 2014, in which both inter- and intra-fractional aspects that might affect the plan quality were evaluated.
Since 2014 twenty pancreatic patients using the scanned beam system at HIT were irradiated. In the course of this thesis, the delivered dose for those that have follow-up data was assessed. These results were analysed in a way to get conclusions that might lead to an improvement of the treatment for future patients.

Inter-fractional variability

The challenging anatomical location of the pancreas, surrounded by hollow organs (bowel and stomach) makes its irradiation highly sensitive to inter-fractional variation. By using daily cone-beam imaging and fiducial markers Horst et al. (2013) detected mean variations of the pancreas center-of-mass (COM) along the treatment of (9.4$\pm$4.8) mm. Additionally, the authors stated that based on the intra-fiducial markers distance a small deformation of the organ was observed. This disagrees with the measured COM variation quantified in this thesis using contours delineated by physicians (1.8$\pm$1.3) mm. This contrasting finding is related with the used method to quantify the inter-fractional tumour motion. The lack of contrast in the weekly CT imaging reduces the physicians ability to detect the tumour margins accurately, a fact that is not present when fiducial markers are used for motion assessment. Jayachandran et al. (2010) looked for this issue and quantified that the mean shift to apply to the patient based just on bony landmarks or on additional fiducial markers differs in a mean vector length of 5.5 mm.
While in photon therapy these changes of the tumour and surrounding organs in the beam path can be overcome with the use of margins, with minor changes in the target coverage, Liu et al. (2012a) obtained a $V_{100\%CTV}$ of (97.8$\pm$ 3.7)% along the treatment using a simple 3 mm expansion of the CTV. In contrast to that, the irradiation with charged particles is vastly affected by changes in tissues densities in the beam path (Lomax 2008b). Even with a 5 mm geometric margin applied to the CTV, its coverage ($V_{95\%CTV}$) might decrease by up to 30% depending of the used beam's configuration. The analysis for the different beam's incidences and margins showed improve-

ment in the target coverage for the combination of a geometric ITV margin of 3 mm and two oblique beams coming from the patient's posterior direction, i.e. $V_{95\%CTV}$ of (99.5±1.2)%. The statement regarding the required CTV-margin was confirmed by the calculation of the WEPL variations per beam direction for this set of patients. The calculation of the ITV_{WEPL}, including the full weekly-CT data, revealed that a symmetrically CTV-expansion of approximately 2.5 mm is sufficient to conserve the $V_{95\%CTV}$ for 75% of the fractions when two posterior oblique beams are used. In case that a different beam angle is selected, the ITV_{WEPL} calculation suggested the need of an asymmetric expansion in depth, in average larger in the proximal direction. For all the beam angles symmetric margins in lateral and cranio-caudal direction can be kept.

In relation to the obtained results, Park et al. (2012) already discussed the design of beam-specific PTV in terms of distal and proximal margins, considering the radiological path length variations. The author stated that for a homogeneous medium the beam-specific PTV will be close to the conventional PTV, which was confirmed using the method presented on this thesis that considered the specific WEPL variation along the treatment course of each patient per beam direction. This approach was performed per beam and the optimisation method (SFO or IMPT) wasn't considered. This is especially meaningful when IMPT is performed and the dose delivered by each beam might be inhomogeneous. However, considering the ITV_{WEPL} per beam and the results from chapter (4.1) that multi-beams tend to be more robust against inter-fractional changes, the resulting ITV_{WEPL} will be smaller. Moreover, this is a population-based approach in contrast to an individualised patient assessment, which would be only possible from multiple imaging sessions.

An alternative to this population-based method is to perform a weekly adaption of the ITV along the treatment though inclusion of the updated imaging information (either CT or MRI).

Hence, the patients started being treated at HIT using usually two oblique posterior beams, an ITV margin to include intra-fractional motion, and a margin to account with set-up errors and range uncertainties of 5-7 mm. The evaluation of eleven patients showed similar results, with a mean $V_{95\%CTV}$ of (2.0±2.9)% with 77% of the fractions showing a $V_{95\%PTV}$ reduction below 3%. As expected, the bowel, located distally to the beam entrance, was the main normal organ at a risk of injury from the result of the pencil beams over-shooting due to the density changes in the beam path. Already Kumagai et al. (2009) has already pointed towards the vulnerability of the gastrointestinal tract to density changes and a consequent decrease of the target coverage and increase of the intestine doses.

Of particular interest for the analysis of this dataset was the detection of seven fractions showing a $V_{95\%CTV}$ superior to 3%. This justifies the need of routine monitoring of the patient anatomy, even when a statistically robust beam configuration is applied, but no robust optimisation is performed. Therefore, a method to define an adaptation point was delineated based on the measurement of the water-equivalent path length variation (∆WEPL) between successive CTs. Also Matney et al. (2016) evaluated a similar method but in the context of the respiratory motion in proton therapy for lung patients, in which the ∆WEPL was used to guide the selection of the beam angles in the reduction of intra-fractional changes.

In the concept defined here the accumulated WEPL variations (∆accWEPL) in BEV were quantified through the percentage of voxels with absolute differences superior to 3 mm(PV_{in}). This simplified approach showed to be sensitive to anatomical variations, which are then translated into changes in the dose distribution. These changes might

result in the tumour over- or under-shooting as well unwanted dose to the OARs. The correlation between the ΔaccWEPL, the $V_{95\%}$ and the gamma criterion (as metric of the three-dimensional dose distribution variations) was shown to be affected by the number of beams and optimization technique. The clinical evaluation of this procedure to the patients treated at HIT, showed similar results to the previous analysis performed for an independent dataset and using single beam's incidence. In conclusion, a list of tolerance and action levels was suggested when evaluating the accWEPL differences, in terms of PV_{in} values, to support in the decision of the re-planning or continue the treatment with the original plan.
Right now this method just intends to decide when a plan should be re-optimized. However, it has potential to be extended to a plan of the day strategy, since it can guide the selection of the most suitable daily beam geometry from a pre-calculated library of plans.
Not many methods are found in the literature to perform plan adaption in ion therapy, which is a consequence of the complexity of the process. As possible techniques, Chen et al. (2015) suggested the creation of an offline library based on different planning-CTs, Kurz et al. (2016) investigated the use of in-room CBCT to perform a new plan optimization, while Wang et al. (2016) looked for the application of proton radiography to quantify anatomical changes.

Intra-fractional motion impact

Additional to the variability of the patient anatomy between treatment sessions, during the treatment itself the tumour is subject to motion induced by the breathing and peristaltic movements of the stomach and bowel. The breathing motion is considered the main source of movement and consequently the surrogate signal at HIT uses this for monitoring.
In terms of motion quantification, for the two sets of patients no significant differences were found, despite the different positioning, with the patients in supine showing CTV changes along the 4DCT of (4.1$\pm$2.7) mm in superior-inferior (SI) direction and the set of prone patients with (4.8$\pm$2.7) mm. Solla et al. (2013) used also the 4DCT but with fiducial markers for the motion assessment, which resulted in a larger motion amplitude of 8.5$\pm$ 4.2 in SI. This result is again justified by the poor soft tissue contrast of the 4DCT. Tai et al. (2013) measured the pancreas motion by just relaying on the 4DCT data and obtained (5.9 $\pm$ 2.8) mm in SI, i.e. closest from the one measured for this thesis dataset.
The quality of the dose distribution using scanned delivery is pointed out as an advantage in the sparing of OARs compared to the passive delivery (Shiomi et al. 2016). However, the appearance of the interplay can decrease this beneficial impact (Bert, Grözinger, and Rietzel 2008).
A first estimation of the interplay impact in pancreatic irradiation was performed, based on a set of patients previously irradiated with photons (dataset B), no strong impact was detected if the dose is delivered through the use of posterior beams to the patient. Later, for the patients irradiated at HIT (dataset H) the 4D dose distributions were simulated and reconstructed. From this second analysis six out of fourteen patients showed at least one fraction with $V_{95\%CTV}$ differences, relative to the static case, superior to 10%. On the other hand, the dose heterogeneity increased from an H_{CTV} of 15.9$\pm$7.5 to 27.8$\pm$8.5. These contrasting results might be associated with different factors as: (1)

larger number of patients included in the dataset H; (2) superior number of patients exhibiting a CTV motion length larger than 5 mm; (3) dose distribution in the original plan already compromises the target irradiation due to the OARs constraints and therefore the $V_{95\%}$ corresponds to a more steep DVH region; (3) optimisation strategy adopted by the clinical TPS different of the one from the research-TPS, used in the dataset B.
With respect to the optimisation strategy, the plans were evaluated in terms of dose modulation with the aim to correlate it with the dose degradation under motion. Lomax (2008a) suggested that IMPT has a potential for delivery with larger range and patient setup uncertainties compared to the SFUD, a consequence from the three-dimensional variation of the beam fluence. Moreover, the TPSs can reach different solutions that might lead to similar dose distributions and otherwise. Therefore, this impact would be larger or smaller depending on the optimiser strategy and the defined constraints.
This justified the reduction of the plan robustness to the intra-fractional motion in the dataset H comparative to the dataset B, which resulted from different TPS optimisations and different number of constraints. In the optimisation of the plans of the dataset B, just four constraints were used and defined in terms of maximum dose to the OARs, while for the dataset H the plans included, in general, a complete IMPT optimisation using a larger set of OARs constraints, either maximum and dose-volume constraints. Additionally, Syngo® RT and TRiP98 use different optimisation algorithms and, therefore, the obtained dose distributions from the two optimisers are different in terms of modulation.
Webb (2003) suggested, in the context of IMRT, that the modulation of a plan should be quantified, in order to understand how the TPS reached the solution, i.e. how the inverse optimisation is performed to get the final dose distribution.
In this thesis a Modulation Index (MI) adapted to particle therapy was used and showed a significant difference between the set B and H, with the plans from the set B, TRiP98 optimised, being more uniform compared to the Syngo® RT optimised, set H. Moreover, patients exhibiting higher MI and larger motion showed to be more susceptible to stronger interplay effects. Nevertheless, this parameter is not directly correlated with the delivered dose distribution, since this is dependent of other factors as breathing frequency and amplitude, intensity of the raster points miss-irradiated and change of patient anatomy. This MI just offers an additional information in order to quantify the probability of dose degradation as consequence of the interference between the beam and the patient's breathing and promises to help in the decision between similar dose distributions.
Additionally in order to mitigate the impact of the intra-fractional motion, strategies to improve the plan robustness must be added in the plan optimisation process. The main approachs under study are the worst-case robust optimisation (Liu et al. 2012b) or the probabilistic methods (Unkelbach et al. 2009).
Another aspect that is missing in this intra-fractional evaluation is the inclusion of variability in the patient internal motion, since no additional 4DCT is used.
Additionally, due to the used external surrogate signal no baseline drifting and amplitude changes of the tumour were included. Sharp et al. (2007b) found that phase delays between the internal and external motion and baseline drifting for liver patients with external surrogates would compromise the gated beam delivery. Hence, these aspects need to be quantified and considered in a further analysis.
In conclusion, the intra-fractional motion has the potential to compromise the dose distribution for some patients. Special attention to patients with large tumour motion should be taken and strategies to reduce its impact must be considered. Beam gating (Mori et

al. 2010) or rescanning (Bernatowicz, Lomax, and Knopf 2013) are the techniques with more potential to be used in the clinical routine at HIT, with beam gating already implemented for selected patients. However, both techniques have drawbacks that must be considered during their application. Beam gating introduces a correlation between the beam and the breathing, which will increase dose degradation if the residual motion is still considerable. Beam rescanning requires a lateral scanning and energy changing speed inferior to the motion periods to avoid coherence between the signal. Moreover, any of these techniques compensate for range variations, which need to be additionally incorporated in the treatment planning.
More demanding strategies, as online adjustment of the individual pencil beam energies (Cheung et al. 2012) or 4D-optimised beam tracking (Eley et al. 2014) are not accomplished with the current beam delivery system and TPS at HIT. These sophisticated 4D techniques need a dedicated quality assessment with a secure verification method of delivery, therefore these methods are currently not yet at a realisation stage for clinical facilities of ion-beam therapy.

Variability of the Intra-fractional motion

Zhang et al. (2014) investigated the motion of the pancreas during radiotherapy sessions and noticed that although the major component of the motion is in general in SI direction, i.e. breathing induced, random patterns were also detected in many cases. This justifies the need to inspect other sources of motion, as intestines and stomach peristalsis, and also the correlation between breathing and pancreas motion that might be rather correlated.
With this aim, 4D-MRI was evaluated as an approach to obtain more intra-fractional information and without increase the imaging dose to the patient. This first approximation used the multi-modality image registration MRI-CT to transfer the MRI-detected motion to the CT image. A similar approach was used by Boye, Lomax, and Knopf (2013) but based on volunteer data, and larger acquisition times in order to stablish a library of MRI data. The use of volunteer data has the advantage to obtain a larger sample but the physiological anatomy of the tumour and the surrounding tissues in pathological subjects is discarded. However, in both analysis different pancreas motion length among 4DCT and MRI sessions, as well amplitude variation along the acquisition of the 4D-MRI were detected. Also the 4D dose calculation exhibits the influence of the different breathing amplitudes and anatomy changes.
Bernatowicz et al. (2016) performed a comparison between the motion quantification population-based and subject-specific and concluded about a better accuracy of the subject-specific liver modelling, although population-based results can be used to improve the clinical workflow.
Despite the encouraging results, some important issues remain to be solved in order to improve the accuracy of the results. One of them is the multi-modality image registration MRI-CT that is still sub-optimal. To overcome it, Björkman (2016) suggested the calculation of pseudo-CT based on the MRI data, i.e., no deformable registration CT-MRI is performed and the MRI is directly transformed to electron density. This method has the potential to include with more accuracy changes in the patient anatomy, as tumour shrinkage/expansion, bowel and stomach density and shape changes, without relying in a pre-information of a CT image.
Concerning the detected geometric distortions, which in this analysis hindered the di-

rect forward calculation in the 4DCT$_{MRI}$, some studies have shown promising improvements (Huang et al. 2016) and phantom-based measurements have been done in the German Cancer Research Center in order to reduce this influence and will be used to improve the image correction.
Another issue, is the time required for the reconstruction of the 4D-MRI, which in a clinical workflow is unsuited. An alternative is 2D cine MRI, which was evaluated by Heerkens et al. (2014) for pancreatic patients and might provide support for online monitoring of the tumour and decision regarding the application or not of beam gating to a specific patient, however, without replacing the complete 4D-MRI information.

In conclusion, this thesis determined the main issues associated with the treatment of pancreatic patients using charged particles and suggested methods and solutions for their quantification and mitigation. All the defined strategies were designed, though, to be clinically feasible in the routine workflow at HIT, from the hardware and software perspective.
The combination of inter-fractional and intra-fractional sources of uncertainties demonstrated the potential to mask the clinical benefit of charged particles to treat this radioresistant pathology with low survival rate. Despite of that, simple strategies as selection of beam geometries, planning margins, motion monitoring and mitigation techniques can dramatically improve the dose distribution and consequently the patient outcome.

The key for a precise delivery of the treatment is the monitoring of anatomical changes, either in the scale of seconds or days, and prompt reaction in order to minimise or eliminate potential uncertainties. In future, it is expected that the methods suggested in this thesis, the experience gained at HIT on treating moving organs and, the developments in treatment planning and treatment delivery will allow us to move towards the robust plan optimisation, prediction of changes in the dose distribution and, to enable treatment without a constant and complex monitoring of the patient movement.

Abstract

Treatment Plan Robustness in Pancreatic Patients treated with Scanned Ion-Beam Therapy: Inter- and Intra-fractional Aspects

Pancreatic cancer is still an unsolved oncological challenge, however radiotherapy with charged particles has been considered a promising approach to improve the patients overall survival. These patients might benefit from dose escalation, although uncertainties during the beam delivery (intra-fractional) or along the treatment course (inter-fractional) can compromise the accuracy of the treatment.
In this thesis, inter- and intra-fractional anatomy changes are explored in order to define the potential source of uncertainties, quantify their effect, and to define strategies towards their reduction.
Anatomical changes along the course of the treatment showed to lead target underdosages up to 20% and an increase in the dose to the normal tissues. However, this can be lowered through the selection of beam arrangements from the patient's posterior side and beam-specific margins. From the results of this work, it was concluded that a combination of an Internal Target Volume (ITV), obtained by a geometric expansion of 3 mm from the Clinical Target Volume (CTV), and two oblique posterior beams can reduce the mean $V_{95\%CTV}$ variations to less than 1%. For other beam directions, the calculation of ITVs including the water-equivalent path length (WEPL), suggested the need of a CTV asymmetric expansion in depth, and minimal in lateral beam direction.
Additionally, weekly monitoring of the patient anatomy using computed tomography (CT) might easily be included in the clinical workflow and will assist in the decision of treatment re-planning, when substantial anatomical changes occur. The suggested prediction model was based on the variations of the accumulated WEPL (ΔaccWEPL) relative to the planning CT, and showed a strong correlation between the ΔaccWEPL and the gamma index of the dose distributions. The gamma criterion was selected as dose distribution quality metric, since it includes dosimetric changes in the target and normal tissues.
Regarding intra-fractional variations, the induced breathing motion together with a dynamic beam delivery, affect the dose distribution in terms of homogeneity and target coverage. This effect is stronger (ΔV_{95CTV} > 10%) for patients with a tumour motion amplitude superior to 5 mm and a highly modulated dose distribution intra- and inter-fields. The concept of modulation index was employed, it showed that different optimisers produce plans with contrasting distribution of the number of particles, resulting in unlike robustness against range and positioning uncertainties. It was concluded that under internal motion, the use of homogeneous plans, multiple beams, and geometric

ITVs, originated dose distributions exhibiting a slight mean decrease of the dose homogeneity (H_{CTV}) and V_{95CTV} of 4% and 1%, respectively.
Finally, a first approach to the use of 4D-Magnetic Resonance Imaging (MRI) for motion detection was performed. The results revealed cases of non-linear correlation between the breathing signal (diaphragm position) and the pancreas motion, and variability of the motion amplitude along the acquisition time and between sessions. This reinforces the need of an alternative method, comparative to the use of external surrogates, for simulation of a 4D dose distribution. Therefore, MRI will allow to include baseline drifts, amplitude variations and anatomical alterations in the 4D dose distribution assessment.
In summary, the key for a precise delivery of the treatment is the monitoring of anatomical changes, and a prompt reaction in order to minimise or eliminate potential uncertainties. In future, it is expected that the methods suggested in this thesis, the experience gained at HIT on treating moving organs and, the developments in treatment planning and treatment delivery will allow us to move towards the robust plan optimisation, prediction of changes in the dose distribution, and enable treatment without a constant and complex monitoring of the patient's movement.

References

Albertini, F, EB Hug, and AJ Lomax (2011). “Is it necessary to plan with safety margins for actively scanned proton therapy?” In: *Physics in medicine and biology* 56.14, p. 4399.

Asim, Zaneera (2016). “Definition of a prediction method for charged particle therapy plan quality: Inter-fractional changes of pancreatic patients”. Instituto Politecnico de Lisboa, Escola Superior da Saude de Lisboa.

Batista, V (2015). “Impact of gated internal target margin on carbon ion planned dose distribution in liver tumors”. MA thesis. University of Heidelberg.

Battistoni, Giuseppe et al. (2016). “The FLUKA code: An accurate simulation tool for particle therapy”. In: *Frontiers in oncology* 6.

Bauer, Julia et al. (2013). “Implementation and initial clinical experience of offline PET/CT-based verification of scanned carbon ion treatment”. In: *Radiotherapy and Oncology* 107.2, pp. 218–226.

Bauer, Julia et al. (2016). “Variable RBE in proton therapy: comparison of model predictions and their impact on clinical-like cranial lesions”. In: *Radiotherapy and Oncology* 118, S6–S7.

Bender, Edward T and Wolfgang A Tomé (2009). “The utilization of consistency metrics for error analysis in deformable image registration”. In: *Physics in medicine and biology* 54.18, p. 5561.

Bentzen, Søren M et al. (2010). “Quantitative Analyses of Normal Tissue Effects in the Clinic (QUANTEC): an introduction to the scientific issues”. In: *International Journal of Radiation Oncology* Biology* Physics* 76.3, S3–S9.

Bernatowicz, K, AJ Lomax, and A Knopf (2013). “Comparative study of layered and volumetric rescanning for different scanning speeds of proton beam in liver patients”. In: *Physics in medicine and biology* 58.22, p. 7905.

Bernatowicz, Kinga et al. (2016). “Four-Dimensional Dose Reconstruction for Scanned Proton Therapy Using Liver 4DCT-MRI”. In: *International Journal of Radiation Oncology* Biology* Physics* 95.1, pp. 216–223.

Bert, Christoph and Marco Durante (2011). “Motion in radiotherapy: particle therapy”. In: *Physics in medicine and biology* 56.16, R113.

Bert, Christoph, Sven O Grözinger, and Eike Rietzel (2008). “Quantification of interplay effects of scanned particle beams and moving targets”. In: *Physics in medicine and biology* 53.9, p. 2253.

Bert, Christoph and Eike Rietzel (2007). “4D treatment planning for scanned ion beams”. In: *Radiat Oncol* 2.1, p. 24.

Bert, Christoph et al. (2007). “Target motion tracking with a scanned particle beam”. In: *Medical physics* 34.12, pp. 4768–4771.

Bert, Christoph et al. (2009). “Gated irradiation with scanned particle beams”. In: *International Journal of Radiation Oncology* Biology* Physics* 73.4, pp. 1270–1275.

Bert, Christoph et al. (2014). “Advances in 4D Treatment Planning for Scanned Particle Beam Therapy—Report of Dedicated Workshops”. In: *Technology in cancer research & treatment* 13.6, pp. 485–495.
Birkfellner, Wolfgang et al. (2012). “Proceedings of the first MICCAI workshop on Image-Guidance and Multimodal Dose Planning in Radiation Therapy”. In:
Björkman, Daniel (2016). “Prediction of pseudoCTs from clinical MRI radiotherapy data for ion beam therapy planning”. MA thesis.
Boye, Dirk, Tony Lomax, and Antje Knopf (2013). “Mapping motion from 4D-MRI to 3D-CT for use in 4D dose calculations: a technical feasibility study”. In: *Medical physics* 40.6, p. 061702.
Brevet, R (2011). “Internal/External Motion Correlation- Diploma thesis”. MA thesis. University of Strasbourg.
Buchler, MW, J Kleeff, and H Friess (2007). “Surgical treatment of pancreatic cancer”. In: *Journal of the American College of Surgeons* 205, pp. 81–86.
Cabal Arango, Gonzalo Alfonso (2012). “Novel methods for treatment planning in Ion Beam Therapy”. In:
Cancer in Germany 2009–2010. 9th edition. (2014).
Chen, W et al. (2015). “Forward-Zero-Padding –A Novel Method for Shift Estimation in PET–based Range Verification”. In: *Proceedings of PTCOG 2015 conference*.
Chen, Wei et al. (2012). “Including robustness in multi-criteria optimization for intensity-modulated proton therapy”. In: *Physics in medicine and biology* 57.3, p. 591.
Cheung, J et al. (2012). “Feasibility of Online Range Adaptive Spot Scanning Proton Therapy”. In: *Medical Physics - AAPM proceedings* 39.6, pp. 3998–3998.
Chu, WT, BA Ludewigt, and TR Renner (1993). “Instrumentation for treatment of cancer using proton and light-ion beams”. In: *Review of Scientific Instruments* 64.8, pp. 2055–2122.
Combs, Stephanie E et al. (2013). “Phase I study evaluating the treatment of patients with locally advanced pancreatic cancer with carbon ion radiotherapy: the PHOENIX-01 trial”. In: *BMC cancer* 13.1, p. 1.
Dalal, Shalini et al. (2012). “Relationships among body mass index, longitudinal body composition alterations, and survival in patients with locally advanced pancreatic cancer receiving chemoradiation: a pilot study”. In: *Journal of pain and symptom management* 44.2, pp. 181–191.
Ding, Xuanfeng et al. (2014). “A comprehensive dosimetric study of pancreatic cancer treatment using three-dimensional conformal radiation therapy (3DCRT), intensity-modulated radiation therapy (IMRT), volumetric-modulated radiation therapy (VMAT), and passive-scattering and modulated-scanning proton therapy (PT)”. In: *Medical Dosimetry* 39.2, pp. 139–145.
Dreher, Constantin et al. (2015). “Optimization of carbon ion and proton treatment plans using the raster-scanning technique for patients with unresectable pancreatic cancer”. In: *Radiation Oncology* 10.1, p. 1.
Durante, Marco and Jay S Loeffler (2010). “Charged particles in radiation oncology”. In: *Nature reviews Clinical oncology* 7.1, pp. 37–43.
Eley, John Gordon et al. (2014). “4D optimization of scanned ion beam tracking therapy for moving tumors”. In: *Physics in medicine and biology* 59.13, p. 3431.
Elsässer, Thilo, Michael Krämer, and Michael Scholz (2008). “Accuracy of the local effect model for the prediction of biologic effects of carbon ion beams in vitro and in vivo”. In: *International Journal of Radiation Oncology* Biology* Physics* 71.3, pp. 866–872.

Emami, B et al. (1991). “Tolerance of normal tissue to therapeutic irradiation”. In: *International Journal of Radiation Oncology* Biology* Physics* 21.1, pp. 109–122.

Engelsman, Martijn, Christoph Bert, and H Paganetti (2011). “Precision and uncertainties in proton therapy for moving targets”. In: *Proton Therapy Physics. Series in Medical Physics and Biomedical Engineering* 1, pp. 435–60.

Farncombe, Troy and Kris Iniewski (2013). *Medical Imaging: Technology and Applications*. CRC press. ISBN: 9781466582620.

Fedorov, Andriy et al. (2012). “3D Slicer as an image computing platform for the Quantitative Imaging Network”. In: *Magnetic resonance imaging* 30.9, pp. 1323–1341. URL: `http://www.slicer.org/`.

Ferley, J et al. (2013). *GLOBOCAN 2012 v1. 0, Cancer Incidence and Mortality Worldwide: IARC CancerBase No. 11 [Internet]. Lyon, Fr Int Agency Res Cancer*.

Fredriksson, Albin (2012). “A characterization of robust radiation therapy treatment planning methods-from expected value to worst case optimization”. In: *Medical physics* 39.8, pp. 5169–5181.

Fredriksson, Albin, Anders Forsgren, and Björn Hårdemark (2011). “Minimax optimization for handling range and setup uncertainties in proton therapy”. In: *Medical physics* 38.3, pp. 1672–1684.

Furukawa, Takuji et al. (2007). “Design study of a raster scanning system for moving target irradiation in heavy-ion radiotherapy”. In: *Medical physics* 34.3, pp. 1085–1097.

Gemmel, A et al. (2011). “Calculation and experimental verification of the RBE-weighted dose for scanned ion beams in the presence of target motion”. In: *Physics in medicine and biology* 56.23, p. 7337.

Goldstein, Seth D et al. (2010). “Use of respiratory-correlated four-dimensional computed tomography to determine acceptable treatment margins for locally advanced pancreatic adenocarcinoma”. In: *International Journal of Radiation Oncology* Biology* Physics* 76.2, pp. 597–602.

Graeff, Christian (2014). “Motion mitigation in scanned ion beam therapy through 4D-optimization”. In: *Physica Medica* 30.5, pp. 570–577.

Graeff, Christian, Marco Durante, and Christoph Bert (2012). “Motion mitigation in intensity modulated particle therapy by internal target volumes covering range changes”. In: *Medical physics* 39.10, pp. 6004–6013.

Graeff, Christian et al. (2013). “A 4D-optimization concept for scanned ion beam therapy”. In: *Radiotherapy and Oncology* 109.3, pp. 419–424.

Graeff, Christian et al. (2014). “Multigating, a 4D optimized beam tracking in scanned ion beam therapy”. In: *Technology in cancer research & treatment* 13.6, pp. 497–504.

Haberer, Th et al. (1993). “Magnetic scanning system for heavy ion therapy”. In: *Nuclear Instruments and Methods in Physics Research Section A: Accelerators, Spectrometers, Detectors and Associated Equipment* 330.1, pp. 296–305.

Haberer, Th et al. (2004). “The Heidelberg ion therapy center”. In: *Radiotherapy and Oncology* 73, S186–S190.

Hansen, Eric K and Mack Roach (2007). “Handbook of evidence-based radiation oncology”. In: *Handbook of Evidence-Based Radiation Oncology 2nd Edition*, p. 711.

Heerkens, Hanne D et al. (2014). “MRI-based tumor motion characterization and gating schemes for radiation therapy of pancreatic cancer”. In: *Radiotherapy and Oncology* 111.2, pp. 252–257.

Hild, Sebastian, Marco Durante, and Christoph Bert (2013). “Assessment of uncertainties in treatment planning for scanned ion beam therapy of moving tumors”. In: *International Journal of Radiation Oncology* Biology* Physics* 85.2, pp. 528–535.
Horst, Astrid van der et al. (2013). “Interfractional position variation of pancreatic tumors quantified using intratumoral fiducial markers and daily cone beam computed tomography”. In: *International Journal of Radiation Oncology* Biology* Physics* 87.1, pp. 202–208.
Huang, Ke Colin et al. (2016). “Phantom-based characterization of distortion on a magnetic resonance imaging simulator for radiation oncology”. In: *Physics in medicine and biology* 61.2, p. 774.
IAEA, International Atomic Energy Agency (2007). “Dose Reporting in Ion Beam Therapy, Proceedings of a meeting organized jointly by the International Atomic Energy Agency and the International Commission on Radiation Units and Measurements, Inc”. In: IAEA-TECDOC-1560.
— (2008). “Relative Biological Effectivness In Ion Beam Therapy”. In: Technical Report Series TRS-461.
ICRU, International Commission on Radiation Units and Measurements (1993). “Report 50: Prescribing, recording and reporting photon beam therapy”. In:
— (1999). “Report 62: Prescribing, recording and reporting photon beam therapy (supplement to ICRU report 50)”. In:
— (2005). “ICRU Report 73: Stopping of ions heavier than helium.” In:
— (2007). “ICRU Report 78: Prescribing, recording, and reporting proton-beam therapy”. In: 7, pp. 7–210.
Jäkel, Oliver (2012). “Treatment Planning for Ion Beam Therapy”. In: *Ion Beam Therapy*. Springer, pp. 503–525.
Jäkel, Oliver et al. (1997). *Koordinatensysteme für die Schwerionentherapie an der GSI*.
Jayachandran, Priya et al. (2010). “Interfractional uncertainty in the treatment of pancreatic cancer with radiation”. In: *International Journal of Radiation Oncology* Biology* Physics* 76.2, pp. 603–607.
Joiner, Michael and Albert van der Kogel (2009). “Basic clinical radiobiology”. In: *Basic Clinical Radiobiology. 4th ed2009*.
Kessel, Kerstin A et al. (2013). “Development and validation of automatic tools for interactive recurrence analysis in radiation therapy: optimization of treatment algorithms for locally advanced pancreatic cancer”. In: *Radiation Oncology* 8.1, p. 1.
Kraft, Gerhard (2000). “Tumor therapy with heavy charged particles”. In: *Progress in Particle and Nuclear Physics* 45, S473–S544.
Krämer, Michael and Michael Scholz (2000). “Treatment planning for heavy-ion radiotherapy: calculation and optimization of biologically effective dose”. In: *Physics in medicine and biology* 45.11, p. 3319.
Krämer, Michael et al. (2000). “Treatment planning for heavy-ion radiotherapy: physical beam model and dose optimization”. In: *Physics in medicine and biology* 45.11, p. 3299.
Krämer, Michael et al. (2014). “Overview of recent advances in treatment planning for ion beam radiotherapy”. In: *The European Physical Journal D* 68.10, pp. 1–6.
Kumagai, Motoki et al. (2009). “Impact of intrafractional bowel gas movement on carbon ion beam dose distribution in pancreatic radiotherapy”. In: *International Journal of Radiation Oncology* Biology* Physics* 73.4, pp. 1276–1281.

Kurz, Christopher (2014). “4D offline PET-based treatment verification in ion beam therapy: experimental and clinical evaluation”. PhD thesis. LMU München: Faculty of Physics.
Kurz, Christopher et al. (2016). “Feasibility of automated proton therapy plan adaptation for head and neck tumors using cone beam CT images”. In: *Radiation Oncology* 11.1, p. 1.
Li, Donghui et al. (2004). “Pancreatic cancer”. In: *The Lancet* 363.9414, pp. 1049–1057.
Li, Zuofeng (2012). “Toward robust proton therapy planning and delivery”. In: *Translational Cancer Research* 1.3. ISSN: 2219-6803.
Ling, Ted C et al. (2015). “Evaluation of normal tissue exposure in patients receiving radiotherapy for pancreatic cancer based on RTOG 0848”. In: *Journal of gastrointestinal oncology* 6.2, p. 108.
Linz, Ute (2011). *Ion Beam Therapy: Fundamentals, Technology, Clinical Applications*. Vol. 320. Springer Science & Business Media.
Liu, Feng et al. (2012a). “Characterization and management of interfractional anatomic changes for pancreatic cancer radiotherapy”. In: *International Journal of Radiation Oncology* Biology* Physics* 83.3, e423–e429.
Liu, Wei et al. (2012b). “Robust optimization of intensity modulated proton therapy”. In: *Medical physics* 39.2, pp. 1079–1091.
Lomax, AJ (2008a). “Intensity modulated proton therapy and its sensitivity to treatment uncertainties 1: the potential effects of calculational uncertainties”. In: *Physics in medicine and biology* 53.4, p. 1027.
— (2008b). “Intensity modulated proton therapy and its sensitivity to treatment uncertainties 2: the potential effects of inter-fraction and inter-field motions”. In: *Physics in medicine and biology* 53.4, p. 1043.
— (2008c). *Intensity modulated proton therapy Proton and Charged Particle*.
Low, Daniel A et al. (1998). “A technique for the quantitative evaluation of dose distributions”. In: *Medical physics* 25.5, pp. 656–661.
Lüchtenborg, Robert et al. (2011). “Experimental verification of a real-time compensation functionality for dose changes due to target motion in scanned particle therapy”. In: *Medical physics* 38.10, pp. 5448–5458.
Lujan, Anthony E et al. (1999). “A method for incorporating organ motion due to breathing into 3D dose calculations”. In: *Medical physics* 26.5, pp. 715–720.
Matney, Jason E et al. (2016). “Perturbation of water-equivalent thickness as a surrogate for respiratory motion in proton therapy”. In: *Journal of Applied Clinical Medical Physics* 17.2.
McGowan, SE et al. (2015). “Defining robustness protocols: a method to include and evaluate robustness in clinical plans”. In: *Physics in medicine and biology* 60.7, p. 2671.
Moding, Everett J, Michael B Kastan, and David G Kirsch (2013). “Strategies for optimizing the response of cancer and normal tissues to radiation”. In: *Nature reviews Drug discovery* 12.7, pp. 526–542.
Mori, Shinichiro, Makoto Shinoto, and Shigeru Yamada (2014). “Four-dimensional treatment planning in layer-stacking boost irradiation for carbon-ion pancreatic therapy”. In: *Radiotherapy and Oncology* 111.2, pp. 258–263.
Mori, Shinichiro et al. (2008). “Quantitative assessment of range fluctuations in charged particle lung irradiation”. In: *International Journal of Radiation Oncology* Biology* Physics* 70.1, pp. 253–261.

Mori, Shinichiro et al. (2009). “Four-dimensional measurement of intrafractional respiratory motion of pancreatic tumors using a 256 multi-slice CT scanner”. In: *Radiotherapy and Oncology* 92.2, pp. 231–237.

Mori, Shinichiro et al. (2010). “Comparison of respiratory-gated and respiratory-ungated planning in scattered carbon ion beam treatment of the pancreas using four-dimensional computed tomography”. In: *International Journal of Radiation Oncology* Biology* Physics* 76.1, pp. 303–312.

Moteabbed, M, J Schuemann, and H Paganetti (2014). “Dosimetric feasibility of real-time MRI–guided proton therapy”. In: *Medical physics* 41.11, p. 111713.

Newhauser, Wayne D and Rui Zhang (2015). “The physics of proton therapy”. In: *Physics in medicine and biology* 60.8, R155.

Nichols, Romaine Charles et al. (2014). “First report of a prospective trial of proton therapy and concomittant capecitabine for patients with nonmetastatic unresectable pancreatic adenocarcinoma.” In: *ASCO Annual Meeting Proceedings*. Vol. 32. 3 suppl, p. 326.

Paganetti, Harald (2014). “Relative biological effectiveness (RBE) values for proton beam therapy. Variations as a function of biological endpoint, dose, and linear energy transfer”. In: *Physics in medicine and biology* 59.22, R419.

Park, Peter C et al. (2012). “A beam-specific planning target volume (PTV) design for proton therapy to account for setup and range uncertainties”. In: *International Journal of Radiation Oncology* Biology* Physics* 82.2, e329–e336.

Parodi, Katia, Andrea Mairani, and Florian Sommerer (2013). “Monte Carlo-based parametrization of the lateral dose spread for clinical treatment planning of scanned proton and carbon ion beams”. In: *Journal of radiation research* 54.suppl 1, pp. i91–i96.

Parodi, Katia et al. (2009). “4D in-beam positron emission tomography for verification of motion-compensated ion beam therapy”. In: *Medical physics* 36.9, pp. 4230–4243.

Particle Therapy Co-Operative Group (PTCOG). *Particle therapy facilities in operation*. URL: `http://www.ptcog.ch/`.

Pedroni, Eros et al. (1995). “The 200-MeV proton therapy project at the Paul Scherrer Institute: Conceptual design and practical realization”. In: *Medical Physics* 22.1, pp. 37–53.

Phillips, Mark H et al. (1992). “Effects of respiratory motion on dose uniformity with a charged particle scanning method”. In: *Physics in medicine and biology* 37.1, p. 223.

Pinter, Csaba et al. (2012). “SlicerRT: Radiation therapy research toolkit for 3D Slicer”. In: *Medical Physics* 39 (10), p. 6332.

Plastimatch. URL: `http://plastimatch.org/`.

Pruim, Randall (2011). “Computational Statistics Using R and R Studio An Introduction for Scientists”. In: *SC 11 Education Program, Seattle in November 2011*.

Rank, Christopher M et al. (2016). “4D respiratory motion-compensated image reconstruction of free-breathing radial MR data with very high undersampling”. In: *Magnetic resonance in medicine*.

RaySearch Laboratories AB (2015). *Robust Optimization in Raystation - white paper*. RaySearch Laboratories AB.

Richter, Daniel (2012). “Treatment planning for tumors with residual motion in scanned ion beam therapy”. PhD thesis. TU Darmstadt.

Richter, Daniel et al. (2013). “Upgrade and benchmarking of a 4D treatment planning system for scanned ion beam therapy”. In: *Medical physics* 40.5, p. 051722.

Richter, Daniel et al. (2014a). “Four-Dimensional Patient Dose Reconstruction for Scanned Ion Beam Therapy of Moving Liver Tumors”. In: *International Journal of Radiation Oncology* Biology* Physics* 89.1, pp. 175–181.
Richter, Daniel et al. (2014b). “Residual motion mitigation in scanned carbon ion beam therapy of liver tumors using enlarged pencil beam overlap”. In: *Radiotherapy and Oncology* 113.2, pp. 290–295.
Rietzel, Eike and Christoph Bert (2010). “Respiratory motion management in particle therapy”. In: *Medical physics* 37.2, pp. 449–460.
Rietzel, Eike, Tinsu Pan, and George TY Chen (2005). “Four-dimensional computed tomography: image formation and clinical protocol”. In: *Medical physics* 32.4, pp. 874–889.
Rietzel, Eike, Dieter Schardt, and Thomas Haberer (2007). “Range accuracy in carbon ion treatment planning based on CT-calibration with real tissue samples”. In: *Radiat. Oncol* 2.1, p. 14.
Saito, Nami et al. (2009). “Speed and accuracy of a beam tracking system for treatment of moving targets with scanned ion beams”. In: *Physics in medicine and biology* 54.16, p. 4849.
Sarkar, Saradwata et al. (2012). “Evaluation of an automatic registration-based algorithm for direct measurement of volume change in tumors”. In: *International Journal of Radiation Oncology* Biology* Physics* 83.3, pp. 1038–1046.
Schardt, Dieter, Thilo Elsässer, and Daniela Schulz-Ertner (2010). “Heavy-ion tumor therapy: Physical and radiobiological benefits”. In: *Reviews of modern physics* 82.1, p. 383.
Schätti, A et al. (2013). “Experimental verification of motion mitigation of discrete proton spot scanning by re-scanning”. In: *Physics in medicine and biology* 58.23, p. 8555.
Schlaff, Cody D et al. (2014). “Bringing the heavy: carbon ion therapy in the radiobiological and clinical context”. In: *Radiation Oncology* 9.1, p. 1.
Schneider, Uwe et al. (2002). “The water equivalence of solid materials used for dosimetry with small proton beams”. In: *Medical physics* 29.12, pp. 2946–2951.
Scholz, Michael and Gerhard Kraft (1996). “Track structure and the calculation of biological effects of heavy charged particles”. In: *Advances in Space Research* 18.1, pp. 5–14.
Schulz-Ertner, Daniela and Hirohiko Tsujii (2007). “Particle radiation therapy using proton and heavier ion beams”. In: *Journal of clinical oncology* 25.8, pp. 953–964.
Shackleford, James A, N Kandasamy, and GC Sharp (2010). “On developing B–spline registration algorithms for multi-core processors”. In: *Physics in medicine and biology* 55.21, p. 6329.
Sharp, GC et al. (2007a). “GPU-based streaming architectures for fast cone-beam CT image reconstruction and demons deformable registration”. In: *Physics in medicine and biology* 52.19, p. 5771.
Sharp, Gregory C et al. (2007b). “Assessing residual motion for gated proton-beam radiotherapy”. In: *Journal of radiation research* 48.Suppl A, A55–A59.
Shinoto, Makoto et al. (2013). “Phase 1 trial of preoperative, short-course carbon-ion radiotherapy for patients with resectable pancreatic cancer”. In: *Cancer* 119.1, pp. 45–51.
Shinoto, Makoto et al. (2016). “Carbon Ion Radiation Therapy With Concurrent Gemcitabine for Patients With Locally Advanced Pancreatic Cancer”. In: *International Journal of Radiation Oncology*Biology*Physics* 95.1. Particle Therapy Special Edition, pp. 498 –504. ISSN: 0360-3016.

Shiomi, Miho et al. (2016). “Comparison of carbon-ion passive and scanning irradiation for pancreatic cancer”. In: *Radiotherapy and Oncology*.

Siebenthal, Martin von et al. (2005). “4D MR imaging using internal respiratory gating”. In: *Medical Image Computing and Computer-Assisted Intervention–MICCAI 2005*. Springer, pp. 336–343.

Solla, Ignazio et al. (2013). “Free-breathing conformal irradiation of pancreatic cancer”. In: *Journal of Applied Clinical Medical Physics* 14.4.

Solutions, MeVis Medical. URL: `http://www.mevislab.de/`.

Steidl, Peter (2011). “Gating for scanned ion beam therapy”. PhD thesis.

Steidl, Peter et al. (2012). “A breathing thorax phantom with independently programmable 6D tumour motion for dosimetric measurements in radiation therapy”. In: *Physics in medicine and biology* 57.8, p. 2235.

Tai, An et al. (2013). “Management of respiration-induced motion with 4-dimensional computed tomography (4DCT) for pancreas irradiation”. In: *International Journal of Radiation Oncology* Biology* Physics* 86.5, pp. 908–913.

Torfeh, Tarraf et al. (2016). “Characterization of 3D geometric distortion of Magnetic Resonance Imaging scanners commissioned for Radiation Therapy planning”. In: *Magnetic Resonance Imaging*.

Torres, Andrés Camilo Vásquez (2011). “Development of a breathing phantom for comparison of two breathing surrogates systems in 4DCT-imaging”. PhD thesis. University of Heidelberg.

Tsujii, Hirohiko et al. (2013). *Carbon-Ion radiotherapy: principles, practices, and treatment planning*. Springer Science & Business Media.

Underberg, René WM et al. (2005). “Use of maximum intensity projections (MIP) for target volume generation in 4DCT scans for lung cancer”. In: *International Journal of Radiation Oncology* Biology* Physics* 63.1, pp. 253–260.

Unholtz, Daniel et al. (2011). “Post-therapeutical β+-activity measurements in comparison to simulations towards in-vivo verification of ion beam therapy”. In: *Nuclear Science Symposium and Medical Imaging Conference (NSS/MIC), 2011 IEEE*. IEEE, pp. 2273–2276.

Unkelbach, Jan et al. (2009). “Reducing the sensitivity of IMPT treatment plans to setup errors and range uncertainties via probabilistic treatment planning”. In: *Medical physics* 36.1, pp. 149–163.

Van Herk, Marcel (2004). “Errors and margins in radiotherapy”. In: *Seminars in radiation oncology*. Vol. 14. 1. Elsevier, pp. 52–64.

Van’t Riet, Arie et al. (1997). “A conformation number to quantify the degree of conformality in brachytherapy and external beam irradiation: application to the prostate”. In: *International Journal of Radiation Oncology Biology Physics* 37.3, pp. 731–736.

Wang, Peng et al. (2016). “Quantitative assessment of anatomical change using a virtual proton depth radiograph for adaptive head and neck proton therapy”. In: *Journal of Applied Clinical Medical Physics* 17.2.

Water, S Van de et al. (2009). “Tumour tracking with scanned proton beams: assessing the accuracy and practicalities”. In: *Physics in medicine and biology* 54.21, p. 6549.

Webb, S (2003). “Use of a quantitative index of beam modulation to characterize dose conformality: illustration by a comparison of full beamlet IMRT, few-segment IMRT (fsIMRT) and conformal unmodulated radiotherapy”. In: *Physics in medicine and biology* 48.14, p. 2051.

Winkelmann, Tim et al. (2014). “Improvements for extending the time between maintenance periods for the Heidelberg ion beam therapy center (HIT) ion sources”. In: *Review of Scientific Instruments* 85.2, 02A951.

Wölfelschneider, Jens et al. (2015). “Impact of fractionation and number of fields on dose homogeneity for intra-fractionally moving lung tumors using scanned carbon ion treatment”. In: *Radiotherapy and Oncology*.

Yamada, S et al. (2010). “Carbon ion radiotherapy for patients with gastrointestinal cancer”. In: *Particle Therapy Co-Operative Group meeting*. Vol. 49.

Yang, Ming et al. (2012). “Comprehensive analysis of proton range uncertainties related to patient stopping-power-ratio estimation using the stoichiometric calibration”. In: *Physics in medicine and biology* 57.13, p. 4095.

Zhang, Huailing et al. (2014). “Determination of Acquisition Frequency for Intrafractional Motion of Pancreas in CyberKnife Radiotherapy”. In: *The Scientific World Journal* 2014.

Appendix A

Complementary results

A.1 Inter-fractional analysis

A.1.1 Beam geometry and planning margins

Figure A.1: Variation of the conformity number (CN) of the CTV for all the patients along the treatment weeks by beam configuration and used planning target margin.

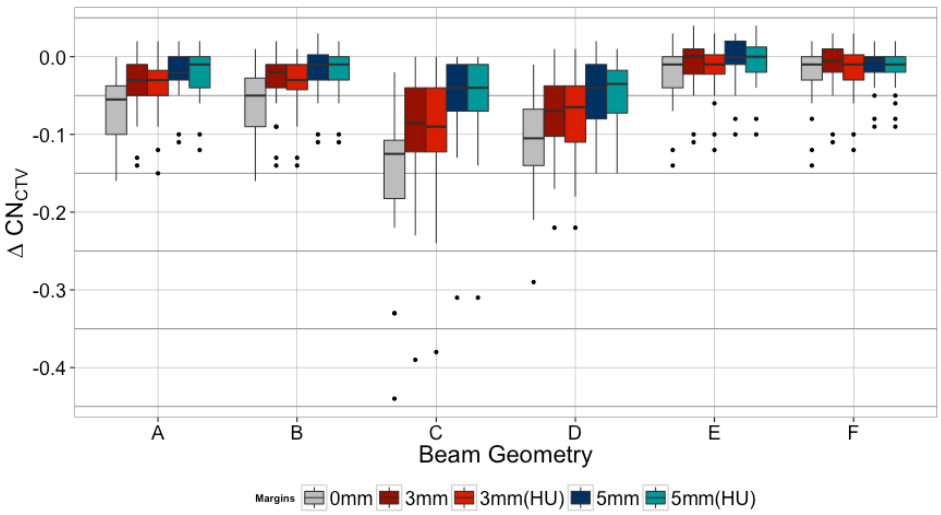

Figure A.2: Variation of the maximum dose to the CTV for all the patients along the treatment weeks by beam configuration and used planning target margin.

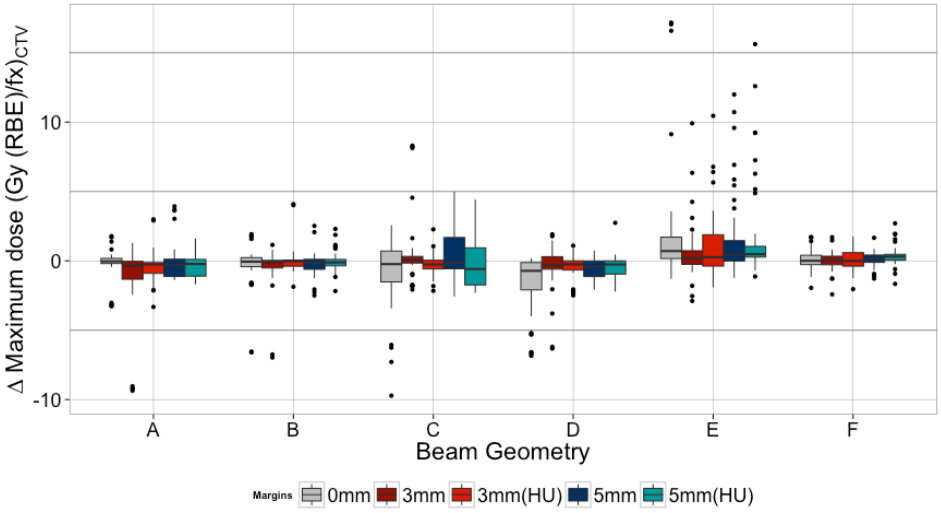

Figure A.3: Variation of the mean dose to the CTV for all the patients along the treatment weeks by beam configuration and used planning target margin.

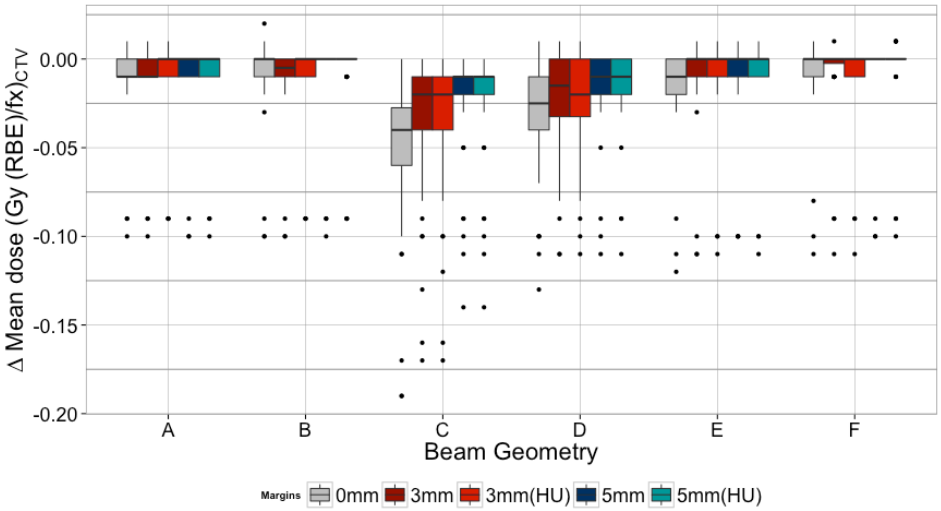

Figure A.4: Forward calculated dose distribution in the CT_3 for all the patients of the dataset A with the lateral beam of the plan optimized to the geometric ITV_{5mm}.

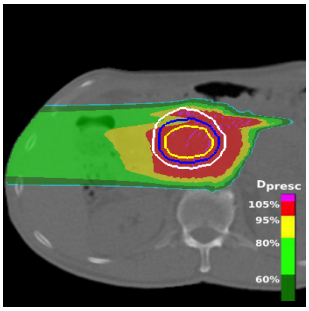

(a) Patient: A1, Geom: D

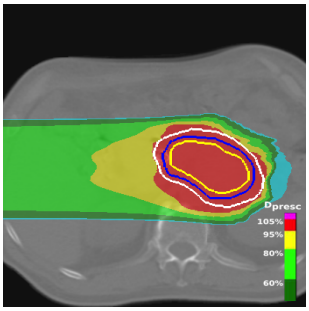

(f) Patient: A2, Geom: D

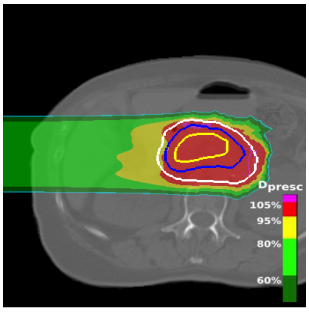

(b) Patient: A3, Geom: D

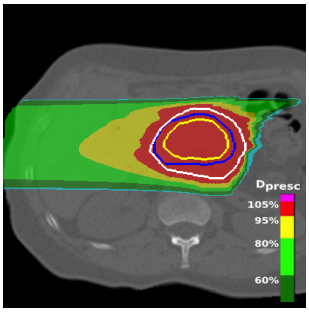

(g) Patient: A4, Geom: D

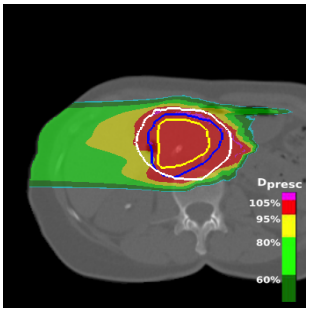

(c) Patient: A5, Geom: D

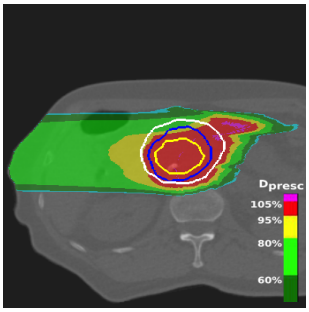

(h) Patient: A6, Geom: D

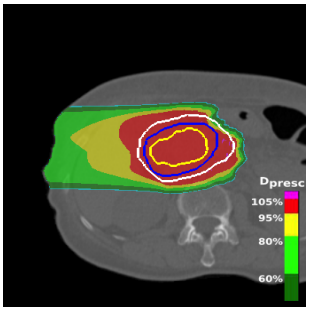

(d) Patient: A7, Geom: D

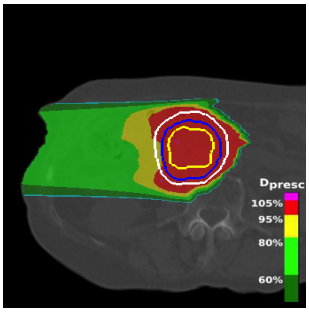

(i) Patient: A8, Geom: D

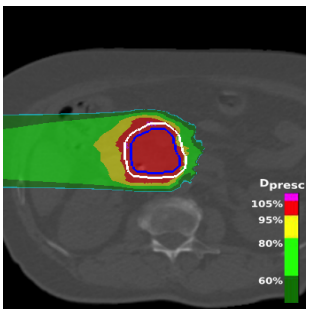

(e) Patient: A9, Geom: D

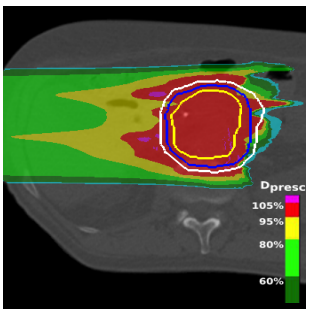

(j) Patient: A10, Geom: D

Figure A.5: Forward calculated dose distribution in the CT_3 for all the patients of the dataset A with a lateral beam and posterior beam of the plan optimized to the geometric ITV_{5mm}.

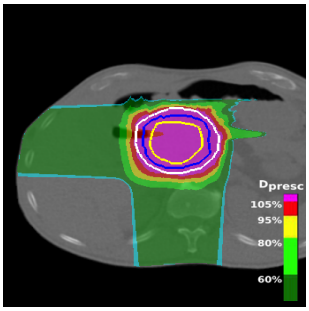

(a) Patient: A1, Geom: E

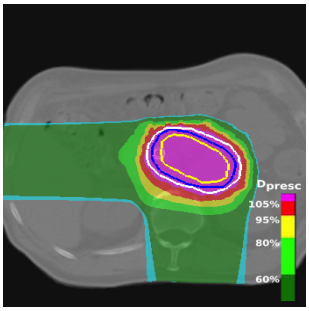

(f) Patient: A2, Geom: E

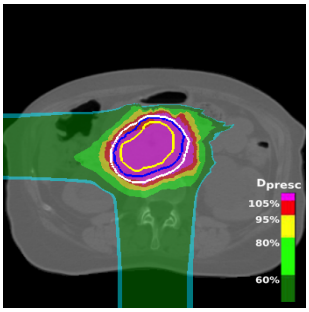

(b) Patient: A3, Geom: E

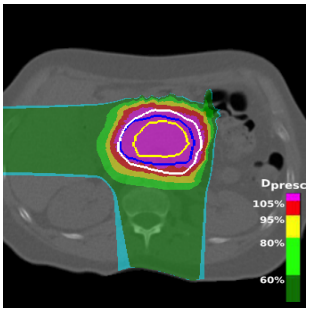

(g) Patient: A4, Geom: E

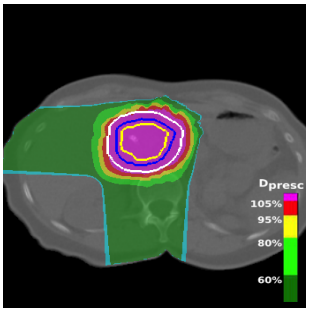

(c) Patient: A5, Geom: E

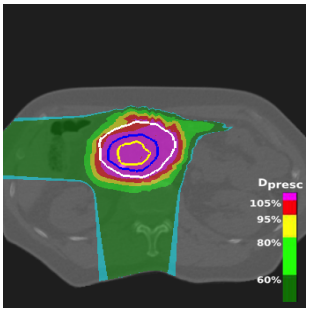

(h) Patient: A6, Geom: E

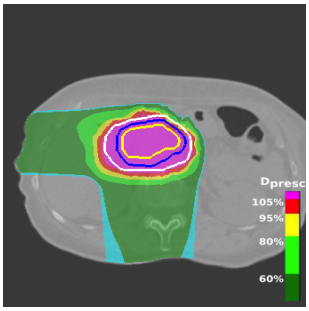

(d) Patient: A7, Geom: E

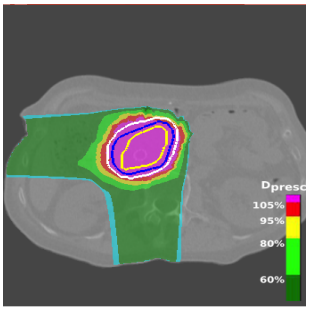

(i) Patient: A8, Geom: E

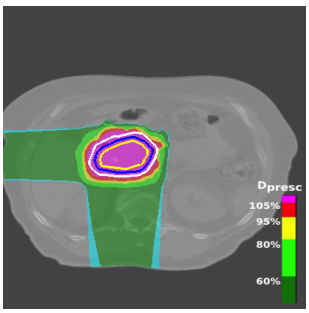

(e) Patient: A9, Geom: E

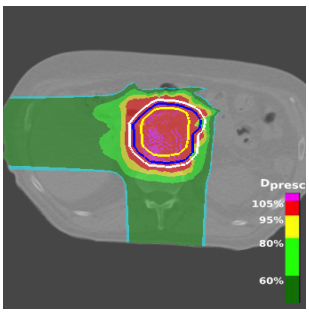

(j) Patient: A10, Geom: E

Table A.1: Evaluation of theITV_{WEPL} for each patient and beam's indicence (anterior, lateral right, posterior and oblique posterior right) in terms of 95% of the Hausdorf distance (HD95), dice similarity coefficient (DSC), difference of Volumes (dV) and variation of the center of mass (COM) in depth, lateral and cranio-caudal (cc) direction relative to the BEV.

Patient	Beam	HD95 (mm)	DSC	dVolume (%)	dCOM (mm)		
		CTV-ITV_{WEPL}	ITV_{G5}-ITV_{WEPL}	ITV_{G5}-ITV_{WEPL}	CTV-ITV_{WEPL} depth	lateral	c-c
A1	Ant	14.6	0.78	-10.5	-7.6	1.0	-1.0
	Lat	7.0	0.78	-30.0	-2.5	0.7	-0.3
	Pos	2.8	0.82	-27.9	0.6	0.0	-0.4
	Obl	3.1	0.82	-28.1	0.6	0.2	-0.4
A2	Ant	8.4	0.77	-8.4	4.9	0.2	0.5
	Lat	4.5	0.76	-29.1	0.6	-0.5	0.5
	Pos	3.3	0.79	-28.9	-0.9	-1.0	0.5
	Obl	2.8	0.79	-28.7	-0.1	-0.8	0.5
A3	Ant	9.8	0.82	-8.6	3.9	1.3	-1.2
	Lat	5.9	0.79	-25.1	-3.6	0.6	1.0
	Pos	4.9	0.84	-22.1	-2.0	0.0	0.1
	Obl	4.1	0.84	-22.6	-1.8	0.1	-0.1
A4	Ant	3.9	0.80	-28.5	0.6	-1.5	0.3
	Lat	4.6	0.77	-31.3	-3.1	0.9	0.5
	Pos	5.3	0.79	-26.3	-3.6	0.8	0.1
	Obl	5.0	0.80	-27.6	-3.6	1.2	-0.1
A5	Ant	5.6	0.80	-30.5	-0.7	-0.8	0.7
	Lat	6.0	0.76	-37.2	-3.2	0.1	0.3
	Pos	4.4	0.77	-36.5	-0.7	1.2	0.4
	Obl	5.4	0.77	-35.3	-0.6	1.1	0.5
A6	Ant	6.1	0.83	-18.9	-1.3	0.3	-0.3
	Lat	5.6	0.80	-23.9	-2.1	-1.5	-0.2
	Pos	4.5	0.82	-25.0	-0.5	0.0	-0.6
	Obl	4.7	0.82	-25.4	-0.8	-0.7	-0.7
A7	Ant	6.0	0.82	-21.1	3.5	-0.4	0.2
	Lat	5.4	0.79	-27.6	0.0	0.1	0.1
	Pos	3.3	0.81	-27.9	0.8	0.3	-0.2
	Obl	3.5	0.81	-28.3	0.6	0.3	0.0
A8	Ant	10.8	0.81	-10.9	-7.5	0.2	0.2
	Lat	7.8	0.78	-22.5	-4.6	1.1	-0.4
	Pos	2.7	0.83	-27.5	-0.6	-0.2	-0.3
	Obl	2.9	0.83	-27.8	-0.9	-0.3	-0.3
A9	Ant	8.6	0.78	-18.1	-1.3	0.6	0.3
	Lat	4.6	0.78	-26.8	4.2	0.5	1.25
	Pos	2.8	0.79	-30.7	-0.5	0.0	0.6
	Obl	2.8	0.79	-30.5	-0.8	0.2	0.6
A10	Ant	10.1	0.82	-13.9	-6.6	0.4	1.16
	Lat	11.8	0.76	-15.5	3.2	0.42	1.0
	Pos	3.3	0.84	-25.9	-0.7	0.1	0.5
	Obl	3.3	0.84	-25.8	-1.3	0.0	0.4

A.1.2 Water-equivalent path length calculations

Table A.2: Evaluation per patient and beam geometry of the differences between the accumulated WEPL, calculated in BEV from the patient's skin to the distal edge of the CTV, of each weeky CT and the planning CT. The used parameters were percentage of voxels with less than 3mm of diefference, mean, standard deviation and variance of the 2D difference map and range look-up values (LUT).

Patient	B.Direc.	PV_{in} (%)	Mean ± Std.Dev. (mm)	Variance (mm)	LUT [min;max] (mm)
A1	Ant	50.6 ±21.7	5.94 ± 2.75	0.24 ±40.57	-5.21 ± 2.64;21.14 ± 7.45
	Lat	82.75 ± 10.83	1.77 ± 3.12	26.89 ± 33.17	-6.78 ± 2.21;20.76 ± 13.33
	Pos	98.25 ±1.26	-0.08 ± 0.29	1.69 ± 0.68	-4.58 ± 1.4; 4.61 ± 1.44
	Obl	99.25 ± 0.54	0.02 ± 0.12	1.03 ±0.24	-3.67 ± 1.29 4.25 ± 2.71
A2	Ant	28.59 ± 18.62	-4.39 ± 0.64	-4.39 ± 0.64	-17.72 ± 8.45; -17.72 ± 8.45
	Lat	48.91 ± 9.22	-0.09 ± 1.46	27.5 ± 14.72	-14.16 ± 4.24; 16.38 ± 10.28
	Pos	92.94 ± 9.15	1.16 ± 0.16	1.56 ± 0.4	-3.62 ± 1.31;5.79 ± 1.44
	Obl	93.25 ± 7.66	0.56 ± 0.13	1.85 ± 0.35	-4.49 ± 1.86; 5.87 ± 1.86
A3	Ant	28.28 ± 4.17	-5.94 ± 0.44	59.94 ± 6.98	-24.81 ± 3.25;10.26 ± 4.48
	Lat	53.99 ± 12.2	2.31 ± 0.73	22.16 ± 6.84	-11.26 ± 2.54;21.05 ± 4.21
	Pos	82.91 ± 13.35	2.05 ± 0.39	2.08 ± 1.05	-2.42 ± 0.35;7.37 ± 2.29
	Obl	80.76 ± 13.37	1.99 ± 0.32	2.56 ± 1.01	-2.87 ± 0.69;6.67 ± 1.07
A4	Ant	62.7 ± 19	-1.74 ± 1.19	12.91 ± 7.49	-9.05 ± 4.76; 5.2 ± 1.58
	Lat	52.04 ± 26.48	1.65 ± 0.51	7.61 ± 3.02	-5.56 ± 4.27;9.91 ± 6.46
	Pos	12.97 ± 9.12	6.27 ± 0.31	5.64 ± 1.49	-0.22 ± 0.43;12.72 ± 1.33
	Obl	22.44 ± 6.07	4.96 ± 0.31	4.94 ± 1.39	-0.73 ± 1.46;9.93 ± 0.97
A5	Ant	53.39 ± 24.84	3.45 ± 0.68	23.24 ± 6.61	-8.46 ± 0.79;13.12 ± 2.5
	Lat	58.51 ± 38.42	3.11 ± 0.81	8.63 ± 4.88	-8.33 ± 1.7;16.52 ± 10.2
	Pos	82.91 ± 8.8	0.69 ± 0.28	5.12 ± 1.24	-6.82 ± 1.35;7.15 ± 0.76
	Obl	78.89 ± 12.13	0.88 ± 0.42	5.34 ± 1.82	-8.73 ± 0.79;8.38 ± 0.92
A6	Ant	48.61 ± 27.84	3.37 ± 0.05	7.69 ± 0.3	-3.41 ± 0.86;10.09 ± 1.59
	Lat	53.71 ± 20.66	3.36 ± 0.81	18.97 ± 6.81	-5.89 ± 1.39;25.32 ± 5.62
	Pos	80.95 ± 21.55	-1.97 ± 0.05	2.09 ± 0.14	-7.56 ± 1.49;2.85 ± 1.62
	Obl	82.44 ± 24.15	-1.44 ± 0.56	3.28 ± 2.05	-6.36 ± 2.26; 5.18 ± 0.02
A7	Ant	40.12 ± 15.2	-3.9 ± 1.21	13.35 ± 8.68	-12.79 ± 0.64;4.76 ± 4.17
	Lat	68.2 ± 13.72	-0.75 ± 1.73	34.4 ± 19.38	-27.9 ± 7.94;7.68 ± 5.44
	Pos	94.7 ± 7.29	-1.09 ± 0.31	1.52 ± 0.73	-5.17 ± 2.19;4.93 ± 3.56
	Obl	96.79 ± 3.1	-0.94 ± 0.28	1.45 ± 0.6	-5.15 ± 1.9;4.37 ± 3.8
A8	Ant	23.9 ± 23.49	8.92 ± 0.9	14.21 ± 6.27	-0.89 ± 1.46;15.86 ± 4.86
	Lat	41.89 ± 19.96	5.51 ± 3.22	35.18 ± 42.19	-7.31 ± 6.57;19.06 ± 9.43
	Pos	94.87 ± 3.03	0.76 ± 0.22	2.37 ± 0.68	-4.11 ± 1.27;5.88 ± 0.93
	Obl	89.69 ± 8.54	1.31 ± 0.41	2.43 ± 1.38	-4.14 ± 1.52;5.13 ± 1.35
A9	Ant	39.59 ± 15.93	-0.38 ± 1.61	71.43 ± 28.3	-22.3 ± 5.79;15.32 ± 3.15
	Lat	24.22 ± 15.34	-5.32 ± 0.25	6.34 ± 1.28	-10.67 ± 3.12; 4.39 ± 1.7
	Pos	80.17 ± 10.59	1.19 ± 0.3	5.21 ± 1.41	-4.28 ± 1.06;10.02 ± 2.11
	Obl	78.68 ± 10.01	1.6 ± 0.4	4.97 ± 1.71	-4.68 ± 2.36;10.16 ± 1.3
A10	Ant	37.66 ± 4.22	1.84 ± 1.48	48.49 ± 19.99	-17.58 ± 4.72;21.11 ± 4.36
	Lat	23.39 ± 7.94	9.78 ± 2.35	151.48 ± 54.68	-37.81 ± 17.17;44.68 ± 17.33
	Pos	59.27 ± 23.56	2.75 ± 0.24	4.13 ± 0.98	-4.24 ± 2.26;10.42 ± 3.69
	Obl	45.25 ± 23.11	3.63 ± 0.2	5.08 ± 0.88	-2.49 ± 2.05;10.77 ± 1.33

Figure A.6: Analysis variation of the accumulated WEPL for an **anterior beam**: performed for all the patients and weeky CTs in terms of percentage of voxels with differences inferior to 3 mm (PVin), Gamma passing rate between the planning dose distribution and each weekly forward-calculated dose distribution and the respective V95.

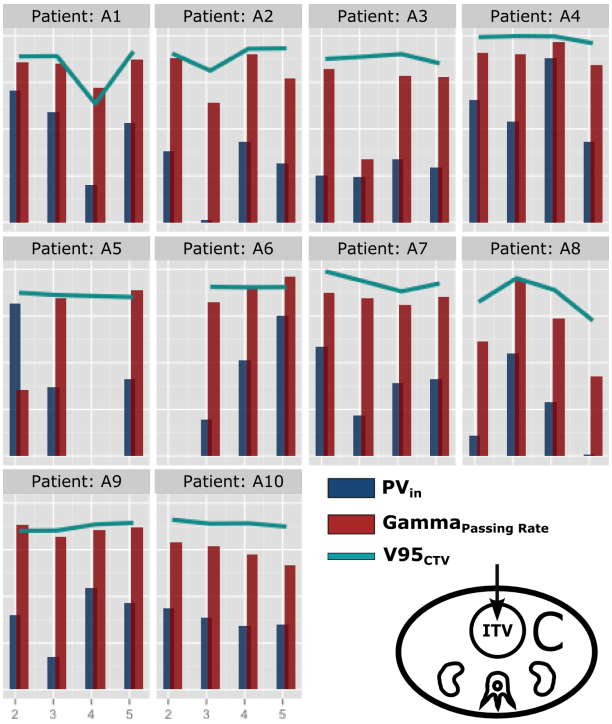

Figure A.7: Analysis variation of the accumulated WEPL for a **lateral right beam**: performed for all the patients and weeky CTs in terms of percentage of voxels with differences inferior to 3 mm (PVin), gamma passing rate between the planning dose distribution and each weekly forward-calculated dose distribution and the respective V95.

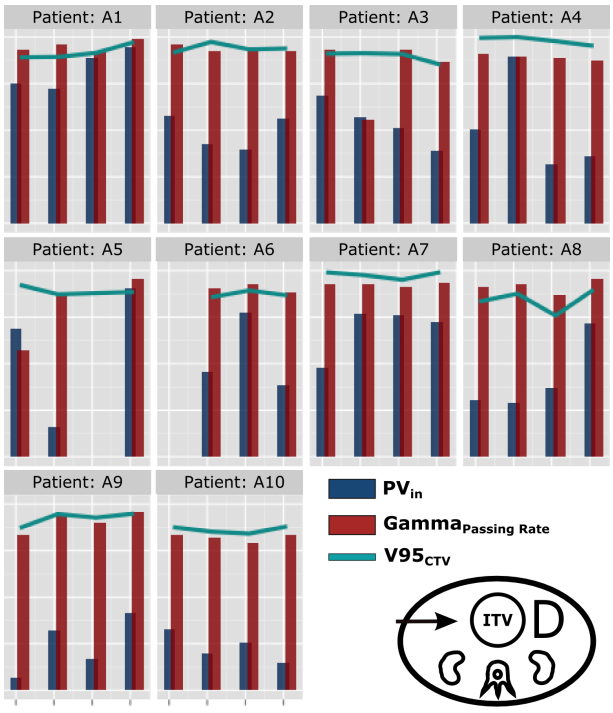

Figure A.8: Analysis variation of the accumulated WEPL for a **posterior beam**: performed for all the patients and weeky CTs in terms of percentage of voxels with differences inferior to 3 mm (PVin), gamma passing rate between the planning dose distribution and each weekly forward-calculated dose distribution and the respective V95.

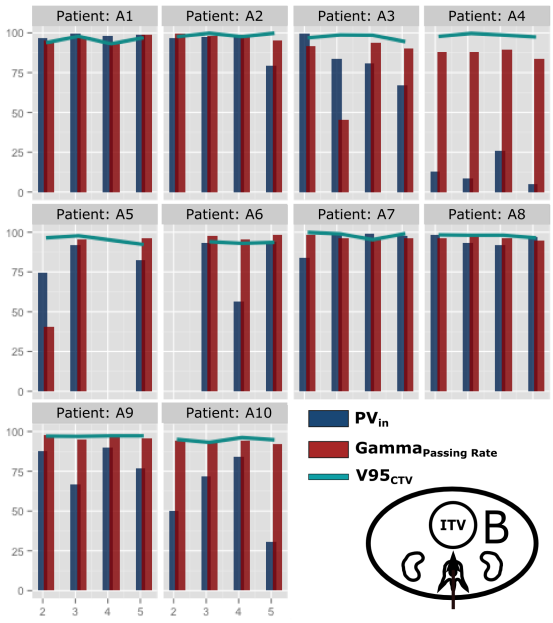

Figure A.9: Analysis variation of the accumulated WEPL for an **oblique posterior right beam**: performed for all the patients and weeky CTs in terms of percantage of voxels with differences inferior to 3 mm (PVin), gamma passing rate between the planning dose distribution and each weekly forward-calculated dose distribution and the respective V95.

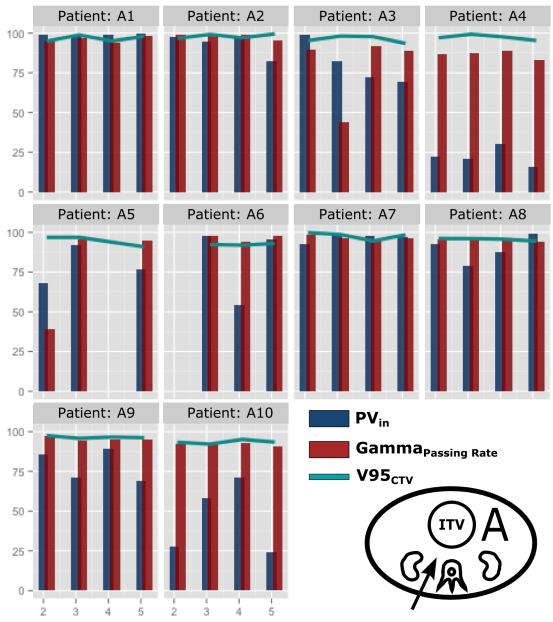

Table A.3: Example of the performed analysis for three patients (A1, A6, A8) for a lateral beam or oblique posterior beam for one of the weekly-CT versus the planning CT. The accumulated WEPL differences are shown through the color map and a histogram

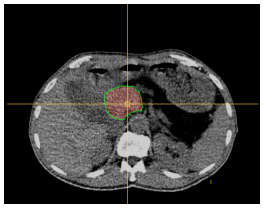 Pt: A1, Geom: D, CT1	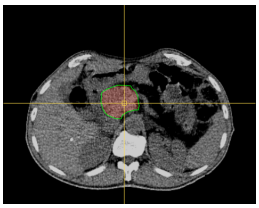 CT2	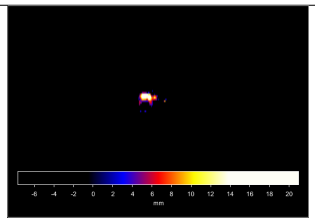 CT1-CT4	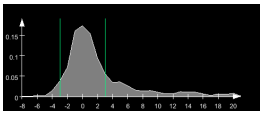 CT1-CT4
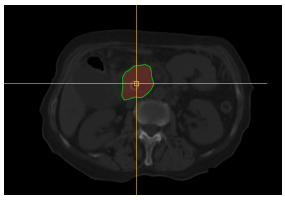 Pt: A8, Geom: D, CT1	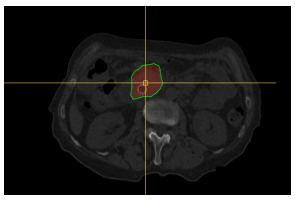 CT2	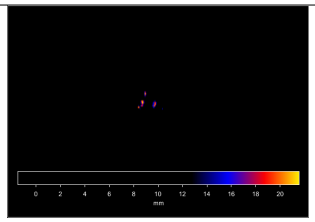 CT1-CT2	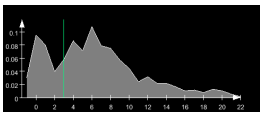 CT1-CT2
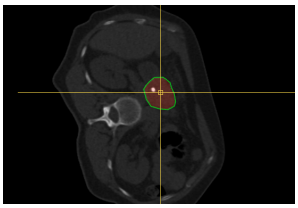 Pt: A6, Geom: B, CT1	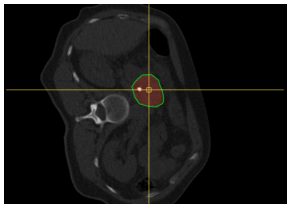 CT3	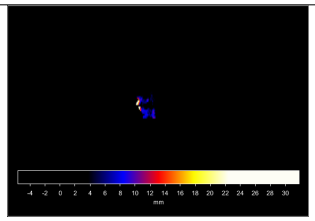 CT1-CT3	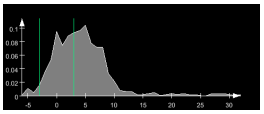 CT1-CT3

A.2 Intra-fractional analysis

Dataset B - 4D dose simulations

Table A.4: Analysis of the 4D simulated dose distribution of the patients of the dataset B, considering the regular and Lujan motion, in terms of impact in the CTV coverage (min, max, median, conformity number (CN), homogeneity (H_{CTV}), $V95_{CTV}$ and $V107_{CTV}$).

Patient	B.Direc.	Min. (%)	Max. (%)	Median Gy (RBE)	CN CN	H_{CTV} (%)	$V95_{CTV}$ (%)	$V107_{CTV}$ (%)
B1	Ant	87.6 ±1.5	110.4 ± 1.4	3.0 ± 0.1	0.5 ± 0.0	6.9 ± 0.2	98.7 ± 0.3	0.2 ± 0.1
	Post	89.1 ± 1.6	109.7 ± 1.8	3.0± 0.0	0.53 ± 0.0	4.4 ± 0.1	99.8 ± 0.1	0.1 ± 0.0
	Obl	89.5 ± 0.9	118.1 ± 2.8	3.1 ± 0.0	0.3 ± 0.0	10.1 ± 0.4	99.4 ± 02	11.7 ± 0.7
B2	Ant	72.5 ± 1.8	127.1 ± 9.2	3.0 ± 0.0	0.4 ± 0.0	14.3 ± 1.6	90.0 ± 2.1	5.3 ± 2.0
	Post	85.1 ± 2.1	111.3 ± 1.1	3.0 ± 0.1	0.4 ± 0.0	8.6 ± 0.2	96.9 ± 0.8	0.8 ± 0.2
	Obl	92.3 ± 1.1	113.5 ± 1.5	3.1 ± 0.0	0.4 ± 0.0	6.9 ± 0.3	99.9± 0.1	4.9± 2.5
B3	Ant	61.7 ± 8.7	127.4 ± 5.3	3.1 ± 0.0	0.5± 0.0	16.3 ± 1.0	89.2 ± 2.4	8.7± 2.0
	Post	87.2 ± 1.5	109.0 ± 1.1	3.0 ± 0.0	0.5± 0.1	7.5 ± 0.3	98.5 ± 0.5	0.4 ± 0.3
	Obl	93.0± 1.3	111.1 ± 1.1	3.1 ± 0.0	0.36 ± 0	6.0 ± 0.2	100.0 ± 0.1	2.3 ± 1.6
B4	Ant	83.8 ± 0.8	112.0 ± 1.1	3.0 ± 0.0	0.5± 0.0	8.2 ± 0.4	97.5 ± 0.6	0.5 ± 0.2
	Post	85.9 ± 1.5	113.3 ± 1.9	3.0± 0.0	0.5± 0.0	7.8± 0.2	97.0± 0.4	0.4 ± 0.1
	Obl	95.4 ± 0.8	112.7 ± 1.2	3.1 ± 0.1	0.5 ± 0.0	5.3 ± 0.2	100.0 ± 0.0	3.2 ± 0.5
B5	Ant	85.1 ± 1.3	113.5± 1.7	3.0± 0.0	0.5± 0.0	8.3 ± 0.2	97.3 ± 0.3	0.4 ± 0.2
	Post	81.8 ± 6.6	108.8 ± 1.7	3.0 ± 0.0	0.5 ± 0.0	7.1 ± 0.9	97.3 ± 1.8	0.1 ± 0.0
	Obl	90.8 ± 3.6	113.6 ± 1.1	3.1 ± 0.0	0.4± 0.0	6.3± 0.1	99.9 ± 0.1	4.2 ± 0.4
B6	Ant	81.9 ± 1.9	123.4 ± 4.1	3.0 ± 0.0	0.6 ± 0.0	7.1 ± 0.4	98.1 ± 0.3	0.8 ± 0.2
	Post	92.0± 0.6	109.0 ± 1.0	3.0 ± 0.0	0.5 ±0.0	5.4 ± 0.1	99.8 ± 0.0	0.1 ± 0.1
	Obl	96.5± 0.7	111.3± 0.5	3.1 ± 0.0	0.5± 0.0	4.8 ± 0.1	100.0 ± 0.0	1.9 ± 0.5
B7	Ant	74.4 ± 2.7	122.1 ± 1.3	3.0 ± 0.0	0.5 ± 0.1	10.5 ± 0.3	94.7 ± 0.5	2.4 ± 0.3
	Post	73.6 ±±4.7	111.3 ± 1.0	3.0 ± 0.1	0.5 ± 0.01	8.3 ± 0.4	95.2 ± 1.0	0.3 ± 0.1
	Obl	86.4 ± 1.9	109.0 ± 1.3	3.0 ± 0.1	0.505 ± 0.0	6.2 ± 0.3	99.5 ± 0.3	0.1 ± 0.1

Dataset H - 4D dose simulations and reconstructions

Table A.5: Analysis of the 4D simulated and reconstructed dose distribution of the patients of the dataset H, in terms of impact in the CTV coverage (min, max, median, conformity number (CN), homogeneity (H_{CTV}), $V95_{CTV}$ and $V107_{CTV}$), in comparison with the static dose distribution (Δ = 4DDSim or 4DDReco - static). For the patients with more than a single reconstruction the mean and standard deviation is presented.

Patient	Type	ΔMin. cGy (RBE)	ΔMax. cGy (RBE)	ΔMedian cGy (RBE)	ΔCN	ΔH_{CTV} (%)	$\Delta V95_{CTV}$ (%) (%)	$\Delta V107_{CTV}$ (%)
H1	4DDSim	-31.0 $\pm$ 6.9	66.3 $\pm$ 9.4	0.7 $\pm$ 1.2	-0.07 $\pm$ 0.02	13.7 $\pm$ 1	-7.2 $\pm$ 3	21.3 $\pm$ 4.1
	4DDReco	-34.5 $\pm$ 3.5	22.5 $\pm$ 7.8	-2.0 $\pm$ 0.0	-0.05 $\pm$ 0.01	5.9 $\pm$ 0.5	-10.7 $\pm$ 0.2	8.6 $\pm$ 1.7
H2	4DDSim	-54.7 $\pm$ 7.6	58 $\pm$ 13	1.8 $\pm$ 0.4	-0.01 $\pm$ 0.01	13.5 $\pm$ 1.6	-1.7 $\pm$ 1.8	20.7 $\pm$ 2.8
	4DDReco	-0.7	0.2	0.0	0.01	8	-5.5	7.9
H3	4DDSim	-28.7 $\pm$ 11	55.5 $\pm$ 4.3	0.3 $\pm$ 0.8	-0.14 $\pm$ 0.01	8.8 $\pm$ 2	2.2 $\pm$ 1.3	11.1 $\pm$ 2.3
	4DDReco	-0.3	0.2	-1.0	0.0	1.5	0.3	8.5
H4	4DDSim	-120.5 $\pm$ 2.6	42 $\pm$ 7.8	2.5 $\pm$ 0.5	-0.04 $\pm$ 0.01	12.4 $\pm$ 0.5	-6.2 $\pm$ 0.5	18.9 $\pm$ 1.5
	4DDReco	-117.0 $\pm$ 2	29.3 $\pm$ 9.0	1.3 $\pm$ 0.6	-0.01 $\pm$ 0.01	13.3 $\pm$ 0.3	-9.7 $\pm$ 1.2	10.5 $\pm$ 1.1
H5	4DDSim	-17.7 pm 3.1	68 pm 9.5	3 pm 0.0	-0.12 $\pm$ 0.01	13.6 $\pm$ 0.6	-5.7 $\pm$ 0.7	18.9 $\pm$ 1.5
	4DDReco	-18.0 $\pm$ 2.8	8.5 $\pm$ 3.5	0.0 $\pm$ 0.0	-0.05 $\pm$ 0	7.5 $\pm$ 0.3	-5.9 $\pm$ 0.6	3.4 $\pm$ 0.3
H6	4DDSim	-93.3 $\pm$ 7.5	54.8 $\pm$ 9.3	1.8 $\pm$ 0.4	-0.07 $\pm$ 0.01	13.9 $\pm$ 1.2	-10.6 $\pm$ 1.3	16.3 $\pm$ 1.9
	4DDReco	-87.8 $\pm$ 54.6	26.0 $\pm$ 12.8	0.0 $\pm$ 1.8	-0.05 $\pm$ 0.01	12.2 $\pm$ 2.7	-11.1 $\pm$ 1.9	6.7 $\pm$ 1.4
H7	4DDSim	-76.3 $\pm$ 2.3	62.7 $\pm$ 6.4	0 $\pm$ 1.8	-0.11 $\pm$ 0.02	21.3 $\pm$ 1.9	-19.8 $\pm$ 2.9	13.4 $\pm$ 4.2
	4DDReco	-0.6	0.2	-5.0	-0.1	17	-27.4	1.0
H8	4DDSim	-36.3 $\pm$ 4.6	47.7 $\pm$ 6.1	2.2 $\pm$ 0.8	-0.03 $\pm$ 0.01	16.5 $\pm$ 1.9	2.7 $\pm$ 1.9	20.5 $\pm$ 2.2
	4DDReco	-0.4	0.3	1.0	0.02	15.7	4.5	19.1
H9	4DDSim	-25.3 $\pm$ 7.3	32.3 $\pm$ 5.2	1.7 $\pm$ 1	-0.07 $\pm$ 0.02	9.1 $\pm$ 1.2	-3.4 $\pm$ 2.2	17.6 $\pm$ 3
	4DDReco	-0.2	0.1	0.0	0.0	1.5	-0.9	6.6
H11	4DDSim	-10.5 $\pm$ 5.7	9.1 $\pm$ 7.5	-1.6 $\pm$ 0.5	0.03 $\pm$ 0.01	0.9 $\pm$ 0.9	1.4 $\pm$ 0.9	1.1 $\pm$ 0.9
	4DDReco	-12.5 $\pm$ 6.4	8.5 $\pm$ 0.7	-2.5 $\pm$ 0.7	0.02 $\pm$ 0.01	-0.6 $\pm$ 0.3	0.2 $\pm$ 1	-0.7 $\pm$ 1.4
H12	4DDSim	-76.8 $\pm$ 4.1	74.8 $\pm$ 19.3	-2.5 $\pm$ 5.6	-0.02 $\pm$ 0.05	32.5 $\pm$ 6.9	-15.8 $\pm$ 8.1	11.1 $\pm$ 8.7
	4DDReco	-95.4 $\pm$ 12.5	73.8 $\pm$ 28.6	1.6 $\pm$ 3.8	0.03 $\pm$ 0.05	26.9 $\pm$ 2.7	-6.6 $\pm$ 6.8	15.1 $\pm$ 5.8
H13	4DDSim	-20 $\pm$ 9.5	12.5 $\pm$ 4	-15.8 $\pm$ 2.4	-0.16 $\pm$ 0.02	3 $\pm$ 0.5	-16.4 $\pm$ 2	0.6 $\pm$ 0.7
	4DDReco	-25 $\pm$ 1.4	19 $\pm$ 1.4	-13.5 $\pm$ 0.7	-0.14 $\pm$ 0.01	3.9 $\pm$ 0.7	-14.5 $\pm$ 0.8	1 $\pm$ 0.1
H14	4DDSim	-16.2 $\pm$ 2.5	29.2 $\pm$ 5.3	-3.5 $\pm$ 1.4	-0.01 $\pm$ 0.01	1.3 $\pm$ 0.7	-3.6 $\pm$ 0.7	0.7 $\pm$ 0.2
	4DDReco	-0.2	0.3	-4.0	-0.02	1.2	-4	0.7
H15	4DDSim	-72.8 $\pm$ 7.2	19.3 $\pm$ 6.5	-1.2 $\pm$ 0.8	-0.03 $\pm$ 0.01	6.9 $\pm$ 0.8	-6.7 $\pm$ 1.6	7.4 $\pm$ 2
	4DDReco	-0.7	0.1	-1.0	-0.03	4.2	-6	3.1

Figure A.10: Axial view of the dose distributions in the static, one example of the possivle 4D simulation and the 4D reconstruction of one of the treated fractions for the patients of the dataset H. The dose-volume histogram of the CTV shows the compresses all the 4D simulations (blue band), the 4D reconstructions (green lines) relative to the static plan (red line).

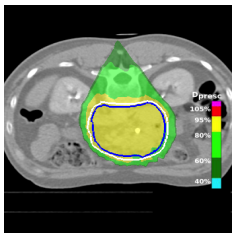

(a) H1 Static

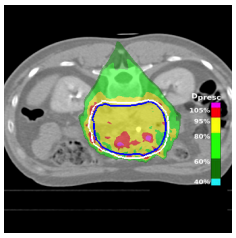

(e) 4DDSim

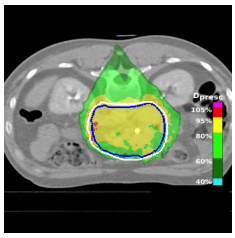

(i) 4DDReco Fx16

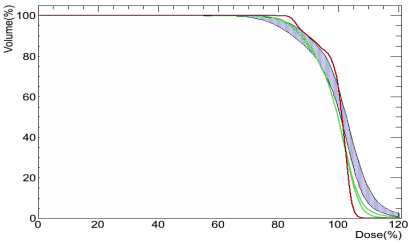

(m) CTV DVHs

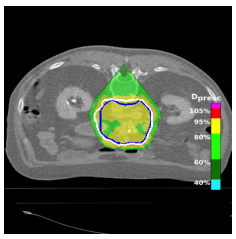

(b) H2 Static

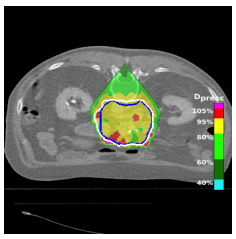

(f) 4DDSim

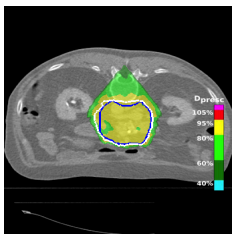

(j) 4DDReco Fx15

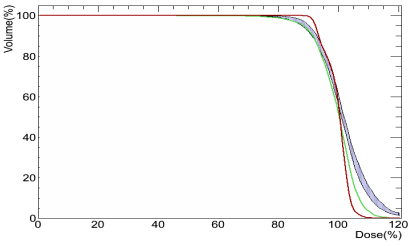

(n) CTV DVHs

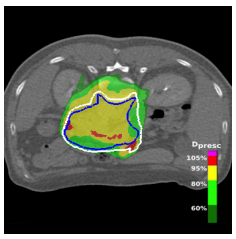

(c) H3 Static

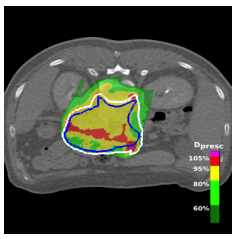

(g) 4DDSim

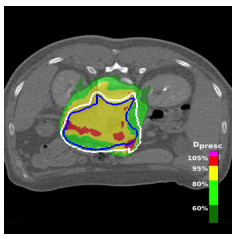

(k) 4DDReco Fx24

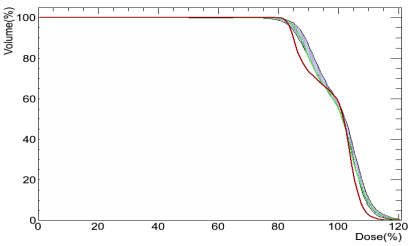

(o) CTV DVHs

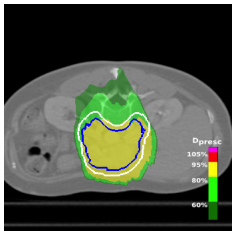

(d) H4 Static

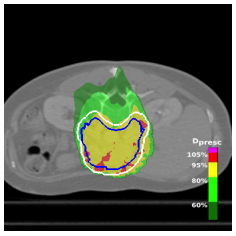

(h) 4DDSim

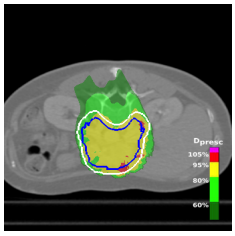

(l) 4DDReco Fx05

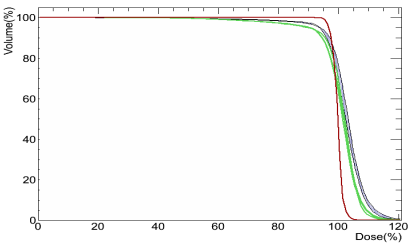

(p) CTV DVHs

Figure A.11: Continuation of figure A.10.

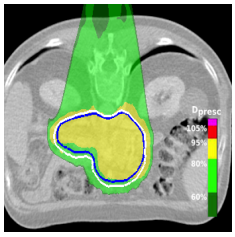

(a) H5 Static

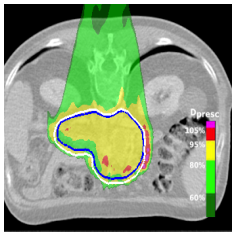

(e) 4DDSim

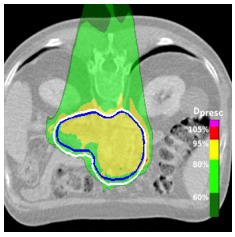

(i) 4DDReco Fx1

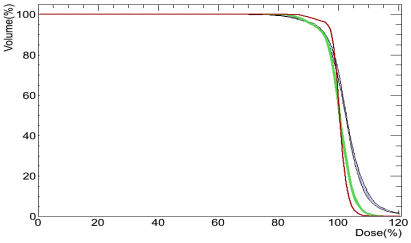

(m) CTV DVHs

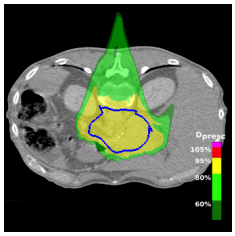

(b) H6 Static

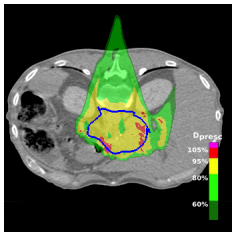

(f) 4DDSim

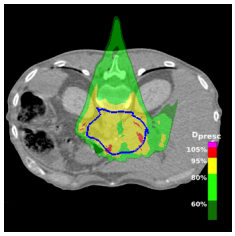

(j) 4DDReco Fx06

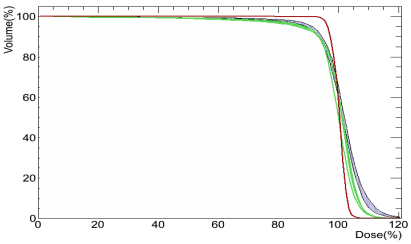

(n) CTV DVHs

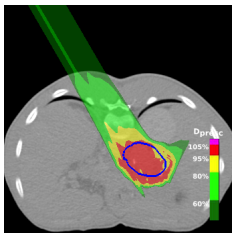

(c) H7 Static

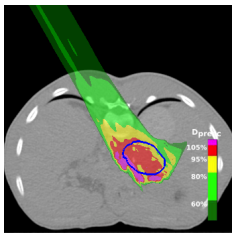

(g) 4DDSim

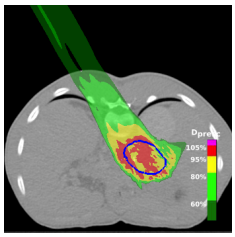

(k) 4DDReco Fx07

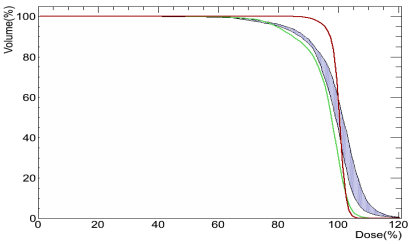

(o) CTV DVHs

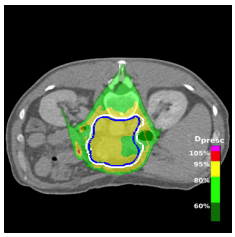

(d) H8 Static

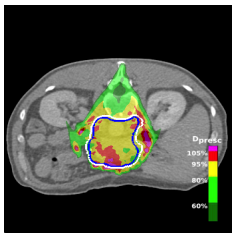

(h) 4DDSim

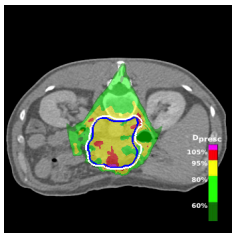

(l) 4DDReco Fx24

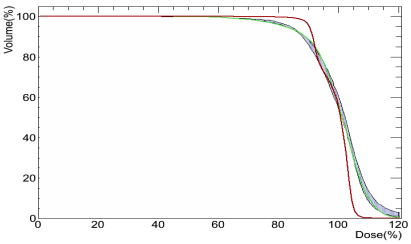

(p) CTV DVHs

Figure A.12: Continuation of figure A.10.

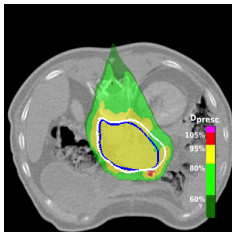

(a) H9 Static

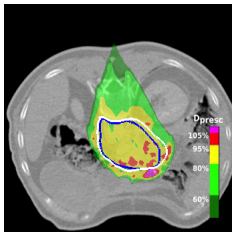

(e) 4DDSim

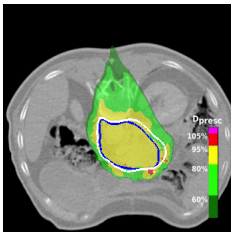

(i) 4DDReco Fx20

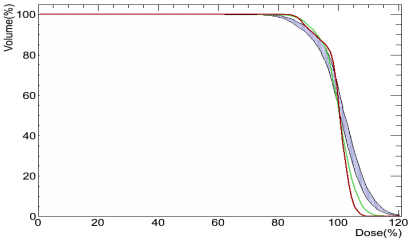

(m) CTV DVHs

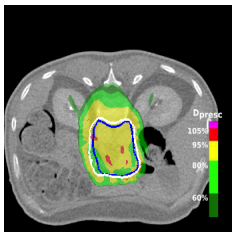

(b) H11 Static

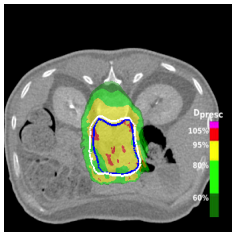

(f) 4DDSim

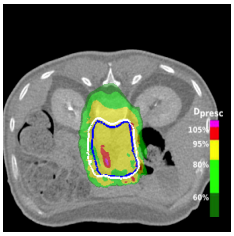

(j) 4DDReco Fx10

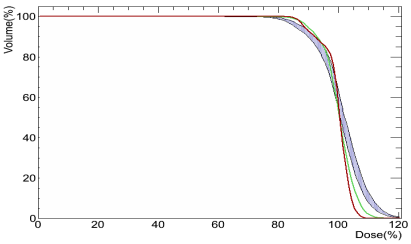

(n) CTV DVHs

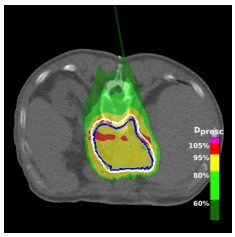

(c) H12 Static

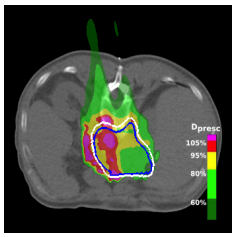

(g) 4DDSim

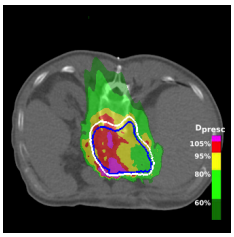

(k) 4DDReco Fx05

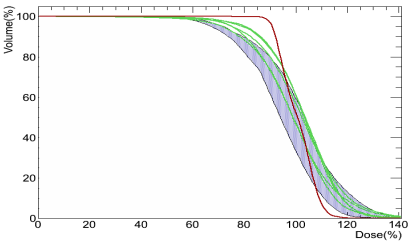

(o) CTV DVHs

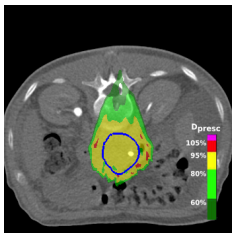

(d) H15 Static

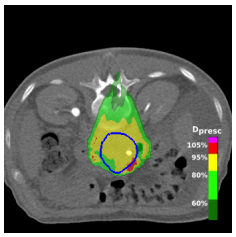

(h) 4DDSim

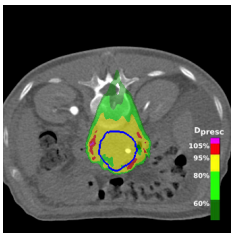

(l) 4DDReco Fx17

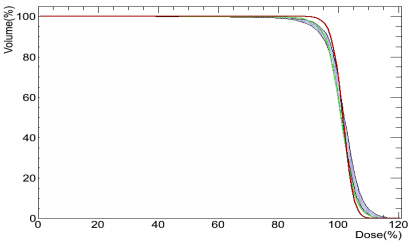

(p) CTV DVHs

Figure A.13: Continuation of figure A.10 - Patients with Carbon Ions.

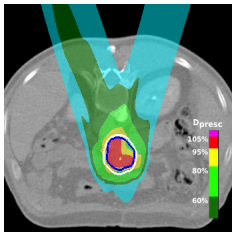

(a) H13 Static

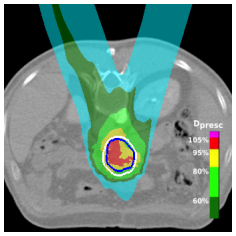

(c) 4DDSim

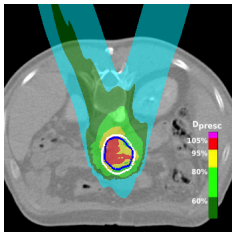

(e) 4DDReco Fx2

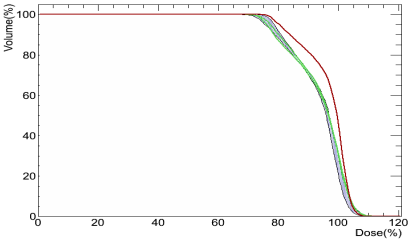

(g) CTV DVHs

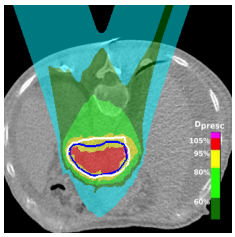

(b) H14 Static

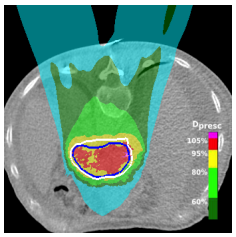

(d) 4DDSim

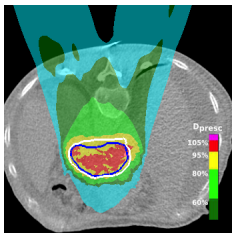

(f) 4DDReco Fx3

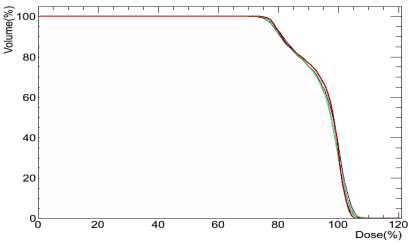

(h) CTV DVHs

Table A.6: Mean number of raster points (NP) per slice, standard deviation of the NP and spectrum of the modulation Index per patient and beam direction (in IEC coordinates).

Patient H1

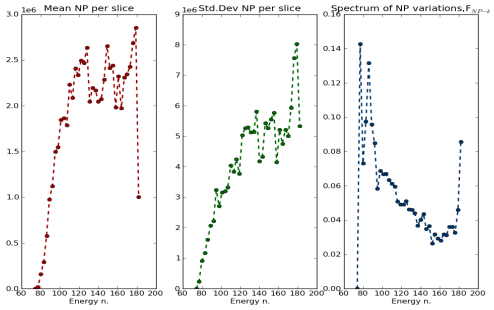

Gantry 20° Couch 0°

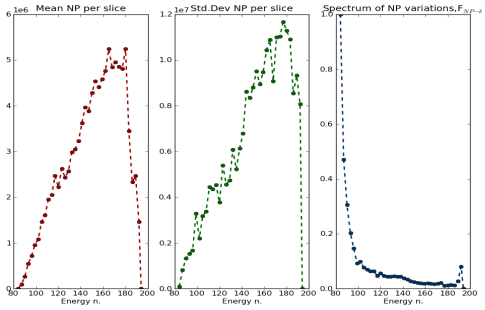

Gantry 340° Couch 0°

Patient H2

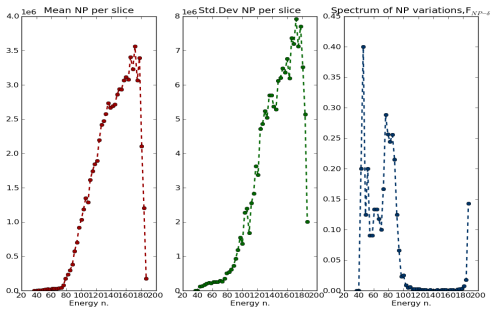

Gantry 30° Couch 0°

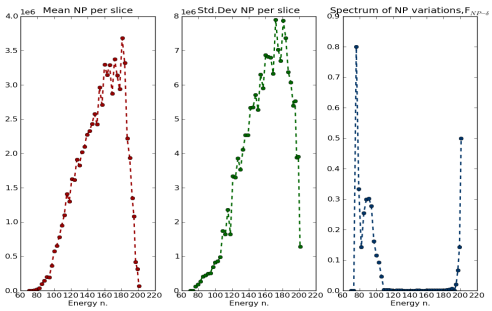

Gantry 330° Couch 0°

Patient H3

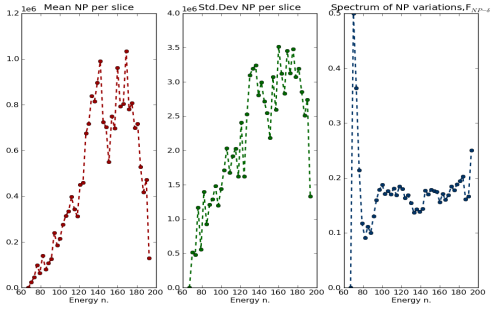

Gantry 300° Couch 340°

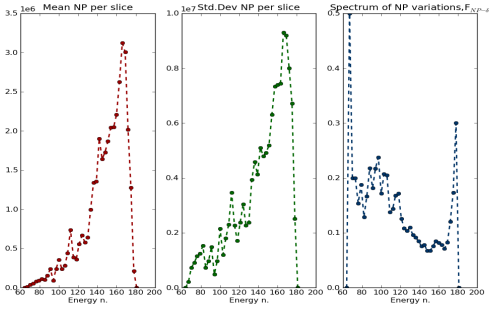

Gantry 20° Couch 35°

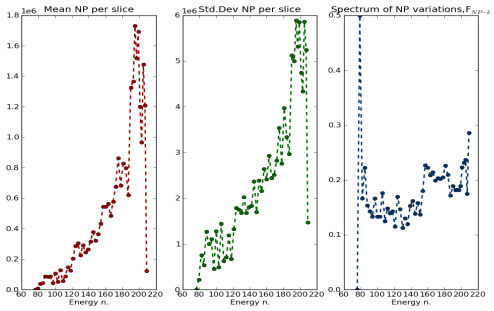

Gantry 60° Couch 20°

Patient H4

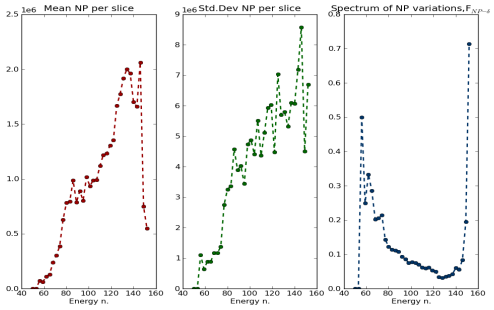

Gantry 340° Couch 0°

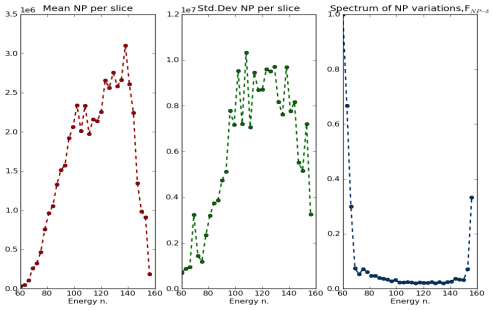

Gantry 25° Couch 0°

Table A.7: Continuation of table A.6.

Patient H5	
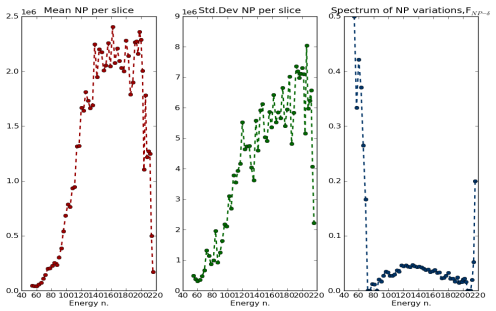	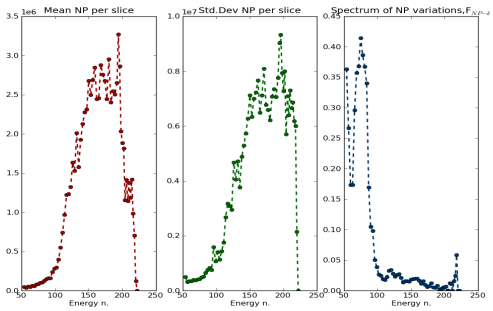
Gantry 350° Couch 0°	Gantry 15° Couch 0°
Patient H6	
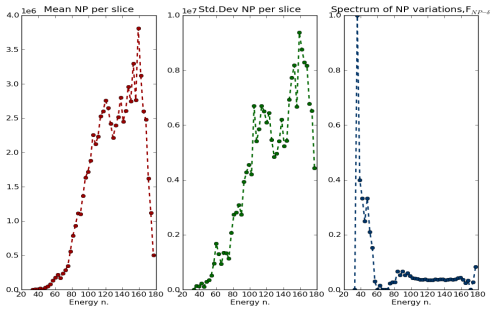	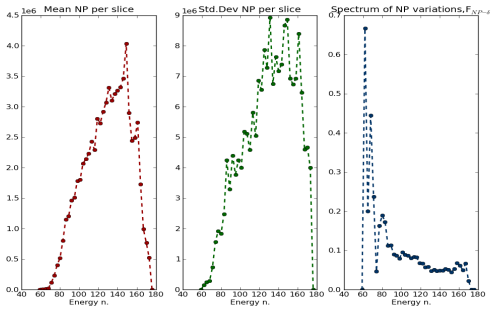
Gantry 345° Couch 0°	Gantry 20° Couch 0°
Patient H7	
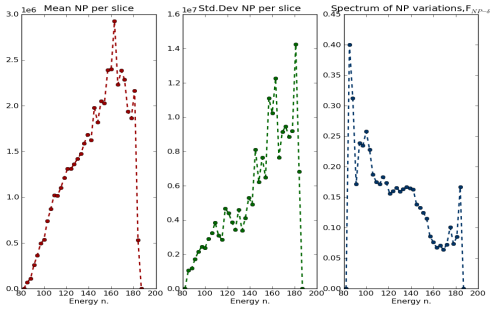	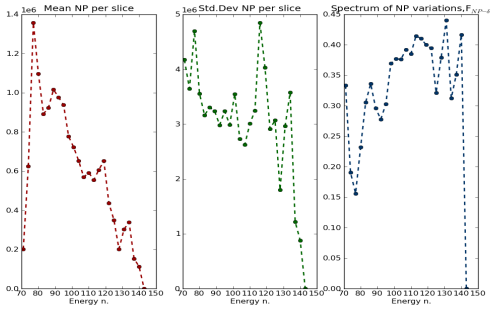
Gantry 330° Couch 0°	Gantry 20° Couch 0°
Patient H8	
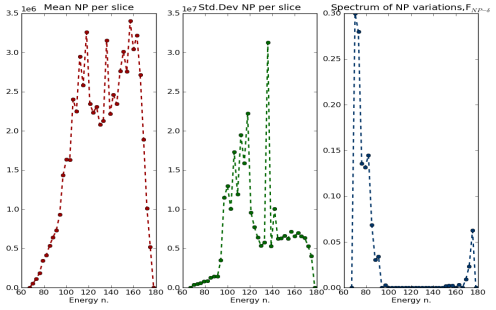	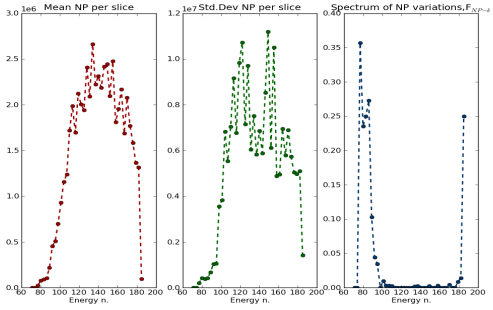
Gantry 340° Couch 0°	Gantry 30° Couch 0°
Patient H9	
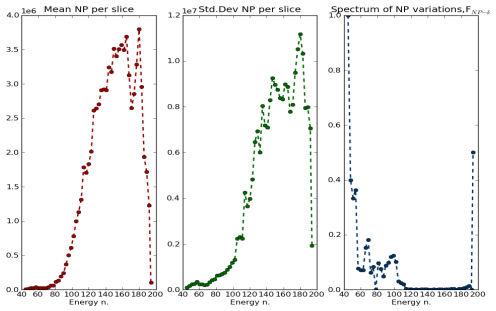	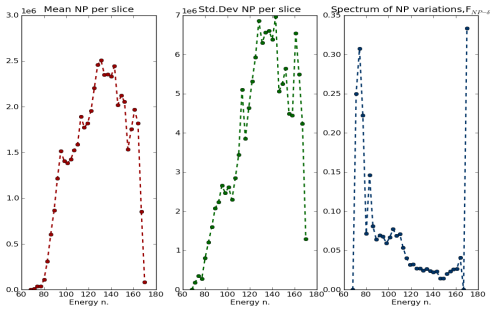
Gantry 330° Couch 0°	Gantry 15° Couch 0°

Table A.8: Continuation of table A.6.

Patient H11	
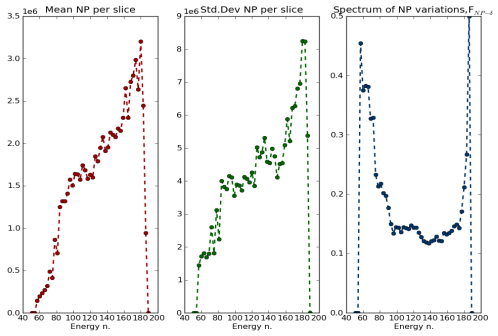	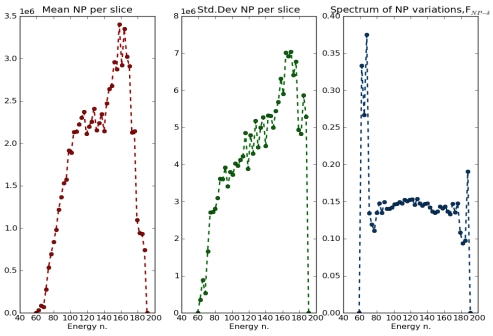
Gantry 330° Couch 330°	Gantry 30° Couch 30°
Patient H12	
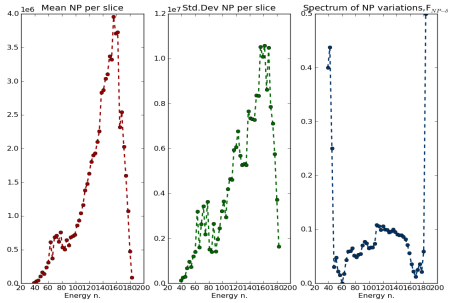	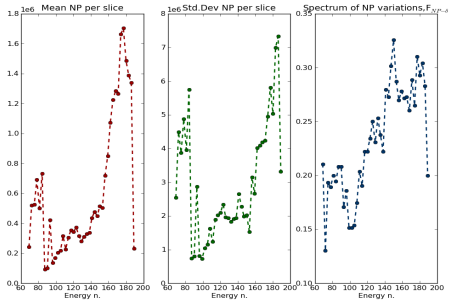
Gantry 350° Couch 0°	Gantry 90° Couch 0°
Patient H13	
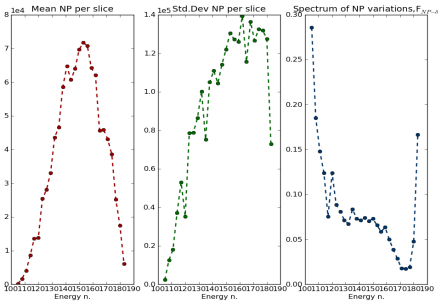	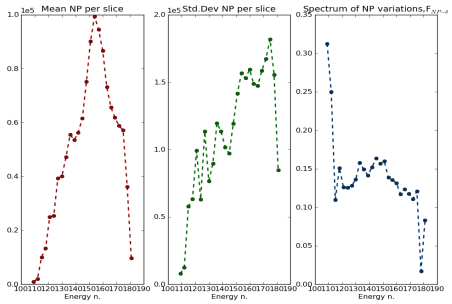
Gantry 20° Couch 20°	Gantry 340° Couch 340°
Patient H14	
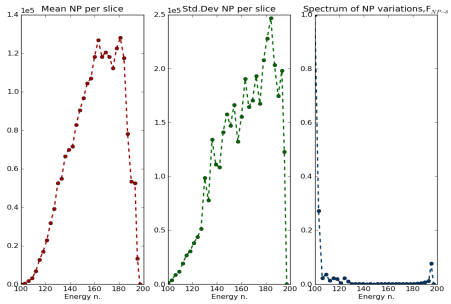	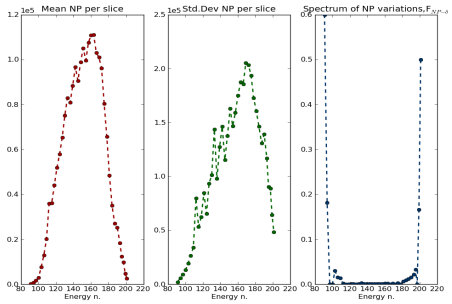
Gantry 20° Couch 0°	Gantry 340° Couch 0°
Patient H15	
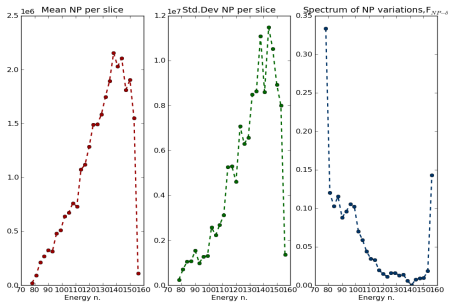	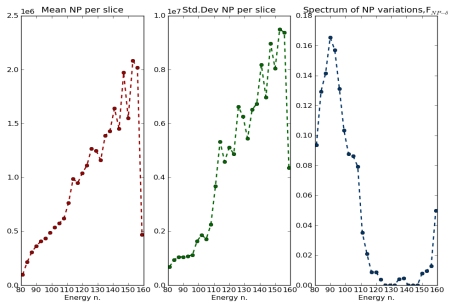
Gantry 20° Couch 0°	Gantry 340° Couch 0°

A.3 Magnetic resonance imaging - motion detection

Figure A.14: Median length of the vector field and its components inside the ITV of the patient H13 obtained from deformable image registration between the each of the MRI-bins and the bin-0 in the session 1 and 2. Dark blue: vector, yellow: cranio-caudal (z) direction, red: anterior-posterior (x) direction, cyan: right-left (y) direction, relative to the patient.

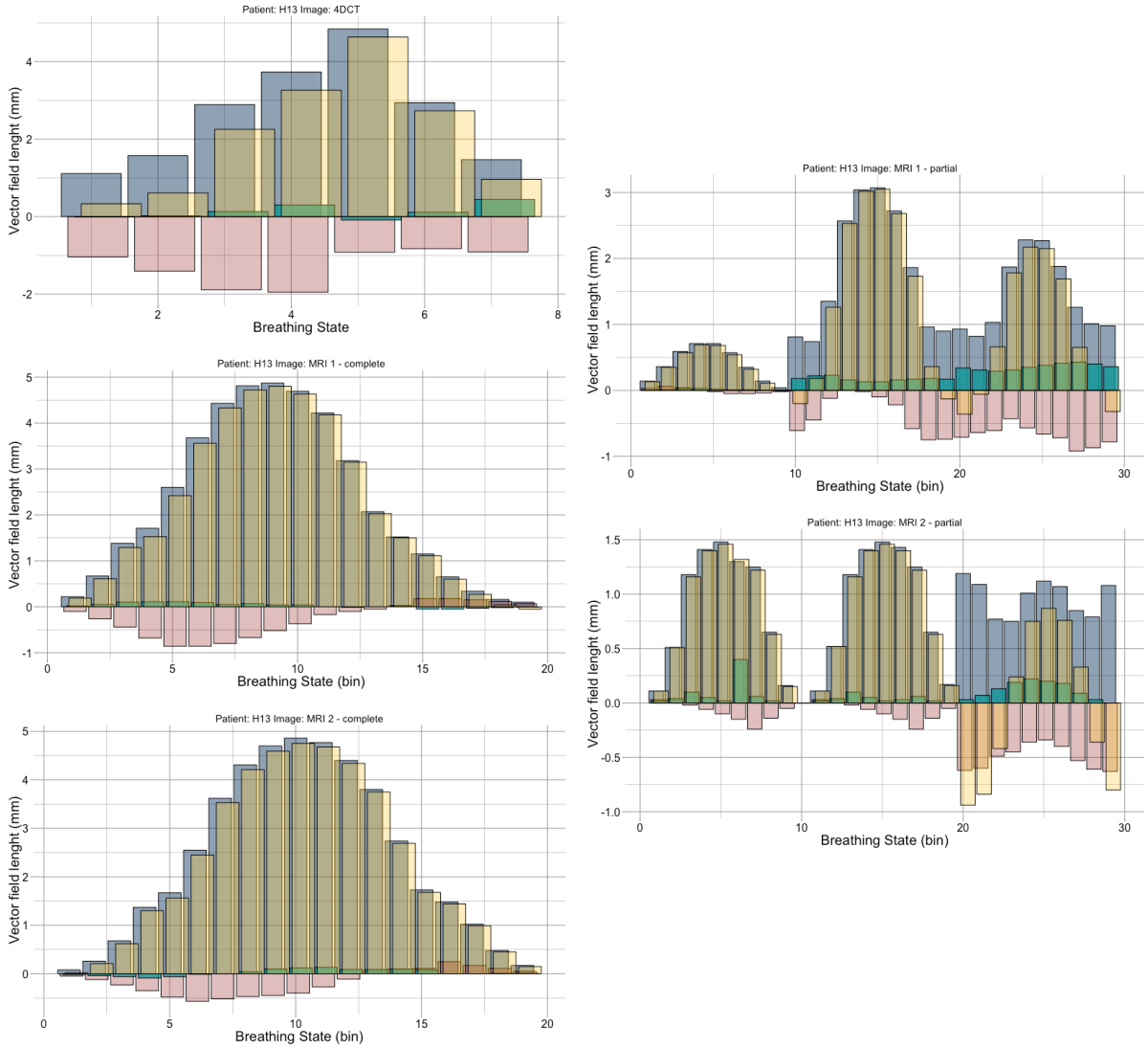

Figure A.15: Median length of the vector field and its components inside the ITV of the patient H14 obtained from deformable image registration between the each of the MRI-bins and the bin-0 in the session 1. Dark blue: vector, yellow: cranio-caudal (z) direction, red: anterior-posterior (x) direction, cyan: right-left (y) direction, relative to the patient.

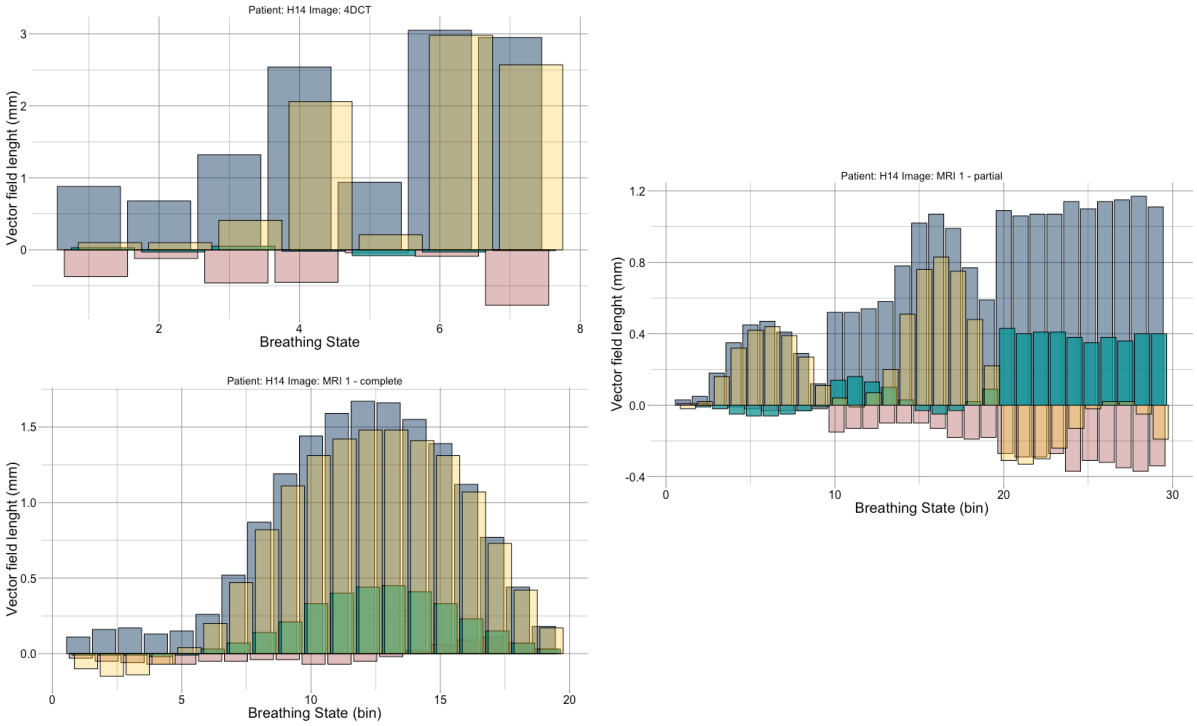

Figure A.16: Median length of the vector field and its components inside the ITV of the patient H15 obtained from deformable image registration between the each of the MRI-bins and the bin-0 in the session 1 and 2. Dark blue: vector, yellow: cranio-caudal (z) direction, red: anterior-posterior (x) direction, cyan: right-left (y) direction, relative to the patient.

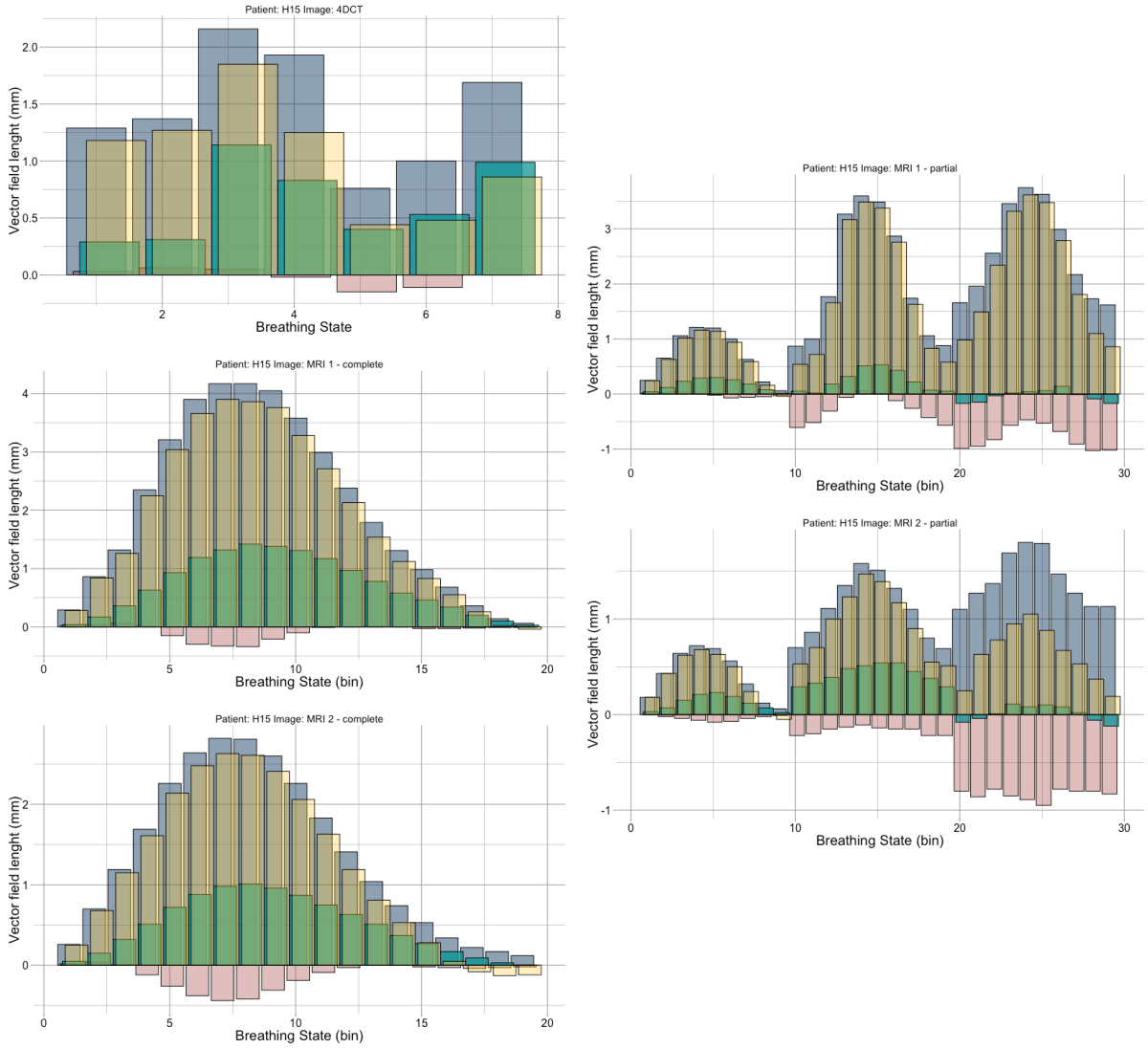

List of Tables

List of Figures

List of publications

Peer-reviewed articles

Batista, V.; Richter, D.; Chaudhri, N.; Naumann P., Herfarth, K., Jäkel, O.: *Significance of intra-fractional motion component in pancreatic patients treated with charged particles.* Submitted to the Radiation Oncology Journal.

Batista, V.; Richter, D.; Combs, S.E.; Jäkel, O.: *Planning strategies for Inter-fractional robustness in pancreatic patients treated with scanned carbon therapy.* Radiation Oncology 12.1 (2017): 94.

Batista, V.; Herfarth, K.; Richter, D.; Jäkel, O.; Chaudhri, N.: *Gated Internal Target margins for liver tumours treated under scanned Carbon-Ion radiotherapy.* Biomedical Physics & Engineering Express 3.1 (2017): 015029.

Conference contributions

Asim, Z.; Chen W.; Ferreira P.; Naumann P.; **Batista, V.**: *Definition of a threshold for plan adaptation in pancreatic patients under particle therapy*. 1st European Congress of Medical Physics, September 2016, Athens, Greece. Oral presentation.

Batista, V.; Saito, N.; Marcea, P.; Jäkel, O.; Pfaffenberger, A.: *MRI-based motion monitoring for 4D-dose calculation in abdominal patients*. 2^{nd} Heidelberg Symposium on Novel Techniques in Ion Beam Radiotherapy, March 2016, Heidelberg, Germany. Poster presentation.

Batista, V.; Chen, W.; Asim, Z. ; Bauer,J.; Parodi,K.; Herfarth,K.;Debus, J.;Jäkel, O.: *Validation of a tool for monitoring inter-fractional anatomical changes in abdominal patients*. 4D Treatment Planning Workshop 2015, Dresden, Germany. Poster presentation.

Batista, V.; Richter, D.; Jäkel, O.; Chaudhri, N.: *Gated Internal Target Volume Concept in Liver patients treated with Scanned Carbon Ion-beams*. Physics Session: Motion Management, 54th PTCOG Conference, San Diego, USA, May 2015. Oral presentation.

Batista, V.; Richter, D.; Combs, S.E.; Jäkel, O.: *Inter- and Intra-fractional Motion Robustness for Pancreatic Patients Treated With Scanned Carbon Ion Therapy*. International Journal of radiation Oncology Biology Physics, 90 (1) (2014) S921 -Proceedings

of the American Society for Radiation Oncology 56th Annual Meeting, San Francisco, USA. Poster presentation.

Batista, V.; Richter, D.; Jäkel, O.; Combs, S.: *Inter-fractional robustness of beam angles and margins in scanned carbon treatment of pancreatic tumors*. Radiotherapy and Oncology, 111 (Suppl.1) (2014) S152-S153. Proceedings of the ESTRO 33, April 2014, Vienna, Austria. Proffered papers: Physics 8 - Advancement in plan optimisation and evaluation. Oral presentation.

Batista, V.; Richter, D.; Jäkel, O.; Combs, S.E.: *Interplay effect on the plan quality for pancreatic patients treated with Scanned Delivery*. 4D Treatment Planning Workshop 2014, London, UK. Poster presentation.

Batista, V.; Richter, D.; Jäkel, O.;Combs, S.E.: *Treatment planning strategies for treatment of pancreatic tumors with scanned carbon ions considering interfractional organ motion*. 4D Treatment Planning Workshop 2013, Zürich, Switzerland. Poster presentation.

Curriculum Vitæ

Personal information

Full name:	Vânia Marisa Santos Batista
Place | date of birth:	Lisbon, Portugal | 2 February 1985
Parents:	António Manuel Marques Batista Susete Conceição Santos Batista

Education

July 2015	Master in Science *Master in "Advanced Physical Methods in Radiotherapy"*, **Medicine Faculty, Heidelberg University**, Heidelberg | Germany Thesis: Gated Internal Target concept for Liver Patients treated with Carbon Ion Therapy.
October 2008	Master in Science *Master in Physics Engineering*, **Universidade Técnica de Lisboa, Instituto Superior Técnico**, Lisbon | Portugal Thesis: Implementation of Intensity Modulated Radiotherapy Technique at Hospital de Santa Maria - Protocol and evaluation of planning systems
July 2008	Bachelor in Science *Bachelor in Physics Engineering*, **Universidade Técnica de Lisboa, Instituto Superior Técnico**, Lisbon | Portugal
July 2003	**High School Madeira Torres**, Torres Vedras | Portugal

Work experience

July 2013 - July 2016	Doctoral student and medical physicist at Heidelberg University Clinic, Heidelberg | Germany
May 2011 - Mar. 2013	Medical physicist at Centro Hospitalar Barreiro-Montijo, Barreiro | Portugal
Jan. 2009 - Apr. 2011	Medical physicist at Centro Hospialar Lisboa Norte, Lisbon | Portugal

Acknowledgement

Nothing in life is to be feared, it is only to be understood.
- Marie Curie -

This dissertation was supported by the Deutschen Forschungsgemeinschaft (DFG) within the Klinische Forschergruppe Schwerionentherapie (KFO 214) and by the University Hospital of Heidelberg.

First, I would like to express my special appreciation and thanks to my supervisor Prof. Dr. Oliver Jäkel, who has supported me throughout these three years, encouraging my research and for allowing me to grow as a research scientist and medical physicist. I would also like to thank to Dr. med. Stephanie E. Combs for giving me the opportunity to be part of this project and by all the support provided in these years.
Most of all, I am fully indebted to Dr. Daniel Richter, for his understanding, time, patience, and encouragement and for pushing me farther than I thought I could go. I am also deeply grateful to the all the others members from the Biophysics Group from GSI for the provided support and stimulating discussions, is especial to Dr. Christian Graeff, Dr. Sebastian Hild and Kristjan Anderle.
From the Heidelberg Ion-Beam Therapy Center, I would like to thank to the medical physics team, where I remark the help of Dr. Naved Chaudhri, Dr. Malte Ellerbrock, Dr. Julia Bauer, Swantje Ecker, Hannah Prokesch, Dr. Stephan Brons and everyone that contributed somehow, in the scientific or personal field, for the conclusion of this work. Also to the medical team, Prof. Dr. med. Klaus Herfarth, Dr. med. Matthias Uhl and Dr. med. Patrick Naumann, I´m specially thanks for all the support. In addition, thanks to the RTT staff, for all the help and support during measurements and other administrative tasks.
I wish to thank also to Prof. Dr. Katia Parodi, chair of the Experimental Medical Physics department at LMU, for her assistance during part of the project.
At the German Cancer Research Center (DKFZ), the help from Dr. Nami Saito, Paul Mercea, Dr. Asja Pfaffenberger, Dr. Christopher Rank and Regula Gnirs were essential to the conclusion of this thesis.
I thank to all my fellow office-mates along these years, with a especial thanks to Martin Härtig and Dr. Mutsumi Tashiro. Also a distinguished thank to my friends in the Heidelberg Ion-Beam Therapy Center and University Clinic of Heidelberg, especially to Dr. Wenjing Chen for the relaxing and funny moments and to Lorena Magallanes for

always listening and giving me words of encouragement.

Finally, I thank to my friends, family and to Joel for helping me survive all the stress from these years and not letting me give up. I promise them this will be my last thesis. Lastly, I´m grateful to Kenshin, the cat, that although he never read my thesis or provided any discussion, he was always present in the most difficult and happy moments of my life.